Proceedings of the

20th Particles and Nuclei International Conference PANIC2014

August 25–29, 2014

Hamburg, Germany

Editors: Alexander Schmidt, Christian Sander

Verlag Deutsches Elektronen-Synchrotron

Impressum

Proceedings of the 20th Particles and Nuclei International Conference (PANIC2014)

August 25–29, 2014, Hamburg, Germany

Conference homepage
`http://panic14.desy.de/`

Slides at
`https://indico.desy.de/event/panic14`

Online proceedings:
DOI: 10.3204/DESY-PROC-2014-04

Editors:
Christian Sander, Alexander Schmidt
March 2015
DESY-PROC-2014-04
ISBN 978-3-935702-91-1
ISSN 1435-8077

Published by
Verlag Deutsches Elektronen-Synchrotron
Notkestraße 85
22607 Hamburg
Germany

Printed by
Kopierzentrale Deutsches Elektronen-Synchrotron

Committees

Conference Chair: Matthias Kasemann

International Advisory Board

Torsten Akesson (Univ. Lund, Sweden), Ursula Bassler (CNRS-IN2P3, France), Reinhard Beck (Univ. Bonn, Germany), Sergio Bertolucci (CERN, Switzerland), Johannes Blümer (KIT, Germany), Martine Bosman (IFAE Barcelona, Spain), Philippe Chomaz (CEA, France), Luisa Cifarelli (Univ. di Bologna, Italy), Jean Cleymans (Univ. of Cape Town, South Africa), Umberto Dosselli (Frascati, Italy), George Dracoulis (ANU Canberra, Australia), Paula Eerola (Univ. of Helsinki, Finland), Masaki Fukushima (Univ. of Tokyo, Japan), Rolf-Dieter Heuer (CERN, Switzerland), Ralf Bernd Kaiser (IAEA, Austria), Matthias Kasemann (Chair, DESY, Germany), Young-Kee Kim (Univ. of Chicago, USA), Reiner Krücken (TRIUMF and UBC, Canada), Karlheinz Langanke (GSI, Germany), Nigel Lockyer (FNAL, USA), David MacFarlane (SLAC, USA), Victor Matveev (JINR Dubna, Russia), Giora Mikenberg (Weizmann, Israel), Richard Milner (MIT, U.S.A), Joachim Mnich (DESY, Germany), Hugh E. Montgomery (JLAB, USA), Tatsuya Nakada (EPFL, Switzerland), Stephan Paul (TU Munich, Germany), Mannque Rho (Hanyang Univ, South Korea), Johanna Stachel (Univ. Heidelberg, Germany), Horst Stöcker (GSI, Germany), Atsuto Suzuki (KEK, Japan), Nicholas Walker (DESY, Germany), Yifang Wang (IHEP, China), Nicolae-Victor Zamfir (ELI, Romania)

Programme Committee

Ralph Assmann (DESY, Germany), Rutger Boels (Univ. Hamburg, Germany), Will Brooks (Jeverson Lab, USA), Pierre Brun (Saclay, France), Jens Dilling (Triumf, Canada), Guido Drexlin (KIT, Germany), Laura Fabbietti (Tech. Univ. Munich, Germany), Sasha Glazov (DESY, Germany), Raphael Granier de Cassagnac (France), Michel Guidal (IPN Orsay, France), Johannes Haller (Univ. Hamburg, Germany), Stephanie Hansmann-Menzemer (Univ. Heidelberg, Germany), Dieter Horns (Univ. Hamburg, Germany), Josef Jochum (Univ. Tübingen, Germany), Andreas Jung (FNAL, USA), Ralf Kaiser (IAEA, Austria), David Kosower (Saclay, France), Kent Paschke (Virginia Univ., USA), Christian Sander (Chair, Univ. Hamburg, Germany), Alexander Schmidt (Chair, Univ. Hamburg, Germany), Thomas Schörner-Sadenius (DESY, Germany), Christoph Schwanda (OAW, Vienna, Austria), Frank Simon (Max-Planck-Inst. Munich, Germany), Andrew Sonnenschein (FNAL, USA), Hartmut Stadie (Univ. Hamburg, Germany), Raju Venugopalan (Brookhaven, USA), Janus Weil (FIAS, Univ. Frankfurt, Germany), Christian Weinheimer (Univ. Bonn, Germany), Drew Weissenberger (Jefferson Lab, USA), Dirk Zerwas (LAL Orsay, France)

Local Organizing Committee

Michaela Clayton - DESY; Manfred Fleischer - DESY; Michaela Grimm - DESY; Volker Gülzow - DESY; Magdalene Hack - University of Hamburg; Matthias Kasemann - DESY; Joachim Mnich - DESY; Kristina Price - DESY; Christian Sander - University of Hamburg; Peter Schleper - University of Hamburg; Alexander Schmidt - University of Hamburg; Thomas Schörner-Sadenius - DESY; Hartmut Stadie - University of Hamburg; Georg Steinbrück - University of Hamburg;

Preface

The PANIC Conference is a major international conference that brings together astroparticle physics, elementary particle physics and nuclear physics. The conference takes place every 3 years, and in 2014 the event was held in Hamburg (Germany). The previous conference was organised by the Massachusetts Institute of Technology (MIT) in Cambridge (Massachusetts, USA) in 2011.
This years conference was jointly organised by the Deutsches Elektronen Synchrotron (DESY) and the Institute for Experimental Physics of the University of Hamburg. One third of the 350 participants came from Germany, one third from Europe and one third from outside of Europe, it was a truly very international event. The conference took place from Monday, August 25, 2014 to Friday, August 29, 2014.
The programme included five days of plenary and parallel sessions and a poster session, all held in the main building of the University of Hamburg, right in the heart of the city of Hamburg. The social programme consisted of a reception at the Hamburg City Hall, a half-day excursion, a concert at DESY, a conference dinner, and a public evening lecture by Prof. Albrecht Wagner, former director of DESY.
During the conference, many results from the Large Hadron Collider (LHC) at CERN (Geneva, Switzerland) were presented together with final results from the experiments at the Tevatron collider at the Fermi National Accelerator Laboratory (Chicago) and at the HERA accelerator at DESY. A large number of physics studies were discussed also for an International Linear Collider (ILC) considered to be built in Japan. The conference programme included dedicated sessions on physics at the ILC and on the status of the project.
In neutrino and nuclear physics, there are a number of medium- and small-size experiments that provide highly accurate results. These experiments are often complementary to those at large accelerators at the energy frontier. The PANIC conference provided an excellent overview of these different fields.
The program was prepared in consultation with the international advisory committee (IAC). In the plenary sessions, 26 presentations of invited lectures and results from large experimental collaborations were given, while in the parallel sessions, a total of 220 talks were presented. The programme was completed by 28 posters, for which a poster contest was held. The three winning posters received a price and were presented in a dedicated plenary session.
DESY is one of the worlds leading accelerator centres. DESY researchers use the large-scale facilities at DESY and elsewhere to explore the microcosm in all its variety: high-energy particle collisions are used in elementary particle and astroparticle physics to investigate from the properties and interactions of elementary particles, and the brilliant light of state-of-the-art synchrotron sources and laser facilities is employed to study e.g.the behaviour of new types of nanomaterials or biomolecular processes that are essential to life. DESY scientists are involved in many international projects such as the LHC (experiments ATLAS and CMS), SuperKEKB (experiment Belle II), CTA and IceCube. DESY is also a central player in the preparatory work towards the next large-scale facility of particle physics, an e+e linear collider.
The particle physics and detector development group of Hamburg University studies the constituents of matter and their fundamental interactions using particle collisions at highest energies. The group is involved in detector construction, operation and data analysis of the Compact Muon Solenoid (CMS) experiment at the LHC. Research is done in several important aspects of particle physics using CMS data, from the study of the properties and production mechanisms of the top quark, the heaviest particle known today, to the search for new even heavier particles predicted by physics theories describing phenomena beyond the standard model of particle physics, such as supersymmetry.

Matthias Kasemann (conference chair), Hamburg, March 2015

Contents

Chapter 1

Plenary contributions

Neutrinos in Nuclear Physics

R. D. McKeown

Jefferson Lab, Newport News, VA, USA
Department of Physics, College of William and Mary, Williamsburg, VA, USA

DOI: http://dx.doi.org/10.3204/DESY-PROC-2014-04/305

Since the discovery of nuclear beta decay, nuclear physicists have studied the weak interaction and the nature of neutrinos. Many recent and current experiments have been focused on the elucidation of neutrino oscillations and neutrino mass. The quest for the absolute value of neutrino mass continues with higher precision studies of the tritium beta decay spectrum near the endpoint. Neutrino oscillations are studied through measurements of reactor neutrinos as a function of baseline and energy. And experiments searching for neutrinoless double beta decay seek to discover violation of lepton number and establish the Majorana nature of neutrino masses.

1 Introduction

The discovery of neutrino oscillations in the distribution of atmospheric neutrinos by the SuperKamiokande experiment in 1998 [1] was a major event in the history of neutrino physics. This result established that neutrino flavors oscillate and that at least one neutrino type has a non-zero rest mass. Subsequently, further experimental studies of neutrino oscillations and masses were pursued with increased vigor and broader scope. Soon thereafter, the Sudbury Neutrino Observatory (SNO) reported the observation of solar neutrinos via the neutral current [2]. The SNO result showed that the total neutrino flux (summed over all three flavors) is consistent with expectation in the standard solar model, and that the ν_e flux is reduced due to flavor transformations, explaining the long-standing solar neutrino puzzle. Shortly after that, the KamLAND experiment reported the observation a deficit of reactor antineutrinos [3] and subsequently a spectral distortion [4], establishing that electron antineutrinos oscillate with a large mixing angle in a manner completely consistent with expectation based on the SNO results.

In the decade since these major discoveries, there has been a great deal of effort to develop a program of experiments to further explore the properties of neutrinos. The important remaining questions include:

- What are the absolute values of neutrino masses (oscillation experiments only reveal squared mass differences Δm^2)?
- What is the correct ordering of the mass eigenstates ("normal" or "inverted" hierarchy)?
- Are the neutrino masses of a Majorana or Dirac type?
- What are the values of the mixing angles, and is there CP violation in the neutrino mixing matrix?

2 Absolute Neutrino Mass

From neutrino oscillation experiments, we now know the values of Δm^2 [5]:

$$\Delta m^2_{21} = 7.5 \times 10^{-5} \text{ eV}^2 \quad (1)$$

$$\Delta m^2_{31} = 2.4 \times 10^{-3} \text{ eV}^2. \quad (2)$$

Thus we can be sure that there is at least one neutrino mass eigenstate with a mass of at least $[\Delta m^2_{31}]^{1/2} \backsimeq 0.049$ eV. The endpoint energy in nuclear beta decay is modified by the effective neutrino mass

$$m_{\nu_e}^{(\text{eff})^2} = \sum_i |U_{ei}|^2 m^2_{\nu_i} \quad (3)$$

where the U_{ei} are neutrino mixing matrix elements the sum is over all the experimentally unresolved neutrino masses m_{ν_i}. During the last decade experiments studying tritium beta decay have constrained this effective neutrino mass to be [5]

$$m_{\nu_e}^{(\text{eff})} < 2 \text{ eV}. \quad (4)$$

So there is presently a gap between 0.05 eV and 2 eV where experiments are needed to establish the absolute mass scale of neutrinos.

The distribution of matter in the universe depends sensitively on the neutrino contribution to the total matter density. Neutrinos are very light compared to all other particles, so at the epoch of structure formation they have a non-negligible thermal velocity, which controls their free-streaming length. Since neutrinos do not clump on scales smaller than their free-streaming length this leads to smearing out of over-dense regions (structure) at small scales, leaving a characteristic imprint in the matter distribution. Current and upcoming surveys that probe the matter distribution can indirectly constrain or measure the sum of the neutrino masses. Current analyses constrain the sum of neutrino masses to be $\sum_i m_i < 0.23$eV(95%CL) [6]. In the next decade there are good prospects to reach, via multiple probes, a sensitivity at the level of $\sum_i m_i < 0.01$eV [7] . Nevertheless, it is essential to address the neutrino mass scale below 2 eV in terrestrial experiments.

The KATRIN experiment [8] is under construction at Forschungszentrum Karlsruhe and will provide measurements of the tritium endpoint spectrum with greater precision in the near future. This ambitious experiment utilizes a gaseous molecular tritium source. a pre-spectrometer to filter out lower energy electrons ($< E_0 - 0.3$ keV), a main spectrometer (resolution 0.93 eV), and a position sensitive detection system. The apparatus is 70 meters long and the main spectrometer has a diameter of 9.8 meters. The experiment will be sensitive to neutrino masses $m_{\nu_e}^{(\text{eff})} > 0.2$ eV with 90% CL (3 years running), extending the range of present knowledge by about an order of magnitude. Commissioning of the experiment is underway and KATRIN is expected to begin acquiring tritium decay data in 2016.

Improvements to the KATRIN experiment may be possible (for example using time of flight techniques) to further increase the sensitivity. However, the tritium source has reached the maximum density for transmission of the the 18 keV electrons of interest and a more sensitive spectrometer would need to be much larger than the main spectrometer of KATRIN. Therefore, it appears that another method may be necessary to make significant progress below 200 meV. A novel technique to detect the cyclotron radiation from a single electron in a uniform magnetic field using high-sensitivity microwave antennae has been proposed [9]. Preliminary R&D on this technique is in progress, and the first detection of cyclotron radiation from a single 30 keV electron has been reported at this conference and in [10].

3 Reactor Neutrinos

The neutrino mixing matrix contains 4 parameters: 3 mixing angles (θ_{12}, θ_{23}, and θ_{13}) and a CP violating phase δ_{CP}. The combination of solar neutrino experiments and KamLAND have provided a value of $\sin^2\theta_{12} \backsimeq 0.31$ [5]. In addition, accelerator based long baseline neutrino experiments determine $\sin^2\theta_{23} \backsimeq 0.39$ [5]. While there is room for improvement in these determinations, much attention has been focused in recent years on measuring the remaining angle θ_{13}. This problem has been effectively attacked by three reactor neutrino experiments: Double CHOOZ [11], RENO [12], and Daya Bay [13].

The formula for survival of electron neutrinos (or antineutrinos) in the 3 flavor case is given by

$$\begin{aligned} P(\nu_e \to \nu_e) &= 1 - \sin^2 2\theta_{13}(\cos^2\theta_{12}\sin^2\Delta_{31} + \sin^2\theta_{12}\sin^2\Delta_{32}) \\ &\quad - \cos^4\theta_{13}\sin^2 2\theta_{12}\sin^2\Delta_{12} \end{aligned} \tag{5}$$

where $\Delta_{ij} \equiv \Delta m^2_{ij} L/4E_\nu$. Note that the 2 terms oscillate with different "frequencies" depending on the values of the Δm^2_{ij}. Thus one can choose the baseline L to maximize (or minimize) the sensitivity to particular Δm^2_{ij}. For an average reactor antineutrino energy of 4 MeV and a value of $\Delta m^2_{32} = (2.43 \pm 0.13) \times 10^{-3}$ eV^2 one finds that the optimum distance for the first minimum is $L \simeq 2000$ m.

While all three reactor experiments have reported consistent values of θ_{13}, the results from the Daya Bay experiment in China are the most precise. The Daya Bay nuclear power plant consists of 6 reactor cores in two groups (Daya Bay and Ling Ao) with a total thermal power capacity of 17.6 GW. The experiment includes 8 antineutrino detectors, each with 20 Tons of Gd-loaded liquid scintillator. Two detectors are located near (364 m) the 2 Daya Bay reactors and two are located near ($\sim$ 500 m) the 4 Ling Ao reactors. Four detectors are located in the far experimental hall at 1912 m from the Daya Bay cores and 1540 m from the Ling Ao cores. The near detectors monitor the antineutrino fluxes from the two reactor groups so that the far detectors are sensitive to the degree of neutrino oscillations at the longer baseline. This method enables measurement of the oscillation effect with only slight sensitivity to the absolute flux of antineutrinos.

The Daya Bay experiment took data with only 6 detectors deployed from December 2011 to July 2012. In summer 2012, two additional detectors were installed, one at the Ling Ao location and one at the far location, which completed the final 8 detector configuration of the experiment described above. Data taking resumed after October 2012. New results, based on the complete data set of the 6-AD period with the addition of the 8-AD period from October 2012 to November 2013 (a total of 621 days) were recently reported [14]. The Daya Bay data display a substantial deficit in measured flux at the far site relative to the near sites, and also a distortion of the measured energy spectrum at the far site, consistent with the interpretation of neutrino oscillations as shown in Fig. 1.

The neutrino oscillation parameters are extracted from a fit to the rates and relative spectral shapes observed at the near and far sites, with the overall normalization of the flux as an independent parameter. The results yield the best fit values

$$\sin^2 2\theta_{13} = 0.084 \pm 0.005 \tag{6}$$

$$\Delta m^2_{ee} = 2.44^{+0.10}_{-0.11} \times 10^{-3}\ (\text{eV})^2 \tag{7}$$

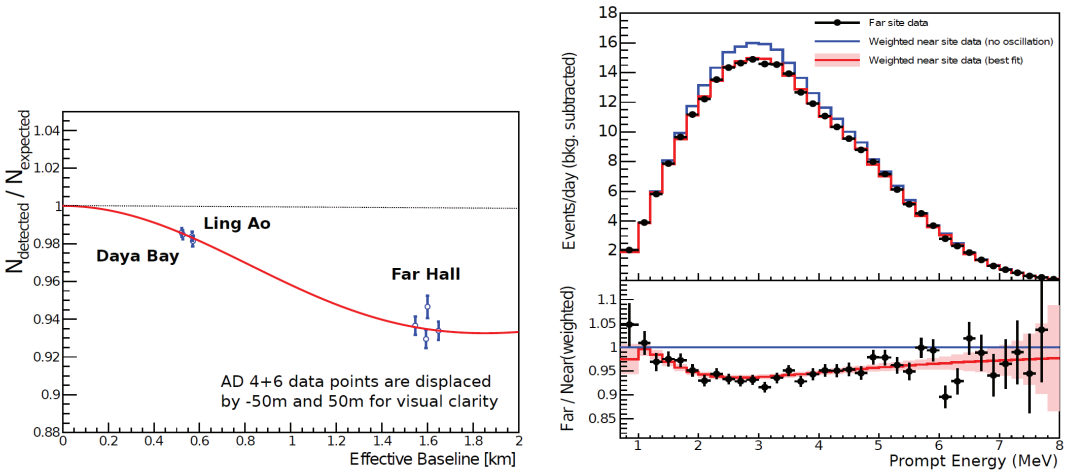

Figure 1: Daya Bay results reported in [14]. (left) Ratio of the detected to expected rates at the 8 antineutrino detectors (ADs) located in three experimental halls as a function of effective baseline. The expected signal accounts for the best-fit reactor antinuetrino flux normalization. The fitted oscillation survival probability is given by the red curve. (right) The top panel shows the measured background-subtracted spectrum at the far site compared to the expected spectrum based on the near site data both without oscillation and with the best-fit oscillation included. The bottom panel shows the ratio of the far site spectrum to the weighted near site spectrum. The red curve shows the expectation at the best-fit oscillation values from the rate and spectral analysis.

where Δm^2_{ee} is defined by $\sin^2(\Delta {m_{ee}}^2 L/4E_\nu) \equiv \cos^2\theta_{12}\sin^2\Delta_{31} + \sin^2\theta_{12}\sin^2\Delta_{32}$. This value of Δm^2_{ee} is consistent, with comparable uncertainty, to the value of $\Delta m^2_{\mu\mu}$ determined by muon neutrino disappearance experiments.

The Daya Bay collaboration has also recently reported a measurement of the absolute flux of antineutrinos [14], shown in Fig. 2. This first precision measurement at larger average baseline (573 m) is consistent with 21 previous short baseline experiments, indicating a flux deficit of $5.3 \pm 2.2\%$ relative to recent model predictions [15, 16].

New reactor neutrino projects [17], JUNO and RENO50, are being planned by international collaborations to constrain neutrino oscillation parameters more precisely and to determine the mass hierarchy. The RENO50 experiment would be sited 50 km away from the Hanbit(Yonggwang)nuclear plant in South Korea. The JUNO experiment would be sited in southern China, 53 km equidistant from two new nuclear power plants currently under construction: Yangjiang (17.4 GWth) and Taishan (18.4 GWth). For JUNO, spherical 20kT liquid scintillator detector would be deployed at a depth of 700 m, with almost complete photocathode coverage to achieve the energy resolution of 3% necessary to see the interference pattern in the energy spectrum for mass hierarchy determination. After 6 years of running, JUNO aims to achieve a $\Delta\chi^2 = 14$ determination of the mass hierarchy. In addition, the values of ${\Delta m_{12}}^2$, ${\Delta m_{23}}^2$ and $\sin^2\theta_{12}$ will be measured with substantially higher precision than at present.

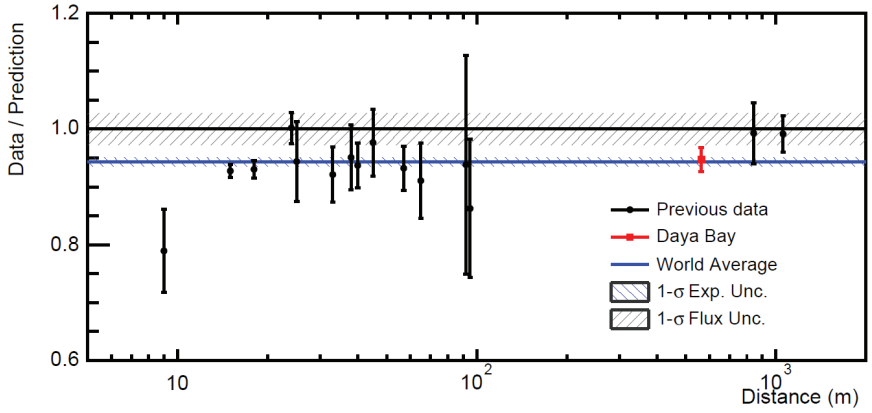

Figure 2: Measurements of antineutrino flux as reported in [14]. The reactor antineutrino interaction rate of the 21 previous short-baseline experiments as a function of the distance from the reactor, normalized to the Huber+Mueller model prediction [15, 16]. The Daya Bay result is placed at the effective baseline of 573 m. The rate is corrected for the survival probability at the distance of each experiment, assuming standard three-neutrino oscillation. The horizontal bar (blue) represents the global average of all experiments and its 1σ uncertainty. The 2.7% reactor flux uncertainty is shown as a band around unity.

4 Neutrinoless Double Beta Decay

Double beta decay is a rare transition between two nuclei with the same mass number A involving change of the nuclear charge Z by two units. The decay can proceed only if the initial nucleus is less bound than the final one, and both must be more bound than the intermediate nucleus. These conditions are fulfilled in nature for many even-even nuclei, and only for them. Typically, the decay can proceed from the ground state (spin and parity always 0^+) of the initial nucleus to the ground state (also 0^+) of the final nucleus, although the decay into excited states (0^+ or 2^+) is in some cases also energetically possible. Such nuclei can decay by the second order weak process, known as $2\nu\beta\beta$ in which two antineutrinos as well as two electrons are emitted. The summed energy of the two electrons is a continuous distribution ranging from $2m_e$ to the endpoint energy E_0 defined by the Q value of the decay. This process conserves lepton number, takes place for both Dirac and Majorana neutrinos, and is the rarest decay process in nature for which half-lives have been measured.

For neutrinoless double beta decay, $0\nu\beta\beta$, the distribution of summed β energies would exhibit a distinctive monoenergetic peak at the endpoint E_0. If it occurs, this process implies nonconservation of lepton number and would imply that neutrinos were Majorana type fermions. The half life for this process can be written

$$T_{1/2}^{0\nu\,-1} \;=\; G^{0\nu}(E_0, Z)\left|M^{0\nu}\right|^2 \langle m_{\beta\beta}\rangle^2 \tag{8}$$

where $G^{0\nu}$ is the exactly calculable phase space integral, $\langle m_{\beta\beta}\rangle$ is the effective neutrino mass and $M^{0\nu}$ is the nuclear matrix element (calculated using nuclear models). The effective neutrino

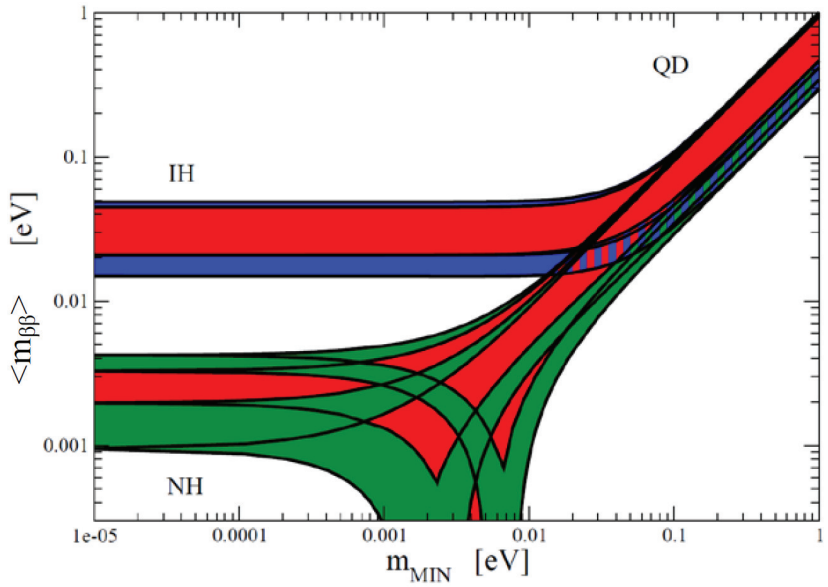

Figure 3: Allowed values of $\langle m_{\beta\beta} \rangle$ as a function of the lightest neutrino mass for the inverted (IH) and normal (NH) hierarchies (QD stands for "quasidegenerate"). The red, blue and green bands correspond to different allowed regions for the unknown CP violating phases in Eq. 9 and allowed 1σ variation in the other known neutrino parameters. (From the Particle Data Group [5].)

mass is

$$\langle m_{\beta\beta} \rangle = | \sum_i {U_{ei}}^2 m_{\nu_i} | \ , \tag{9}$$

where the sum is only over light neutrinos ($m_i < 10$ MeV), and contains the sensitivity to the neutrino masses and the elements of the neutrino mixing matrix U_{ei}. The U_{ei} depend upon the mixing angles discussed above, but also two additional phases that do not contribute to neutrino oscillation experiments. The range of allowed values of $\langle m_{\beta\beta} \rangle$ is indicated in Fig 3.

As can be seen in Fig. 3 the case of inverted mass hierarchy can lead to substantial values of $\langle m_{\beta\beta} \rangle$ even for very light values of the smallest neutrino mass. Thus there is considerable interest in performing experiments to address this region of parameter space. The current set of worldwide experimental efforts is summarized in Table 1. These efforts aim to achieve a sensitivity exceeding 10^{26} years in the next 5 years, and provide crucial information on background reduction in order to assess the feasibility of scaling the next generation experiment up to the Tonne scale. Complete coverage of the inverted mass hierarchy band in Fig. 3 will require multi-Tonne scale experiments.

Table 1: Current double beta decay projects, the fiducial isotopic mass, and the currently achieved half-life limit (90% CL).

Project	Isotope	Isotope fiducial mass (kg)	Currently achieved $T_{1/2}$ limit (10^{26} years)
CUORE	^{130}Te	206	> 0.028 [18]
Majorana	^{76}Ge	24.7	
GERDA	^{76}Ge	18-20	> 0.21 [19]
EXO200	^{136}Xe	79	> 0.11 [20]
NEXT-100	^{136}Xe	100	
SuperNEMO	^{82}Se, +	7	> 0.001 [21]
KamLAND-Zen	^{136}Xe	434	> 0.19 [22]
SNO+	^{130}Te	160	
LUCIFER	^{82}Se	8.9	

5 Summary

The study of neutrino properties with nuclear physics experiments is a very active field, with many experiments in progress and others in the planning stage. The absolute neutrino mass should be constrained by KATRIN to 0.2 eV before the end of the decade. Beyond KATRIN, R&D on the Project 8 method may offer a window to higher sensitivity measurements in the future. The present generation of reactor experiments will continue to reduce the uncertainties in θ_{13} and $\Delta {m_{ee}}^2$, and further study the flux and spectrum of reactor antineutrinos. A future experiment, JUNO, will be constructed in China with excellent potential to address the neutrino mass hierarchy. And an impressive suite of double beta decay experiments is underway that will extend the sensitivity towards the inverted mass hierarchy region in $\langle m_{\beta\beta} \rangle$.

These are indeed exciting times in the field of neutrino physics, with historic discoveries in the recent past, and the promise of much more to come in the future.

Acknowledgments

The recent Daya Bay results were first reported by Dr. Chao Zhang at the Neutrino 2014 conference, and I am very grateful to Dr. Zhang for supplying me with this material. The financial support of the U.S. National Science Foundation grant PHY-1205411 is gratefully acknowledged along with the support of the U.S. Department of Energy, Office of Science, Office of Nuclear Physics under contract DE-AC05-06OR23177.

References

[1] Y. Fukuda, *et al.*, Phys. Rev. Lett. **81**, 1562 (1998).

[2] Q. R. Ahmad *et al.*, Phys. Rev. Lett. **89**, 011301 (2002).

[3] K. Eguchi *et al.*, Phys. Rev. Lett. **90**, 021802 (2003).

[4] T. Araki *et al.*, Phys. Rev. Lett. **94**, 081801 (2005).

[5] J. Beringer *et al.* (Particle Data Group), Phys. Rev. **D86**, 010001 (2012).

[6] P. A. R. Ade, *et al.*, Astron. Astrophys. DOI: 10.1051/0004-6361/201321591 (2014) .

[7] K. N. Abazajian, et al., Astropart. Phys. 35, 177 (2011).

[8] G. Drexlin, *et al.*, Advances in High Energy Physics, 2013, Article ID 293986 (2013) .

[9] J. Formaggio and B. Monreal, Phys. Rev. D **80**, 051301(R), 2009.

[10] D. M. Asner, *et al.*, arxiv: 1408.5362 (2014).

[11] Y. Abe, *et al.*, Phys. Rev. D **86**, 052008 (2012).

[12] J. K. Ahn, *et al.*, Phys. Rev. Lett. 108, 191802 (2012).

[13] F. P. An, *et al.*, Phys. Rev. Lett. **108**, 171803 (2012); F. P. An, *et al.*, Phys. Rev. Lett. **112**, 061801 (2014); F. An, *et al.*, Nucl. Instr. Meth. A. **685**, 78 97 (2012); F. P. An, *et al.*, Chinese Phys. C. **37**, 011001 (2013). 569-647 (2003).

[14] Chao Zhang, https://indico.fnal.gov/getFile.py/access?contribId=256&sessionId=15&resId=0&materialId=slides&confId=8022 and to be published.

[15] P. Huber, Phys. Rev. C **84**, 024617 (2011).

[16] Th. A. Mueller, *et al.*, Phys. Rev. C **83**, 054615 (2011).

[17] L. Wen, https://indico.fnal.gov/materialDisplay.py?contribId=376&sessionId=15&materialId=slides&confId=8022 and to be published.

[18] E. Andreotti *et al.*, Astropart. Phys. **34**, 822 (2011).

[19] M. Agostini *et al.*, Phys. Rev. Lett. **111**, 122503 (2013) .

[20] J.B. Albert *et al.*, Nature **510**, 229-234 (2014).

[21] R. Arnold, *et al.*, Phys. Rev. D **89**, 111101 (2014).

[22] A. Gando *et al.*, (KamLAND-Zen Collaboration)] Phys. Rev. Lett. **110**, 062502 (2013).

Hadron structure from lattice QCD - outlook and future perspectives

Constantia Alexandrou

Department of Physics, University of Cyprus, PO Box 20537, 1678 Nicosia, Cyprus,
Computation-based Science and Technology Research Center, Cyprus Institute, 20 Kavafi Str., Nicosia 2121, Cyprus,
NIC, DESY, Platanenallee 6, D-15738 Zeuthen, Germany

DOI: http://dx.doi.org/10.3204/DESY-PROC-2014-04/307

We review results on hadron structure using lattice QCD simulations with pion masses close or at the physical value. We pay particular attention to recent successes on the computation of the mass of the low-lying baryons and on the challenges involved in evaluating energies of excited states and resonance parameters, as well as, in studies of nucleon structure.

1 Introduction

An impressive progress in algorithms and increased computational resources have allowed lattice QCD simulations with dynamical quarks with masses fixed at their physical values. Such simulations remove the need for a chiral extrapolation, thereby eliminating a significant source of a systematic uncertainty that has proved difficult to quantify in the past. However, new challenges are presented: An increase of statistical noise leads to large uncertainties on most of the observables of interest. New approaches to deal with this problem are being developed that include better algorithms to speed up the computation of the quark propagators, as well as, efficient (approximate) ways to increase the statistics. Another challenge is related to the fact that most of the particles become unstable if the lattice size is large enough and methods to study decays on a finite lattice in Euclidean time need further development.

In this talk we review recent results on hadron structure obtained using improved discretization schemes, notably Wilson-type fermion actions and domain wall fermions. In particular, the Wilson-type twisted mass fermion (TMF) action is particularly suitable for hadron structure studies, mainly due to the automatic $\mathcal{O}(a)$ improvement, where a is the lattice spacing. Several TMF ensembles have been produced including an ensemble simulated with two degenerate light quarks ($N_f = 2$) with mass being approximately the physical value, which, for technical reasons, also includes a clover term in the action but avoids smearing of the gauge links [1]. We will refer to this ensemble as the 'physical point ensemble' and present a number of new results. The other TMF ensembles are simulated with light quarks having masses larger than physical but where simulations are performed for three values of a allowing to study the dependence on the lattice spacing and to take the continuum limit. These ensembles include simulations with strange and charm quarks in the sea ($N_f = 2 + 1 + 1$) besides $N_f = 2$ TMF ensembles. In particular, we will use an $N_f = 2 + 1 + 1$ ensemble having a pion mass $m_\pi = 373$ MeV

to study lattice systematics by performing a high statistics analysis including all disconnected contributions to key nucleon observables.

2 Lattice formalism

An *ab Initio* non-perturbative solution of Quantum Chromodynamics (QCD) is based on defining the theory on a four-dimensional Euclidean lattice that ensures gauge invariance. While this approach allows a direct simulation of the original theory, it introduces systematic uncertainties. These so called lattice artifacts need to be carefully investigated before lattice QCD results can be compared to observables. In summary, in order to obtain final results in lattice QCD we need to take into account the following:

- Due to the finite lattice spacing, simulations for at least three values of a are needed in order to take the continuum limit $a \to 0$.
- Due to the finite lattice volume $L^3 \times T$, simulations at different volumes are needed in order to take the infinite volume limit $L \to \infty$. For zero-temperature calculations, as the ones reported here, the temporal extent T is typically twice the spatial extent L.
- Due to the tower of QCD eigenstates entering a typical correlation function one needs a careful identification of the hadron state of interest. How severe this so called contamination due to the excited states is differs depending on the observable e.g. for the nucleon axial charge g_A is found to be minimal, while for the σ-terms is large.
- In most hadron structure calculations contributions arising from the coupling of e.g. the electromagnetic current to sea quarks are neglected. These so called disconnected contributions are technically difficult to evaluate and have large gauge noise. They thus require new techniques and much larger statistics as compared to the connected contributions. Taking advantage of new approaches that are particularly suited for new computer architectures such as graphic cards (GPUs) the evaluation of these diagrams to sufficient accuracy has become feasible. This has been demonstrated for pion masses of about 300 MeV to 400 MeV [2, 3, 4, 5]. Their applicability for the physical point is being tested.
- Up to very recently, lattice QCD simulations were performed at larger than physical values of the light quark masses and thus the results required chiral extrapolation. Simulations with light quark masses fixed to their physical values are now feasible, which eliminates a systematic error inherent in all lattice QCD computations in the past. However, most lattice QCD results at the physical point are still preliminary since lattice artifacts have not been studied to the required accuracy. This issue is currently being addressed.

In order to evaluate hadron masses one needs the computation of two-point functions. For a hadron h we construct the two-point function of momentum $\mathbf{p}$ by acting on the vacuum with a creation operator $J_h^\dagger$ that has the quantum numbers of h

$$\langle J_h(t_s) J_h^\dagger(0)\rangle = \sum_{n,\mathbf{x}} e^{i\mathbf{p}.\mathbf{x}} \langle 0|J_h\, e^{-H_{QCD} t_s}|n><n|J_h^\dagger|0\rangle \quad (1)$$

$$= \sum_n |\langle 0|J_h|n\rangle|^2 e^{-E_n t_s} \overset{t_s\to\infty;\mathbf{p}=\mathbf{0}}{\longrightarrow} |\langle 0|J_h|h\rangle|^2\, e^{-m_h t_s}, \quad (2)$$

which yields its mass for $\mathbf{p} = \mathbf{0}$ in the large Euclidean time limit. Note that the noise to signal increases with t_s e.g. like $e^{(m_h - \frac{3}{2}m_\pi)t_s}$ for a baryon and thus in any lattice QCD computation there is a delicate balance between taking the large Euclidean time limit and controlling the gauge noise. So called smearing techniques are developed that allow the construction of interpolating fields that have larger overlap with the ground state and equivalently smaller overlap with excited states so that the latter are damped out faster.

3 Recent achievements

A number of collaborations are currently producing simulations with physical values of the quark mass with each collaboration typically using a different $\mathcal{O}(a)$-improved discretization scheme. Notably, the MILC [6], BMW (Budapest-Marseille-Wuppertal) [7] and ETM (European Twisted Mass) [1] collaborations have already generated simulations with light quark masses fixed to their physical value using staggered, clover and twisted mass fermions, respectively. Clover gauge configurations have also been produced by the QCDSF [8] and PACS-CS [9] collaborations at near physical pion mass value. Recently the RBC/UKQCD collaboration reported results using domain wall fermions (DWF) simulated with physical values of the light quark masses [10]. These recent developments are paving the way for lattice QCD to provide results, which can be directly compared to experimental measurements.

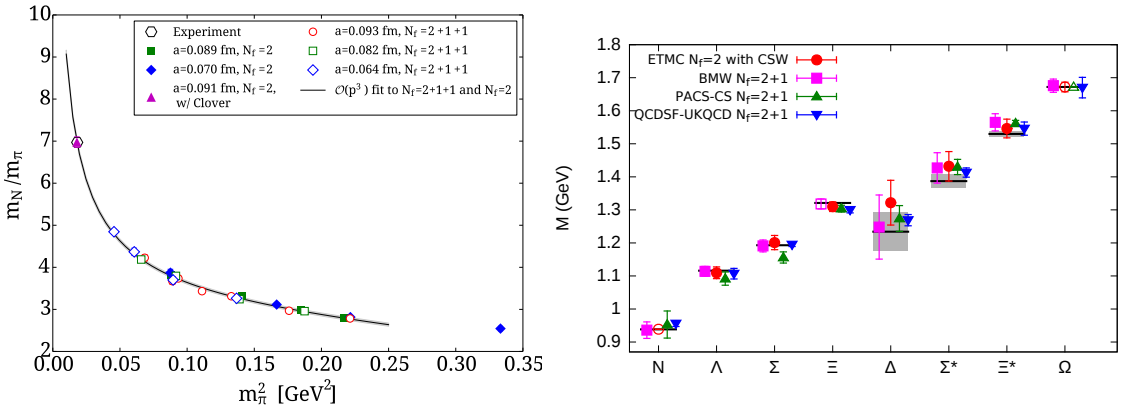

Figure 1: Left: Results on the ratio of the proton to the pion mass versus m_π^2 using TMF. The solid line is a leading oder chiral fit using $m_\pi < 300$ MeV excluding the value at the physical point. Right: Lattice QCD results on the octet and decuplet baryon masses compared to the experimental values shown by the horizontal bands. Results by the ETM collaboration are shown in red circles for the physical point ensemble [11]. Also shown are results using clover fermions from BMW [12] (magenta squares), from PACS-CS [13] (green triangles), and from QCDSF-UKQCD [14] (blue inverted triangles). Open symbols show the baryon mass used as input to the calculations.

In Fig. 1 we show the ratio of the nucleon mass to the pion mass m_N/m_π versus m_π^2 for a number of $N_f = 2$ and $N_F = 2 + 1 + 1$ TMF ensembles including the one with the physical point ensemble (with pion mass $m_\pi = 130$ MeV, $a = 0.094$ fm and $L = 4.5$ fm) for which the dimensionless ratio m_N/m_π agrees with its experimental value. In the same figure we also

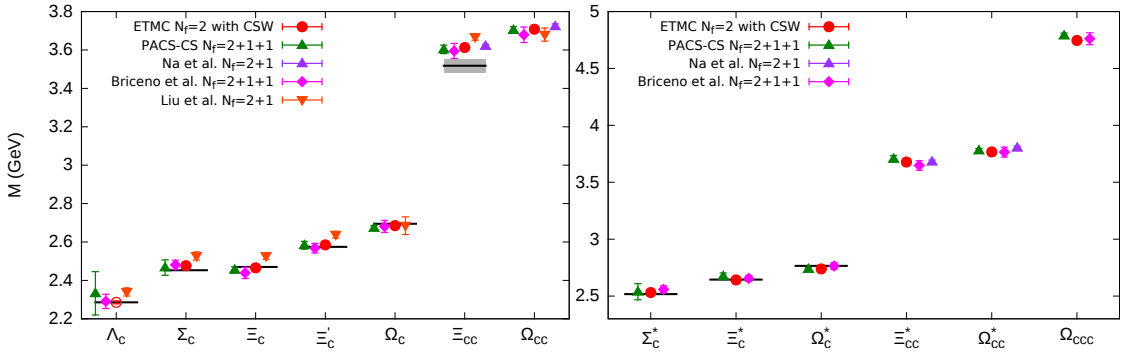

Figure 2: Results by ETMC are shown in red circles for the mass of the spin-1/2 (left) and spin-3/2 (right) charmed baryons for the physical point ensemble. Included are results from various hybrid actions with staggered sea quarks from Refs. [15] (purple triangles), [16] (magenta diamonds) and [17] (orange inverted triangles). Results from PACS-CS [18] are shown in green triangles.

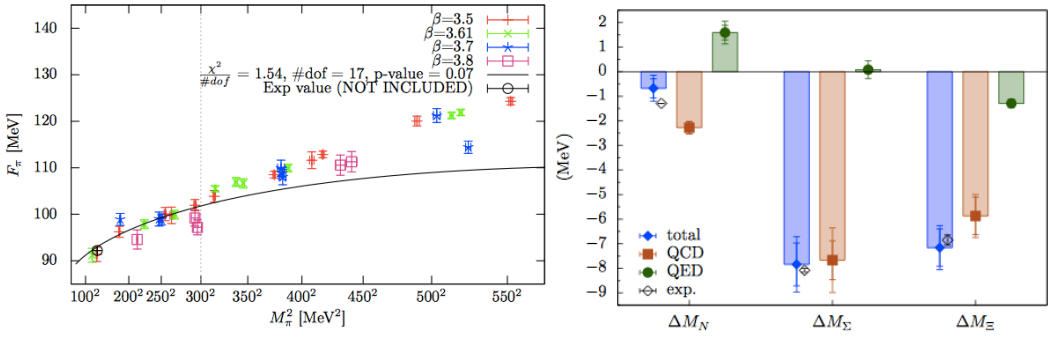

Figure 3: Left: Results on the pion decay constant f_π by BMW. The solid line is the result of fitting NLO SU(2) chiral perturbation theory for $m_\pi < 300$ MeV, taken from Ref. [7]. Right: Baryon spectrum with mass splitting by BMW taken from Ref. [21].

show results on the low-lying baryon spectrum from the ETM, BMW, PACS-CS and QCDSF-UKQCD collaborations. The set of TMF results shown in Fig. 1 is obtained using the physical point ensemble, thus requiring no chiral extrapolation, reducing drastically the systematic error that was found to be dominated by the chiral extrapolation in an earlier study using TMF [19]. These results are, however, obtained at one lattice spacing and volume. The analysis of Ref. [19] has shown that lattice artifacts both due to the finite volume and lattice spacing a are small and thus the values obtained for the physical point ensemble are expected to have small lattice artifacts. This is indeed corroborated by the fact that the 'raw' lattice data agree with the experimental values [11]. In Fig. 2 we show the corresponding results for the mass of the charmed baryons using the physical point ensemble in the case of TMF. As can be seen, the known values of the masses of the charmed baryons are reproduced and thus our computation

provides a prediction for the yet unmeasured masses. Our preliminary values for the Ξ^*_{cc} is 3.678(8) GeV, for the Ω^+_{cc} is 3.708(10) GeV, for Ω^{*+}_{cc} 3.767(11) GeV and for Ω^{++}_{ccc} 4.746(3) GeV.

The BMW collaboration has produced a number of ensembles using $N_f = 2 + 1$ clover improved Wilson fermions with HEX smearing. They represent the most comprehensive set of ensembles for light pion masses close to and at the physical point. Their results on the pion decay constant f_π are shown in Fig. 3. Fitting to NLO SU(2) chiral perturbation theory using pion masses up to 300 MeV they reproduce the physical value of f_π.

The BMW and QCDSF-UKQCD [20] collaborations investigated the mass splitting due to isospin breaking and electromagnetic effects. In Fig. 3 we show the results on the nucleon, Σ and Ξ baryons by the BMW collaboration [21] where isospin and electromagnetic effects were treated to lowest order. The agreement with the experimental values is a spectacular success of lattice QCD.

4 Challenges and future perspectives

The results shown in the previous section highlight the success of lattice QCD and the promise it holds to provide insight on many other observables. We will briefly discuss some of the challenges that need to be addressed in order for this to happen.

4.1 Excited states and resonances

In order to go beyond the low-lying spectrum one needs a formulation to extract excited states. The standard approach is to use a variational basis of interpolating fields to construct a correlation matrix of two-point functions:

$$G_{jk}(t_s) = \langle J_j(t_s) J^\dagger_k(0) \rangle \, , j, k = 1, \ldots N \tag{3}$$

and then solve the generalized eigenvalue problem (GEVP) defined by

$$G(t) v_k(t; t_0) = \lambda_k(t; t_0) G(t_0) v_k(t; t_0) \rightarrow \lambda_k(t; t_0) = e^{-E_k(t-t_0)} \quad , \tag{4}$$

which yields the N lowest eigenstates.

A lot of effort has been devoted to construct appropriate bases using lattice symmetries by e.g. the Hadron Spectrum Collaboration. In order to determine the energy of an excited state one: i) must extract all states lying below the state of interest, ii) include disconnected diagrams, iii) treat appropriately resonances and unstable particles that require including multi-hadron states. Given the increased complexity of the problem it comes with no surprise that the calculations performed so far have not reached the maturity of ground state mass computations. In Fig. 4 we show results obtained on the ρ-meson excited spectrum [22] at $m_\pi = 400$ MeV, as well as, on the width of the ρ-meson using using $N_f = 2 + 1$ clover fermions and 3 asymmetric lattices [23]. These results, although still at larger than physical pion masses, provide a promising framework for the study of unstable particles.

4.2 Nucleon Structure

In order to evaluate hadron matrix elements one needs the appropriate three-point functions. There are two contributions we typically need to evaluate: the so called connected and disconnected parts, the former having the current coupled to a valence quark, while the later to a sea

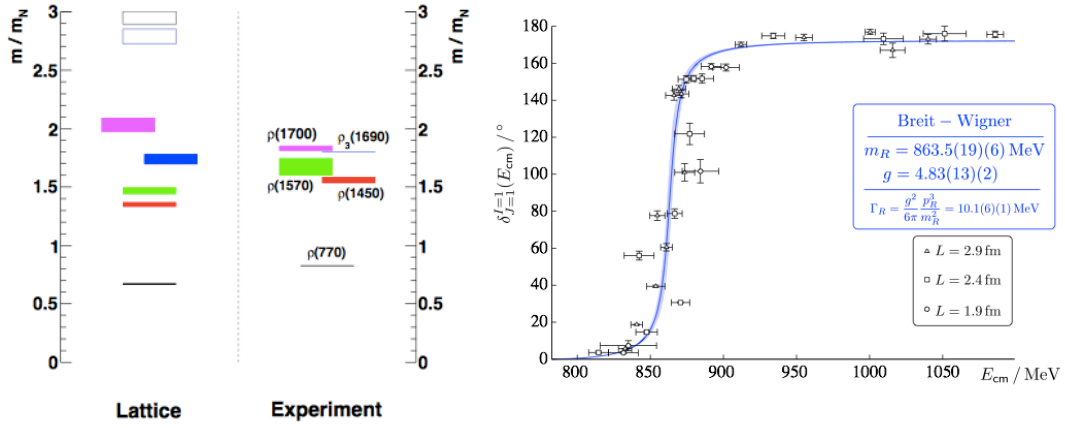

Figure 4: Left: Excited states of the ρ-meson at $m_\pi \sim 400$ MeV at one lattice spacing and one lattice volume, compared to experiment [22]. Right: The ρ-meson width, taken from Ref. [23].

quark. Methods to evaluate the connected contribution are well developed see e.g. [24]. The disconnected contributions are much more demanding for technical reasons but also because they are prone to large gauge noise. Thus in most hadron structure computations they were neglected.

4.2.1 Axial charges

Some important nucleon observables only need the connected part. These are isovector quantities for which the disconnected contributions vanish in the isospin limit. The nucleon axial charge g_A is extracted from the nucleon matrix element of the isovector axial-vector current and thus it is protected from disconnected contributions. It is also well-determined experimentally from β-decays and can be extracted directly at zero momentum transfer squared q^2 from $\langle N(\mathbf{p}')|j_A|N(\mathbf{p})\rangle|_{q^2=0}$. It thus comprises an ideal benchmark quantity for lattice QCD.

We show in Fig. 5 results on the nucleon axial charge using the TMF ensembles. They are the 'raw' lattice QCD data in the sense that they have not been volume corrected nor extrapolated to the continuum limit, but have been non-perturbatively renormalized. They are obtained by fitting to the plateau of an appropriately defined ratio of the three- to two-functions using a sink-source separation of about 1 fm. Within the current errors no dependence on the lattice spacing and volume is observed. While results at higher pion mass underestimate g_A, a fact observed by all lattice QCD collaborations, at the physical point we find a value that is in agreement with experiment. Despite the fact that the statistical error is still large, this is a very welcome result that would resolve a puzzle that persisted for some time showing the importance of computing observables at the physical point.

Having computed the axial charge it is straight forward to calculate the isovector scalar and tensor charges. The value of the latter is particularly relevant for searching for new type of interactions beyond the Standard Model. There is a planned SIDIS on ^{3}He/Proton experiment to take place at JLab after the upgrade at 11 GeV. In lattice QCD it is computed by replacing the axial-vector current by the tensor current $j_T^3 = \bar{\psi}(x)\sigma^{\mu\nu}\frac{\tau^3}{2}\psi(x)$. Studies have shown that

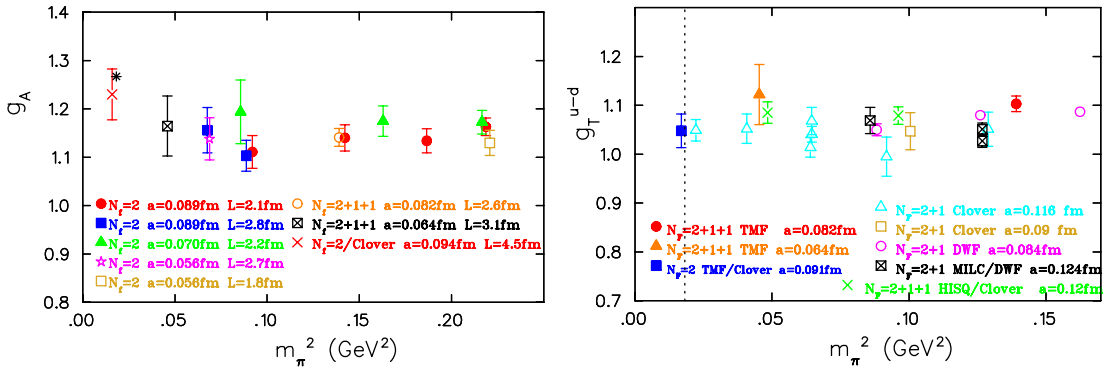

Figure 5: Left: Nucleon axial charge using TMF fermions. Right: Nucleon isovector tensor charge using TMF (ETMC) [25], DWF (RBC) [26], $N_f = 2$ (QCDSF-UKQCD) [27] and $N_f = 2 + 1$ (LHPC) [28] clover fermions, and clover on $N_f = 2 + 1 + 1$ staggered (PNDME) [29].

g_T^{u-d} has a similar behavior to g_A as far as the contribution from excited states is concerned. We show results in Fig. 5 obtained using TMF, clover, DWF and in a mixed action set-up of staggered sea and clover valence quarks. As can seen, all lattice QCD results are in agreement and a preliminary value of $g_T^{u-d} = 1.048(34)$ in $\overline{\text{MS}}$ at 2 GeV is obtained from the TMF ensemble directly at the physical point.

4.2.2 Disconnected quark loop contributions

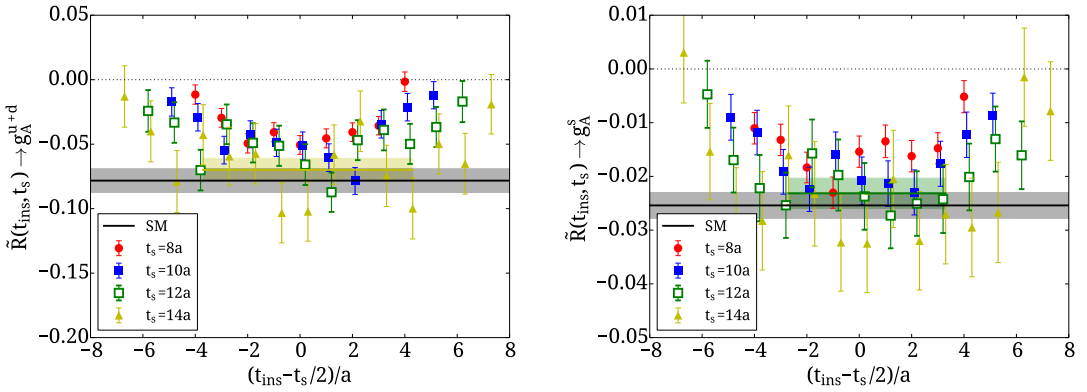

Figure 6: Disconnected contributions to the isoscalar (left) and strange (right) nucleon axial charge for the B55 ensemble.

Disconnected quark loop contributions arise from the coupling of the current to sea quarks. They are notoriously difficult to compute in lattice QCD. The technical reason is that one must compute a close quark loop given by $L(x) = Tr\left[\Gamma G(x;x)\right]$ for a general bilinear ultra-local operator of the form $\bar{\psi}(x)\Gamma\psi(x)$. This requires the computation of quark propagators from all $\mathbf{x}$ (all-to-all propagator) and thus it is L^3 more expensive as compared to the calculation

of hadron masses. The other reason is that these loops tend to have large gauge noise and therefore large statistics are necessary to obtain a meaningful result. Special techniques that utilize stochastic noise on all spatial lattice sites are utilized in order to allow for the computation of the all-to-all propagator reducing the number of inversions to N_r with $N_r \ll L^3$. The gauge noise is reduced by increasing statistics at low cost using low precision inversions and correcting for the bias (truncated solver method (TSM) or all-mode-averaging). Despite these new approaches the computation of these contributions would be too expensive using conventional computers. We take advantage of graphics cards (GPUs) for which we developed special multi-GPU codes. These computer architectures are ideal for approaches like TSM. We have illustrated the applicability of these methods by performing a high-statistics analysis using an $N_f = 2+1+1$ TMF ensemble with $L = 2.6$ fm, $a = 0.082$ fm at $m_\pi = 373$ MeV, referred to as the B55 ensemble. We analyzed 4700 gauge configurations yielding a total of $\sim 150,000$ statistics. The results on the disconnected contributions to the nucleon axial charge due to the light quarks g_A^{u+d} and due to the strange g_A^s are shown in Fig. 6. We obtain a non-zero negative value, which is $\mathcal{O}(10\%)$ for the u- and d-quarks and has to be taken into account when e.g. discussing the intrinsic spin $\frac{1}{2}\Delta\Sigma$ carried by quarks in the nucleon.

4.2.3 Electromagnetic form factors

The nucleon electromagnetic form factors are extracted from

$$\langle N(p',s')|j^\mu(0)|N(p,s)\rangle = \bar{u}_N(p',s')\left[\gamma^\mu F_1(q^2) + \frac{i\sigma^{\mu\nu}q_\nu}{2m}F_2(q^2)\right]u_N(p,s) \quad . \tag{5}$$

We would like to discuss here two studies at near physical pion mass: the one with the physical point ensemble of ETMC at $m_\pi = 130$ MeV [30] and the one by LHPC using $N_f = 2+1$ clover fermions configurations produced by the BMW collaboration with $a = 0.116$ MeV and $m_\pi = 149$ MeV [31].

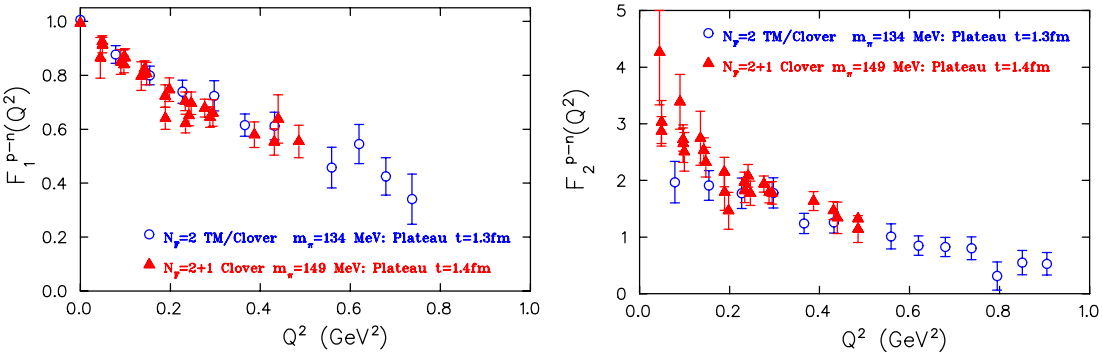

Figure 7: Results on the isovector Dirac (left) and Pauli (right) form factors versus $Q^2 = -q^2$. The statistics is about $\sim 10^3$ for ETMC and 7750 for LHPC.

Comparing the results on the Dirac and Pauli form factors between ETMC and LHPC in Fig. 7 we observe an overall agreement independently of the discretization scheme. The Dirac and Pauli radii can be extracted by fitting the Q^2-dependence of $F_1(Q^2)$ and $F_2(Q^2)$ to a dipole form, $\frac{A_i}{(1+Q^2/M_i^2)^2}$, with $i = 1, 2$, $A_1 = 1$ and taking the derivative: $\langle r_i^2\rangle = -\frac{6}{F_i}\frac{dF_i}{dQ^2}|_{Q^2=0} = \frac{12}{M_i^2}$.

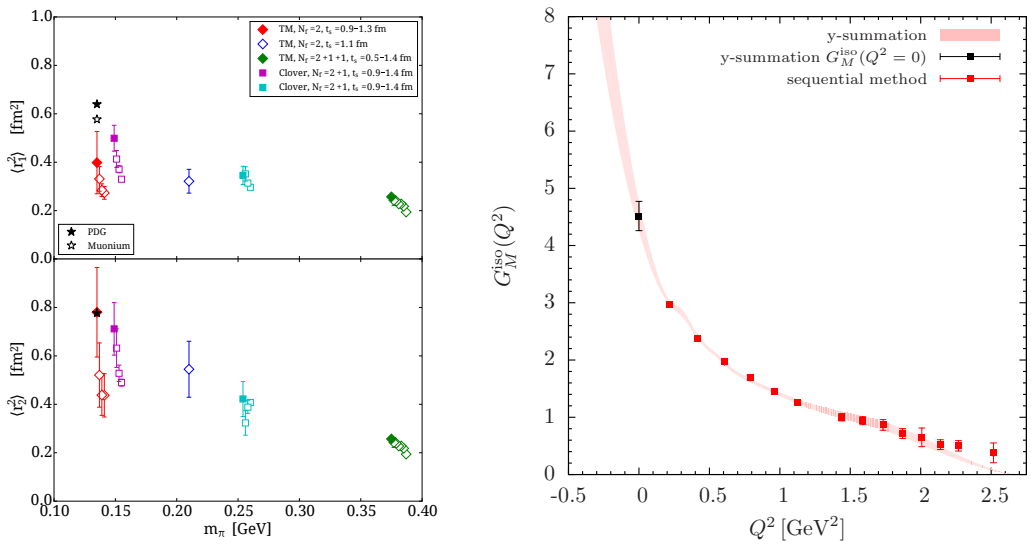

Figure 8: Left: Results on the isovector Dirac (top) and Pauli (bottom) radii versus m_π^2 from ETMC (diamonds) and LHPC (squares) [30]. Right: Magnetic form factor directly at $Q^2 = 0$, as determined by the red band [32]. The red points show the results with the conventional method.

The results are shown is Fig. 8 and clearly increase as the pion mass decreases, as well as the sink-source separation increases from ~ 1 fm to ~ 1.3 fm (see Ref. [30] for more details). However, fitting to a dipole to extract the radii introduces a model-dependence. We developed a novel method that extracts the value directly at $Q^2 = 0$. The first application of this method was to extract the anomalous magnetic moment determined by the magnetic form factor $G_M(0)$ or equivalently $F_2(0)$. In Fig. 8, our results on the isovector G_M for the B55 ensemble are shown with the red band. As can be seen, the method provides a good determination of $G_M(0)$ without requiring any assumption of its Q^2-dependence (see Ref. [32] for more details).

5 Conclusions

Simulations at the physical point are now feasible and this opens exciting possibilities for the study of hadron structure. In this work we presented an overview of lattice QCD results obtained directly at or close to the physical point from a number of lattice QCD collaborations, such as results on the hyperon and charmed baryon masses and isospin splitting, the pion decay constant, as well as, on the axial and tensor charges, and electromagnetic form factors of the nucleon. We find a value of g_A that is in agreement with experiment and provide a preliminary value for the tensor charge. The computation of disconnected contributions are briefly reviewed focusing on the disconnected quark contributions to the nucleon axial charge. First results at the physical point highlight the need for higher statistics in order that careful cross-checks can be carried out. Noise reduction techniques such as all-mode-averaging, improved methods for disconnected diagrams and smearing techniques are currently being pursued aiming at decreasing our errors on the quantities obtained at the physical point.

When this is achieved, lattice QCD can provide reliable predictions on quantities probing beyond the standard model physics such as g_T, as well as, on the nucleon σ-terms.

Acknowledgments

I would like to thank the members of the ETMC and in particular my close collaborators A. Abdel-Rehim, M. Constantinou, K. Jansen, K. Hadjiyiannakou, C. Kallidonis, G. Koutsou, K. Ottnad, M. Petschlies and A. Vaquero for their contributions to the TMF results shown in this talk. Partial support was provided by the EU ITN project PITN-GA-2009-238353 (ITN STRONGnet) and IA project IA-GA-2011-283286 HadronPhysics3 . This work used computational resources provided by PRACE, JSC, Germany and the Cy-Tera project (NEA ΥΠΟΔΟΜΗ/ΣΤΡΑΤΗ/0308/31).

References

[1] , A. Abdel-Rehim *et al.* (ETMC), PoS(LATTICE2013) 264 (2013); A. Abdel-Rehim *et al.*, (ETMC) PoS(LATTICE2014) 119 (2014).

[2] C. Alexandrou *et al.*, Comput. Phys. Commun. **185**, 1370 (2014) [arXiv:1309.2256].

[3] A. Abdel-Rehim *et al.*, Phys. Rev. D **89**, no. 3, 034501 (2014) [arXiv:1310.6339].

[4] C. Alexandrou *et al.*, PoS(LATTICE2014) 140 (2014).

[5] S. Meinel *et al.*, PoS(LATTICE2014) 139 (2014).

[6] A. Bazavov *et al.* [Fermilab Lattice and MILC Collaboration], arXiv:1407.3772 [hep-lat].

[7] S. Durr *et al.*, arXiv:1310.3626 [hep-lat].

[8] G. S. Bali *et al.*, Nucl. Phys. B **866**, 1 (2013).

[9] S. Aoki *et al.* [PACS-CS Collaboration], Phys. Rev. D **81**, 074503 (2010).

[10] S. Syritsyn *et al.*, (RBC/UKQCD) PoS(LATTICE2014) 134 (2014).

[11] C. Alexandrou *et al.*, PoS(LATTICE2014) 151 (2014).

[12] S. Durr *et al.* Science **322**, 1224 (2008).

[13] S. Aoki *et al.* [PACS-CS Collaboration], Phys. Rev. D **79**, 034503 (2009).

[14] W. Bietenholz *et al.*, Phys. Rev. D **84**, 054509 (2011).

[15] H. Na and S. A. Gottlieb, PoS LAT **2007**, 124 (2007); H. Na and S. Gottlieb, PoS LATTICE **2008**, 119 (2008).

[16] R. A. Briceno, H. W. Lin and D. R. Bolton, Phys. Rev. D **86**, 094504 (2012).

[17] L. Liu, H. W. Lin, K. Orginos and A. Walker-Loud, Phys. Rev. D **81**, 094505 (2010).

[18] Y. Namekawa *et al.* [PACS-CS Collaboration], Phys. Rev. D **87**, 094512 (2013).

[19] C. Alexandrou, V. Drach, K. Jansen, C. Kallidonis and G. Koutsou, arXiv:1406.4310 [hep-lat].

[20] R. Horsley *et al.* (QCDSF-UKQCD) Phys. Rev. D **86**, 114511 (2012); PoS Lattice **2013**, 499 (2013).

[21] Sz. Borsanyi *et al.*, Phys. Rev. Lett. 111 (2013) 252001.

[22] J. Bulava *et al.*, [arXiv:1310.7887[hep-lat]].

[23] J. J. Dudek, R. G. Edwards and C.E. Thomas, Phys. Rev. D 87 (2013) 034505.

[24] C. Alexandrou, Prog. Part. Nucl. Phys. **67**, 101 (2012) [arXiv:1111.5960 [hep-lat]].

[25] C. Alexandrou, M. Constantinou, K. Jansen, G. Koutsou and H. Panagopoulos, arXiv:1311.4670 [hep-lat].

[26] Y. Aoki *et al.*, Phys. Rev. D **82**, 014501 (2010).

[27] D. Pleiter *et al.* [QCDSF/UKQCD], PoS LATTICE **2010**, 153 (2010) [arXiv:1101.2326 [hep-lat]].

[28] J. R. Green *et al.*, Phys. Rev. D **86**, 114509 (2012).
[29] T. Bhattacharya *et al.*, Phys. Rev. D **89**, 094502 (2014).
[30] C. Alexandrou *et al.* (ETMC), PoS (LATTICE2014) 148 (2014).
[31] J. R. Green *et al.*, Phys. Rev. D **90**, 074507 (2014).
[32] C. Alexandrou *et al.* (ETMC), PoS (LATTICE2014) 144 (2014).

Recent Heavy Ion Results on the Hard Scattering and Jet Quenching from the ATLAS and CMS experiments at the LHC

Andrzej Olszewski[1] on behalf of the ATLAS and CMS Collaborations

[1]Institute of Nuclear Physics, PAS, Radzikowskiego 152, 31-342 Kraków, Poland

DOI: http://dx.doi.org/10.3204/DESY-PROC-2014-04/287

Recent results on studies of hard scattering processes and jet quenching in nuclear collisions from the ATLAS and CMS experiments at the Large Hadron Collider (LHC) are reviewed. They are based on high statistics samples of PbPb collisions at $\sqrt{s_{\rm NN}} = 2.76$ TeV collected at the LHC in 2011, and pp collisions at $\sqrt{s} = 2.76$ TeV and pPb collisions at $\sqrt{s_{\rm NN}} = 5.02$ TeV collected in 2013. New results for the jet nuclear modification factor, $R_{\rm AA}$, confirm a strong suppression of jet production. Modifications of jet fragmentation properties in PbPb collisions, are observed. In pPb collisions jets are not strongly modified, but some non-scaling behavior of jet rates in collisions with different centralities is observed by ATLAS. New measurements for the electroweak boson production in pPb collisions allow a more precise testing of parton distributions in lead nuclei with the conclusion that the EPS09 description of nuclear modifications of parton distribution functions is preferred.

1 Introduction

In collisions of heavy nuclei at very high energies, one expects creation of a hot and dense medium which may, under certain conditions, undergo transition to the so called Quark-Gluon Plasma (QGP) phase, where quarks and gluons are free to interact directly. In experiments at RHIC and LHC, it has been observed that properties of high transverse momentum particles and particle jets are modified in heavy nuclei collisions compared to collisions of protons and this was attributed to interactions of these particles with the medium created in the collision. It has been found that the best way to understand properties of the produced medium and whether it fits the properties of QGP is to study hard scattering processes. In such studies, we use nuclear modification factor $R_{\rm AB}$, defined as:

$$R_{\rm AB} = \frac{\frac{1}{\rm N}\frac{{\rm d}^2 N^{\rm jet}_{\rm cent}}{{\rm d}p_{\rm T}{\rm d}y}}{\langle T_{\rm AB}\rangle_{\rm cent}\frac{{\rm d}^2\sigma^{\rm jet}_{pp}}{{\rm d}p_{\rm T}{\rm d}y}}; \qquad N_{\rm coll} = T_{\rm AB}\times\sigma_{\rm NN},$$

to measure the deviation of yields produced in heavy ion collisions from the yield in pp scaled by the number of nucleon-nucleon collisions, $N_{\rm coll}$, proportional to the mean nuclear thickness, $T_{\rm AB}$, of the incoming nucleon fluxes. $R_{\rm AB} = 1$ means that production properties have not been modified with respect to pp collisions.

In the last few years experiments at LHC registered data from runs with collisions of lead nuclei at the center of mass energy of $\sqrt{s_{\rm NN}} = 2.76$ TeV, from proton-proton runs taken as a reference data at the same energy and from pPb runs at the energy of $\sqrt{s_{\rm NN}} = 5.02$ TeV resulting from a combination of asymmetric energies of lead nuclei at 1.58 TeV/N and protons at 4 TeV. Recent analyses from ATLAS [1] and CMS [2] are now using high statistics PbPb data from 2011, new pPb data from 2013, and high statistics pp data from 2013 with statistics 20 times higher than available before.

2 Jets in PbPb collisions

Jets provide a powerful tool to probe the hot and dense medium created in heavy ion collisions. Experiments at RHIC have shown first evidence of jet quenching by observation of suppression of high transverse momentum particles. At the LHC, a direct evidence of parton energy loss has been observed in significant modification of dijet and photon-jet $p_{\rm T}$-balance and suppression of inclusive jet spectra with increasing collision centrality.

Recently ATLAS has shown new results on the jet suppression in PbPb collisions [3]. The jet nuclear modification factor, $R_{\rm AA}$, has been measured as a function of jet transverse momentum, rapidity and centrality. A significant suppression of jets is observed at all centralities. The $R_{\rm AA}$ is as low as 0.5 in the most central (0-10%) collisions for jets with $p_{\rm T}$ up to 400 GeV. With increasing $p_{\rm T}$ a slow rise of $R_{\rm AA}$ is observed, with the slope varying with centrality and reaching zero in peripheral collisions. The jet $R_{\rm AA}$ measured as a function of rapidity shows no significant dependence within the measured rapidity range (Fig.1, top). $R_{\rm AA}$ measured as a function of centrality, expressed by number of participating nucleons, $\langle N_{\rm part}\rangle$, is decreasing monotonically from the value of 0.8 in most peripheral collisions to 0.4 in 1% of the most central ones (Fig.1, bottom), the behaviour observed before by CMS [4].

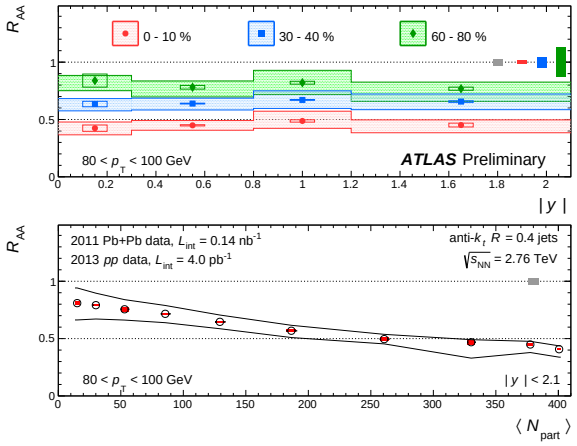

Figure 1: Top: $R_{\rm AA}$ for jets with $80 < p_{\rm T} < 100$ GeV shown as a function of $|y|$ for three centrality bins. Bottom: $R_{\rm AA}$ for jets with $80 < p_{\rm T} < 100$ GeV and $|y| < 2.1$ as a function of $\langle N_{\rm part}\rangle$ [3].

ATLAS presented also updated results on modifications of the jet fragmentation in PbPb collisions [5]. Modifications of distributions of longitudinal, $D(z)$, $z = p_{\rm T}^{\rm had}/p_{\rm T}^{\rm jet}\cos(\Delta R)$, and transverse, $D(p_{\rm T})$, momentum of jet particles relative to the jet axis have been studied by calculating ratios of distributions measured in central and peripheral collisions, $R_{D(z)} = D(z)_{\rm cent}/D(z)_{\rm periph}$. A significant modification of fragmentation is seen in more central collisions with enhancement of fragment yields at small values of momenta ($z < 0.04$, $p_{\rm T} < 4$ GeV) and at high ones ($z > 0.2$, $p_{\rm T} > 30$ GeV), and reduction at intermediate values (Fig.2). The enhancement at large z or $p_{\rm T}$ is seen more clearly for jets with small jet radii, $R = 0.2, 0.3$. Similar modifications in

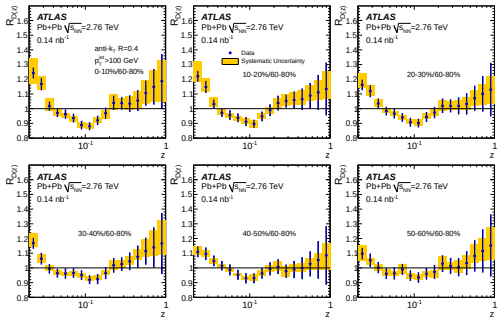

Figure 2: Ratios of $D(z)$ for six bins in collision centrality to those in peripheral (60-80%) collisions, for $R = 0.4$ jets [5].

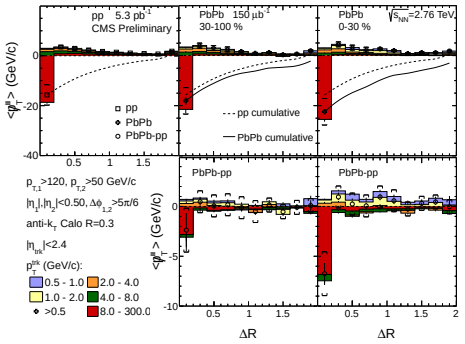

Figure 3: Top: Differential missing p_{T} distributions for pp and PbPb collisions, as a function of ΔR. Bottom: Difference between the PbPb and pp distributions [7].

jet fragmentation are seen also by the CMS experiment from the comparison of pp and PbPb collision data [6].

The CMS experiment studied also particle momentum balance in jets [7]. It has been found that jets in PbPb collisions comprise more particles than pp jets and the difference increases with the collision centrality leading to 15 extra particles in jets with large momentum asymmetry and high (0-10%) collision centrality. Furthermore, contributions from jet particles have been studied in bins of transverse momentum and it has been found that in PbPb jets there is an excess of particles with low $p_{\mathrm{T}} < 2$ GeV. The particle transverse momentum balance has been studied also as a function of ΔR, the distance from the jet axis. Results are shown in Fig.3. The momentum balance, shown by dashed and continuous lines for pp and PbPb collisions, respectively, is achieved only at large distances $\Delta R = 2$ and the excess of low p_{T} particles is seen up to large distances from the jet axis. A detailed measurement of the radial distribution of transverse momentum inside the core of the jet cone, called differential jet shape, has been shown by CMS in [8]. It has been found that jet shapes in peripheral (70-100%) PbPb collisions are similar to those in pp while in more central collisions (0-70%) a depletion is found in the range of $0.1 < R < 0.2$. In the most central PbPb collisions (10-30% and 0-10%), an excess of transverse momentum fraction emitted at large radii, $R > 0.2$, starts to show up, confirming moderate broadening of jets in the hot medium created in PbPb collisions.

3 Jets in pPb collisions

Studies of dijet properties in pPb collisions are of great importance to establish a QCD baseline for hadronic interactions with a cold nuclear matter. This is because these collisions are not expected to produce large volumes of hot partonic medium similar to PbPb collisions where both effects contribute.

Recently ATLAS performed measurements of jet production in pPb collisions [9]. In this analysis, inclusive jet modication factors, $R_{p\mathrm{Pb}}$, have been calculated as a function of p_{T} using as a reference 2013 pp data interpolated to pPb energy. Results are shown in Fig.4. The $R_{p\mathrm{Pb}}$ factors are all close to 1, so there is no jet suppression seen in inclusive pPb collisions.

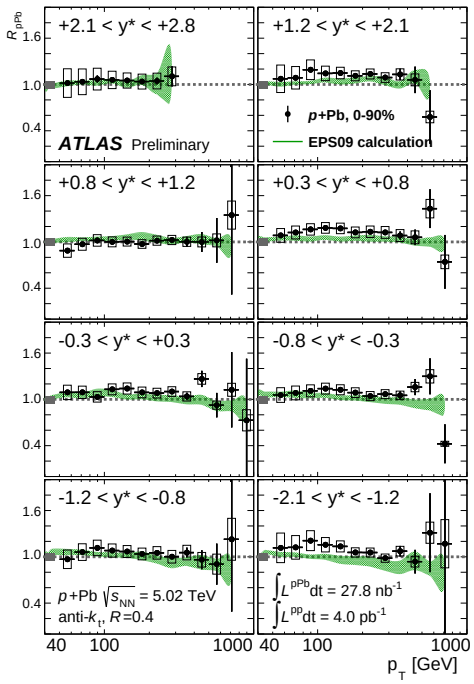

Figure 4: $R_{p\mathrm{Pb}}$ for $R = 0.4$ jets in 0-90% pPb collisions at different rapidity ranges. The green band represents a calculation using the EPS09 parton distribution function [9].

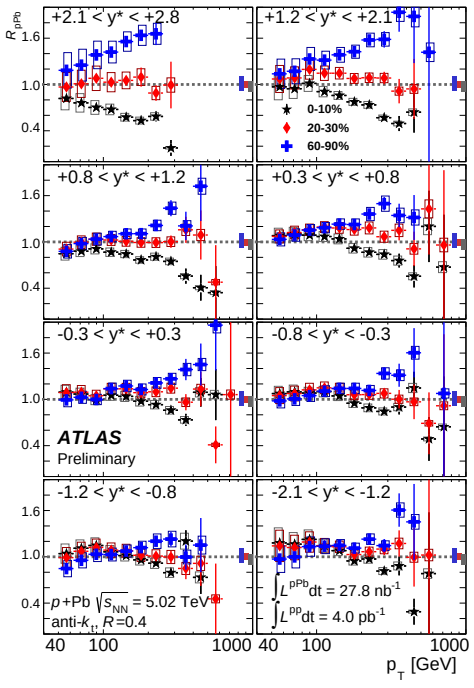

Figure 5: $\mathrm{R}_{p\mathrm{Pb}}$ for $R = 0.4$ jets in pPb collisions in central (black), mid-central (red) and peripheral (blue) events at different rapidity ranges [9].

Instead, a small 5-10% enhancement is visible over the scaled pp results. CMS has performed a similar measurement [10] and has come to similar conclusions except for observing some decrease in $R_{p\mathrm{Pb}}$ modification factors with jet p_{T} in the most backward range of the center-of-mass pseudorapidity, $-2.0 < \eta_{\mathrm{CM}} < -1.5$. ATLAS has measured also $R_{p\mathrm{Pb}}$ factors in 3 subsamples of events with different collision centrality (Fig.5). In such samples, jet rates have been found enhanced in peripheral collisions and suppressed in central collisions at forward rapidities, while not modified at low p_{T} and negative center-of-mass rapidity, y^* [9]. This pattern of the jet modification has been confirmed by R_{CP}, ratios of jet rates in central to peripheral pPb collisions. In addition, it has been found that R_{CP} ratios scale as a function of momentum p, in forward (proton going) direction $y^* > 0$, but not at $y^* < 0$ [9].

In order to study flavor dependence of the jet suppression CMS has measured also $R_{p\mathrm{Pb}}$ factors in production of b-quark jets [11] and B particles [12]. The b-jet measurements have been compared to PYTHIA Z2 tune pp calculations. The obtained $R_{p\mathrm{Pb}}$ ratios were found to be consistent with no suppression in the b-jet production. The same conclusion has been drawn also from the study of B meson production [12]. No flavor dependence of jet suppression has been found in PbPb collisions [13], despite the fact that jets are strongly quenched in these collisions.

A particularly useful tool for studying jet quenching are back to back jet pairs, called

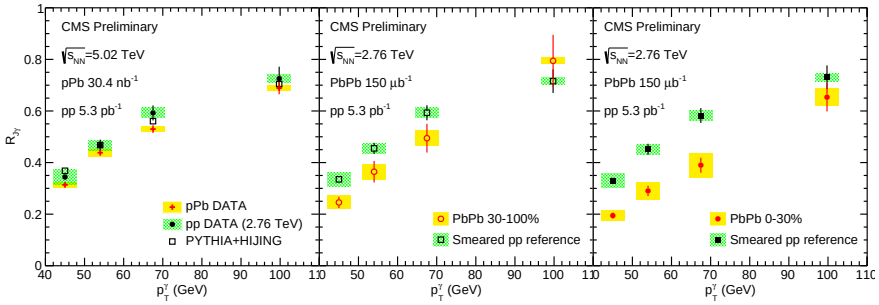

Figure 6: Fraction of photons associated to a jet (R_{J_γ}) as a function of the leading photon p_T in pPb (left), peripheral PbPb (middle), and central PbPb (right) [14].

dijets. CMS has measured a fraction of photons with a high p_T jet partner in pPb and in PbPb collisions and compared results to the measurements in pp collisions and to PYTHIA calculations [14]. It has been found (see Fig.6) that such dijets are not changed in pPb while they are suppressed in PbPb collisions. CMS has also measured directly distributions of the relative directions and momentum ratios of jets in pPb dijets and compared them with dijet properties in pp collisions. It has been found that in pPb collisions jets are not deflected and the jet momenta are essentially unmodified [15], while in PbPb collisions, the partner jets are pushed to lower p_T values [16].

Another dijet property studied by CMS in pPb collisions was an average dijet position in rapidity. This property is directly sensitive to momenta of interacting partons that could be modified in nuclear projectiles. CMS compared the pPb data with PYTHIA pp predictions and found that the best match is obtained if the EPS09 nuclear parton distribution function (PDF) is used in the model calculations [15].

4 Electroweak bosons in PbPb collisions

Electroweak (EW) bosons are colorless particles which are supposed not to interact with the hot and dense medium created in heavy ion collisions. Measured together with jets they may be used as a calibration tool in studies of jet quenching. In addition, the EW boson production mechanism (via $q\bar{q}$ annihilation) makes them sensitive to parton distribution functions, thus suitable for studying nuclear modifications to PDFs (nPDFs).

In PbPb collisions, ATLAS measured R_{AA} ratios for isolated, direct photon yields to the reference pp rates calculated by JETPHOX model [17]. They were shown as a function of photon transverse momentum and compared with JETPHOX calculations in pp and PbPb collisions. Also a ratio of yields in forward to central rapidity regions has been studied. The photon cross-sections have been found to agree with simple scaling of pp rates, but the measurements could not discriminate between different PDF versions due to large systematic uncertainties.

ATLAS has updated also their results on the production of W bosons in PbPb collisions [18]. Yields of $W^{\pm}$ bosons have been studied as a function of the number of participating nucleons (collision centrality) and compared to PYTHIA CT10 model calculations (Fig.7). Results have been found compatible with simple pp scaling and in agreement with model calculations.

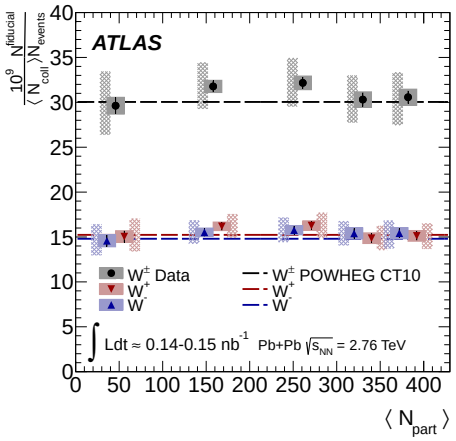

Figure 7: W boson production yield per binary collision as a function of the mean number of participants compared to the NLO QCD prediction [18].

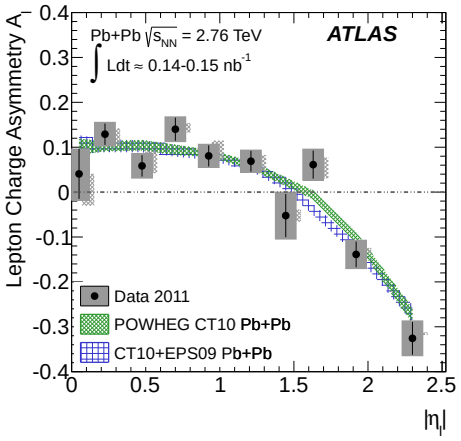

Figure 8: The lepton charge asymmetry $A_l = (N(l^+) - N(l^-))/(N(l^+) + N(l^-))$ from $W^{\pm}$ bosons as a function of the absolute pseudorapidity compared to predictions with CT10 and CT10+EPS09 NLO PDF sets [18].

The more sensitive to parton distributions, charge asymmetry in pseudorapidity, has also been studied (Fig.8) and found to be well described by model calculations, but results are not precise enough to see possible nuclear modifications to parton distributions.

5 Electroweak bosons in pPb collisions

Search for the effects of nuclear modifications to PDFs is even easier in pPb collisions, where final state effects are expected to be small or none. In such collisions, ATLAS measured recently the Z^0 boson production [19]. The cross-section measured as a function of boson rapidity exhibits a significant asymmetry in rapidity with excess over predictions from PYTHIA CT10 model in the backward (Pb-going) rapidity region. In the same measurement performed by CMS [20], Z^0 cross section has also asymmetric behavior, but a comparison is made with PYTHIA MSTW08 model and a good agreement with predictions is found (Fig.9). The forward to backward ratio of Z^0 production cross-sections measured by CMS favors parton distributions with nuclear modifications (Fig.10).

The production cross-sections for W boson in pPb collisions have been measured so far only by the CMS experiment [21]. They agree well with the scaled PYTHIA model predictions – only a small excess is seen in the production of W^- at negative η. This excess is investigated in the W^+/W^- charge asymmetry (Fig.11), which is a sensitive probe of the ratio of up to down quark PDFs. Explanation of the deviation between data and model predictions would require to assume a smaller nuclear modification to the down quark than to the up quark in the EPS09 nPDF. The forward/backward asymmetry in W boson production has been investigated by CMS to probe nuclear modifications in parton x distributions. There is a significant difference in this asymmetry as a function of $\eta_{\rm lab}$ between predictions from PYTHIA CT10 and EPS09

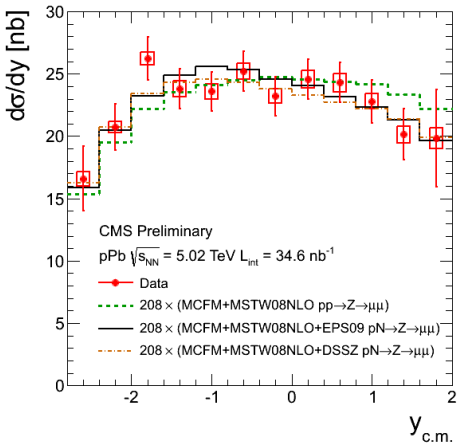

Figure 9: Differential cross-section of the Z^0 boson production in pPb collisions as a function of rapidity, compared to predictions from PYTHIA generator with different versions of PDFs [20].

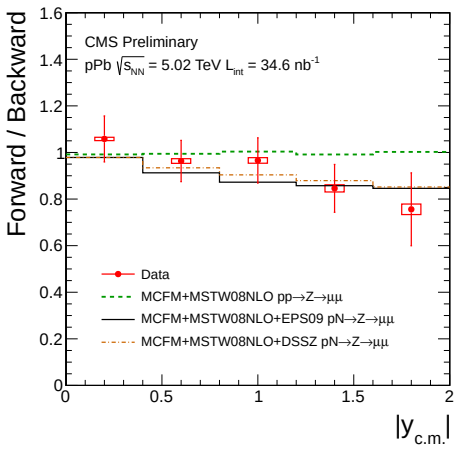

Figure 10: Forward-backward ratio of Z^0 boson cross-section in pPb collisions as a function of rapidity compared to predictions with nuclear modifications (EPS09 or DSSZ) and without them (green, dashed line) [20].

versions, but results of the measurement don't fully agree with either version (Fig.12), although a slightly better agreement is found with EPS09 nPDF calculations.

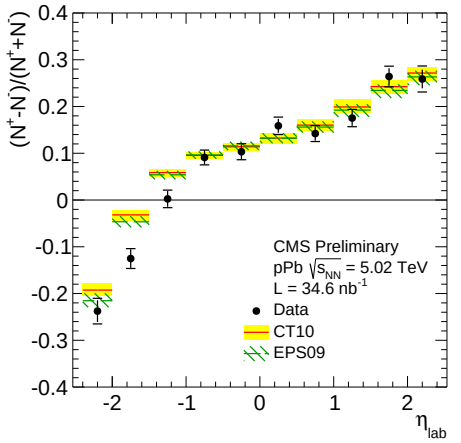

Figure 11: W boson charge asymmetry, $(\mathrm{N}^+ - \mathrm{N}^-)/(\mathrm{N}^+ + \mathrm{N}^-)$, as a function of the lepton pseudorapidity in the laboratory frame [21].

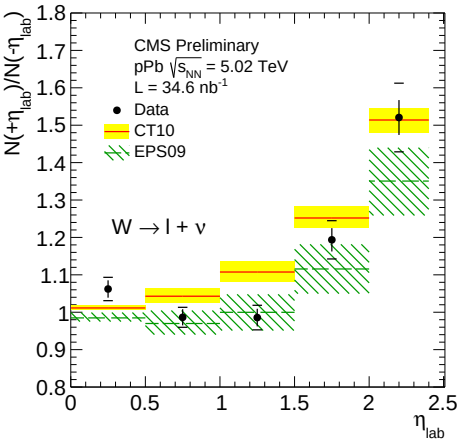

Figure 12: W boson forward/backward asymmetries $\mathrm{N}(+\eta_{\mathrm{lab}})/N(-\eta_{\mathrm{lab}})$ for positively charged leptons [21].

6 Summary

Recent results on hard scattering processes in nuclear collisions, obtained by ATLAS and CMS, are presented. They confirm that in PbPb collisions, jets are strongly quenched. The suppression of jet yields increases with centrality (down to $R_{AA} \simeq 0.5$), and continues to $p_T \simeq 400$ GeV. No strong flavor (b-quark) dependence of suppression is seen at high transverse momenta. Jet fragmentation is modified in PbPb collisions. ATLAS and CMS observe enhancements at low and high values of longitudinal and transverse momenta of jet fragments, and a suppression at intermediate values. CMS finds that the jet energy is distributed in PbPb collisions to more particles with lower p_T and going to large angles as compared to pp jets. In electroweak boson production, ATLAS observes a scaling of cross-sections with the number of elementary NN collisions. In pPb collisions, jets are not strongly suppressed. However, ATLAS observes no scaling-like variation of yields with centrality at forward rapidities. Latest results from pPb collisions allow more precise tests of parton distribution functions and indicate that EPS09 nPDF is preferred.

Acknowledgments

This work was supported in part by the National Science Center grants DEC-2011/03/B/ST/02631, by DEC-2013/08/M/ST2/00320 and by PL-Grid Infrastructure.

References

[1] ATLAS Collaboration, JINST 3 (2008) S08003.
[2] CMS Collaboration, JINST 3 (2008) S08004.
[3] ATLAS Collaboration, ATLAS-CONF-2014-025, http://cds.cern.ch/record/1702988.
[4] CMS Collaboration, CMS-PAS-HIN-12-004, http://cds.cern.ch/record/1472722.
[5] ATLAS Collaboration, arXiv:1406.2979 [hep-ex] (2014).
[6] CMS Collaboration, Phys. Rev. **C90** 024908 (2014).
[7] CMS Collaboration, CMS-PAS-HIN-14-010, http://cds.cern.ch/record/1703014.
[8] CMS Collaboration, Phys. Lett. **B730** 243 (2014).
[9] ATLAS Collaboration, ATLAS-CONF-2014-024, http://cds.cern.ch/record/1702986.
[10] CMS Collaboration, CMS-PAS-HIN-14-001, http://cds.cern.ch/record/1703004.
[11] CMS Collaboration, CMS-PAS-HIN-14-007, http://cds.cern.ch/record/1703013.
[12] CMS Collaboration, CMS-HIN-14-004, http://cds.cern.ch/record/1703520.
[13] CMS Collaboration, arXiv:1312.4198 [nucl-ex] (2013).
[14] CMS Collaboration, CMS-PAS-HIN-13-006, http://cds.cern.ch/record/1631991.
[15] CMS Collaboration, Eur. Phys. J. **C74** 2951 (2014).
[16] CMS Collaboration, Phys. Lett. **B718** 773 (2013).
[17] ATLAS Collaboration, ATLAS-CONF-2014-026, http://cds.cern.ch/record/1702992.
[18] ATLAS Collaboration, ATLAS-CONF-2014-023, http://cds.cern.ch/record/1702982.
[19] ATLAS Collaboration, ATLAS-CONF-2014-020, http://cds.cern.ch/record/1702971.
[20] CMS Collaboration, CMS-PAS-HIN-14-003, http://cds.cern.ch/record/1703012.
[21] CMS Collaboration, CMS-PAS-HIN-13-007, http://cds.cern.ch/record/1703270.

Hot and dense matter at RHIC and LHC

Eugenio Scapparone

INFN-Bologna, Via Irnerio 46, 40126 Bologna, Italy

DOI: http://dx.doi.org/10.3204/DESY-PROC-2014-04/288

The results obtained by RHIC and LHC experiments in the study of nucleus-nucleus collisions shed light on the behaviour of the hot and dense matter produced in heavy ion interactions at high energy. The recent p-Pb run at the LHC added another piece of information, showing p-nucleus interactions provide interesting and unexpected features. The most recent results, the open questions and the perspectives will be discussed.

1 Introduction

During the last decades, high energy heavy ion physics provided impressive and outstanding results. RHIC experiments produced several fascinating discoveries: the hot and dense matter created in the nuclei collisions at a centre of mass energy $\sqrt{s_{\rm NN}}$=200 GeV behaves as a nearly viscosity-free fluid. The nuclear medium, opaque to hadrons but transparent to photons, suppresses the away-side jet in events with two back-to-back jets. Later LHC experiments showed that increasing the energy to $\sqrt{s_{\rm NN}}$=2.76 TeV gives a fireball hotter, larger and lasting longer. New phenomena manifest or become more pronounced: the suppression of the J/ψ in head-on central collisions (low impact parameter) and/or at low p_T is less pronounced compared to RHIC and this vector meson shows a non-zero elliptic flow. Charmed meson nuclear modification factor is larger than ordinary hadron one, and it looks smaller than that measured with b-quark hadrons. In addition the study of p-Pb interactions showed an unexpected collective behaviour and one cannot exclude yet the quark gluon plasma is created in this lighter system too.

Although these exciting results provided a remarkable step forward in the comprehension of this new state of matter, a precise measurement of the parameters characterizing this fluid is still missing; as an example the shear viscosity (η/s) has an uncertainty as large as a factor four and a similar uncertainty affects the jet transport parameter ($\hat{q}$) measurement. The above discoveries raised a number of compelling questions. What is the mechanism behind a so fast quark thermalization ? Does the QGP contain quasi-particle or long lived excitations are cancelled by the strong field ? What is the origin of the ridge, observed in p-p collision too ? These questions can be answered in the next years when a plenty of new data will be available: LHC will offer the opportunity to study the QGP at the highest temperatures ($\sqrt{s_{\rm NN}}$= 5.5 TeV) and RHIC will improve the beam energy scan (BES) to study the phase transition boundary and to search for the phase space critical point.

Given the available space I will not try to give a comprehensive review of heavy ion results at RHIC and LHC, but I will focus on few subjects. Jets and high p_T events will not be discussed

here, since a dedicated talk on this subject was presented at this conference.

2 Global properties

The Hanbury-Brown and Twiss(HBT) [1] correlation played an important role in astrophysics in the '50s, when it was used to measure the star angular size. Years later, particle physicists relied on this method to assess the spatial scale of the emitting source size by studying identical bosons, as charged pion pairs. The two particle correlation function can be defined as the ratio of two measured distributions based on two different samples, using pion pairs from the same event and from different events, respectively. The pair three-momentum difference **q** can be decomposed into the three components (q_{out}, q_{side}, q_{long}), where the *out* axis points along the pair transverse momentum, the *side* axis is perpendicular to the transverse momentum plane and the *long* axis points along the beam. The three-dimensional correlation function is fitted to an expression accounting for the Bose-Einstein enhancement, containing a term $G(q) = e^{-q^2R^2}$, where $R = (R_{out}, R_{long}, R_{side})$ is the HBT radius of the production region.

The ALICE results[2] give at the LHC a source volume $V \simeq 300\ fm^3$, a factor 2 larger than the volume measured at RHIC and a lifetime $\tau \simeq 10$ fm/c, a 20% larger than the one measured at RHIC. As pointed out by PHENIX [3], the fireball shines, emitting direct photon with a temperature T=221±19(sta)±19(sys) MeV [3]. ALICE measured a 30% hotter medium, obtaining T = 304±51 (sta+sys) MeV [4]. It is worth noting this is the average fireball temperature: hydro-dynamical models predict the highest temperature reached in the early stage is expected up to a factor 3 higher. The energy density can be estimated by using the Bjorken-formula approximation. At the LHC the hot and dense matter reaches ≃15 GeV/fm^3 [5], a factor 3 larger than the energy density measured at RHIC. In summary, the increase in centre of mass energy from $\sqrt{s_{\rm NN}}$=200 GeV to 2.76 TeV reflects in a fireball with a factor 2 larger volume, a factor 3 larger energy density, lasting 20% longer and with a temperature 30% hotter, equivalent to ($3{\cdot}10^{12}$K). Compared to this temperature record, the interior of the sun is an almost cold place, reaching a modest $2{\cdot}10^{7}$K !

3 Collectivity

The azimuthal momentum distribution of the emitted particles is usually expressed as

$$\frac{dN}{d\Phi} \propto 1 + \sum_n 2v_n \cos(2n(\Phi - \Psi_n) \tag{1}$$

where v_n is the magnitude of the $n-th$ order harmonic term relative to the angle of the plane Ψ_n.

One of the most exciting results obtained at the RHIC was the evidence that the bulk of the produced hot matter is well described by fluid-dynamics, predicting a non vanishing elliptic flow v_2. At the LHC the p_T integrated v_2 showed an increase of about 30% compared to RHIC, mainly due to the increase of the average transverse momentum of the produced particles. Recently, the ALICE collaboration, taking advantage of the detector powerful particle identification, published a paper focused on identified hadron elliptic flow [6]: a clear mass ordering was observed, with heavier particles showing a smaller v_2. This not-trivial result,

predicted by fluid-dynamic models, indicates the radial flow boosts heavier particles to higher p_T, $\Delta p_T \simeq \Delta \mathrm{m}\beta$.

One of the most urgent questions to be answered is how perfect this fluid is, that is to provide a precise measurement of the shear viscosity η/s. Initial system condition, feeding the hydro models, are a very important source of uncertainty, when extracting the medium parameters from data. As pointed out in [7], the comparison of PHOBOS elliptic flow with hydro-models gives a best fit η/s ranging from 0.08 to 0.16 when applying initial conditions based on the Colour Glass Condensate or the Glauber model, respectively. Improving our knowledge on the initial conditions is therefore mandatory to reduce the uncertainties on the shear viscosity η/s. STAR studied the U-U interactions at $\sqrt{s_{\mathrm{NN}}}$= 193 GeV. The prolate shape of this nucleus, provides the possibility to study the initial condition effect on the azimuthal distributions: interactions may occur in a body-body configuration (giving large v_2 and a relatively small number of charged particles) or tip-tip (characterized by a small v_2 and a large number of charged particles). To minimize the effect due to the impact parameter, the analysis has to be restricted to events with top 0.1% centrality. Zeta Degree Calorimeters tag these two different configurations, measuring the energy of spectator nuclei. The elliptic flow was measured as a function of the normalized multiplicity(mult/<mult>): while the Glauber model predicted a too step dependence, the IP-Glasma model [8] gives a satisfactory prediction. This model provides initial conditions for systematic flow studies. It combines the IP-Sat (impact parameter saturation) model of high energy nucleon (and nuclear) wave functions with the classical SU(3) Yang-Mills (CYM) dynamics of the Glasma fields produced in a heavy-ion collision. Event by event fluctuations studied by ATLAS [9] at the LHC provide another successful test for the IP-Glasma model. The eccentricity ϵ_2, ϵ_3, ϵ_4 are expected to be proportional to v_2 ,v_3, v_4 in most hydrodynamic calculations. It is worth nothing recently few studies showed this statement hardly applies to v_4 [10]. Any deviation of the proportionality constant can be used to constrain the shear viscosity and the initial system geometry. In the ATLAS analysis, for each event, the v_2,v_3,v_4 are extracted. The v_n probability distributions are compared to the eccentricity, rescaled to match the $<v_n>$ of the data. Initial condition were provided by two different models: the Glauber model and the MC-KLN model, the latter including gluon saturation effect. Both the Glauber and the MC-KLN models predict correctly the data at low centrality, but fail for peripheral collisions [9], underestimating the probability for large v_n. On the contrary, as pointed out in ref. [11], the IP Glasma model, coupled to the MUSIC code, a 3+1 dimensional relativistic viscous hydrodinamic simulation model, predicts quite well these distributions for peripheral events too. Fluctuations are a gold mine in modern physics: as an example temperature fluctuations in the microwave background provided invaluable informations on the universe composition. Geometric nucleon position and intrinsic subnucleon scale colour charge fluctuations are quenched by the shear viscosity: their magnitude gives therefore a direct indication on how perfect this fluid is. One of the most remarkable effects of the fluctuations is the generation of harmonics of order higher than v_2(v_n,$n \geq$3). It was shown in [12] the higher orders are very sensitive to the shear viscosity. Several experiments at the LHC measured v_n in different intervals of centrality [13, 14]. In Fig. 1 the PHENIX data [15] are compared to the IP-Glasma+Music prediction for harmonics of any order. A satisfactory agreement is obtained, with η/s=0.12 as favourite parameter. Applying the fit to the ATLAS [13] or ALICE [14] results gives a nice fit too, with a preferred η/s=0.2. The above result may suggest η/s is changing from RHIC to LHC energies. An attempt to fit all the data with a η/s temperature (and hence energy) dependent was attempted. The fit at $p_T > 1.5$ GeV/c poorly reproduces the RHIC data(fig. 2, left panel). The η/s(T) functional

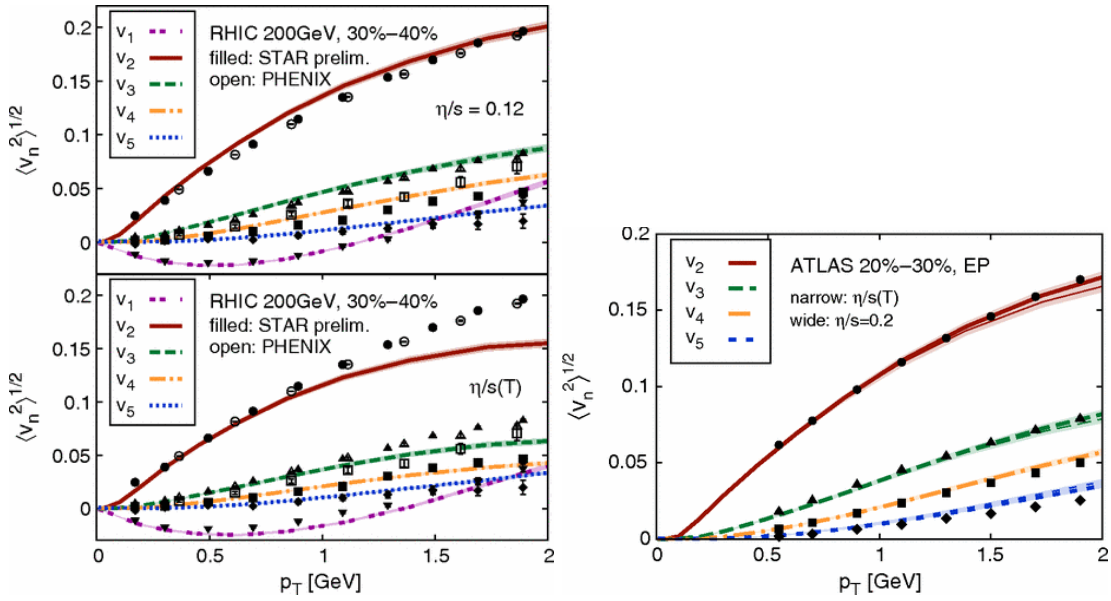

Figure 1: Comparison of $v_n(p_T)$ at RHIC (left) using constant η/s=0.12 and a temperature dependent $(\eta/s)(T)$, and at the LHC(right) using constant η/s=0.20 and a temperature dependent $(\eta/s)(T)$

form should be improved and more data at different energies, as those coming from RHIC BES, are required. Ultra central collisions are marginally dependent on initial conditions: Luzum and Ollitreatus showed [16] the root mean square of the harmonic eccentricity decreases with centrality. In addition the predictions obtained by using several different models get closer. The shear viscosity can be extracted comparing the ATLAS p_t integrated v_n data [17] to different model predictions. As a result a shear viscosity $0.07 \leq \eta/s \leq 0.43$ was obtained. The large allowed interval (factor 6) is mostly due to a tension between the v_2 and the v_3 constrain. G. Denicol et al. [18] included in the simulation the repulsive effect of nucleon-nucleon correlation, playing a non negligible role for the most central events. The fit of the IP-Glasma+Music model to the ATLAS v_n data, improves the v_2 and v_3 predictions, reduce their mutual tension and gives a preferred value of η/s=0.21. Further improvements may came from the recent data published by CMS, studying v_n at centrality as small as 0-0.2% [19].

4 Nuclear modification factor

The energy loss of scattered partons traversing the hot and dense medium can be quantified using the nuclear modification factor R_{AA}, defined as

$$R_{AA}(p_T) = \frac{Yield_{AA}(p_T)}{< N_{coll} >_{AA} \; Yield_{pp}(p_T)}, \tag{2}$$

where $Yield_{AA}$ is the yield obtained in nucleus-nucleus collisions, $Yield_{pp}$ is the yield obtained in pp collisions and $< N_{coll} >_{AA}$ is the average number of nucleon-nucleon collisions in A-A events.

A nuclear modification factor close to unit indicate that nucleus-nucleus collisions are equivalent to the superposition of nucleon-nucleon collisions, properly normalized. Partons are expected to lose energy in the hot and dense medium via gluon radiation and elastic collisions, leading to $R_{AA} < 1$. The QCD picture of parton energy loss in high energy heavy ion interactions predicts a gluon energy loss higher than the quark energy loss. In addition heavy quarks are expected to lose less energy compared to ligher quarks, due to the lack of gluon radiation in a forward cone (Casimir cone), whose angle $\theta = M_q/E_q$. Hints for a charged mesons (D^0, D^+, D^-) R_{AA} larger than that of charged particles has been reported by the ALICE experiment [20]. CMS showed the nuclear modification factor for non prompt J/Ψ(coming from b decay) is larger than D meson R_{AA}. These are clear indications the energy loss in the hot and dense matter follows the expected quark hierarchy.

The beam energy scan performed at RHIC is a nice opportunity to study the parton energy loss at different temperatures. At $\sqrt{s_{\rm NN}}$=200 GeV PHENIX found[21] a strong suppression for heavy flavour electrons compared to pp interactions (R_{AA} <1), while at $\sqrt{s_{\rm NN}}$=62 GeV the nuclear modification factor is compatible or larger than unit [22]. Although an higher statistics and a pp run at the same energy is required, this result indicates a change in the competition between the Cronin enhancement, that is prevalent in lower energy collisions, and the suppressing effects of the hot medium, that dominates at high energies. Another remarkable result obtained during the RHIC BES comes from STAR, measuring [23] the central-to-peripheral nuclear modification factor R_{CP} as a function of the centre of mass energy, where R_{CP} is defined as

$$R_{CP}(p_T) = \frac{< N_{Coll} >^{60-80\%}}{< N_{Coll} >^{0-5\%}} \frac{Yield_{AA}^{0-5\%}(p_T)}{Yield_{AA}^{60-80\%}(p_T)} \quad (3)$$

where $< N_{Coll} >^{60-80\%}$ is the average number of nucleon-nucleon collisions in events with centrality 60-80%, $< N_{Coll} >^{0-5\%}$ is the average number of nucleon-nucleon collisions in events with centrality 0-5%. While at $\sqrt{s_{\rm NN}}$=200 GeV $R_{CP} < 1$, as expected for partonic energy loss, at $\sqrt{s_{\rm NN}}$=7.7 GeV it exceeds 5 at p_T= 3 GeV/c. These two opposite trends show a smooth transition, with $R_{CP} \simeq 1$ reached between $\sqrt{s_{\rm NN}}$=27 GeV and $\sqrt{s_{\rm NN}}$=39 GeV: is the phase transition boundary within this energy interval ?

5 Quarkonia

The evidence for J/ψ suppression was a smoking gun of QGP formation at CERN-SPS experiments. Years later the RHIC experiments showed an unexpected result: the amount of suppression at $\sqrt{s_{\rm NN}}$=200 GeV was almost unchanged with respect to the SPS energies. The J/ψ suppression measured by ALICE at the LHC, was less pronounced at small centrality compared to RICH, both at forward and mid-rapidity. A possible explanation is provided by the recombination mechanism, playing an important role in J/ψ formation in heavy ion collisions at high energy. On average 70-80 $c\bar{c}$ pairs/events are expected at the LHC, to be compared to $\simeq$10 pairs at RHIC. J/ψ from $c\bar{c}$ recombination are expected to show a softer p_T spectrum and hence the J/ψ suppression should be stronger at higher p_T. Indeed ALICE results confirms this interpretation, as shown in Fig. 2(left panel). Moreover, in contrast to primordial J/ψ, the J/ψs from recombination are expected to inherit from c and $\bar{c}$ quarks their elliptic flow, due to the c quark thermalization. At RHIC a J/ψ elliptic flow consistent with zero was reported [24], while at the LHC ALICE [25] and CMS showed [26] a non zero v_2, with a $\simeq 4\sigma$ significance.

Due to the lower b$\bar{b}$ production cross section compared to the $c\bar{c}$ one, Υ is a powerful tool to study colour screening at the LHC. Nevertheless the feed-down from higher mass bottomonia, complicates data interpretation. Lattice QCD predicts a vector meson sequential suppression pattern with temperature: large uncertainties exist in the absolute calibration of this thermometer: Υ is expected to melt at a temperature 2-5 T_C, depending on the model considered, while the J/ψ melting temperature ranges from $1.5T_C$ to $3T_C$. STAR and PHENIX at RHIC showed hints for a Υ suppression in Au-Au interactions at $\sqrt{s_{\rm NN}}$=200 GeV. This suppression is compatible with the suppression reported at the LHC by CMS [27], suggesting the measured Υ suppression is consistent, both at RHIC and at the LHC, with the $\Upsilon(2s)$, $\Upsilon(3s)$ and χ_B full melting only, suggesting the $\Upsilon(1s)$ melting threshold was not reached yet. CMS measured the suppression of the three excited state: the $\Upsilon(1s)$ suppression increases with the centrality and is not suppressed in very peripheral collisions. On the contrary $\Upsilon(2s)$ is suppressed in peripheral collisions too. Finally the suppression of $\Upsilon(3s)$ is quite strong: an upper limit in the $\Upsilon(3s)/\Upsilon(1s)$ ratio <0.04 was set.

The ratio of $\Upsilon(2s)/\Upsilon(1s)$ is quite similar in pp (0.26 ± 0.01(sta) $\pm$ 0.01(sys) $\pm$ 0.02(glob))) and p-Pb interactions (0.22 ± 0.01(sta)$\pm$ 0.01(sys) $\pm$ 0.01(glob)) [27]. As a consequence, the strong $\Upsilon(2s)$ suppression seen in Pb-Pb collision (0.09 ± 0.02(sta) $\pm$ 0.02(sys) $\pm$ 0.01(glob)) cannot be explained by cold matter effects.

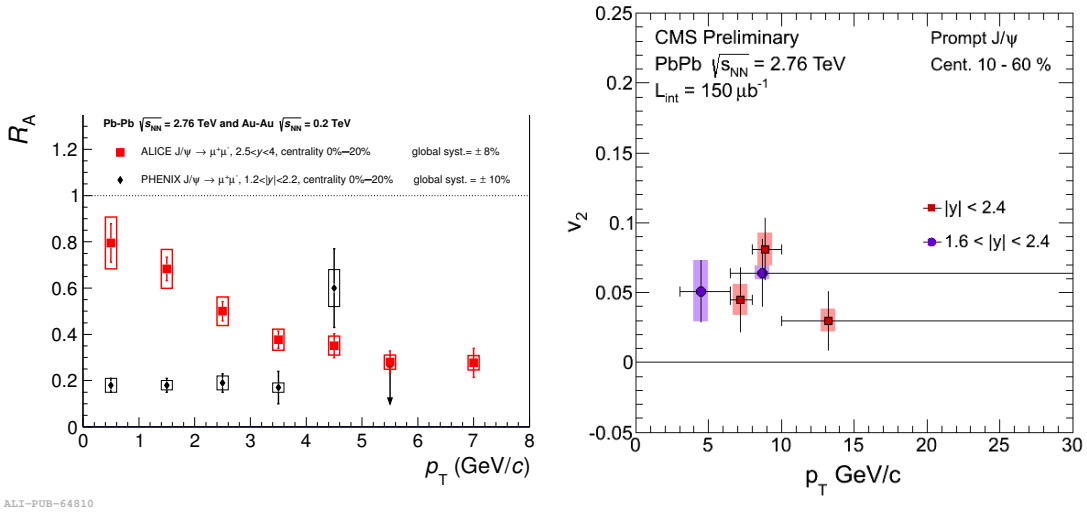

Figure 2: Left: comparison of J/ψ suppression as a function of the transverse momentum measured at the RHIC and at the LHC in the centraliy bin 0-20%. ALICE points show a less pronounced suppression at low p_T. Right: the elliptic flow measured by CMS. Both the result support a J/ψ recombination scenario.

6 The Ridge

Is Cold Nuclear Matter produced in p-Pb collisions at the LHC really cold ? Looking at electrons produced in heavy flavour decay (R_{pPb} $\simeq$1), to be compared with a much smaller

nuclear modification factor obtained in Pb-Pb collisions, the answer is affirmative. A similar conclusion can be drawn considering D meson production [28] or inclusive jet production [29] in p-Pb collisions. In addition the study of J/ψ in p-Pb collisions shows a modest to zero suppression, depending on the considered rapidity region; this result can be fully explained by initial state effects, as gluon shadowing. CMS discovered a ridge-like structure in events with a large number of produced charged particles in pp collisions [30]. A similar structure was previously found in Au-Au collisions by the RHIC experiments. The p-Pb collisions showed a ridge-like structure too, very similar, at a first look, to that observed in Pb-Pb collisions. This unexpected feature triggered a large amount of experimental [31, 32, 33] and theoretical studies. The ridge-like structure in pp and p-Pb collisions is surprisings, since these systems were not expected to produce a fireball dense and hot enough to produce strong collective effects. Several methods to separate the jet and the ridge components have been used. Namely ALICE subtracted the sample with a centrality 60-100% from the most 0-20% central events. As a result a double ridge-like structure was obtained [31]. The projection in the $\Delta\Phi$ plane can be fitted to a function:

$$\frac{1}{N_{trig}}\frac{dN}{d\Delta\Phi} = a_0 + 2\sum_{n>1} a_n \cos(n\Delta\Phi), \tag{4}$$

with v_n=$\sqrt{a_n/b}$, where b is the function baseline. As a result most of the Φ dependence comes from v_2 component, but higher orders are present too. ATLAS studied the v_n harmonics (n=1,2,3,4,5) in events with high multiplicity (220≤N<260) [33]: the results are fully consistent with the CMS analysis using the same charged particle intervals [34]. The v_n harmonics (n=1,2,3,4,5) distributions show an impressive similarities to those obtained in Pb-Pb collisions with similar multiplicity (20-30% centrality) [17]. To quantify this evidence CMS used multiparticle correlation in p-Pb interactions [35]: any effect coming from a genuine cumulative dynamics should not depend on the number of particles used to compute the v_2. The v_2 coefficient was extracted from the cumulant ($v_2(4)$,$v_2(6)$,$v_2(8)$ and $v_2(LYZ)$). For a given multiplicity range in either the Pb-Pb or p-Pb system, the values of $v_2(4)$,$v_2(6)$,$v_2(8)$ and $v_2(LYZ)$ are found to be in agreement within ±10%. The data support the multiparticle nature of the observed long-range correlations in p-Pb collisions. In addition ALICE and CMS measured the elliptic flow for identified hadrons in p-Pb collisions[36]: a mass ordering was observed (softer hadrons show larger v_2), as expected by hydro models. The above results give a convincing evidence that a large collectivity exist in p-Pb data. We cannot conclude Quark Gluon Plasma is formed in p-Pb collisions too, but this system looks hotter than expected. Another interesting effect reported in p-Pb collisions is the possible enhancement of R_{pPb} reported by ATLAS and CMS at high transverse momentum, ($p_T \geq 20$ GeV/c): more data are required and a dedicated pp run at $\sqrt{s_{\rm NN}}$=5 TeV is mandatory to have a firm conclusion on this effect.

7 Conclusions

An integrated luminosity as high as $1nb^{-1}$ will be delivered at the LHC during Run 2(2015-2018) for Pb-Pb collisions. The pp centre of mass energy will reach 13 TeV ($\simeq$ 5.1 TeV in Pb-Pb collisions). During Run 3 (2019-2026) an integrated luminosity $10nb^{-1}$ will be available to perform high statistic Pb-Pb studies; major detector upgrades during the Long Shutdown 2 will allow a reduction of the systematic error and an increase of the data samples.

After a successful Au-Au run in 2014, RHIC will provide p-Au collisions in 2015. A new beam energy scan (BES II) will be performed starting from 2018, with $\sqrt{s_{\rm NN}}\leq$ 20 GeV, focusing

on the critical point search and on a detailed study of the phase transition. The main goal of the electron-ion collider at BNL(eRHIC) is the exploration of the nucleus structure with the precision of electromagnetic probes at high energy and with sufficient intensity to access the gluon-dominated regime. The project foresees a startup on 2025 and new experiments, as sPHENIX and eSTAR [37].

References

[1] R. Hanury and R.Q.Twiss, Nature(London) 178, 1046 (1956).
[2] The ALICE Collaboration, Phys. Lett. **B696** (2011) 328.
[3] The PHENIX Collaboration, Phys. Rev. Lett **104** (2010) 132301.
[4] M. Wilde on behalf of the ALICE Collaboration, Nucl. Phys. **A904-905** (2013) 573c.
[5] The ALICE Collaboration *et al.*, Phys. Rev. Lett. (2010) 252301.
[6] The ALICE Collaboration, arXiv: 1405.4632, Submitted to JHEP.
[7] M. Luzum and R. Romantschke, Phys. Rev. **C78** (2008) 034915.
[8] B. Schenke *et al.*, Phys. Rev. **C86** (2012) 034908.
[9] The ATLAS Collaboration, JHEP 11(2013) 183.
[10] Z. Qiu and U. Heinz, arXiv:1104.0650v3.
[11] G. Gale *et al.*,Phys. Rev., Lett. **110** (2013) 012302.
[12] S. Schenke *et al.*, Phys. Rev. **C85** (2012) 024901.
[13] The ATLAS Collaboration, Phys. Rev. **C86** (2012) 014907.
[14] The ALICE Collaboration, Phys. Rev. Lett. **107** (2011) 032301
[15] The PHENIX Collaboration, Phys. Rev. Lett. **107** (2011) 2523
[16] M. Luzum and J. V. Ollitreaut, Nucl. Phys **904-905** (2013) 377c.
[17] The ATLAS Collaboration, Phys. Rev. **C86** (2012) 014907.
[18] G. Denicol *et al*, Proc. of Quark Matter 2014, in preparation.
[19] The CMS Collaboration, JHEP **02** (2014) 088.
[20] The ALICE Collaboration, JHEP 09 (2012) 112.
[21] The PHENIX Collaboration, Phys. Rev. Lett.**C84**(2011)044905.
[22] The PHENIX Collaboration, arXiv:1405.3301.
[23] the STAR Collaboration, Nucl. Phys.**A**905 (2013) 771c.
[24] The STAR Collaboration, Phys. Rev. Lett. **111** (2013) 52301.
[25] The ALICE Collaboration,Phys. Rev. Lett. **111** (2013) 162301.
[26] D. Manu on behalef of the CMS Collaboration, Proceedings of the Conference Quark Matter 2014, in press.
[27] The CMS Collaboration, JHEP 04 (2014) 103.
[28] The ALICE Collaboration, arXiv:1405.3452.
[29] E. A. Appelt on behalf of the CMS Collaboration, Proc. of Quark Matter 2014, in preparation.
[30] The CMS Collaboration, JHEP **1009** (2010) 091.
[31] The ALICE Collaboration, Phys. Lett. **B 719** (2013) 29.
[32] The CMS Collaboration, Phys. Lett. **B 724** (2013) 213.
[33] The ATLAS Collaboration, ATLAS-CONF-2014-021.
[34] The CMS Collaboration, CMS-HIN-014-006.
[35] The CMS Collaboration, CMS-HIN-014-006.
[36] The CMS Collaboration, Phys. Lett. **B 726** (2013) 164.
[37] The EIC White Paper, $https://wiki.bnl.gov/eic/index.php/Main_Page$.

Quark gluon plasma studies within a partonic transport approach

Florian Senzel[1], *Moritz Greif*[1], *Jan Uphoff*[1], *Christian Wesp*[1], *Zhe Xu*[2], *Carsten Greiner*[1]

[1]Goethe-Universität, Max-von-Laue-Str. 1, 60438 Frankfurt am Main, Germany
[2]Tsinghua University, Beijing 100084, China

DOI: http://dx.doi.org/10.3204/DESY-PROC-2014-04/289

Aiming for the simultaneous description of the hard and the soft regime of ultra-relativistic heavy-ion collisions, we present our recent findings within the partonic transport model BAMPS (Boltzmann Approach to Multi-Parton Scatterings). While using both elastic and radiative interactions provided by perturbative QCD, BAMPS allows the full 3+1D simulation of the quark-gluon plasma (QGP) at the microscopic level by solving the relativistic Boltzmann equation for quarks and gluons. BAMPS facilitates investigations of jet quenching, heavy flavor and elliptic flow within the partonic phase of heavy-ion collisions as well as studies of QGP medium properties in terms of e.g. transport coefficients like η/s and the electric conductivity.

1 Introduction

When heavy nuclei collide at ultra-relativistic energies, a system of hot and dense matter is created. Due to the enormous available energy densities within these collisions, quasi-free quarks and gluons represent the relevant degrees of freedom. Therefore the produced medium is commonly called the "quark-gluon plasma" (QGP). Experiments at both the Relativistic Heavy-Ion Collider (RHIC) at BNL and the Large Hadron Collider (LHC) at CERN show that the created medium exhibits interesting properties [1]: While high energy particles traversing the medium are quenched, the system shows at the same time a collective behavior similar to a nearly perfect liquid. Among the most prominent observables for quantifying these properties are the nuclear modification factor, R_{AA}, and the elliptic flow, v_2. While R_{AA} measures the suppression of inclusive particle yields compared to scaled p+p collisions, the elliptic flow v_2, defined in terms of the second Fourier coefficient of the azimuthal particle distribution, gives insight to the collectivity of the medium.

Although both phenomena are commonly attributed to the partonic phase of the heavy-ion collision, a simultaneous understanding of jet quenching and bulk phenomena on the microscopic level remains a challenge. In this paper we report on our progress in understanding the QGP within the partonic transport model *Boltzmann Approach to Multi-Parton Scatterings* (BAMPS). Based on cross sections calculated in perturbative quantum chromodynamics (pQCD), soft and hard particles are treated on the same footing in a common framework. While we take explicitly the running of the coupling into account, we study the energy loss of highly energetic [2, 3] and heavy flavor particles [4, 5] as well as the collective behavior in terms of the elliptic flow [3] and the electric conductivity of the underlying QGP medium [6].

2 The BAMPS framework

The partonic transport model *Boltzmann Approach to Multi-Parton Scatterings* (BAMPS) [7, 8] describes the full 3+1D evolution of both the QGP medium as well as high energy particles traversing it by numerically solving the relativistic Boltzmann equation,

$$p^\mu \partial_\mu f(\vec{x},t) = \mathcal{C}_{22} + \mathcal{C}_{2\leftrightarrow 3}\,, \tag{1}$$

for on-shell partons, quarks and gluons, and perturbative quantum chromodynamics (pQCD) interactions. To this end, a stochastical modeling of the collision probabilities together with a test-particle ansatz is employed.

Within BAMPS, both elastic $2 \to 2$ scattering processes calculated in leading-order pQCD, like e.g. $g\,g \to g\,g$, and inelastic $2 \leftrightarrow 3$ interactions, like e.g. $g\,g \leftrightarrow g\,g\,g$, are considered. The inelastic cross sections are calculated within an *improved Gunion-Bertsch (GB) approximation* [9, 10],

$$\left|\overline{\mathcal{M}}_{X\to Y+g}\right|^2 = 48\pi\alpha_s(k_\perp^2)\,(1-\bar{x})^2\,\left|\overline{\mathcal{M}}_{X\to Y}\right|^2 \left[\frac{\mathbf{k}_\perp}{k_\perp^2} + \frac{\mathbf{q}_\perp - \mathbf{k}_\perp}{(\mathbf{q}_\perp - \mathbf{k}_\perp)^2 + m_D^2\,(\alpha_s(k_\perp^2))}\right]^2 , \tag{2}$$

which agrees well with the exact pQCD matrix element over a wide phase space region [10]. As a remark, $\left|\overline{\mathcal{M}}_{X\to Y}\right|$ denotes the matrix element of the respective elastic process, while $k_\perp$ and $q_\perp$ are the transverse momentum of the emitted and internal gluons, respectively.

The running of the QCD coupling $\alpha_s(k_\perp^2)$ is considered within BAMPS by setting the scale of the coupling to the momentum transfer of the considered channel and thereby evaluating it for each collision at the microscopic level.

For modeling the Landau-Pomeranchuk-Migdal (LPM) effect, which is an important quantum effect within a partonic QCD medium, an effective cutoff function $\theta\,(\lambda - X_{LPM}\,\tau_f)$ in the radiative matrix elements is used, where λ is the mean free path of the radiating particle, τ_f the gluon formation time and X_{LPM} a parameter that effectively controls the independence between consecutive gluon emissions. The value $X_{LPM} = 0.3$ is fixed by comparing to R_{AA} data of neutral pions at RHIC [3]. Any further divergences occurring in the integration of the pQCD matrix elements are cured by a screening Debye mass m_D^2, which is dynamically computed on the basis of the current quark and gluon distribution [7].

3 Jet quenching within heavy-ion collisions

While employing PYTHIA [11] initial conditions together with a Monte Carlo Glauber sampling as described in detail in Ref. [7, 12], Fig. 1 (left) shows the nuclear modification factor R_{AA} obtained by BAMPS for gluons, light quarks and charged hadrons at the LHC [3]. Due to their larger QCD color factor, gluons are stronger suppressed than light quarks over the whole p_t range. For comparison with data, we also show the R_{AA} for charged hadrons resulting from fragmentation via AKK fragmentation functions [13]. According to this fragmentation functions, hadrons at low p_t are dominated by fragmenting gluons, while at higher p_t the quark contribution increases. Together with the rising shape of the R_{AA} this effect leads to a hadronic R_{AA} that is close to the quark R_{AA}.

Another method for characterizing the energy loss of high p_t partons within the QGP is the reconstruction of jets within heavy-ion collisions. Both the ATLAS [14] and CMS experiments

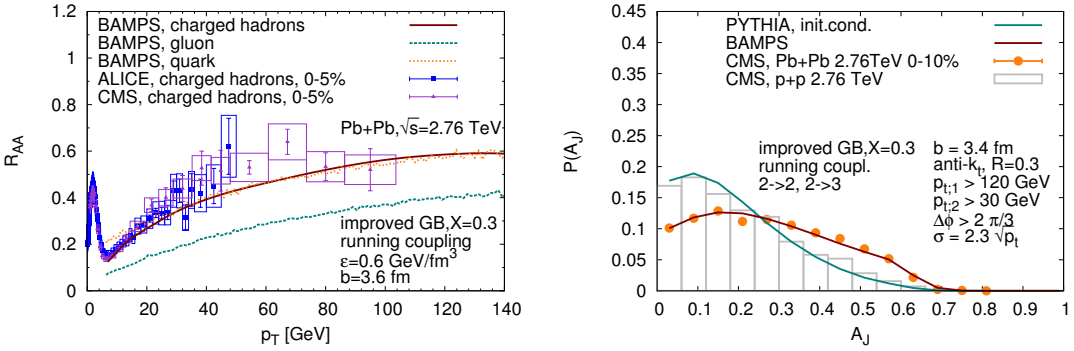

Figure 1: Left: Nuclear modification factor R_{AA} of gluons, light quarks, and charged hadrons at LHC (left) for a running coupling and LPM parameter $X = 0.3$ together with data of charged hadrons [16] as published in Ref. [3]. Right: A_J distribution calculated by BAMPS [2] with impact parameter $b_{\text{mean}} = 3.4$ fm together with PYTHIA initial conditions in comparison with $\sqrt{s} = 2.76$ TeV p+p and $\sqrt{s} = 2.76$ ATeV 0-10% Pb+Pb data measured by CMS [15] as published in Ref. [2].

[15] reported the measurement of an enhanced number of events with an asymmetric pair of back-to-back reconstructed jets in comparison to p+p events, which is quantified in terms of the momentum imbalance $A_J\,(p_{t;1}, p_{t;2}) = \frac{p_{t;1}-p_{t;2}}{p_{t;1}+p_{t;2}}$, where $p_{t;1}$ ($p_{t;2}$) is the transverse momentum of the leading (subleading) jet—the reconstructed jet with the highest (second highest) transverse momentum per event. While employing all experimental trigger conditions, Fig. 1 (right) shows the momentum imbalance A_J calculated within BAMPS together with data. Consistent with the R_{AA} studies the momentum imbalance of reconstructed jets within BAMPS is in agreement with data. For more details about the studies of reconstructed jets within BAMPS we refer to Ref. [2].

4 Heavy flavor within heavy-ion collisions

Quantitative studies of heavy flavor within BAMPS [17, 18, 4] show that, although elastic processes with a running coupling and an improved screening procedure contribute significantly to the energy loss of heavy quarks, they alone cannot reproduce the data of the nuclear modification factor or the elliptic flow of any heavy flavor particle species. Therefore, before radiative heavy quark processes have been implemented in BAMPS, we mimicked their influence by effectively increasing the elastic cross section by a factor $K = 3.5$, which is tuned to the v_2 data of heavy flavor electrons at RHIC [4]. With this fixed parameter it is furthermore possible to describe the R_{AA} of heavy flavor electrons at RHIC as well as the experimentally measured R_{AA} and v_2 of all heavy flavor particles at LHC (see Fig. 2). However, the need of the phenomenological K factor is rather unsatisfying from the theory perspective. Therefore, the question arises whether radiative processes can account for the missing contribution parameterized by the K factor. To this end, we present in the left panel of Fig. 3 the nuclear modification factor at LHC calculated within BAMPS while treating both heavy and light partons on the same footing consisting of radiative processes based on the improved GB matrix element, a running

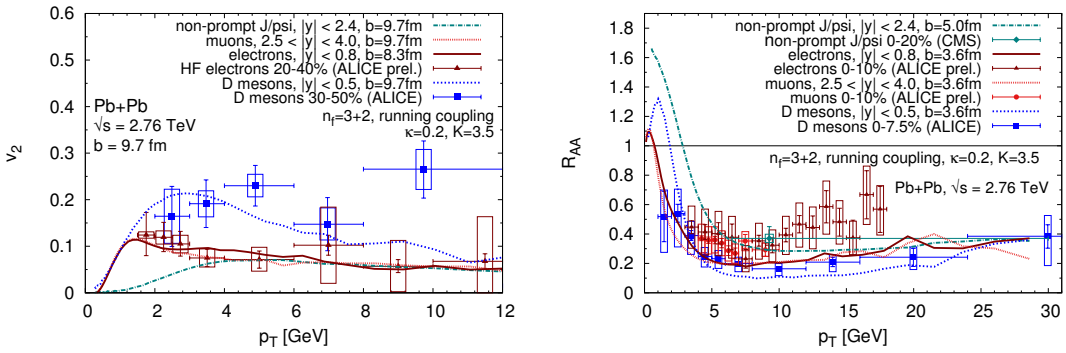

Figure 2: Elliptic flow v_2 (left) and nuclear modification factor R_{AA} (right) of various heavy flavor particles at LHC as published in Ref. [4] together with data [19, 20, 21, 22, 23, 24]. Only binary heavy flavor processes are considered and multiplied with $K = 3.5$.

coupling and an effective modeling of the LPM effect ($X_{LPM} = 0.3$) [5]. A good agreement between the BAMPS calculations and the nuclear modification factor of D mesons at LHC is found. As shown in Ref. [5] the energy loss of light and charm quarks is similar what explains why the nuclear modification factors of charged hadrons and D mesons in heavy-ion collisions have also the same values. Furthermore, mass effects in the fragmentation of gluons and light quarks to charged hadrons and charm quarks to D mesons lead to a similar suppression of charged hadrons and D mesons in BAMPS.

5 Properties of the underlying QGP medium

After presenting results on jet quenching and heavy flavor, we investigate the bulk evolution by employing the same setup as already described above together with the fixed LPM parameter $X_{LPM} = 0.3$ and a freeze-out energy density $\epsilon_c = 0.6\,\mathrm{GeV/fm}$ [26]. Since the microscopic hadronization processes within the soft regime are not fully understood yet, we show in Fig. 3 (right) our results for the integrated, partonic v_2 as a function of the number of participants N_{part} in comparison with LHC data.

Remarkably, by using the same microscopic pQCD interactions for both the hard and the soft momentum regime, BAMPS media build up a sizable amount of flow within the partonic phase. The reason for this lies in the isotropization of inelastic $2 \leftrightarrow 3$ processes as well as the running coupling, which affects the elliptic flow of particles with small p_T and the R_{AA} of particles with large p_T differently. The difference of the integrated, partonic v_2 of BAMPS and the measured, hadronic v_2 both at LHC is about $10-20\%$ and is supposed to be caused by the missing hadronic phase.

As advocated in dissipative hydrodynamic fits, an important quantity for the bulk medium in heavy-ion collisions is the shear viscosity to entropy density ratio η/s. In Fig. 4 (left) the temperature dependence of this value in a static medium allowing all $2 \to 2$ and $2 \leftrightarrow 3$ processes is shown. The shear viscosity is calculated via the Green-Kubo relation, which links the autocorrelation function of the medium energy-momentum tensor of the medium to the transport coefficient η [27]. The ratio η/s decreases with decreasing temperature and reaches

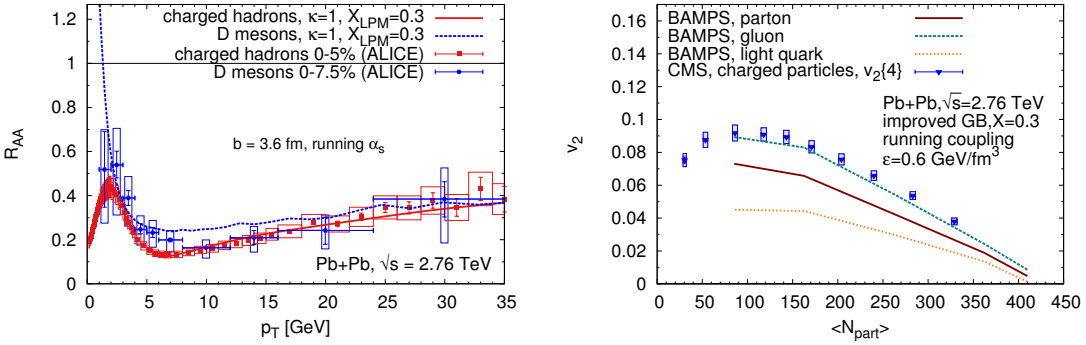

Figure 3: Left: Nuclear modification factor R_{AA} of charged hadrons and D mesons at LHC as published in Ref. [5] in comparison to data [16, 23]. Both binary and radiative processes with a LPM parameter set to $X_{LPM} = 0.3$ are considered. Right: Elliptic flow v_2 of gluons, light quarks, and both together (light partons) within $|\eta| < 0.8$ at LHC as a function of the number of participants N_{part} for a running coupling and LPM parameter $X = 0.3$ as published in Ref. [3]. As a comparison we show experimental data by CMS for charged hadrons within $|\eta| < 0.8$ [25].

a minimum at the phase transition. The value of η/s in the region around $T = 0.2\,\text{GeV}$ that is most important for the elliptic flow is approximately 0.2 for $n_f = 0$, which agrees very well with the shear viscosity extraction from dissipative hydrodynamic models employing a constant $\eta/s = 0.2$ together with initial fluctuations modeled by IP-Glasma [28]. Thus our calculation employing pQCD cross sections can give a microscopic explanation of the small shear viscosity to entropy density ratio extracted from hydrodynamics.

Besides the shear viscosity it is also possible to study other transport coefficients of the QGP medium, like e.g. the heat conductivity κ [39] or the electric conductivity σ_{el} [6]. The electric conductivity is related to the soft dilepton production rate and the diffusion of magnetic fields in the medium. Studies of the electric conductivity allows to compare the effective cross sections of medium constituents between several theories, including transport models [29, 40], lattice gauge theory [32, 33, 34, 35, 36, 37, 38] and Dyson-Schwinger calculations [41].

The longitudinal static electric conductivity σ_{el} relates the response of the electric diffusion current density $\vec{j}$ to an externally applied static electric field $\vec{E}$, $\vec{j} = \sigma_{\text{el}}\vec{E}$. Additionally, the electric conductivity can also be obtained by the Green-Kubo [42, 43] formula for the electric current density in x-direction $j_x(t)$,

$$\sigma_{\text{el}} = \beta V \int_0^\infty \langle j_x(0) j_x(t) \rangle \, \mathrm{d}t \quad \text{with} \quad j^x(t) = \frac{1}{V N_{\text{test}}} \sum_{k=1}^{M} q_k \sum_{i=1}^{N_k} \frac{p_i^x}{p_i^0}\bigg|_t \,, \tag{3}$$

where V denotes the volume, $\beta = T^{-1}$ the inverse temperature, M the number of particle species and N_k the number of particles of species k. The electric current autocorrelation function $\langle j_x(0) j_x(t) \rangle$ can be obtained numerically, as it has been done in e.g. Ref. [27] for the shear stress tensor correlation function.

By employing BAMPS with the described pQCD cross sections, it is possible to extract

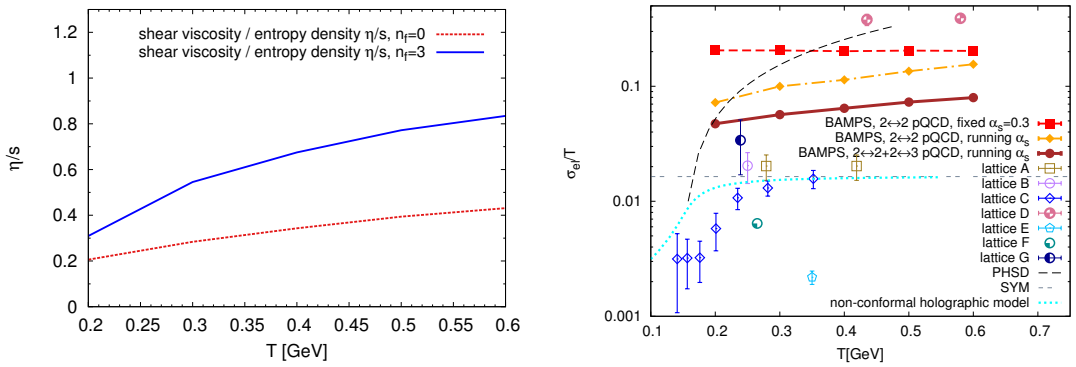

Figure 4: Left: Shear viscosity over entropy density η/s for running coupling and $X_{\mathrm{LPM}} = 0.3$ in a static medium of temperature T with number of quark flavors n_f as published in Ref. [3]. Right: Electric conductivity σ_{el} within BAMPS (filled symbols) as published in Ref. [6] compared to recent results from literature. The open symbols represent results from lattice QCD. PHSD: [29], SYM: [30], non-conformal holographic model: [31], lattice A: [32], lattice B: [33], lattice C: [34], lattice D: [35], lattice E: [36], lattice F: [37], lattice G: [38]. The electric charge is explicitly multiplied out, $e^2 = 4\pi/137$.

the electric conductivity of a plasma consisting of quarks and gluons in the massless limit using both approaches, via the response of the electric diffusion current density and the Green-Kubo relation. These studies have shown that both methods show identical results [6], what has been additionally justified by comparison with analytically formulas employing constant, isotropic cross sections. Figure 4 depicts the results for the electric conductivity using pQCD cross sections together with either a running coupling or a fixed coupling $\alpha_s = 0.3$. The electric conductivity reflects in a profound way the effect of inelastic pQCD scatterings and the running of the coupling α_s. The presented results from the BAMPS transport simulation lie between $0.04 \leq \sigma_{\mathrm{el}}/T \leq 0.08$ for temperatures 0.2 GeV $\leq T \leq$ 0.6 GeV. As a remark, the quantitative comparison with lattice QCD data is difficult since the published results from lattice QCD for the electric conductivity vary widely between $0.001 \leq \sigma_{\mathrm{el}}/T \leq 0.1$.

6 Conclusions

By solving the relativistic Boltzmann equation for on-shell partons, the partonic transport approach BAMPS allows the full 3+1D microscopic simulation of the QGP created in ultra-relativistic heavy-ion collisions. Consequently, investigations of both the suppression of high p_t particles and the collectivity of the bulk medium within a common framework are possible within BAMPS. By employing an improved Gunion-Bertsch matrix element and a running coupling evaluated at the microscopic level, we are able to describe high p_t and heavy flavor observables at LHC. Furthermore, the same microscopic pQCD interactions lead to a sizable elliptic flow of the bulk medium within the partonic phase. Furthermore, we investigated medium properties of the QGP in terms of the shear viscosity to entropy density ratio η/s and the electric conductivity σ_{el} from a microscopic perspective.

Acknowledgments

This work was supported by the Bundesministerium für Bildung und Forschung (BMBF), HGS-HIRe, H-QM, and the Helmholtz International Center for FAIR within the framework of the LOEWE program launched by the State of Hesse. Numerical computations have been performed at the Center for Scientific Computing (CSC).

References

[1] Berndt Müller, Jurgen Schukraft, and Boleslaw Wyslouch. First Results from Pb+Pb collisions at the LHC. *Ann.Rev.Nucl.Part.Sci.*, 62:361–386, 2012.

[2] Florian Senzel, Oliver Fochler, Jan Uphoff, Zhe Xu, and Carsten Greiner. Influence of multiple in-medium scattering processes on the momentum imbalance of reconstructed di-jets. arXiv:1309.1657, 2013.

[3] Jan Uphoff, Oliver Fochler, Florian Senzel, Christian Wesp, Zhe Xu, et al. Elliptic flow and nuclear modification factor in ultra-relativistic heavy-ion collisions within a partonic transport model. arXiv:1401.1364, 2014.

[4] Jan Uphoff, Oliver Fochler, Zhe Xu, and Carsten Greiner. Open Heavy Flavor in Pb+Pb Collisions at $\sqrt{s} = 2.76$ TeV within a Transport Model. *Phys.Lett.*, B717:430–435, 2012.

[5] Jan Uphoff, Oliver Fochler, Zhe Xu, and Carsten Greiner. Elastic and radiative heavy quark interactions in ultra-relativistic heavy-ion collisions. arXiv:1408.2964, 2014.

[6] Moritz Greif, Ioannis Bouras, Zhe Xu, and Carsten Greiner. Electric Conductivity of the Quark-Gluon Plasma investigated using a pQCD based parton cascade. arXiv:1408.7049, 2014.

[7] Zhe Xu and Carsten Greiner. Thermalization of gluons in ultrarelativistic heavy ion collisions by including three-body interactions in a parton cascade. *Phys.Rev.*, C71:064901, 2005.

[8] Zhe Xu and Carsten Greiner. Transport rates and momentum isotropization of gluon matter in ultrarelativistic heavy-ion collisions. *Phys.Rev.*, C76:024911, 2007.

[9] J.F. Gunion and G. Bertsch. Hadronization by color bremsstrahlung. *Phys.Rev.*, D25:746, 1982.

[10] Oliver Fochler, Jan Uphoff, Zhe Xu, and Carsten Greiner. Radiative parton processes in perturbative QCD – an improved version of the Gunion and Bertsch cross section from comparisons to the exact result. *Phys.Rev.*, D88:014018, 2013.

[11] Torbjorn Sjostrand, Stephen Mrenna, and Peter Skands. PYTHIA 6.4 physics and manual. *JHEP*, 05:026, 2006.

[12] Jan Uphoff, Oliver Fochler, Zhe Xu, and Carsten Greiner. Heavy quark production at RHIC and LHC within a partonic transport model. *Phys.Rev.*, C82:044906, 2010.

[13] S. Albino, B.A. Kniehl, and G. Kramer. AKK Update: Improvements from New Theoretical Input and Experimental Data. *Nucl.Phys.*, B803:42–104, 2008.

[14] Georges Aad et al. Observation of a Centrality-Dependent Dijet Asymmetry in Lead-Lead Collisions at $\sqrt{s_{NN}} = 2.77$ TeV with the ATLAS Detector at the LHC. *Phys.Rev.Lett.*, 105:252303, 2010.

[15] Serguei Chatrchyan et al. Jet momentum dependence of jet quenching in PbPb collisions at $\sqrt{s_{NN}} = 2.76$ TeV. *Phys.Lett.*, B712:176–197, 2012.

[16] Betty Abelev et al. Centrality Dependence of Charged Particle Production at Large Transverse Momentum in Pb–Pb Collisions at $\sqrt{s_{\rm NN}} = 2.76$ TeV. *Phys.Lett.*, B720:52–62, 2013.

[17] Jan Uphoff, Oliver Fochler, Zhe Xu, and Carsten Greiner. Heavy quarks at RHIC and LHC within a partonic transport model. *Nucl.Phys.*, A855:444–447, 2011.

[18] Jan Uphoff, Oliver Fochler, Zhe Xu, and Carsten Greiner. Elliptic flow and energy loss of heavy quarks in ultra-relativistic heavy ion collisions. *Phys.Rev.*, C84:024908, 2011.

[19] B. Abelev et al. D meson elliptic flow in non-central Pb-Pb collisions at $\sqrt{s_{\rm NN}} = 2.76$TeV. *Phys.Rev.Lett.*, 111:102301, 2013.

[20] Shingo Sakai. Measurement of R_{AA} and ν_2 of electrons from heavy-flavour decays in Pb-Pb collisions at $\sqrt{s_{NN}} = 2.76$ TeV with ALICE. *Nucl.Phys.*, A904-905:661c–664c, 2013.

[21] Zaida Conesa del Valle. Heavy-flavor suppression and azimuthal anisotropy in Pb-Pb collisions at $\sqrt{(}s_{NN}) = 2.76$ TeV with the ALICE detector. *Nucl.Phys.*, A904-905:178c–185c, 2013.

[22] Betty Abelev et al. Production of muons from heavy flavour decays at forward rapidity in pp and Pb-Pb collisions at $\sqrt{s_{NN}} = 2.76$ TeV. *Phys.Rev.Lett.*, 109:112301, 2012.

[23] Alessandro Grelli. D meson nuclear modification factors in Pb-Pb collisions at $\sqrt{s_{NN}} = 2.76$ TeV with the ALICE detector. *Nucl.Phys.*, A904-905:635c–638c, 2013.

[24] Serguei Chatrchyan et al. Suppression of non-prompt J/psi, prompt J/psi, and Y(1S) in PbPb collisions at $\sqrt{s_{NN}} = 2.76$ TeV. *JHEP*, 1205:063, 2012.

[25] Serguei Chatrchyan et al. Measurement of the elliptic anisotropy of charged particles produced in PbPb collisions at nucleon-nucleon center-of-mass energy = 2.76 TeV. *Phys.Rev.*, C87:014902, 2013.

[26] Zhe Xu and Carsten Greiner. Elliptic flow of gluon matter in ultrarelativistic heavy- ion collisions. *Phys.Rev.*, C79:014904, 2009.

[27] C. Wesp, A. El, F. Reining, Z. Xu, I. Bouras, et al. Calculation of shear viscosity using Green-Kubo relations within a parton cascade. *Phys.Rev.*, C84:054911, 2011.

[28] Charles Gale, Sangyong Jeon, Bjorn Schenke, Prithwish Tribedy, and Raju Venugopalan. Event-by-event anisotropic flow in heavy-ion collisions from combined Yang-Mills and viscous fluid dynamics. *Phys.Rev.Lett.*, 110:012302, 2013.

[29] W. Cassing, O. Linnyk, T. Steinert, and V. Ozvenchuk. Electrical Conductivity of Hot QCD Matter. *Physical Review Letters*, 110(18):182301, May 2013.

[30] Simon C Huot, Pavel Kovtun, Guy D Moore, Andrei Starinets, and Laurence G. Yaffe. Photon and dilepton production in supersymmetric Yang-Mills plasma. *Journal of High Energy Physics*, 2006(12):015–015, December 2006.

[31] S. I. Finazzo and Jorge Noronha. Holographic calculation of the electric conductivity of the strongly coupled quark-gluon plasma near the deconfinement transition. *Physical Review D*, 89(10):106008, May 2014.

[32] Gert Aarts, Chris Allton, Justin Foley, Simon Hands, and Seyong Kim. Spectral functions at small energies and the electrical conductivity in hot quenched lattice QCD. *Physical Review Letters*, 99(2):022002, 2007.

[33] Bastian B. Brandt, Anthony Francis, Harvey B. Meyer, and Hartmut Wittig. Thermal correlators in the ρ channel of two-flavor QCD. *Journal of High Energy Physics*, 2013(3):100, March 2013.

[34] Alessandro Amato, Gert Aarts, Chris Allton, Pietro Giudice, Simon Hands, and Jon-Ivar Skullerud. Electrical Conductivity of the Quark-Gluon Plasma Across the Deconfinement Transition. *Physical Review Letters*, 111(17):172001, October 2013.

[35] Sourendu Gupta. The electrical conductivity and soft photon emissivity of the QCD plasma. *Physics Letters B*, 597(1):57–62, September 2004.

[36] P. V. Buividovich, M. N. Chernodub, D. E. Kharzeev, T. Kalaydzhyan, E. V. Luschevskaya, and M. I. Polikarpov. Magnetic-Field-Induced Insulator-Conductor Transition in SU(2) Quenched Lattice Gauge Theory. *Physical Review Letters*, 105(13):132001, September 2010.

[37] Y Burnier and M Laine. Towards flavour-diffusion coefficient and electrical conductivity without ultraviolet contamination. *The European Physical Journal C*, 72(2):1–8, 2012.

[38] H.-T. Ding, A. Francis, O. Kaczmarek, F. Karsch, E. Laermann, and W. Soeldner. Thermal dilepton rate and electrical conductivity: An analysis of vector current correlation functions in quenched lattice QCD. *Physical Review D*, 83(3):034504, February 2011.

[39] M. Greif, F. Reining, I. Bouras, G.S. Denicol, Z. Xu, and C. Greiner. Heat conductivity in relativistic systems investigated using a partonic cascade. *Physical Review E*, 87(3):033019, March 2013.

[40] T. Steinert and W. Cassing. Electric and magnetic response of hot QCD matter. *Physical Review C*, 89(3):035203, March 2014.

[41] Si-xue Qin. A Divergence-Free Method to Extract Observables from Meson Correlation Functions. arXiv:1307.4587, 2013.

[42] Melville S. Green. Markoff Random Processes and the Statistical Mechanics of Time-Dependent Phenomena. II. Irreversible Processes in Fluids. *The Journal of Chemical Physics*, 22(3):1281, 1952.

[43] Ryogo Kubo. Statistical-Mechanical Theory of Irreversible Processes. I. General Theory and Simple Applications to Magnetic and Conduction Problems. *Journal of the Physical Society of Japan*, 12(6):570–586, June 1957.

New Accelerator Projects: Rare Isotope Facilities and Electron Ion Colliders

Thomas Roser
BNL, Upton, NY, 11973, USA

DOI: http://dx.doi.org/10.3204/DESY-PROC-2014-04/291

Presently there are two major areas of new accelerator projects in particle physics: a next generation of Rare Isotope facilities in the field of Nuclear Structure Physics and high luminosity Electron Ion Colliders as next generation QCD faciliies in the field of Hadron Physics. This paper presents a review of the present and future facilities and the required novel accelerator technologies for these two types of accelerator projects.

1 Introduction

Over the last century progress in accelerator technology is motivated by and has driven advances in both particle and nuclear physics. This started with Ernest Lawrence's first cyclotron built in 1932, small enough to fit in one's hand, and continues today with large hadron collider such as Brookhaven's Relativistic Heavy Ion Collider (RHIC) (Fig. 1) and CERN's Large Hadron Collider (LHC). Presently there are two major areas of new accelerator projects in particle physics: a next generation of Rare Isotope facilities in the field of Nuclear Structure Physics and high luminosity Electron Ion Colliders a next generation QCD facilities in the field of Hadron Physics.

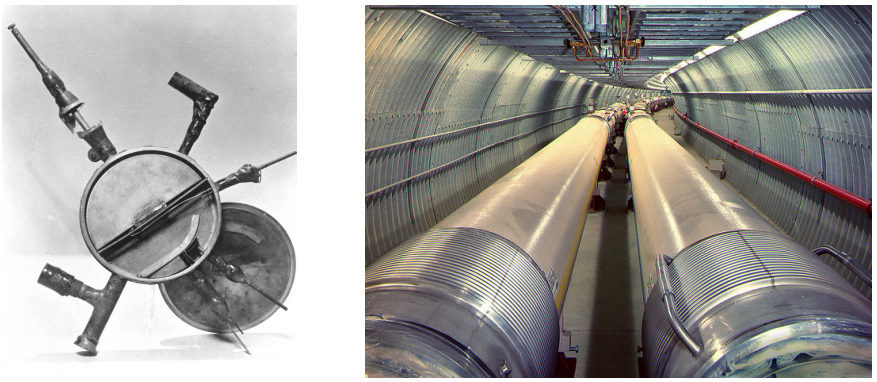

Figure 1: Accelerators used for nuclear and particle physics spanned an enormous range of scales form Ernest Lawrence's cyclotron that fit into one's hand to large hadron colliders such as the 3.8 km circumference Relativistic Heavy Ion Collider at BNL

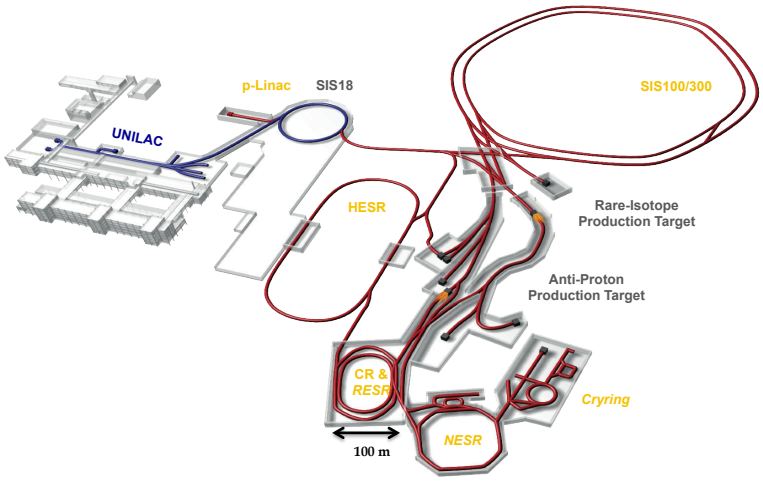

Figure 2: Layout of the FAIR facility near Darmstadt, Germany

2 Next generation of Rare Isotope facilities

The next generation of Rare Isotope facilities will dramatically increase the intensity of the driver accelerator. The three facilities under construction or close to the start of construction use a heavy ion driver beam. Enabling technologies are: Continuous Wave (CW), superconducting RF (SRF) Linear accelerators for partially stripped heavy ion beams; radiation hardened devices to strip electrons from the beams such as high speed rotating Carbon disks, liquid Lithium films or stable plasma windows; highly efficient heavy ion sources and charge breeders such as high intensity Electron Beam Ion Sources (EBIS) and high intensity Electron Cyclotron Resonance (ECR) sources; and acceleration of high intensity, partially stripped heavy ion beams in synchrotrons using Ultra High Vacuum (UHV) together with continuous collimation.

Three new Rare Isotope facilities are under construction or close to the start of construction:

- Construction has started for the Facility for Rare Isotope Beams (FRIB), a 0.2 GeV/n, 400 kW heavy ion driver that will produce beams of radioactive isotopes through fragmentation of uranium beam on a high power target. This will be the first installation of a large, CW SRF linac for hadron beams. It requires cavities for non-relativistic particle with a high quality factor to minimize the cryogenic cooling power. The heavy ion beams are produced partially stripped and then pass through an ion stripper for additional charge stripping as they gain energy. The ion stripper for the high intensity beams will be implemented either with a liquid metal film or a high pressure gas target. The construction period is planned from 2014 to 2020.

- The GSI laboratory near Darmstadt, Germany, is expanding its facility with a 30 GeV proton-equivalent heavy ion driver plus multiple accumulation and storage rings. The new facility will be called "Facility for Antiproton and Ion Research" (FAIR) (Fig. 2). The new 30 GeV synchrotron will be using fast cycling super-ferric magnets and will be optimized for the acceleration and storage of high intensity, partially stripped uranium ions. Construction has started and is now planned to be completed by about 2020.

- At the Institute of Modern Physics (IMP) in Lanzhou, China, preparations have started for a high intensity Heavy Ion Accelerator Facility (HIAF). The focus will also be on the production of rare isotopes and of high density plasma. The planned intensity of uranium beams in the SRF linac will be four times the planned intensity at FRIB. Construction is planned for the 2015 - 2021 period.

3 Electron Ion Colliders

There is renewed interest in a electron-ion collider with dramatically increased luminosity compared to the very successful electron-proton HERA facility at DESY. Most of the new proposals would also use polarized proton and light ion beams as well as heavy ion beams. Fig. 3 gives an overview of the peak luminosity versus center-of-mass energy for past, existing and future electron-proton facilities. Past and present facilities are indicated in black. The two proposals in the U.S. (MEIC at JLab and eRHIC at BNL) focus on the collision of polarized electrons with polarized protons at very high luminosity to measure the gluon spin structure at low x and electrons colliding with heavy ions for high-resolution imaging of gluon-dominated matter.

Two types of schemes to reach very high electron-ion luminosities are being pursued:

- The first scheme has the electron and hadron beam both circulating in a storage ring. In this case the beam-beam effects of the hadron beam on the lower energy electron beam severely limits the brightness of the hadron beam in order to keep the electron beam stable. To reach high luminosity many lower intensity bunches, with bunch spacing as short as 1 ns, are then needed, which then requires the operation with a large crossing angle to

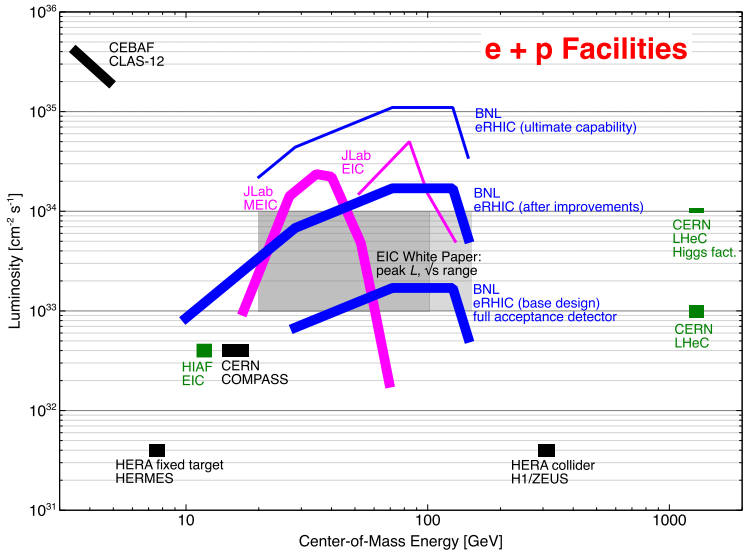

Figure 3: History and plans of the peak luminosity vs center-of-mass energy of lepton-hadron colliders

avoid parasitic collisions. This scheme is pursued for MEIC at JLab and HIAF-EIC at IMP.

- The second scheme uses an electron beam accelerated in a Energy Recovery Linac (ERL) to collide with a hadron beam in a storage ring. Since there is only a single collision of an electron bunch with the hadron beam a much higher beam-beam effect and therefore luminosity is possible. However the electron beam has to be continuously replenished from the source. This requires a new high intensity polarized electron source. This scheme is planned for eRHIC at BNL and LHeC at CERN.

3.1 MEIC at JLab

The first stage EIC proposal at JLab is called Medium Energy Electron-Ion Collider (MEIC) and would add a 3 - 12 GeV electron storage ring, using the present CEBAF as a full energy injector, and a new polarized proton (20 - 100 GeV) and heavy ion (12 - 40 GeV/n) accelerator complex (Fig. 4). The high luminosity of about $10^{34} cm^{-2} s^{-1}$ would be achieved with a very short bunch spacing of 1.3 ns as well as strong electron cooling of the ion beams. The whole complex would be laid out in the shape of a figure-8 to preserve beam polarization, including polarized deuteron beams, without needing Siberian snakes. Construction of this first stage could start after the present 12 GeV CEBAF upgrade is completed. A second stage would include a 20 GeV electron ring and a 250 GeV proton ring.

3.2 HIAF-EIC at IMP

The IMP laboratory in Lanzhou, China, also has plans to upgrade its HIAF to a Electron-Ion Collider by adding Figure-8 shaped polarized electron and proton rings. The electron energy will be 3 GeV, colliding with a 12 GeV polarized proton beam. With electron cooling of the proton beam a luminosity of $3 - 5 \times 10^{32} cm^{-2} s^{-1}$ could be reached.

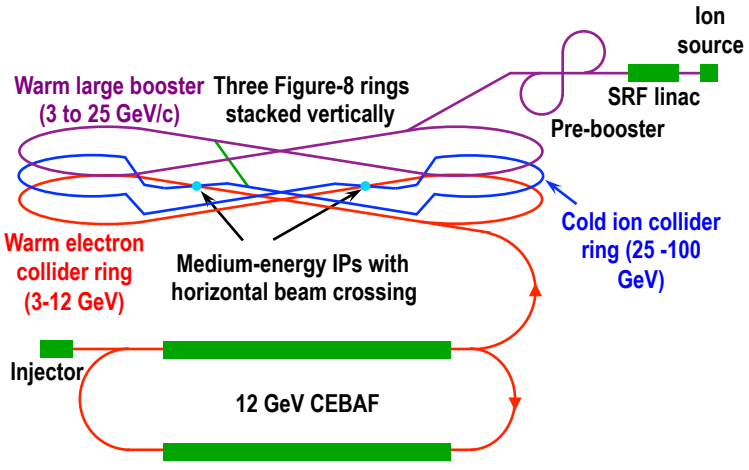

Figure 4: Layout of the proposed MEIC facility at JLab.

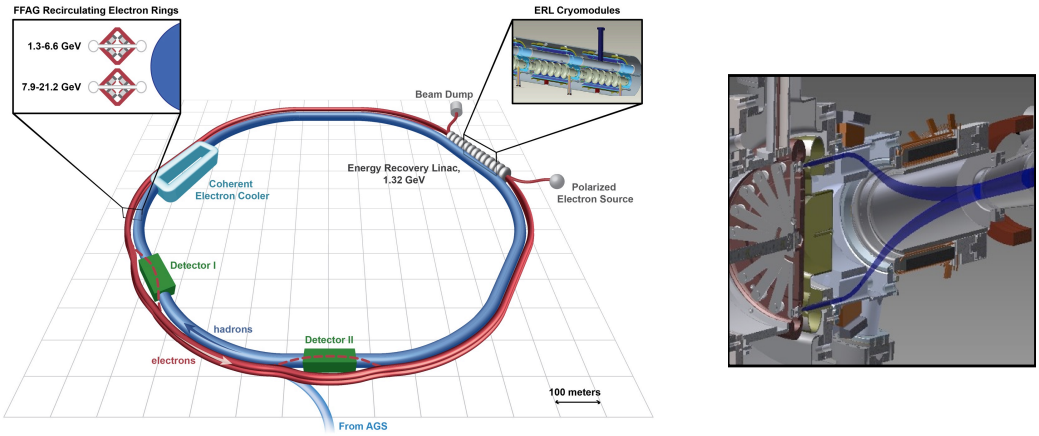

Figure 5: Layout of the proposed eRHIC facility at BNL (left) and schematic view of the high current, polarized "Gatling" electron source (right).

3.3 eRHIC at BNL

eRHIC at BNL would add a 21.2 GeV electron accelerator, based on an Energy Recovery Linac (ERL) with up to 16 recirculating passes inside the existing RHIC tunnel, to collide with the existing RHIC beams of 250 GeV polarized protons and 100 GeV/n heavy ions (Fig. 5). The 16 beam passes will be transported around the RHIC tunnel with two Fixed Field Alternating Gradient (FFAG) arcs. With the ERL the electron bunches would collide with the ion bunches only once and would allow for a very large disruption from the beam-beam interaction, which results in luminosities of about $2 \times 10^{33} cm^{-2} s^{-1}$. With modest upgrades (such as coating of the RHIC vacuum chambers) the luminosity could be increased ten-fold to about $2 \times 10^{34} cm^{-2} s^{-1}$. Because of the single pass nature of the collider a very intense (50 mA) polarized electron gun is required, which is about a factor of ten beyond the state-of-the-art. R&D is underway to build such an electron source that houses 24 individual cathodes that can be used one after the other in the style of a "Gatling" machine gun. A schematic view of this Gatling gun is shown on the right side of Fig. 5. To reach the high luminosity the ion beam will also have to be strongly cooled using coherent electron cooling. Construction of the eRHIC facility could be completed by 2024.

3.4 LHeC at CERN

There is also a proposal to collide a polarized electron beam from a 60 GeV ERL with the high energy LHC proton or heavy ion beam. Such a facility, called LHeC, would continue the search for lepton-quarks, started at HERA, but also could produce a copious number of Higgs particles if the luminosity could be increased to $10^{34} cm^{-2} s^{-1}$. The 60 GeV ERL would be the highest energy device of its kind and would use three recirculation arcs and a 20 GeV CW SRF Linac. The ERL would be in a tunnel separate from the LHC tunnel and the electron beam would collide with the LHC beam in a single interaction region. The highest luminosities would require that the electron bunch is captured by the space charge of the hadron beam at the collision point. The layout of the LHeC facility is shown in Fig. 6. Construction could occur

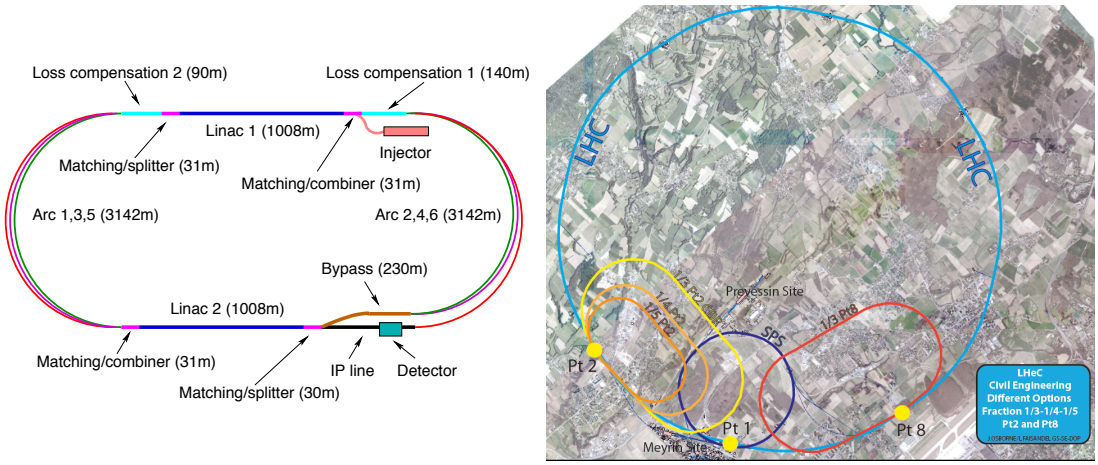

Figure 6: The 60 GeV ERL for LHeC is shown on the left. On the right are the possible locations for the electron ERL in the LHC ring.

during the 2020s.

4 Acknowledgments

I gratefully acknowledge Max Klein (Liverpool), Edgar Mahner (GSI/FAIR), Jie Wei (FRIB), Yuhong Zhang (JLab), Hongwei Zhao (IMP/Lanzhou), and Frank Zimmermann(CERN) for providing me with information on the status and plans of these projects.

Low-Energy Tests of the Standard Model - $(g-2)_\mu$ and Dark Photons

Achim Denig

Institute for Nuclear Physics and PRISMA Cluster of Excellence, Johannes Gutenberg University Mainz, Johann-Joachim-Becher-Weg 45, D-55099 Mainz, Germany

DOI: http://dx.doi.org/10.3204/DESY-PROC-2014-04/293

Low-energy tests of the Standard Model provide complementary insights to Beyond Standard Model Physics. We review two topical issues, namely the status of the anomalous magnetic moment of the muon $(g-2)_\mu$ as well as searches for a hypothetical extra-U(1) GeV-scale particle beyond the Standard Model - the so-called Dark Photon.

1 Introduction

The discovery of the Higgs boson in 2012[1] represents an impressive confirmation of the concepts of the Standard Model (SM) of particle physics. The last particle of the SM is now finally discovered, the production rate as well as the decay pattern of the Higgs particle seem to follow the predictions of the theory[2]. While searches for Beyond Standard Model (BSM) physics are of course continued at the *high-energy frontier*[3] and stringent mass bounds up to the TeV scale are established, measurements at the *precision frontier*[1] provide compementary insights. By loop-induced processes, the experimental values of low-energy observables might indeed be affected by particles with very high masses. It was found that the mass scales of BSM particles, which are tested in low-energy experiments, do indeed exceed the mass scales tested at high energies by large factors in many cases.

In this paper we are going to discuss two topical subjects of the *precision frontier*, which have triggered an enormous amount of work both in experiment and theory in the past years. The **anomalous magnetic moment of the muon** $(\mathbf{g-2})_\mu$ is one of the few physics observables, in which for more than a decade a deviation between the SM theory and the direct experiment persists. New and improved measurements of $(g-2)_\mu$ at FNAL[4] and JPARC[5] are upcoming and it is hence a good moment to review the status of this precision quantity. Originally motivated by the dark sector and their relation to dark matter, it was realized that extra-*U(1)* gauge bosons beyond the ordinary photon - therefore often called **Dark Photons** - could indeed explain the deviation in the $(g-2)_\mu$ system mentioned above. Low-energy searches for the dark photon have been carried out as a consequence and will be presented in chapter 3.

There are of course many more low-energy tests of the SM ongoing beyond the ones covered in this paper. Flavour physics (see Ref.[6]) played for instance an important role in particle

[1] often also denoted as the intensity frontier

physics in the first decade of the 21^{st} century and is continuing to do so in the LHC era . Searches for lepton flavour violation (LFV) have been carried out at flavour factories and at dedicated muon beam lines [7]. New LFV experiments are upcoming with the potential to improve upon existing results by orders of magnitude. As a legacy of the LEP-SLC era, there remain precision measurements of the electroweak mixing angle, $\sin^2\Theta_W$, which plays a central role in the SM. Unfortunately, a discrepancy between LEP and SLC could never be clarified [8]. New low-energy experiments are currently being performed or are in the design stage with the goal to measure $\sin^2\Theta_W$ at very low momentum transfer. Measurements of that kind do not only have the potential to resolve the LEP-SLC discrepancy, but have also the resolving power for New Physics contributions up to the highest mass scales in the multiple TeV range. Different measurements of $\sin^2\Theta_W$, for instance in electron-electron scattering or electron-proton scattering, are also testing complementary BSM models.

2 The anomalous magnetic moment of the muon $(g-2)_\mu$

The gyromagnetic factors of the electron and muon (g_l, l=e,μ) belong to the best known quantities in physics, both experimentally and theoretically. [9] The high accuracy is indeed motivated by the fact, that calculations of g_l are very sensitive to loop corrections and hence allow for very accurate tests of the underlying theory.

The anomalous magnetic moment of the electron $a_\mu \equiv (g-2)_e/2$ – i.e. one half of the

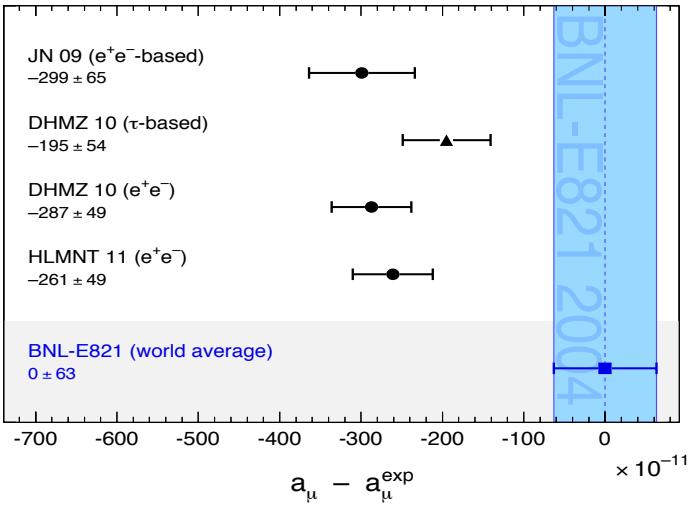

Figure 1: Comparison between the direct measurement of $(g-2)_\mu$ (BNL-E821, blue) and several theoretical evaluations within the Standard Model (black). A discrepancy larger than 3 standard deviations is found.

deviation of the g-factor from the Dirac value $g_e = 2$ – has been measured a few years ago by Gabrielse with an accuracy of 1 part in 10^{13} [10]. This accuracy is a test of the theory of quantum electrodynamics QED with unprecedented precision. The anomalous magnetic moment of the muon, $(g-2)_\mu$, is known with less accuracy. It allows, however, to resolve effects not only of QED but also of weak and strong interactions and eventually of BSM contributions.

Presently, the experimental and Standard Model values of $(g-2)_\mu$ differ by more than 3 standard deviations [11] [12], see Fig. 1, which triggered many speculations whether this might be an indication of a missing contribution due to New Physics. In the following two subchapters we will briefly review the status ot theory and experiment. We stress that the physics of $(g-2)_\mu$ is indeed testing an extremely wide class of New Physics models. Supersymmetric theories (SUSY), in which the masses of the SUSY particles are on the weak scale, could a priori explain the presently seen deviation in $(g-2)_\mu$ very nicely. There is however an increasing tension with SUSY mass limits from the LHC reaching now the TeV scale . Nevertheless, non-traditional SUSY models are still viable [13]. We will show later that light particles with very weak coupling to the SM, so-called Dark Photons, could explain the $(g-2)_\mu$ deviation very elegantly as well.

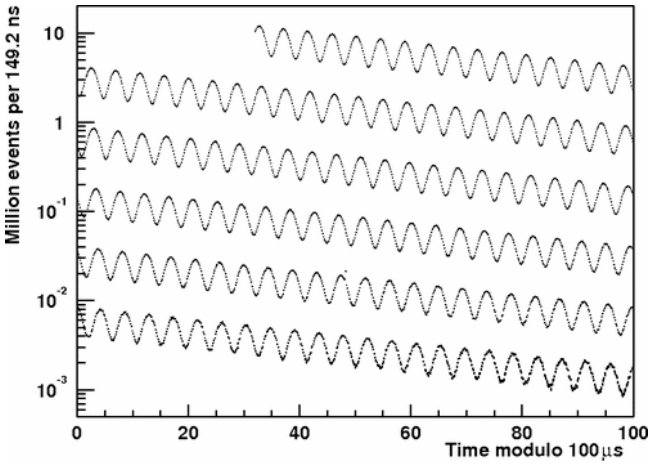

Figure 2: Measured event yield of positrons by the BNL-E821 experiment. From the modulation the value of $(g-2)_\mu$ can be extracted.

2.1 Experimental value

The most recent and most accurate experimental value of $(g-2)_\mu$ stems from a measurement at BNL. The E821 collaboration has improved the accuracy of the previous CERN measurement by a factor 14 and finds the following value:

$$a_\mu^{\text{exp}} = (11659208.9 \pm 5.4_{\text{stat}} \pm 3.3_{\text{syst}}) \cdot 10^{-10} \text{ [14]}. \quad (1)$$

To achieve such an accuracy a high-intensity polarized muon beam is injected into a storage ring with known magnetic field. The muon spin is rotating around the momentum vector due to the $\approx 0.1\%$ difference between the cyclotron and spin precession frequencies. After circling the ring many times, the muon decays into electrons plus neutrinos. Weak interaction guarantees a correlation between the electron flight direction and the original muon spin direction. As the decay electrons are detected in the experiment, the measured event yield shows a modulation proportional to the difference between the cyclotron and spin precession frequencies, i.e. proportional to $(g-2)_\mu$, see Fig. 2. Electric fields are required for a focussing of the muon beam, which complicates a precise extraction of $(g-2)_\mu$. As realized already in previous experiments

at CERN, these effects cancel if a so-called magic relativistic gamma value of the muon beam is used, which corresponds to a muon beam momentum of 3.09 GeV/c.
In 2013 the BNL $(g-2)_\mu$ ring was shipped to FNAL, where a new experiment is presently set up with the overall goal to improve the accuracy by a factor of 4 [4]. Apart from a higher muon flux compared to BNL, a series of additional improvements will lead to smaller systematic uncertainties. A second new experiment is in preparation at JPARC [5]. Differently from the BNL/FNAL approach, here the magic muon momentum will not be used, as no electric focussing fields are needed for the experiment. The solution of JPARC is the production of ultracold muons, which are then reaccelerated and injected into a 3 Tesla MRT magnet. The muon flux will be higher compared to the FNAL experiment and the overall goal is to achieve a similar accuracy as in the FNAL project.

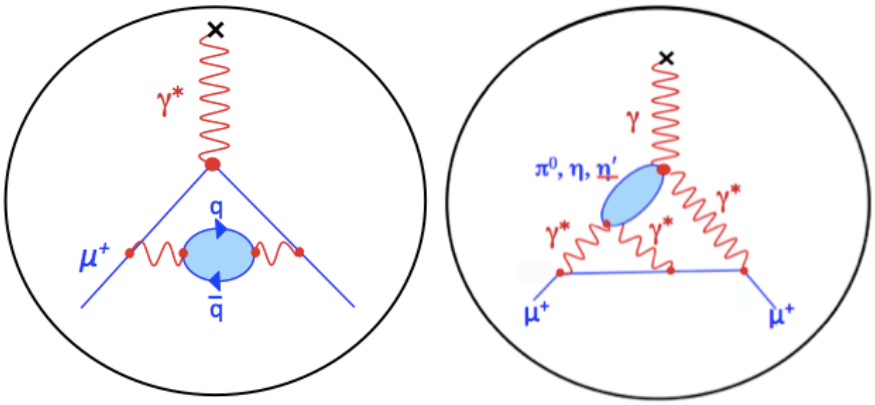

Figure 3: Hadronic contributions to $(g-2)_\mu$: the hadronic vacuum polarization (left) and the hadronic Light-by-Light contribution (right).

2.2 Standard Model prediction

Given the experimental accuracy reported above, there are measurable contributions to a_μ not only from QED, but also from weak and strong interactions. These individual contributions are listed below:

$$\begin{aligned} a_\mu^{\mathrm{SM}} &= a_\mu^{\mathrm{QED}} + a_\mu^{\mathrm{weak}} + a_\mu^{\mathrm{hadr}} \\ &= [11658471.808_{\pm 0.015} + 15.4_{\pm 0.2} + 693.0_{\pm 4.9}] \cdot 10^{-10} \\ &= [11659182.8_{\pm 4.9}] \cdot 10^{-10} \end{aligned} \tag{2}$$

The calculation of the by far dominating QED contribution was a heroic effort and has been pursued by Kinoshita and co-workers in the past decades [15]. An evaluation of up to 5 loops requires the calculation of more than 12,000 Feynman diagrams. The weak contribution has been computed up to NLO and is found to be many orders of magnitude smaller than the QED one [16]. Both the uncertainties of the QED and weak contributions are negligible in comparison to the experimental uncertainty. As can be seen from Equation 2, the bottleneck of the Standard Model prediction of $(g-2)_\mu$ is the hadronic contribution. It is split into two

parts, namely the Hadronic Vacuum Polarization HVP (see left Feynman diagram in Fig. 3) and the Hadronic Light-by-Light Scattering HLbL (Fig. 3, right) contributions. It should be noted that both contribute to only 60 ppm of the absolute contribution, they however dominate completely the uncertainty.

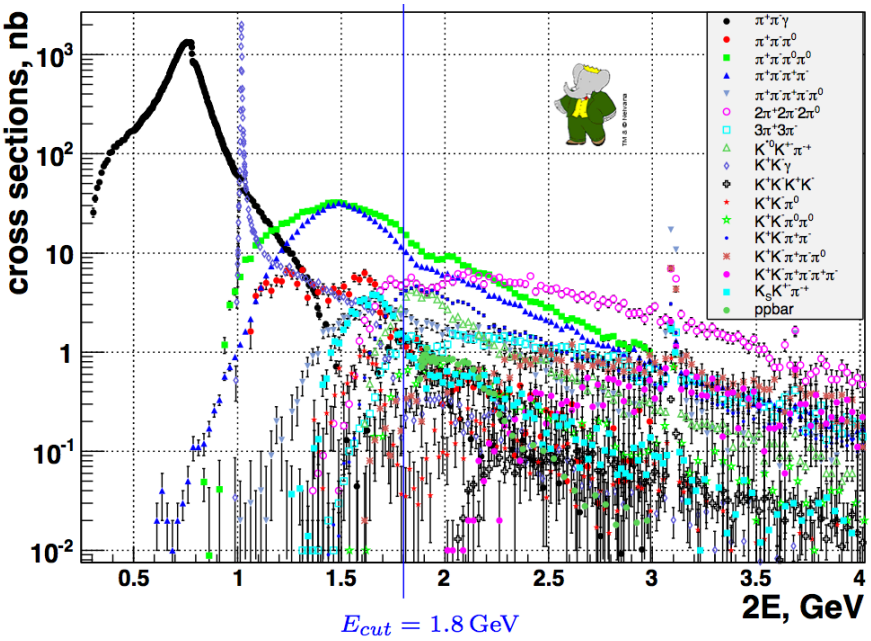

Figure 4: Exclusive hadronic final states measured by BaBar via Initial State Radiation (ISR).

The leading order HVP contribution is related via a dispersion integral to experimental data on the cross section $e^+e^- \to$ hadrons. Such a relation is based on unitarity and analyticity and is hence theoretically on safe grounds. Due to a kernel function in the dispersion integral, it comes out that low energy data of the hadronic cross section is particularily important. Indeed, the hadronic cross section below approximately 3 GeV is required with an accuracy on the level of 1%. This quest for accuracy triggered a series of cross section measurements at electron-positron facilities and led to the construction of the Novosibirsk colliders VEPP-2M and more recently of VEPP-2000 with the detectors CMD-2/CMD-3 and SND.
Major new results on hadronic cross section data were achieved at the particle factories DAΦNE (experiment KLOE) and PEP-II (experiment BaBar). As those particle factories were designed to operate at a fixed center-of-mass energy, a classical energy scan is therefore impossible. A new and very successful method has however been worked out, which allows for cross section measurements by using events, in which one of the beam electrons/positrons has emitted a high-energetic photon (intial state radiation, ISR) [17]. Depending on the energy of the ISR photon, the available hadronic mass is reduced and the hadronic cross section can be extracted for all masses below the center-of-mass energy of the collider. A good knowledge of the QED radiative corrections is required for this radiative approach. These are calculated up to next-to-leading order within the PHOKHARA [18] Monte-Carlo event generator. An overview of hadronic cross section measurements of various exclusive hadronic states via ISR by the BaBar

experiment is shown in Fig. 4. Essentially all channels up to 6 hadrons in the final state have been measured with systematic accuracies of few percent [17]. The two-pion final state $e^+e^- \to \pi^+\pi^-$ plays a special role for $(g-2)_\mu$. As can be seen in Fig. 4, the ρ resonance, which is almost entirely decaying into two pions, is dominating the cross section and hence is also playing a leading role in the dispersion integral for the HVP contribution to $(g-2)_\mu$ with approximately 75% of the total contribution steming from this channel. Unfortunately, the BaBar measurement of $\sigma(e^+e^- \to \pi^+\pi^-)$ [20], which has a claimed systematic accuracy of 0.5%, shows quite some deviation from ISR-measurements of KLOE kloe, which claims a 0.8% accuracy for the most precise of its data sets. The deviation is in the order of 3% on the ρ peak and increases towards higher masses. Precision data points from Novosibirsk [21] [22] have larger statistical and systematic uncertainties and hence can confirm neither the BaBar nor the KLOE results. As a matter of fact, this deviation is dramatically limiting our knowledge of the HVP contribution and hence a_μ^{SM}. Presently, an average of the world data set for hadronic cross section measurements yields the following value for the LO-HVP contribution to $(g-2)_\mu$: $a_\mu^{\mathrm{HVP}} = (692.3)_{\pm 4.2} \cdot 10^{-10}$.

The next important contribution beyond HVP is the HLbL contribution shown in Fig. 3, right. Here the leading subdiagram is shown, namely the coupling of photons to the pseudoscalar mesons π^0, η, or η'. So far hadronic models have been used for the calculation of the HLbL diagram. Although most groups report similar values for the absolute size of the HLbL contribution, the assumed uncertainties differ largely. The calculation with the lowest uncertainties stems from Prades, de Rafael, and Vainshtein [23]. They find the following value: $a_\mu^{\mathrm{HLbL}} = (10.5)_{\pm 2.6} \cdot 10^{-10}$. In most compilations of $(g-2)_\mu$ this result is used.
Very recently new theoretical approaches have been proposed by two groups from Bern and Mainz, namely the use of dispersion relations [24] [25]. Form factor measurements of the two-photon coupling $\gamma\gamma \to$ P, where P is a one hadron or two hadron system, are therefore of special interest for the dispersive approaches. The B-factory experiments BELLE [26] and BaBar [27] have recently measured so-called single-tag form factors for the lightest pseudoscalar mesons, however data has been reported only at very large momentum transfer above 4 GeV^2, while for the HLbL contribution measurements at low momentum transfer are required. In that kinematic range new spacelike measurements are expected from KLOE-II in Frascati and the BESIII experiment in Beijing. Important timelike measurements of the η form factor have recently been performed by the A2 collaboration in Mainz [28].

2.3 Conclusions $(\mathbf{g-2})_\mu$

With the persisting deviation between the SM prediction and the direct measurement of $(g-2)_\mu$, an interpretation in terms of BSM physics is very tempting. It is good to know that new direct measurements of $(g-2)_\mu$ with a factor 4 improved accuracy are underway at FNAL and JPARC and hopefully these projects will be able to report their results around the end of this decade. For the final interpretation of these experiments a reduction of the uncertainty of the SM prediction of $(g-2)_\mu$ is highly desirable. Fortunately, new cross section measurements via the ISR rechnique are ongoing at the BESIII facility in China and new energy scan campaigns are performed at Novosibirsk. This will eventually help to clarify the discrepancies seen between hadronic cross section measurements from BaBar and KLOE for the 2π cross section and will hence improve our knowledge of the HVP contribution. Moreover, measurements of transition form factors are ongoing at several hadron and electron facilities around the world and together

with the new developments in theory will lead to a significant progress in the HLbL contribution, which otherwise might be the leading uncertainty of the SM on the long run. As discussed in a recent whitepaper [29], there is very good hope that all these developments will lead to a further reduction of a factor 2 of the SM prediction of $(g-2)_\mu$. The combined effort in theory and experiment will therefore tell us in few years from now, whether the hint for BSM physics becomes evidence.

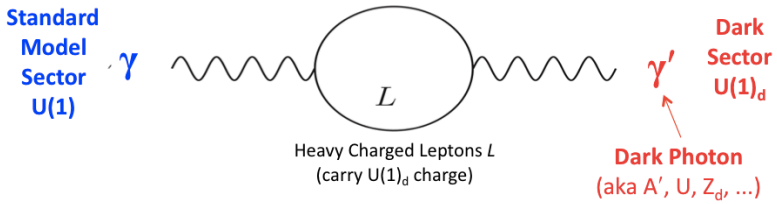

Figure 5: Dark Photon coupling to the ordinary photon in a kinetic mixing model.

3 Dark Photons

Extra U(1) gauge bosons beyond the Standard Model photon appear in essentially all string compactifications as they result naturally from symmetry breaking mechanisms towards lower gauge symmetries. A search for such kind of hypothetical particles is carried out from the lowest energies – e.g. the search for axion or axion-like particles – up to the highest energies at the LHC. More recently, particles at the GeV mass scale were proposed by several authors as they might be connected with the following puzzles in particle and astroparticle physics:

- It was shown by Arkani-Hamed and collaborators [30] that a GeV-scale particle – which was dubbed Dark Photon – could explain a surprisingly large number of astrophysical anomalies such as for instance the positron excess in the cosmic ray spectrum.
- A Dark Photon of a very similar mass scale [31] could also explain the discrepancy seen between the Standard Model predicition of $(g-2)_\mu$ and the direct measurement, see previous chapter.

The simplest mechanism with which a Dark Photon could couple to SM matter – the kinetic mixing model – was proposed by Holdom [32] already in the eighties. As depicted in Fig. 5 such a coupling can be realized by introducing a loop of charged leptons, which couple to the Standard Model U(1) photon as well to the Dark Photon. Hereby a portal between the hypothetical Dark Sector and the Standard Model is established. Of course the coupling α' must be extremely weak - much weaker than the coupling given by the electromagnetic fine structure constant $\alpha_{\rm em}$. There remain two unknown parameters of the model: the mass of the Dark Photon $m_{\gamma'}$ and the coupling constant α', which is also often expressed as $\epsilon' = \sqrt{\alpha'/\alpha_{\rm em}}$. In case dark matter particles couple to a Dark Photon, it would couple according to the kinetic mixing model to the Standard Model photon, which in turn decays into electron-positron pairs. Like this, a very elegant explanation for the positron excess is given. Regarding the $(g-2)_\mu$ puzzle, the Dark Photon would give rise to an additional exchange term, see Fig. 6, which is

missing in the SM calculation. The currently seen deviation in $(g-2)_\mu$ can be expressed as a well-constraint parameter range for $m_{\gamma'}$ and ϵ'. Taking into account constraints from various precision observables and from old beam dump experiments at FNAL and SLAC, the following parameter range would allow for a solution of the $(g-2)_\mu$ discrepancy: 20 MeV $< m_{\gamma'} <$ 200 MeV and $\epsilon' \approx 2-4 \cdot 10^{-3}$.

The possible existence of a GeV-scale Dark Photon triggered an enormous theoretical and experimental interest in the particle and nuclear physics community. In the following we will distinguish between electron scattering experiments and results from various hadron and e^+e^- accelerators. No significant signal of a Dark Photon has been found before and only 90% confidence limits have been published.

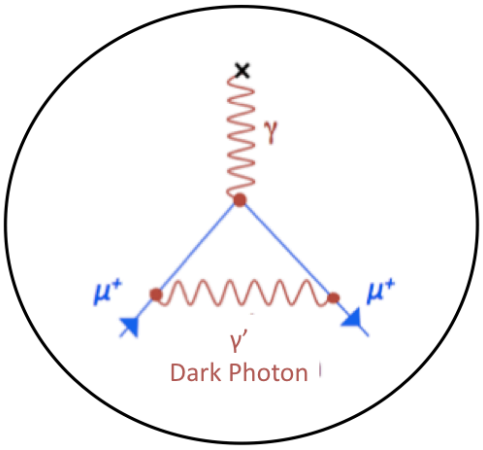

Figure 6: Hypothetical Dark Photon contribution to $(g-2)_\mu$.

3.1 Electron accelerator fixed target experiments

As Bjoerken and collaborators [33] have pointed out, low-energy electron accelerators in combination with high-resolution detectors are very well suited for Dark Photon searches. By scattering the electron beam on a nuclear target, the Dark Photon may be emitted in the initial or final state, see Fig. 7. Its coupling to an e^+e^- pair allows for an identification by looking for a bump in the e^+e^- invariant mass. The huge background is almost entirely given by QED processes, such as for instance Bethe-Heitler processes.

Successful pilot experiments have been carried out in 2011 at MAMI [34] (experiment A1) and JLAB [35] (APEX experiment) with electron beam energies of 0.9 GeV and 2.3 GeV, respectively. These runs could improve upon exisiting Dark Photon limits from BaBar (2009 results) in the mass range around 200 MeV. More recently, a very wide parameter range between approximately 40 MeV and 200 MeV was tested by MAMI with the high resolution spectrometer (HRS) setup A1 [36]. No significant signal was found and the ϵ' parameter range down to 10^{-3} was excluded, constraining a large part of the parameter range motivated by $(g-2)_\mu$, see Fig. 8.
For the near and mid-term future several dedicated experiments are in preparation at JLAB.

The APEX experiment [37], which is using an existing HRS setup at JLAB, will extend the mass range covered by A1/MAMI towards higher masses and lower ϵ' values. The HPS experiment [38] will exploit a displaced vertex technique, which allows to test even lower values of ϵ'. Finally, the Dark Light [39] experiment at the FEL accelerator at JLAB aims for testing the low mass region below the results already covered by A1. A new spectrometer setup at the MESA accelerator [40] in Mainz will also be able to cover this mass range.

3.2 Results from hadron and e^+e^- accelerators

A search for the Dark Photon is of course possible in physics environments beyond the ones tested in electron scattering. We list here the most recent results, which have been obtained in the past five years. All these results are displayed in Fig. 8 and have been obtained by looking for a bump in the e^+e^- or $\mu^+\mu^-$ invariant mass spectrum.

- The KLOE experiment at the ϕ factory DAΦNE in Frascati has searched for a bump in $\phi \to \eta e^+e^-$ events [41]. A constraint at higher masses existed already before from BaBar by similarily investigating Υ decays (BaBar 2009 [42]).

- The WASA@COSY collaboration has produced a huge statistics of π^0 events in proton proton scattering and has looked for the Dark Photon in $\pi^0 \to e^+e^-\gamma$ Dalitz events [43].

- A similar search strategy is possible in heavy ion collission and has been pursued by the HADES experiment at GSI. In addition to Dalitz decays of the π^0 also η Dalitz decays as well as decays of baryons are used [44].

- The most stringent Dark Photon limits have recently been published by the BaBar collaboration at SLAC [45]. Using ISR events and investigating the $e^+e^-\gamma$ and $\mu^+\mu^-\gamma$ final states, a very competitive search for the Dark Photon becomes available. BaBar has analyzed the full data set of approximately 500 fb^{-1} for this analysis and has obtained limits in the extremely wide mass range from 10 GeV down to threshold. Again no Dark Photon has been found and stringent constraints have been placed for the Dark Photon coupling to SM matter down to few 10^{-4}, see Fig. 8. A similar strategy had been followed already before by KLOE below 1 GeV.

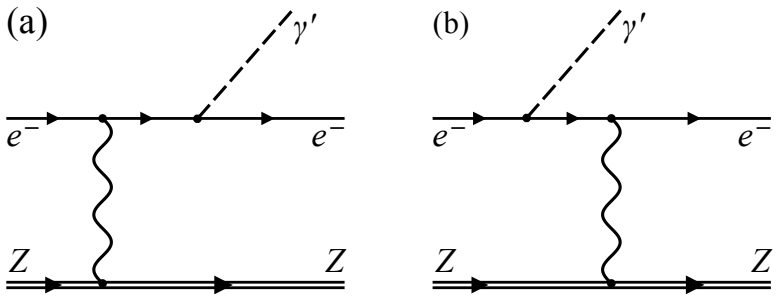

Figure 7: Feynman diagrams depicting the production of the Dark Photon in electron-nucleus scattering.

In the meantime also the Phenix experiment at RHIC has produced competitive exclusion limits by analyzing Dalitz decays of π^0 and η [46]. Those results are not yet displayed in Fig. 8 and are further constraining the favoured parameter range of $(g-2)_\mu$, such that after five years of active research the Dark Photon seems to be excluded as an explanation of the $(g-2)_\mu$ discrepancy. Of course, this range may change with new results for the direct measurement of $(g-2)_\mu$ and its SM prediction. It should be noted, that the relation of the Dark Photon to Dark Matter is still a very strong motivation. For this all the uncovered parameter space of Fig. 8 is of interest. In this context also more involved models are discussed in which either the Dark Photon is ligher than twice the electron mass or in which the Dark Photon coupling to SM matter is different from the one known from the ordinary photon. Also proposals have been brought forward to use electron accelerators as a source to produce a Dark Photon beam. This would be a unique way to search for light Dark Matter particles [47].

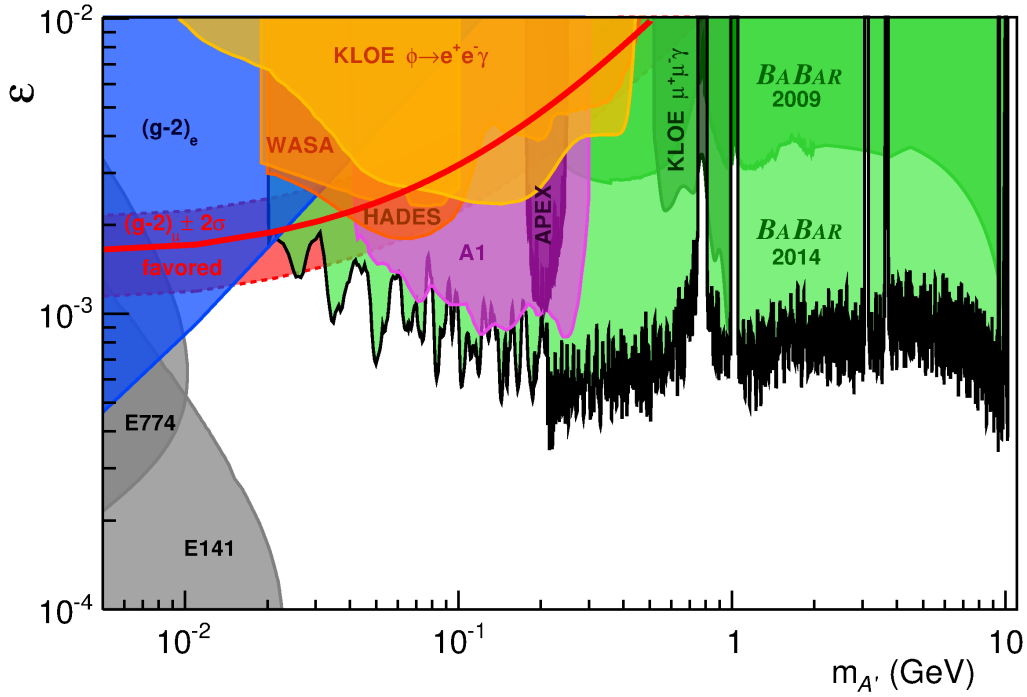

Figure 8: Dark Photon exclusion limits from various experiments.

Acknowledgments

We acknowledge support for this work from Deutsche Forschungsgemeinschaft DFG within the collaborative research center SFB-1044 and the PRISMA cluster of excellence. The author would like to thank the organizers of PANIC2014 for the invitation and for an exciting and successful conference.

References

[1] S. Chatrchyan *et al.* [CMS Collaboration], Phys. Lett. B **716** (2012) 30;
G. Aad *et al.* [ATLAS Collaboration], Phys. Lett. B **716** (2012) 1.

[2] see contribution of D. Rousseau, these proceedings.

[3] see contribution of K. Hatakeyama, these proceedings.

[4] see contribution of K. David, these proceedings.

[5] The J-PARC. 2009. g-2 collaboration, proposal submitted to J-PARC PAC (P34).

[6] see contribution of T. E. Latham, these proceedings.

[7] W. J. Marciano, T. Mori and J. M. Roney, Ann. Rev. Nucl. Part. Sci. **58** (2008) 315.

[8] The ALEPH, DELPHI, L3, OPAL, SLD Collaborations, the LEP Electroweak Working Group, the SLD Electroweak and Heavy Flavour Groups, Phys. Rept. 427 (2006) 257.

[9] F. Jegerlehner and A. Nyffeler, Phys. Rept. **477** (2009) 1.

[10] D. Hanneke, S. Fogwell and G. Gabrielse, Phys. Rev. Lett. **100** (2008) 120801.

[11] M. Davier, A. Hoecker, B. Malaescu and Z. Zhang, Eur. Phys. J. C **71** (2011) 1515 [Erratum-ibid. C **72** (2012) 1874].

[12] K. Hagiwara, R. Liao, A. D. Martin, D. Nomura and T. Teubner, J. Phys. G **38** (2011) 085003.

[13] H. Fargnoli, C. Gnendiger, S. Paehr, D. Stckinger and H. Stckinger-Kim, JHEP **1402** (2014) 070.

[14] G. W. Bennett *et al.* [Muon G-2 Collaboration], Phys. Rev. D **73** (2006) 072003.

[15] T. Aoyama, M. Hayakawa, T. Kinoshita and M. Nio, Phys. Rev. Lett. **109** (2012) 111808.

[16] M. Knecht, S. Peris, M. Perrottet and E. De Rafael, JHEP **0211** (2002) 003.

[17] V. P. Druzhinin, S. I. Eidelman, S. I. Serednyakov and E. P. Solodov, Rev. Mod. Phys. **83** (2011) 1545.

[18] S. Binner, J. H. Kühn and K. Melnikov, Phys. Lett. B **459** (1999) 279;
http://ific.uv.es/ rodrigo/phokhara/.

[19] D. Babusci *et al.* [KLOE Collaboration], Phys. Lett. B **720** (2013) 336;
F. Ambrosino *et al.* [KLOE Collaboration], Phys. Lett. B **700** (2011) 102
F. Ambrosino *et al.* [KLOE Collaboration], Phys. Lett. B **670** (2009) 285;
A. Aloisio *et al.* [KLOE Collaboration], Phys. Lett. B **606** (2005) 12.

[20] J. P. Lees *et al.* [BaBar Collaboration], Phys. Rev. D **86** (2012) 032013;
B. Aubert *et al.* [BaBar Collaboration], Phys. Rev. Lett. **103** (2009) 231801.

[21] R. R. Akhmetshin *et al.* [CMD-2 Collaboration], Phys. Lett. B **648** (2007) 28; R. R. Akhmetshin, V. M. Aulchenko, V. S. Banzarov, L. M. Barkov, N. S. Bashtovoy, A. E. Bondar, D. V. Bondarev and A. V. Bragin *et al.*, JETP Lett. **84** (2006) 413; R. R. Akhmetshin *et al.* [CMD-2 Collaboration], Phys. Lett. B **578** (2004) 285.

[22] M. N. Achasov, K. I. Beloborodov, A. V. Berdyugin, A. G. Bogdanchikov, A. V. Bozhenok, A. D. Bukin, D. A. Bukin and T. V. Dimova *et al.*, J. Exp. Theor. Phys. **103** (2006) 380.

[23] J. Prades, E. de Rafael and A. Vainshtein, (Advanced series on directions in high energy physics. 20) [arXiv:0901.0306 [hep-ph]].

[24] G. Colangelo, M. Hoferichter, B. Kubis, M. Procura and P. Stoffer, Phys. Lett. B **738** (2014) 6;
G. Colangelo, M. Hoferichter, M. Procura and P. Stoffer, JHEP **1409** (2014) 091.

[25] V. Pauk and M. Vanderhaeghen, arXiv:1409.0819 [hep-ph].

[26] S. Uehara *et al.* [Belle Collaboration], Phys. Rev. D **86** (2012) 092007.

[27] B. Aubert *et al.* [BaBar Collaboration], Phys. Rev. D **80** (2009) 052002.

[28] P. Aguar-Bartolome *et al.* [A2 Collaboration], Phys. Rev. C **89** (2014) 044608.

[29] T. Blum, A. Denig, I. Logashenko, E. de Rafael, B. Lee Roberts, T. Teubner and G. Venanzoni, arXiv:1311.2198 [hep-ph].

[30] N. Arkani-Hamed, D. P. Finkbeiner, T. R. Slatyer and N. Weiner, Phys. Rev. D **79** (2009) 015014.

[31] M. Pospelov, Phys. Rev. D **80** (2009) 095002.

[32] B. Holdom, Phys. Lett. B **166** (1986) 196.

[33] J. D. Bjorken, R. Essig, P. Schuster and N. Toro, Phys. Rev. D **80** (2009) 075018.

[34] H. Merkel *et al.* [A1 Collaboration], Phys. Rev. Lett. **106** (2011) 251802.

[35] S. Abrahamyan *et al.* [APEX Collaboration], Phys. Rev. Lett. **107** (2011) 191804.

[36] H. Merkel *et al.* [A1 Collaboration], Phys. Rev. Lett. **106** (2011) 251802.

[37] R. Essig, P. Schuster, N. Toro and B. Wojtsekhowski, JHEP **1102** (2011) 009.

[38] http://nuclear.unh.edu/HPS/HPS_proposal.pdf.

[39] http://dmtpc.mit.edu/DarkLight/DarkLightProposal_PAC39.pdf.

[40] K. Aulenbacher, M. Dehn, H. J. Kreidel, R. Heine and R. Eichhorn, ICFA Beam Dyn. Newslett. **58** (2012) 145.

[41] D. Babusci *et al.* [KLOE-2 Collaboration], Phys. Lett. B **720** (2013) 111.

[42] B. Aubert *et al.* [BaBar Collaboration], Phys. Rev. Lett. **103** (2009) 081803.

[43] P. Adlarson *et al.* [WASA-at-COSY Collaboration], Phys. Lett. B **726** (2013) 187.

[44] G. Agakishiev *et al.* [HADES Collaboration], Phys. Lett. B **731** (2014) 265.

[45] J. P. Lees *et al.* [BaBar Collaboration], arXiv:1406.2980 [hep-ex].

[46] A. Adare *et al.* [PHENIX Collaboration], arXiv:1409.0851 [nucl-ex].

[47] E. Izaguirre, G. Krnjaic, P. Schuster and N. Toro, Phys. Rev. D **90** (2014) 014052.

Dark Matter: experimental results and theory

Marco Cirelli[1]

[1]Institut de Physique Théorique, CNRS, URA 2306 & CEA/Saclay,
F-91191 Gif-sur-Yvette, France

DOI: http://dx.doi.org/10.3204/DESY-PROC-2014-04/295

I discuss four recent anomalies in Dark Matter Indirect Detection (the positron excess, the 130 GeV line, the GeV GC excess and the 3.5 KeV line) and some relevant constraints.

1 Introduction

Indirect searches for Dark Matter (DM) aim at detecting the signatures of the annihilations or decays of DM particles in the fluxes of Cosmic Rays (CRs), intended in a broad sense: charged particles (electrons and positrons, protons and antiprotons, deuterium and antideuterium), photons (gamma rays, X-rays, synchrotron radiation), neutrinos. In general, a key point of all these searches is to look for channels and ranges of energy where it is possible to beat the background from ordinary astrophysical processes. This is for instance the basic reason why searches for charged particles focus on fluxes of antiparticles (positrons, antiprotons, antideuterons), much less abundant in the Universe than the corresponding particles, and searches for photons or neutrinos have to look at areas where the DM-signal to astro-noise ratio can be maximized (typically the Galactic Center and DM-dominated structures such as dwarf satellite galaxies).

Pioneering works have explored indirect detection (ID) as a promising avenue of discovery since the late-70's. Since then, innumerable papers have explored the predicted signatures of countless particle physics DM models. In the past 6 years or so, however, the field has experienced a significant burst of activity, mainly due to the results presented by a few very well performing experiments, above all the Pamela satellite, the Fermi satellite and the Hess telescope. It is fair to say that the field has passed, for better or for worse, from a theory-driven state to a data-driven phase.

In this presentation I intend to briefly review the current status of the field, using the pretext of discussing four recent experimental 'anomalies' and the ensuing phenomenological activity. The four anomalies are: 1) the positron and electron excesses, first soundly detected by Pamela in 2008 in the positron fraction and then corroborated by many results from Fermi, Hess and recently Ams-02; 2) the '130 GeV line' from the Galactic Center (GC), first identified in 2012 by Christoph Weniger and collaborators in Fermi data; 3) the 'GeV Galactic Center γ-ray excess', promoted since 2010 most notably by Dan Hooper; 4) the 3.5 KeV X-ray line, supposedly detected in march 2014 in data from the Xmm-Newton satellite from several galaxy clusters and the Andromeda galaxy (M31).

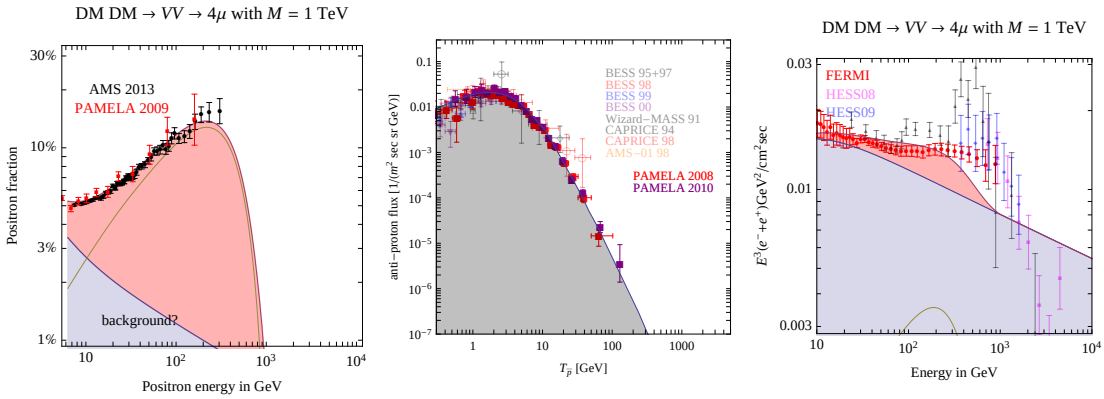

Figure 1: A compilation of recent and less recent data in charged cosmic rays, superimposed on plausible but uncertain astrophysical backgrounds from secondary production and on the flux produced by Dark Matter annihilations for a specific model. Left: positron fraction. Center: antiproton flux. Right: sum of electrons and positrons. Figures from ref. [9].

2 The positron and electron excesses

There has been a flurry of positive results from a few indirect detection experiments looking at the fluxes of charged cosmic rays. In particular, the signals pointed to an excess of electrons and positrons at the TeV and sub-TeV scale:

- Notorius data from the PAMELA satellite [1] showed, back in 2008, a steep increase in the energy spectrum of the positron fraction $e^+/(e^+ + e^-)$ above 10 GeV up to 100 GeV, compatibly with previous hints from HEAT [2] and AMS-01 [3]. These findings have later been confirmed with independent measurements by the FERMI satellite [4] and, recently, by the AMS-02 experiment [5] and extended to about 430 GeV.

- Data from PAMELA [6] also showed no excess in the $\bar{p}$ energy spectrum compared with the predicted background.

- In the $e^+ + e^-$ energy spectrum, the results of the FERMI satellite [7], combined with the results from the HESS telescope [8], hint to an excess (with respect to the expected background) reproduced by a simple power law up to about 1 TeV and eventually a steepening at energies of a few TeVs.

The data are displayed in fig. 1, together with the expected astrophysical 'backgrounds' and with the contribution from an annihilating DM particle which fits them reasonably well (see below). The properties of such a particle are pin-pointed quit precisely by the data. The DM has to be:

- With a mass of *1 to few TeV*, in order to reproduce the feature in the $e^+ + e^-$ spectrum. Actually, the hint of a flattening in the positron fraction suggested by AMS-02 favours a DM mass below about 1 TeV with about 3σ statistical significance, depending on the DM annihilation channel, so that a little bit of a tension is present with the $e^+ + e^-$ spectrum, which requires a slightly larger value.

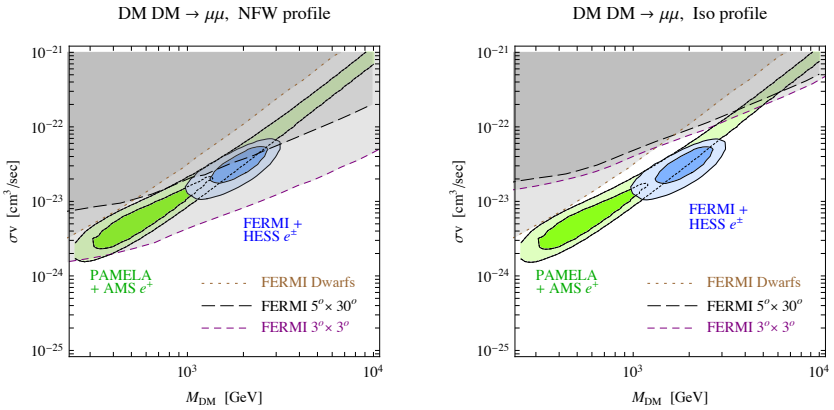

Figure 2: Best fit regions for the positron and electron excesses, together with some representative γ-ray constraints. Figure from ref. [9].

- ▷ *Leptophilic*, i.e. annihilating almost exclusively into leptonic channels, otherwise the antiproton measurements would be exceeded.
- ▷ With a *very large annihilation cross section*, of the order of $10^{-23}\,\mathrm{cm}^3/\mathrm{sec}$ or more (for the masses under consideration), much larger than the thermal one, in order to produce a large enough flux that can fit the positron rise and the $e^+ + e^-$ bump.

As tantalizing as these hints of DM can be, they have to be confronted with associated constraints. Many possible constraints can be considered, but here I will focus on two classes only. The first one is observations of γ-rays. In fig. 2 we show representative γ-ray bounds (the constraints are taken from [10, 11], more recent analyses find similar or slightly more stringent bounds). We see that the fit region shows some tension with γ-ray data (or it is rather clearly excluded) if (left) we have chosen a benchmark NFW galactic Dark Matter profile. Choosing the shallower isothermal profile (right), however, makes the constraints looser. It is therefore difficult to get a final answer from γ-rays. The second class of constraints comes from observations of the cosmic microwave background (CMB), which imposes bounds on DM annihilations (based on the fact that they would have re-ionized the primordial universe) that disfavor at various degrees and for most channels the DM interpretation of the positron excess [12].

3 The 130 GeV line

The '130 GeV line' claim has gathered a lot of attention in the past two years (for a more thorough review see [13]). Originally spotted by [14] and, above all, by [15] in the publicly available FERMI data from an extended region including the GC (fig. 3 left reports the most evocative of the original analysis' figures), it has later found support in other analyses [16, 17, 18, 19], with varying degrees of accuracy and claimed significance. [16, 19] have seen it in what could possibly be DM subhaloes of the MW, and there might be two lines, at 111 GeV and 129 GeV [20, 17]. [18] has seen it in galaxy clusters too. For a response, [21, 22, 23] challenged the analyses in a number of ways, suggesting that the line(s) could be due to unidentified

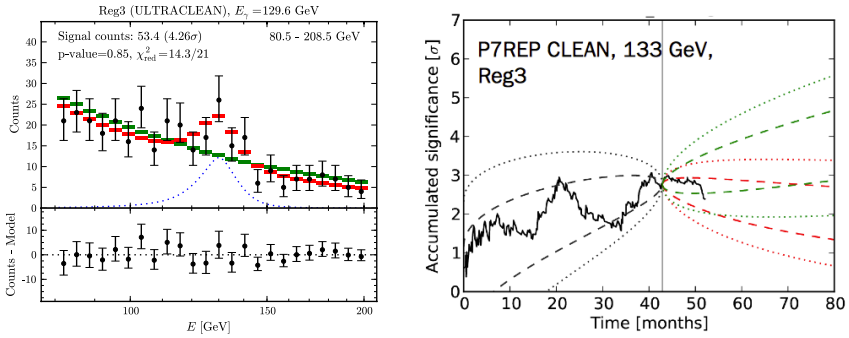

Figure 3: Left: FERMI γ-ray data and fits pointing to a line at about 130 GeV. Right: behavior with time of the accumulated significance for this signal. Figures from ref. [15] and ref. [24].

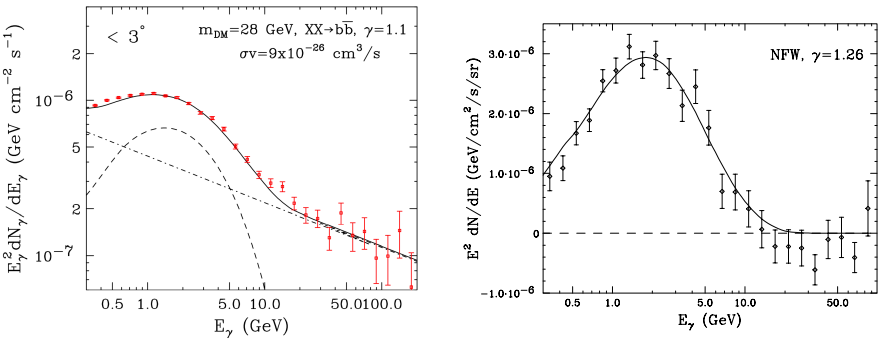

Figure 4: Earliest and latest fits to the GeV excess at the GC. From ref. [25] and ref. [27].

instrumental, statistical or astrophysical origin. Although it is probably too early for a final conclusion on this claim, it is fair to say that the current consensus seems to be that the line has been a rather unfortunate combination of an instrumental effect and a statistical fluctuation. The right panel of fig. 3 illustrates that, as more data are accumulated, the significance of the signal lowers, hence pointing at something which is probably not an actual signal.

4 The GeV Galactic Center excess

Several authors have reported since 2009 the detection of a gamma-ray signal from the inner few degrees around the GC [25, 26], with the most notable early claims by Dan Hooper. Its spectrum and morphology are found to be compatible with those expected from annihilating DM particles: to fix the ideas, the results of one of the most recent analysis [27] confirm the presence of this excess at an incredibly high level of significance (if taken at face value) and find this signal to be best fit by 31-40 GeV DM particles distributed according to a (contracted) NFW profile and annihilating into $b\bar{b}$ with $\langle\sigma v\rangle = 1.4 \div 2 \times 10^{-26}$ cm^3/s. Fig. 4 displays the earliest fit to the data (from [25]) and one of the most recent ones (from [27]).

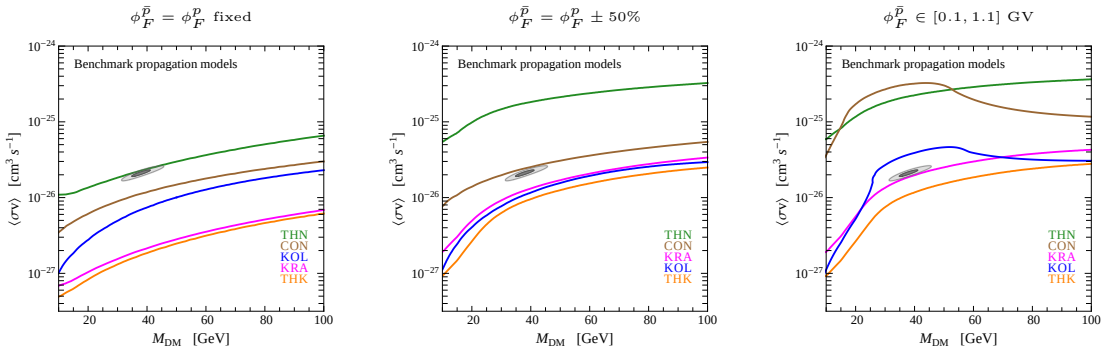

Figure 5: 3-σ exclusion contours on $\langle \sigma v \rangle$ for 100% DM annihilation into $b\bar{b}$, for the three approaches to solar modulation briefly discussed in the text. The grey area is the best-fit region. Fig. from ref. [32].

Of course, one should not forget that, in very general terms, the identification of an 'excess' strongly relies on the capability of carefully assessing the background over which the excess is supposed to emerge. The claim under scrutiny constitutes no exception, quite the contrary. The extraction of the residuals strongly relies on the modeling of the diffuse gamma-ray background (in particular the one publicly made available by the FERMI collaboration) as well as on additional modeling of astrophysical emissions, e.g. from FERMI bubbles, isotropic component, unresolved point sources, molecular gas... While this is probably the best that can be done, it is not guaranteed to be (and in general is not expected to be) the optimal strategy. Also, one should not forget that there might be alternative astrophysical explanations for the excess. A population of milli-second pulsars has been extensively discussed since the beginning [28], as well as the possibility of a spectral break in the emission of the central Black Hole [29]. More recently, the possibility has been suggested that isolated injections of charged particles (electrons [30] or protons [31]) sometime in the past, possibly connected with the activity of the central Black Hole, can produce secondary radiation able to account for the anomalous signal. While reproducing with these models all the details of the observed emission might be not easy, they represent plausible and useful counterexamples to the DM interpretation.

Still, it is interesting to insist on the tantalizing DM hypothesis and to explore ways to confirm or disprove the result within the DM framework. In particular, given the alleged hadronic origin of the signal, it is very useful to analyze the antiproton channel to put constraints on the DM interpretation of such excess. Ref. [32] delved precisely into this issue, and the condensed results are displayed in fig. 5. It considered several galactic propagation models for antiprotons (THN, CON, KOL, KRA, THK, roughly distinguished by the thickness of the diffusive halo, the diffusion properties and the presence of side effects such as convection) and several assumptions for the so-called solar modulation, i.e. the complicated effect of the magnetic field and solar cosmic ray wind of the heliosphere on the last segment of the antiproton journey. More precisely, it considered a solar force field for $\bar{p}$ fixed and equal to p one (left panel of fig. 5), variable within 50% (central panel) or free within a wide range (right panel). The overall conclusions are the following: adopting the most realistic propagation models and well motivated choices for the solar modulation potential, the hadronic ($b\bar{b}$) DM interpretation for the GeV excess is definitely in strong tension with the antiproton data. Nevertheless, given

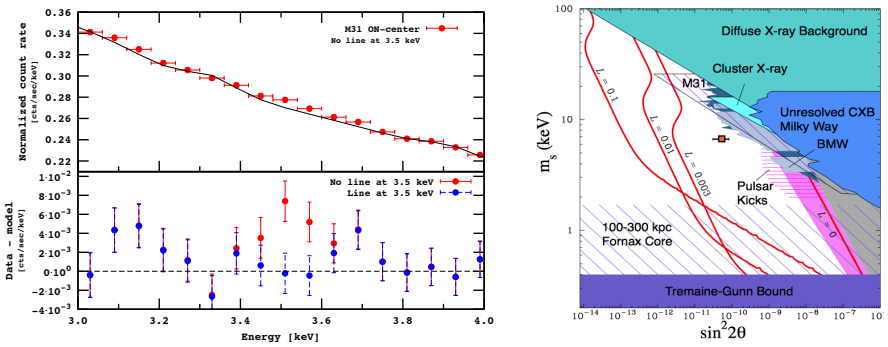

Figure 6: Identification of the 3.5 KeV line in XMM-NEWTON data (left) and the parameter space of its interpretation in terms of a decaying sterile neutrino. From ref. [35] and ref. [34].

that our knowledge of CR diffusion both in the Galaxy and in the heliosphere is far from being accurate and complete, there are still conservative choices of the parameters involved that do not result in ruling it out, namely thin halo models and large solar modulation potentials. The authors of ref. [33] have also discussed the antiproton bounds, reaching somewhat different conclusions.

5 The 3.5 KeV X-ray line

One of the latest claims in the field of indirect detection comes from a different range of energies: X-rays. In datasets from the XMM-NEWTON satellite, two independent groups [34, 35] have found evidence for an unexplained line at 3.5 KeV. The former group found it in observations of a set of 73 galaxy clusters with redshift between 0.01 and 0.35. The latter one in observations both of the Perseus cluster and of Andromeda, with no detection in "blank sky" measurements. Fig. 6, left, displays an extraction of the spectrum showing the line, from [35].

The complication is that the X-ray spectrum in this range of energies is crowded with atomic de-excitation lines from elements such as Cr, Mn, K, Fe, Ni, Ca, Cu... Ref. [36] has indeed very recently argued that previously-unaccounted-for potassium lines can well explain the signal. Ref. [37] reiterates, however, that data from Andromeda are instead solid and make the potassium interpretation problematic. On another side, ref. [38] has argued that no line is seen in Chandra data from the GC, although this conclusion depends on how one models the local background. The discussion is currently unfolding and probably more data from independent instruments will be needed.

If confirmed, however, the most straightforward explanation of the line in terms of new physics is of great interest for the field of DM indirect detection as it consists of a sterile neutrino of mass 7 KeV decaying into an ordinary ν and a photon (the detected X-ray). The decay rate turns out to be $\mathcal{O}(10^{-29})$ sec^{-1}. This, translated in terms of particle physics parameters by the effective mixing angle, lies in a region of parameter space still allowed by other constraints, as illustrated by the right panel of fig. 6. The production mechanism of a population of sterile neutrinos in the early universe would involve active-sterile oscillations helped by the presence of a sizable leptonic asymmetry, quite uncompelling, but possible.

6 Conclusions

There are arguably no firm conclusions in this field at this moment in time. There are tantalizing hints (the positron and electron excess, the gamma-ray line, the GeV GC excess and the X-ray line) and there are stringent constraints. Such constraints, however, are often relaxed by appropriate assumptions, which can be extreme or not (the illustration with the antiproton constraints on the GeV excess in section 4 is exemplar). The only firm albeit generic conclusions seem to be that:

- ◇ current experiments are clearly reaching (and in some cases have already reached) the sensitivities for which they were designed, and hence they probe very promising regions of the parameter space;
- ◇ astrophysics, in different manifestations, is the main killjoy, introducing alternative compelling explanation, irreducible uncertainties, unbeatable background noise...;
- ◇ hence, it is important to pursue a multi-messenger approach in all instances, investigating associated signals in other channels, cross-checking constraints and confirmations from independent targets etc;
- ◇ in any case, the profusion of data from the recent experiments have spurred a remarkable proliferation of DM models, so that 'traditional' DM models (such as SuSy DM) have, for better or for worse, been joined by many other possibilities.

Acknowledgments

I thank my collaborators on the papers which led to the results presented here and who helped me with many useful discussions. I acknowledge the hospitality of the Institut d'Astrophysique de Paris, where part of this work was done. Funding and research infrastructure acknowledgements: European Research Council (ERC) under the EU Seventh Framework Programme (FP7/2007-2013)/ERC Starting Grant (agreement n. 278234 — 'NEWDARK' project); French national research agency ANR under contract ANR 2010 BLANC 041301.

References

[1] O. Adriani *et al.* [PAMELA Collaboration], Nature 458, 607-609, 2009, arXiv:0810.4995.

[2] S. W. Barwick *et al.* [HEAT Coll.], Astrophys. J. **482** (1997) L191 [astro-ph/9703192].

[3] M. Aguilar *et al.* [AMS-01 Coll.], Phys. Lett. B **646** (2007) 145 [astro-ph/0703154].

[4] M. Ackermann *et al.* [The Fermi LAT Collaboration], arXiv:1109.0521 [astro-ph.HE].

[5] M. Aguilar *et al.* [AMS Collaboration], Phys. Rev. Lett. **110** (2013) 141102.
(An updated measurement has only been presented in a talk by S. Ting (and subsequent talks elsewhere).)

[6] O. Adriani *et al.* [PAMELA Coll.], Phys. Rev. Lett. **105** (2010) 121101 [arXiv:1007.0821].

[7] A. Abdo *et al.* [Fermi-LAT Coll.], Phys. Rev. Lett. **102** (2009) 181101, arXiv:0905.0025.
M. Ackermann *et al.* [Fermi LAT Coll.], Phys. Rev. D **82** (2010) 092004, arXiv:1008.3999.

[8] F. Aharonian *et al.* [H.E.S.S. Coll.], Phys. Rev. Lett. **101** (2008) 261104 [arXiv:0811.3894].
F. Aharonian *et al.* [H.E.S.S. Coll.], Astron. Astrophys. **508** (2009) 561 [arXiv:0905.0105].

[9] M. Cirelli, M. Kadastik, M. Raidal and A. Strumia, Nucl. Phys. B **813** (2009) 1 [Addendum-ibid. B **873** (2013) 530] [arXiv:0809.2409 [hep-ph]].

[10] M. Cirelli, P. Panci and P. D. Serpico, Nucl. Phys. B 840 (2010) 284 [arXiv:0912.0663]. M. Papucci and A. Strumia, JCAP 1003 (2010) 014 [arXiv:0912.0742].

[11] Fermi-LAT collaboration, Phys. Rev. Lett. 107 (2011) 241302 [arXiv:1108.3546]. Fermi-LAT collaboration, Astrophys. J. 761 (2012) 91 [arXiv:1205.6474]. For this figure we used the dwarfs data presented by A. Drlica-Wagner at the 2012 Fermi symposium.

[12] S. Galli, F. Iocco, G. Bertone and A. Melchiorri, Phys. Rev. D 80 (2009) 023505 [arXiv:0905.0003]. T.R. Slatyer, N. Padmanabhan, D.P. Finkbeiner, Phys. Rev. D 80 (2009) 043526, 0906.1197. G. Huetsi, A. Hektor, M. Raidal, Astron. Astrophys. 505 (2009) 999, arXiv:0906.4550. M. Cirelli, F. Iocco and P. Panci, JCAP 0910 (2009) 009, arXiv:0907.0719. See also: T. Kanzaki, M. Kawasaki and K. Nakayama, Prog. Theor. Phys. 123 (2010) 853, arXiv:0907.3985. Q.Yuan, B.Yue, X.-J.Bi, X.Chen, X.Zhang, JCAP 1010 (2010) 023, arXiv:0912.2504. G. Hutsi, J. Chluba, A. Hektor and M. Raidal, arXiv:1103.2766. S.Galli, F.Iocco, G.Bertone, A.Melchiorri, Phys. Rev. D 84 (2011) 027302, arXiv:1106.1528. A. Natarajan, arXiv:1201.3939. G. Giesen, J. Lesgourgues, B. Audren and Y. Ali-Haimoud, JCAP 1212 (2012) 008 [arXiv:1209.0247]. J. M. Cline and P. Scott, JCAP 1303 (2013) 044 [arXiv:1301.5908].

[13] T. Bringmann and C. Weniger, arXiv:1208.5481 [hep-ph].

[14] T. Bringmann, X. Huang, A. Ibarra, S. Vogl and C. Weniger, arXiv:1203.1312 [hep-ph].

[15] C. Weniger, JCAP **1208** (2012) 007 [arXiv:1204.2797 [hep-ph]].

[16] E. Tempel, A. Hektor and M. Raidal, arXiv:1205.1045 [hep-ph].

[17] M. Su and D. P. Finkbeiner, arXiv:1206.1616 [astro-ph.HE].

[18] A. Hektor, M. Raidal and E. Tempel, arXiv:1207.4466 [astro-ph.HE].

[19] M. Su and D. P. Finkbeiner, arXiv:1207.7060 [astro-ph.HE].

[20] A. Rajaraman, T. M. P. Tait and D. Whiteson, arXiv:1205.4723 [hep-ph].

[21] A. Boyarsky, D. Malyshev and O. Ruchayskiy, arXiv:1205.4700 [astro-ph.HE].

[22] N. Mirabal, arXiv:1208.1693 [astro-ph.HE].

[23] A. Hektor, M. Raidal and E. Tempel, arXiv:1208.1996 [astro-ph.HE].

[24] C. Weniger, presentation at the FERMI meeting for alternative observations, 25 Jul 2013.

[25] L. Goodenough and D. Hooper, arXiv:0910.2998 [hep-ph].

[26] V. Vitale *et al.* [Fermi-LAT Collaboration], arXiv:0912.3828 [astro-ph.HE]. D. Hooper and L. Goodenough, Phys. Lett. B **697** (2011) 412 [arXiv:1010.2752 [hep-ph]]. D. Hooper and T. Linden, Phys. Rev. D **84** (2011) 123005 [arXiv:1110.0006 [astro-ph.HE]]. D. Hooper, Phys. Dark Univ. **1** (2012) 1 [arXiv:1201.1303 [astro-ph.CO]]. K. Abazajian, M. Kaplinghat, Phys. Rev. D **86** (2012) 083511 [arXiv:1207.6047. D. Hooper, T. Slatyer, Phys. Dark Univ. **2** (2013) 118 [arXiv:1302.6589 [astro-ph.HE]]. C. Gordon and O. Macias, Phys. Rev. D **88** (2013) 083521 [arXiv:1306.5725 [astro-ph.HE]]. W.-C. Huang, A. Urbano and W. Xue, arXiv:1307.6862 [hep-ph]. K. N. Abazajian, N. Canac, S. Horiuchi and M. Kaplinghat, arXiv:1402.4090 [astro-ph.HE].

[27] T. Daylan, D. P. Finkbeiner, D. Hooper, T. Linden, S. K. N. Portillo, N. L. Rodd and T. R. Slatyer, arXiv:1402.6703 [astro-ph.HE].

[28] K. N. Abazajian, JCAP **1103** (2011) 010 [arXiv:1011.4275 [astro-ph.HE]]. D. Hooper, I. Cholis, T. Linden, J. Siegal-Gaskins and T. Slatyer, Phys. Rev. D **88** (2013) 083009 [arXiv:1305.0830 [astro-ph.HE]]. Q. Yuan and B. Zhang, arXiv:1404.2318 [astro-ph.HE].

[29] A. Boyarsky, D. Malyshev and O. Ruchayskiy, Phys. Lett. B **705** (2011) 165 [arXiv:1012.5839 [hep-ph]].

[30] J. Petrovic, P. D. Serpico and G. Zaharijas, arXiv:1405.7928 [astro-ph.HE].

[31] E. Carlson and S. Profumo, arXiv:1405.7685 [astro-ph.HE].

[32] M. Cirelli, D. Gaggero, G. Giesen, M. Taoso and A. Urbano, arXiv:1407.2173 [hep-ph].

[33] T. Bringmann, M. Vollmann and C. Weniger, arXiv:1406.6027 [astro-ph.HE].

[34] E. Bulbul, M. Markevitch, A. Foster, R. K. Smith, M. Loewenstein and S. W. Randall, Astrophys. J. **789** (2014) 13 [arXiv:1402.2301 [astro-ph.CO]].

[35] A. Boyarsky, O. Ruchayskiy, D. Iakubovskyi and J. Franse, arXiv:1402.4119 [astro-ph.CO].

[36] T. E. Jeltema and S. Profumo, arXiv:1408.1699 [astro-ph.HE].

[37] A. Boyarsky, J. Franse, D. Iakubovskyi and O. Ruchayskiy, arXiv:1408.4388 [astro-ph.CO].

[38] S. Riemer-Sorensen, arXiv:1405.7943 [astro-ph.CO].

Searching for New Physics in b-hadron decays

Thomas Latham on behalf of the LHCb collaboration

Department of Physics, University of Warwick, Coventry, CV4 7AL, United Kingdom

DOI: http://dx.doi.org/10.3204/DESY-PROC-2014-04/297

Recent results from the realm of b-hadron physics are presented, with a focus on anomalous results and *CP* violation studies. Results are shown from the B-factories: *BABAR* and Belle; the Tevatron experiments: CDF and D0; and the LHC experiments: ATLAS, CMS and LHCb. Together these give some tantalising hints of cracks in the Standard Model.

1 Introduction

One of the primary goals of the field of flavour physics is to uncover evidence of physics beyond the Standard Model (SM) of particle physics — so called "New Physics". This is achieved by looking for discrepancies between the SM predictions and experimental results in observables such as decay rates and *CP*-violating asymmetries. It is therefore essential to have good precision in both experiment and theory. The searches that can be performed using flavour observables are complementary to the searches for New Physics (NP) particles at the energy frontier. Indeed, they can potentially probe higher energy scales than those that are currently directly accessible. The study of b-hadrons and their decays provides an excellent laboratory in which to make such measurements. Such studies are a world-wide effort, with experiments in the USA, Europe and Japan all contributing. Some of latest results from these experimental collaborations will be presented here.

2 Measurements of *CP*-violating phases

2.1 CKM angle γ

Of the three angles of the UT, the angle γ is the least well determined. Of particular importance is that the angle γ can be determined from purely tree-level processes. In addition, these determinations are theoretically extremely clean; the correspondence between the experimental measurements and the SM value of γ is accurate to the level of 10^{-7} [1]. Such measurements are therefore a "standard candle" for the SM and can be compared with measurements from loop-dominated processes to look for discrepancies. Hence, it is very important to achieve the best possible experimental precision.

The two tree-level diagrams $b \to c\bar{u}s$ and $b \to u\bar{c}s$ have a relative weak phase of γ. For this phase to be measurable the two diagrams must interfere. This can happen in the decays $B^+ \to \overline{D}^0 K^+$ and $B^+ \to D^0 K^+$ if the D^0 and $\overline{D}^0$ decay to the same final state. The experimental method depends on the nature of the D decay. The most recent results from LHCb use the decays $D \to K^0_S \pi^+\pi^-$ and $K^0_S K^+ K^-$, and hence the so-called GGSZ method [2, 3]. The strong

phase difference between the D^0 and $\overline{D}^0$ decays can be determined as a function of the position in the Dalitz plot, either by using a model of the decay amplitudes, e.g. from *BABAR* [4], or via a model-independent approach that uses measurements of the phase difference in bins of the Dalitz plot provided by the CLEO-c experiment [5]. The LHCb collaboration have recent results using both of these approaches. The model-dependent analysis [6] uses the data sample collected in 2011, corresponding to an integrated luminosity of $1\,\text{fb}^{-1}$. The model-independent analysis [7], described here, uses the $3\,\text{fb}^{-1}$ Run 1 dataset (from 2011 and 2012).

The model-independent nature of the method essentially reduces the analysis to counting the number of B^+ and B^- signal events in each bin of the Dalitz plot. The binning scheme is symmetric about $m^2_+ = m^2_-$, the bins in one half are labelled $+i$, while the corresponding bin in the other half is labelled $-i$. The signal yields are related to the quantities of interest via

$$\begin{aligned} N^+_{\pm i} &= h_{B^+}\left[F_{\mp i} + (x_+^2 + y_+^2)F_{\pm i} + 2\sqrt{F_i F_{-i}}(x_+ c_{\pm i} - y_+ s_{\pm i})\right] , \\ N^-_{\pm i} &= h_{B^-}\left[F_{\pm i} + (x_-^2 + y_-^2)F_{\mp i} + 2\sqrt{F_i F_{-i}}(x_- c_{\pm i} - y_- s_{\pm i})\right] , \end{aligned} \tag{1}$$

where F_i is the fraction of events in bin i in the flavour-specific $D^0 \to K^0_S\pi^+\pi^-$ Dalitz plot (obtained from semileptonic $B^+ \to \overline{D}^0\mu^+\nu_\mu$ data), $h_{B^\pm}$ are normalisation factors, c_i and s_i are the cosine and sine of the strong phase difference in bin i measured by CLEO-c, and $x_\pm \equiv r_B\cos(\delta_B \pm \gamma)$ and $y_\pm \equiv r_B\sin(\delta_B \pm \gamma)$, where r_B and δ_B are the ratio of magnitudes and strong phase difference of the two B decay diagrams. A simultaneous fit to the B candidate invariant mass in each Dalitz-plot bin is used to determine $x_\pm$ and $y_\pm$. Interpreting these results in terms of the physical parameters gives

$$r_B = 0.080^{+0.019}_{-0.021}\,, \quad \delta_B = \left(134^{+14}_{-15}\right)^\circ\,, \quad \gamma = \left(62^{+15}_{-14}\right)^\circ\,,$$

which constitutes the single most precise measurement of γ.

2.2 B^0_s-$\overline{B}^0_s$ mixing phase

The neutral B mesons exhibit mixing between B and $\overline{B}$ through a box diagram. Decays to *CP* eigenstates, which are accessible for both B and $\overline{B}$, therefore allow the mixing phase to be probed via interference between the direct decay process and decay after mixing. In the B^0_s system, the SM prediction for the mixing phase is small, $\phi_s \approx (-0.0363 \pm 0.0016)\,\text{rad}$, while many NP models enhance this value.

The decay mode $B^0_s \to J/\psi\,\phi$ is experimentally very clean. However, the vector-vector final state is an admixture of *CP* eigenstates. An angular analysis is required to disentangle the *CP*-odd and *CP*-even components. The signal model is then a sum of terms containing both angular and time dependence. It is necessary to determine the flavour of the signal B meson at production. This can be achieved by using either flavour-specific decays of the other b-hadron in the event or particles (such as charged kaons) associated with the hadronisation of the signal B. It is also necessary to account for the efficiency as a function of both the decay time and the angular variables, as well as the experimental resolution on the same quantities. The ATLAS, CMS and LHCb collaborations have all recently reported new or improved measurements of ϕ_s, which are shown in Fig. 1. The ATLAS [8] and CMS [9] results use the decay $B^0_s \to J/\psi\,\phi$, while LHCb have a combination of the channels $B^0_s \to J/\psi\,\pi^+\pi^-$ and $B^0_s \to J/\psi\,K^+K^-$ using $1\,\text{fb}^{-1}$ of data [10], as well as an update of the $B^0_s \to J/\psi\,\pi^+\pi^-$ channel using the $3\,\text{fb}^{-1}$ data set [11]. This latest LHCb results constitutes the single most precise measurement of

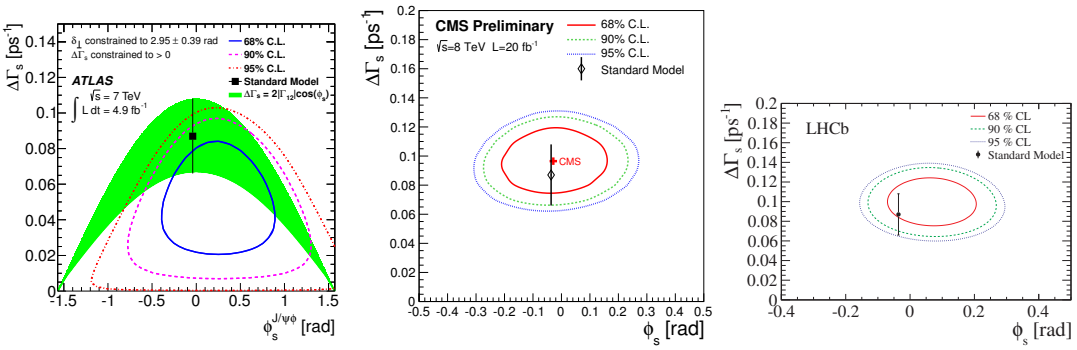

Figure 1: Results from (left) ATLAS, (middle) CMS, and (right) LHCb in the $\Delta\Gamma_s$ vs ϕ_s plane.

$\phi_s = (70 \pm 68 \pm 8)$ mrad. All of these results are consistent with the SM prediction. More precise measurements are needed to search for small deviations.

3 Semi-leptonic B decays

Semi-leptonic decays of b hadrons can be used to measure the sides of the UT by determining the absolute values of the CKM elements V_{cb} and V_{ub}. There are some persistent puzzles in this area. Firstly, poor consistency between the values of V_{xb} measured in inclusive and exclusive decays, and secondly, the sum of the measured branching fractions of exclusive semi-leptonic B to charm decays falls well short of the well measured inclusive rate (inclusive − exclusive $= (1.57 \pm 0.26)\%$). More precise measurements and measurements of extra decay channels are needed to either resolve these issues or to determine if they arise from NP contributions.

3.1 Anomalies in $\overline{B} \to D^{(*)}\tau\overline{\nu}_\tau$

In addition to the above puzzles, the *BABAR* experiment sees a large deviation from the SM in semi-tauonic B to charm decays [12, 13]. Measurements are made of the ratio of branching fractions

$$R(D^{(*)}) = \frac{\mathrm{BF}(\overline{B} \to D^{(*)}\tau^-\overline{\nu}_\tau)}{\mathrm{BF}(\overline{B} \to D^{(*)}\ell^-\overline{\nu}_\ell)} = \frac{N_{\mathrm{sig}}}{N_{\mathrm{norm}}} \times \frac{\varepsilon_{\mathrm{norm}}}{\varepsilon_{\mathrm{sig}}}\,. \tag{2}$$

The results are $R(D) = 0.440 \pm 0.072$ and $R(D^*) = 0.332 \pm 0.030$, which are 2.0σ and 2.7σ larger than the SM predictions 0.297 ± 0.017 and 0.252 ± 0.003, respectively. The combined significance of the deviation is 3.4σ. Including also the results from Belle [14, 15] increases the significance. Additionally, the *BABAR* results are incompatible (at the level of 3.1σ) with Type-II 2-Higgs-Doublet models of the possible charged Higgs contributions to these decays. The $R(D)$ and $R(D^*)$ results prefer different values of $\tan\beta/m_{H^+}$ in these models. In addition, *BABAR* and Belle results of the branching fraction of $B^- \to \tau^-\overline{\nu}_\tau$ prefer further different values of $\tan\beta/m_{H^+}$. The results can, however, be accommodated in more general 2-Higgs-Doublet models. The final results from the full Belle dataset are awaited with much anticipation.

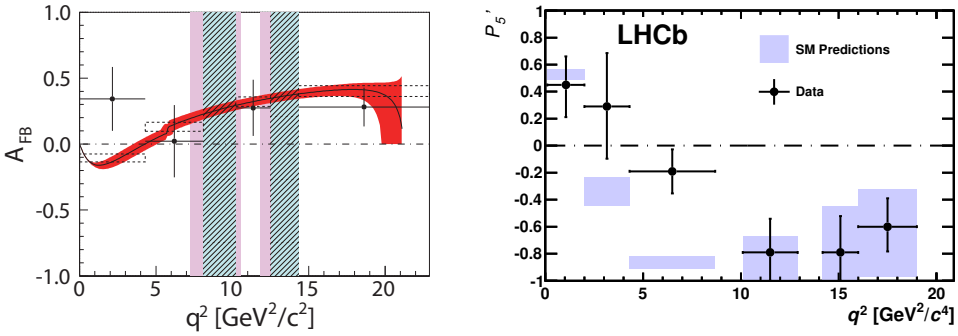

Figure 2: (left) Forward backward asymmetry as a function of q^2 for inclusive $B \to X_s \ell^+ \ell^-$. The red band is the SM prediction. (right) Distribution of the P_5' angular observable for $B^0 \to K^{*0} \mu^+ \mu^-$ decays.

3.2 Improved understanding of $\overline{B} \to D^{**} \ell \overline{\nu}_\ell$

The largest systematic uncertainty on the *BABAR* $\overline{B} \to D^{(*)} \tau^- \overline{\nu}_\tau$ results is due to the modelling of backgrounds from $B \to D^{**} \ell \nu_\ell$ decays. Many of these decays are not measured and this lack of knowledge could also be contributing to the "gap" between the inclusive and sum of exclusive branching fraction measurements mentioned earlier. Branching fractions of both charged and neutral B mesons decaying to $D^{(*)} \pi^\pm \ell \nu_\ell$ and $D^{(*)} \pi^+ \pi^- \ell \nu_\ell$ final states are measured by the *BABAR* experiment. For the latter class of decay, these are all first measurements, while those of the first type greatly improve their precision. The combined significance of the $D \pi^+ \pi^- \ell \nu_\ell$ decays is 5.1σ, while that of the $D^* \pi^+ \pi^- \ell \nu_\ell$ decays is 3.5σ. The inclusive–exclusive branching fraction gap is reduced from $\sim 7\sigma$ to $\sim 3\sigma$. These new results should also help to improve the systematic uncertainties on future analyses of $\overline{B} \to D^{(*)} \tau \overline{\nu}_\tau$. A journal paper describing the analysis and its results is in preparation.

4 Rare decays

Decays of the type $b \to s \ell^+ \ell^-$ proceed either via electroweak penguin or box diagrams. The Wilson coefficients C_7, C_9 and C_{10} encode the strength of the short-distance interactions. Many NP models predict additional contributions to the decay amplitudes at a similar level to the SM. Complementary information can be gained from branching fractions, *CP* asymmetries and angular moments, which are generally determined as a function of the 4-momentum transfer to the dimuon system, q^2.

The Belle collaboration have made the first measurements of the forward-backward asymmetry for inclusive $B \to X_s \ell^+ \ell^-$ decays [16]. The analysis uses a sum of 10 exclusive final states: 3 B^0 decays to a charged kaon and 1–3 pions, and 7 B^+ decays to a charged kaon and 0–3 pions or a K^0_S and 1–3 pions. The data sample used comprises 772 million $B\overline{B}$ pairs. The results are shown in Fig. 2 (left), where the red band is the SM prediction. Everything looks consistent with the SM at this level of precision, with the largest deviation being 1.8σ in the first bin.

The LHCb collaboration have performed an analysis of angular observables that have been

optimised to reduce their dependence on form factors [17] in the decay $B^0 \to K^{*0}\mu^+\mu^-$ [18]. The analysis uses the $1\,\text{fb}^{-1}$ data sample from 2011 and the results exhibit a large local deviation (3.7σ) in one bin of the P_5' distribution, as can be seen in Fig. 2 (right). The probability to observe a fluctuation $\geq 3.7\sigma$ in the 24 bins is 0.5%. The residual degree of dependence on form factors and hence the size of the theoretical uncertainties is a hot topic in the theory community. Improved determination of these as well as increased precision from the experimental side will help to determine if this is a genuine effect from NP contributions.

Including this result in global fits to the Wilson coefficients [19, 20, 21] indicates that it can be accommodated if the value of the C_9 coefficient is reduced. If this is indeed the case then one would expect the branching fractions of decays such as $B \to K^{(*)}\mu^+\mu^-$ and $B_s^0 \to \phi\mu^+\mu^-$ to be lower than predicted. LHCb measurements of these quantities [22, 23, 24] are indeed lower than the predictions from both Lattice QCD [25, 26] and Light Cone Sum Rules [27, 28].

One possible explanation for a low value of C_9 is contributions from a Z' particle, see for example Ref. [29]. Some NP models that include a Z' have preferred coupling to muons over electrons [30]. Due to destructive interferences this means that the branching fraction of $B^+ \to K^+\mu^+\mu^-$ should be lower than that for $B^+ \to K^+e^+e^-$. LHCb also has results for this ratio of branching fraction using the full Run 1 data sample [31]

$$R_K = \frac{\text{BF}(B^+ \to K^+\mu^+\mu^-)}{\text{BF}(B^+ \to e^+e^-)} = 0.745^{+0.090}_{-0.074} \pm 0.036\,, \tag{3}$$

which deviates from the SM prediction of unity by 2.6σ.

It would seem therefore that there is a reasonably consistent picture. However, there is much still to be understood, such as the importance of $c\bar{c}$ resonances at high q^2 [32, 33]. It is important to update all measurements to the full Run 1 data sample and to include additional decay modes, such as $\Lambda_b \to \Lambda\mu^+\mu^-$ and $B^+ \to K^+\pi^+\pi^-\ell^+\ell^-$, to further increase the sensitivity.

5 Dimuon charge asymmetry

Measurements of the dimuon charge asymmetry are sensitive to possible *CP* violation in the mixing of the neutral B mesons, which would imply $\Gamma(B \to \overline{B} \to \mu^- X) \neq \Gamma(\overline{B} \to B \to \mu^+ X)$. The D0 experiment measures the inclusive dimuon asymmetry

$$A_{sl} = \frac{N(\mu^+\mu^+) - N(\mu^-\mu^-)}{N(\mu^+\mu^+) + N(\mu^-\mu^-)}\,, \tag{4}$$

which is related to both the semi-leptonic charge asymmetries of B^0 and B_s^0 mesons.

Corrections for backgrounds have been applied (the single muon asymmetry is used to help reduce systematic uncertainties), as well as those for *CP* violation that occurs in the interference between mixing and decay. After this, the result obtained by D0 [34] is $A_{sl} = (-0.496 \pm 0.153 \pm 0.072)\,\%$, which differs from the SM prediction, $A_{sl}^{\text{SM}} = (-0.023 \pm 0.004)\,\%$, at the level of 2.8σ. Comparing separately each bin of the impact parameter distribution with the SM, the level of disagreement rises to 3.6σ.

The interpretation of the result in terms of the individual semi-leptonic asymmetries depends strongly on the assumed value of $\Delta\Gamma_d/\Gamma_d$, the discrepancy with the SM varying between 1.9σ and 3.6σ. This highlights the importance of improved measurements of $\Delta\Gamma_d/\Gamma_d$. Indeed, a recent LHCb result [35] based on $1\,\text{fb}^{-1}$ of data and using the decay modes $B^0 \to J/\psi\, K^{(*)0}$ gives a value $-0.044 \pm 0.025 \pm 0.011$, which is becoming competitive with the B-factory results.

6 Direct CP violation in charmless three-body B decays

In general, CP asymmetries can arise when there is more than one contributing amplitude to a decay and where those amplitudes have both different weak and strong phases. In charmless B^+ decays there are contributing tree and loop diagrams, which have similar magnitudes and a relative weak phase of γ. In three-body decays, the strong phase difference could arise from an intrinsic difference in the two decay diagrams, from rescattering or from interference between intermediate resonances in the Dalitz plot.

6.1 Large CP violation in $B^+ \to h^+h^+h^-$

The LHCb experiment has performed an analysis of CP violation in the phase-space of three-body charmless decays of B^+ mesons to $h^+h^+h^-$ final states ($h = K/\pi$) [36]. The measured raw asymmetries are corrected for the effects of production, detection and matter-interaction asymmetries using data control modes. The inclusive asymmetries for each mode are determined to be between $2-13\%$ in magnitude and positive (negative) for $B^\pm \to K^\pm\pi^+\pi^-$ and $\pi^\pm\pi^+\pi^-$ ($B^\pm \to K^\pm K^+K^-$ and $\pi^\pm K^+K^-$) decays. The local asymmetries in regions of the phase space are much more pronounced. Figure 3 shows the raw asymmetry as a function of the position in the Dalitz plot for the decays to $K^\pm K^+K^-$ and $K^\pm\pi^+\pi^-$. There are regions of very large positive (negative) asymmetry at low values of the $\pi^+\pi^-$ (K^+K^-) invariant mass. A similar pattern is seen for the other two decay modes.

The larger data sample than the previous analyses [37, 38] allows a more detailed examination of the variation of the asymmetries in the phase space. Figure 4 shows the $m_{\pi^+\pi^-}$ dependence of the difference between the B^- and B^+ signal yields in the $B^\pm \to \pi^\pm\pi^+\pi^-$ decay. The distributions are shown separately for the two regions $\cos\theta > 0$ and $\cos\theta < 0$, where θ is the angle between the like-sign pions in the $\pi^+\pi^-$ rest frame. The most striking features are the change in sign of the asymmetry on either side of the $\rho(770)$ resonance pole and that the sign is opposite for the two regions of $\cos\theta$. This indicates that the interference between the $\rho(770)$ and an underlying S-wave component is playing a significant role in generating the CP asymmetry. In addition, it is possible that $\pi\pi \leftrightarrow KK$ rescattering is contributing in the region between 1.2 and 1.5 GeV/c^2. Amplitude analyses of these decays will be required to fully understand the origin of these very large asymmetries.

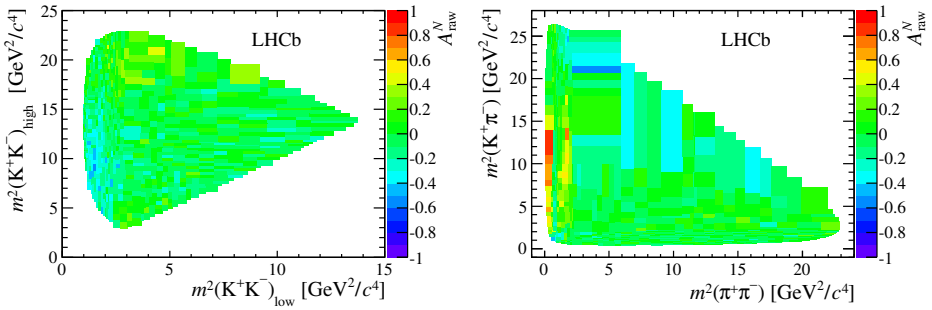

Figure 3: Raw asymmetries as a function of the DP position for $B^\pm$ decays to (left) $K^\pm K^+K^-$, and (right) $K^\pm\pi^+\pi^-$ final states.

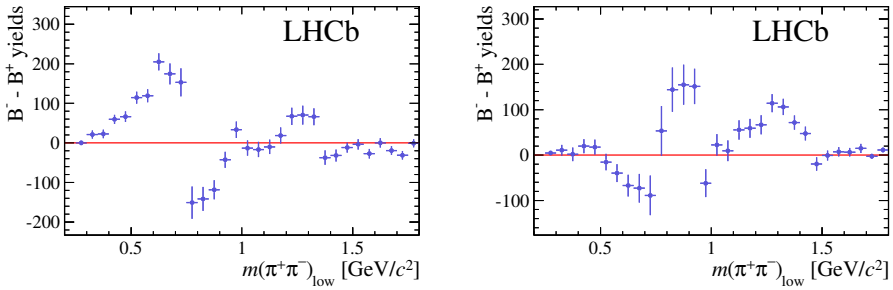

Figure 4: Difference of the B^- and B^+ signal yields as a function of the $\pi^+\pi^-$ invariant mass in the $B^\pm \to \pi^\pm\pi^+\pi^-$ decay. The yields have been background-subtracted and efficiency-corrected.

6.2 Amplitude analysis of $B^+ \to K^0_S\pi^+\pi^0$

The *BABAR* experiment has recently performed an amplitude analysis of the decay $B^+ \to K^0_S\pi^+\pi^0$. In addition to providing measurements of the branching fractions and *CP* asymmetries of the various intermediate states, a Dalitz-plot analysis allows the determination of their relative phases. Of particular interest are the relative phases of the two $K^*\pi$ components, which can be used to determine the CKM angle γ [39, 40].

A maximum likelihood fit is performed to separate signal from background and to determine the signal Dalitz-plot amplitudes. The fitted signal yield is 1014 ± 63, where the uncertainty is statistical only. The signal Dalitz-plot model follows the isobar model formalism, where the total amplitude is formed from the sum of the amplitudes for the various intermediate states. The complex coefficient for each contributing amplitude is determined from the fit. The branching fractions, *CP* asymmetries and relative phases are derived from these fitted coefficients. The signal model includes contributions from both the charged and neutral $K^*(892)$ resonances and the corresponding $K\pi$ S-wave as well as the $\rho(770)^+$ resonance.

The *CP* asymmetry of $B^+ \to K^*(892)^+\pi^0$ has a very large, negative central value (-52%) and is found to have a significance of 3.4σ, corresponding to first evidence of *CP* violation in this decay. The projection of the fit onto the $K^0_S\pi^+$ invariant mass can be seen in Figure 5, separated by the charge of the B candidate, where the asymmetry in the $K^*(892)^+$ region can be clearly seen. A journal paper describing the analysis and its results is in preparation.

7 Conclusion

With increasingly precise and sophisticated measurements, some anomalies have started to appear within the realm of b-hadron physics. Whether these are true hints of contributions from physics beyond the Standard Model will only become apparent with improved measurements and theoretical understanding. The coming years will provide better experimental precision as the LHC Run 1 data is fully exploited and the samples from Run 2 are collected and analysed. With the start of the Belle II experiment and the upgrade of the LHCb experiment both expected within the next few years, we look forward to the unprecedented precision that these complementary experiments will offer across the whole range of b-hadron physics.

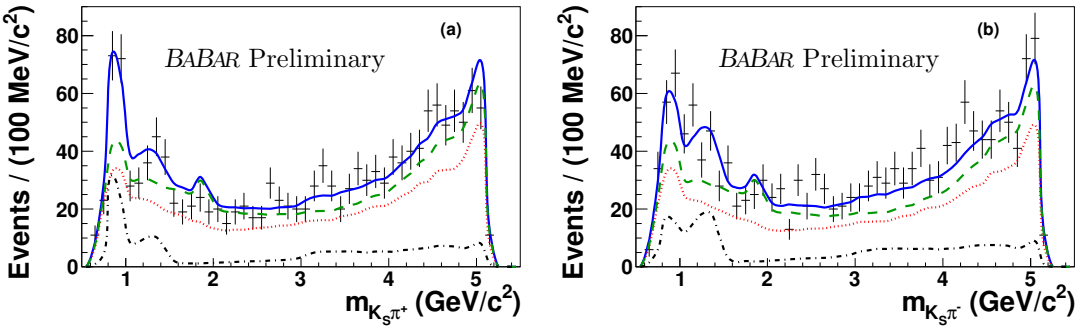

Figure 5: Data distributions of $m_{K^0_S\pi^+}$ and the corresponding fit projections for (a) B^+, and (b) B^- candidates. Points with error bars are the data, the solid (blue) lines are the total fit result, the dashed (green) lines are the total background contribution, and the dotted (red) lines are the $q\bar{q}$ component. The dash-dotted lines represent the signal contribution.

Acknowledgments

Work supported by the European Research Council under FP7 and by the Science and Technology Facilities Council.

References

[1] J. Brod and J. Zupan, JHEP **1401** (2014) 051.
[2] A. Bondar, Proceedings of BINP special analysis meeting on Dalitz analysis, 24-26 Sept, 2002. Unpublished.
[3] A. Giri, Y. Grossman, A. Soffer and J. Zupan, Phys. Rev. D **68** (2003) 054018.
[4] P. del Amo Sanchez *et al.* [BaBar Collaboration], Phys. Rev. Lett. **105** (2010) 081803.
[5] J. Libby *et al.* [CLEO Collaboration], Phys. Rev. D **82** (2010) 112006.
[6] R. Aaij *et al.* [LHCb Collaboration], Nucl. Phys. B **888** (2014) 169.
[7] R. Aaij *et al.* [LHCb Collaboration], Submitted to JHEP, arXiv:1408.2748 [hep-ex].
[8] G. Aad *et al.* [ATLAS Collaboration], Phys. Rev. D **90** (2014) 052007.
[9] CMS Collaboration, CMS-PAS-BPH-13-012 (2014).
[10] R. Aaij *et al.* [LHCb Collaboration], Phys. Rev. D **87** (2013) 112010.
[11] R. Aaij *et al.* [LHCb Collaboration], Phys. Lett. B **736** (2014) 186.
[12] J. P. Lees *et al.* [BaBar Collaboration], Phys. Rev. Lett. **109** (2012) 101802.
[13] J. P. Lees *et al.* [The BaBar Collaboration], Phys. Rev. D **88** (2013) 072012.
[14] I. Adachi *et al.* [Belle Collaboration], arXiv:0910.4301 [hep-ex].
[15] A. Bozek *et al.* [Belle Collaboration], Phys. Rev. D **82** (2010) 072005.
[16] Y. Sato *et al.* [Belle Collaboration], arXiv:1402.7134 [hep-ex].
[17] J. Matias, F. Mescia, M. Ramon and J. Virto, JHEP **1204** (2012) 104.
[18] R. Aaij *et al.* [LHCb Collaboration], Phys. Rev. Lett. **111** (2013) 191801.
[19] S. Descotes-Genon, J. Matias and J. Virto, Phys. Rev. D **88** (2013) 074002.
[20] W. Altmannshofer and D. M. Straub, Eur. Phys. J. C **73** (2013) 2646.

[21] F. Beaujean, C. Bobeth and D. van Dyk, Eur. Phys. J. C **74** (2014) 2897.
[22] R. Aaij *et al.* [LHCb Collaboration], JHEP **1307** (2013) 084.
[23] R. Aaij *et al.* [LHCb Collaboration], JHEP **1308** (2013) 131.
[24] R. Aaij *et al.* [LHCb Collaboration], JHEP **1406** (2014) 133.
[25] C. M. Bouchard, G. P. Lepage, C. J. Monahan, H. Na and J. Shigemitsu, arXiv:1310.3207 [hep-lat].
[26] R. R. Horgan, Z. Liu, S. Meinel and M. Wingate, Phys. Rev. Lett. **112** (2014) 212003.
[27] C. Bobeth, G. Hiller and D. van Dyk, JHEP **1107** (2011) 067.
[28] C. Bobeth, G. Hiller, D. van Dyk and C. Wacker, JHEP **1201** (2012) 107.
[29] R. Gauld, F. Goertz and U. Haisch, JHEP **1401** (2014) 069.
[30] W. Altmannshofer, S. Gori, M. Pospelov and I. Yavin, Phys. Rev. D **89** (2014) 095033.
[31] R. Aaij *et al.* [LHCb Collaboration], Phys. Rev. Lett. **113** (2014) 151601.
[32] R. Aaij *et al.* [LHCb Collaboration], Phys. Rev. Lett. **111** (2013) 112003
[33] J. Lyon and R. Zwicky, arXiv:1406.0566 [hep-ph].
[34] V. M. Abazov *et al.* [D0 Collaboration], Phys. Rev. D **89** (2014) 012002.
[35] R. Aaij *et al.* [LHCb Collaboration], JHEP **1404** (2014) 114.
[36] R. Aaij *et al.* [LHCb Collaboration], Submitted to Phys. Rev. D, arXiv:1408.5373 [hep-ex].
[37] R. Aaij *et al.* [LHCb Collaboration], Phys. Rev. Lett. **111** (2013) 101801.
[38] R. Aaij *et al.* [LHCb Collaboration], Phys. Rev. Lett. **112** (2014) 011801.
[39] M. Ciuchini, M. Pierini and L. Silvestrini, Phys. Rev. D **74** (2006) 051301.
[40] M. Gronau, D. Pirjol, A. Soni and J. Zupan, Phys. Rev. D **75** (2007) 014002.

Search for beyond the standard model physics at the LHC

Kenichi Hatakeyama for the CMS and ATLAS collaborations
Baylor University, One Bear Place #97316, Waco, TX, U.S.A.

DOI: http://dx.doi.org/10.3204/DESY-PROC-2014-04/316

Both CMS and ATLAS collaborations have performed searches for physics beyond the standard model of particle physics in a variety of final states using the proton-proton collision data collected during the LHC Run 1 at the center-of-mass energy of $\sqrt{s}$ = 7–8 TeV. In this paper, a review of recent results from these searches are presented. Future prospects for these searches from the LHC experiments are also discussed.

1 Introduction

The Run 1 operation of the Large Hadron Collider (LHC) from 2009 to 2012 was extremely successful. The long-sought Higgs boson was discovered by the CMS and ATLAS collaborations, which completed the standard model (SM). However, there are still many open questions in particle physics, such as the gauge hierarchy problem and the identify of dark matter, and the standard model is often considered as a low-energy approximation of a more complete theory. Both CMS and ATLAS have performed a variety of new physics searches using the Run 1 data, and more than 100 results based on the 2012 data of 8 TeV proton-proton collisions are made public [1, 2]. In this conference proceedings, I will present only some highlights of these results.

2 Search for resonances

Mass resonances are simple yet powerful probes to discover new particles, and new particles that will produce mass resonance signatures are predicted in many beyond-the-standard-model (BSM) scenarios. Single mass resonances are predicted by, e.g., extended gauge theories [W'/Z'], compositeness [excited fermions], Randall-Sundrum (RS) model [Kaluza-Klein gravitons/gluons], and paired mass resonances may be produced by, e.g., gluinos/squarks in the case of supersymmetry, and also by leptoquarks, vector-like quarks, and colorons. Searches for new physics in dilepton mass spectra were performed by both CMS [3] and ATLAS [4]. The m_{ee} spectrum measured by ATLAS is shown in Fig. 1(a). No resonant structure is observed and Z's with the SM Z couplings are excluded up to 2.9 TeV [3, 4].

The forward-backward asymmetry of dielectron pairs in the same dataset, $A_{\mathrm{FB}} = (N_{\mathrm{F}} - N_{\mathrm{B}})/(N_{\mathrm{F}} + N_{\mathrm{B}})$ where N_F (N_B) is the number of events with $\cos\theta^* > 0$ ($\cos\theta^* < 0$) and θ^* is the dielectron decay angle, provides extra handles to search for non-resonant new physics signatures originating from contact interactions or large extra spatial dimensions. No significant

deviations from the SM background expectations are observed as shown in Fig. 1(b) and lower limits are set on the contact interaction scale Λ up to 26 TeV [5].

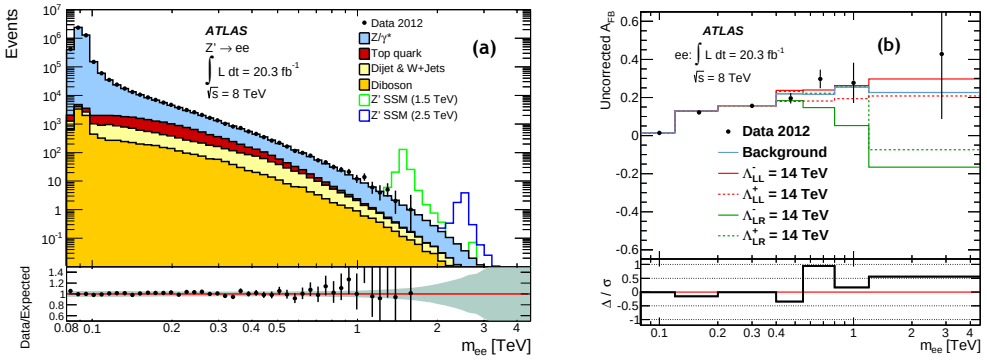

Figure 1: (a) The m_{ee} distributions with two selected Z' signals overlaid, compared to the stacked sum of all expected backgrounds, and the ratios of data to the background expectation [4]. (b) Reconstructed A_{FB} distributions for data and the SM background estimation versus m_{ee} together with the predictions of different Λ values for the contact interaction model [5].

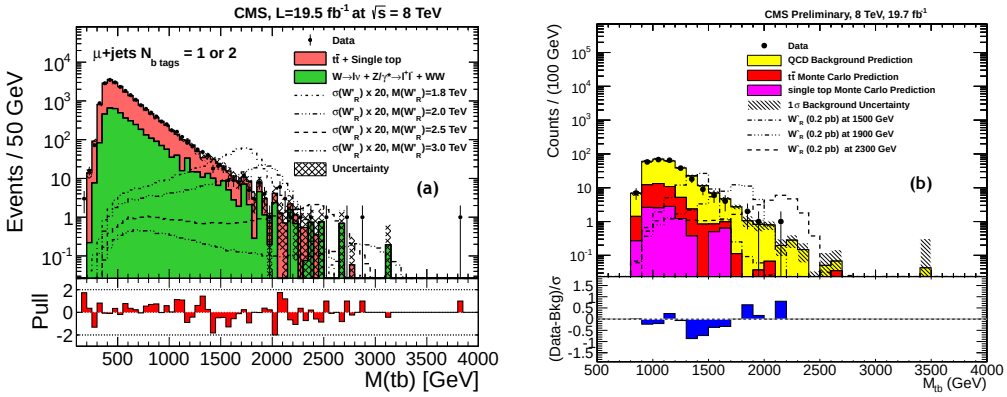

Figure 2: The m_{tb} distributions in the (a) semi-leptonic [6] and (b) all-hadronic [7] channel together with simulated W' signal distributions.

Searches for W's decaying to the top-bottom quark pairs have been performed by both CMS [6, 7] and ATLAS [8, 9]. The m_{tb} mass spectra measured in the semi-leptonic ($\mathrm{W}' \to \mathrm{tb}, \mathrm{t} \to \mathrm{Wb} \to (\mathrm{l}\nu)\mathrm{b}$) and all-hadronic ($\mathrm{W}' \to \mathrm{tb}, \mathrm{t} \to \mathrm{Wb} \to (\mathrm{q}\bar{\mathrm{q}}')\mathrm{b}$) channels by CMS are shown in Fig. 2. The right-handed W' is excluded up to about 2 TeV. For the all-hadronic searches [7, 9], the jet substructure technique is used to identify hadronically-decaying boosted top quarks from W' decays. New physics searches at the LHC often involve high-p_{T} boosted top/W's, and jet substructure tools based on "fat" jets with the size parameters $R = 0.8$–1.5 are widely used.

New heavy vector-like quarks emerge as a characteristic feature of some BSM models, including extra dimensions and composite Higgs models. They have been extensively searched for by CMS [10, 11] and ATLAS [12, 13, 14]. A new charge +2/3 quark, T, undergo three decay modes: T → Zt, Ht, and Wb. Searches have been performed in different channels to cover various branching fraction hypotheses. Searches in the opposite-sign dileptons and ≥ 3 leptons + b-tags channels are sensitive to the T → Zt decay [12]. A search with boosted W + b-tags [13] provides sensitivities to T → Wb, and a search with the same-sign dileptons + b-tags [14] is sensitive to T → Zt and T → Ht. As shown in Fig. 3, these complementary searches provide sensitivities to a wide range of branching fractions. The current lower bounds on the T mass are about 690–780 GeV from CMS [10] and 550–850 GeV from ATLAS [12, 13, 14].

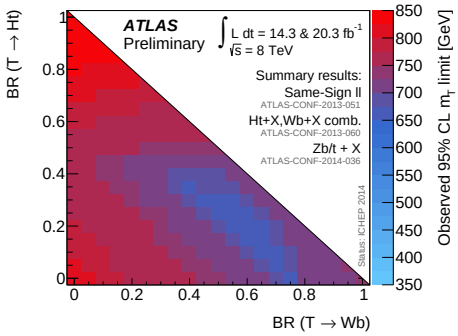

Figure 3: Observed lower limits on the mass of vector-like T quarks from ATLAS searches in the branching-ratio plane.

3 Search for dark matter

Currently one of the most important questions in particle physics is the identify of dark matter (DM). There are strong indications from many astronomical observations that there are DM particles which do not interact via strong or electromagnetic forces and are heavy enough so that they move slowly compared to the speed of light; however, such particles have not been observed in the laboratory yet. Many ground-based experiments looking for DM-nucleon scattering (direct searches) and experiments in space looking for signals from DM annihilation or decays (indirect searches) have been built. At the LHC, DM particles may be pair-produced in proton-proton collisions either directly or through cascade decays of heavier new particles. The DM particles do not interact with the CMS and ATLAS detectors; however, they can still be observed when they are boosted against initial state radiation of gluons, quarks, vector-bosons, and photons. If these radiated particles have high p_{T}, they result in the final state of mono-"X" and large missing E_{T}. Since particles that mediate interactions between SM particles and DM particles are not known, the effective field theory (EFT) is often used to model these interactions as contact interactions in interpretation of LHC DM search results. This is considered as a good model for heavy mediator masses ($>$ 3 TeV); however, a special care is necessary for lighter mediators.

CMS and ATLAS have searched for DM particles in mono-jet [15], mono-photon [16], mono-W/Z [17, 18, 19, 20], mono-top [21, 22], and di-top [23] final states associated with large missing E_T in the 8 TeV data. The mono-jet search results from CMS are shown in Fig 4(a). Searches in different final states provide the information about couplings of mediator particles to different flavors of quarks and gluons. Limits are set on the EFT contact interaction scale Λ using effective operators, and they are further translated to limits on elastic DM-nucleon cross section as a function of DM particle mass as shown in Fig. 4(b). Compared to results from direct dark matter searches, LHC results are more independent of DM masses up to kinematic limits of a few hundred GeV, more stringent at low DM masses, and less sensitive to the spin-dependence of the couplings.

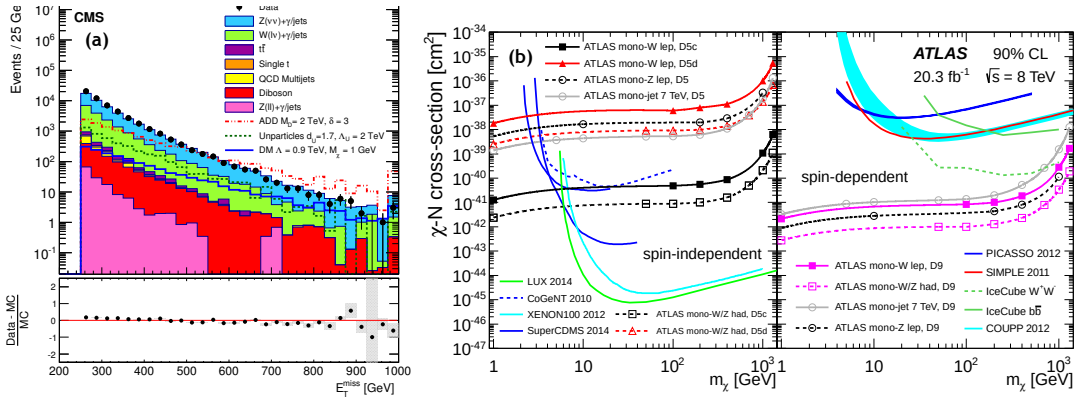

Figure 4: (a) Missing E_{T} distributions from the mono-jet search [15]. (b) The upper limits on the DM-nucleon cross section as a function of DM particle mass from searches in the mono-jet, mono-W, and mono-Z channels [19] for the spin-independent and spin-dependent EFT operators, together with limits from other experiments.

Some class of BSM models, called Higgs portal DM models, predict that a DM particle ($\tilde{\chi}$) interacts with SM particles only through the Higgs exchange process and the Higgs decays in the $\mathrm{H} \to \tilde{\chi}\tilde{\chi}$ mode. CMS searched for this signature in the vector boson fusion (VBF) channel and the $\mathrm{Z}(\to \ell\ell, \mathrm{b\bar{b}})$ + H channel [24]. The limit was placed on $\mathrm{Br}(\mathrm{H} \to \tilde{\chi}\tilde{\chi}) < 0.68$ (0.81) from the VBF (ZH) channel search, and the results are also presented in terms of the DM-nucleon cross section as shown in Fig. 5.

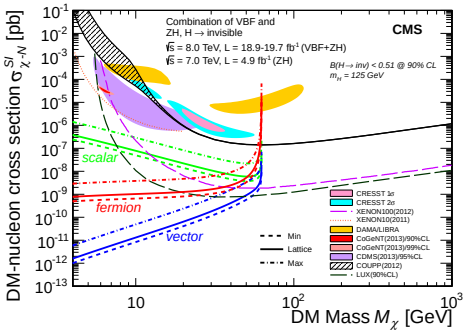

Figure 5: The upper limits on the DM-nucleon cross section versus DM particle mass from the $\mathrm{H} \to \tilde{\chi}\tilde{\chi}$ searches [24].

4 Search for supersymmetry

Supersymmetry (SUSY) is a well motivated BSM theory. In SUSY, the lightest supersymmetric particle (LSP) is considered a valid DM candidate. A broad class of SUSY scenarios with light third generation squarks and gluiness, known as natural models, can address the gauge hierarchy problem.

An extensive program to search for SUSY was carried out by CMS and ATLAS. Searches in the jets + missing E_{T} final state provide sensitivities to a wide class of SUSY models [25, 26]. Search results from ATLAS in this channel [25] are shown in Fig. 6(a). Mass exclusions reach up to about 1.4 TeV for gluinos ($\tilde{\mathrm{g}}$) and 0.9 TeV for the first- and second-generation squarks ($\tilde{\mathrm{q}}$). The inclusive searches with b-tags test natural SUSY models with TeV-scale gluinos, lighter top and bottom squarks, and nearly mass-degenerate charginos/neutralinos [27, 28]. Results from CMS [27] are shown in Fig. 6(b) for models with various gluino decay modes. The sensitivities generally degrade when there are more top quarks in the final state due to complex top quark decays.

The top squark ($\tilde{\mathrm{t}}_1$) is extensively searched for by CMS [29, 30, 31] and ATLAS [32, 33, 34, 35]

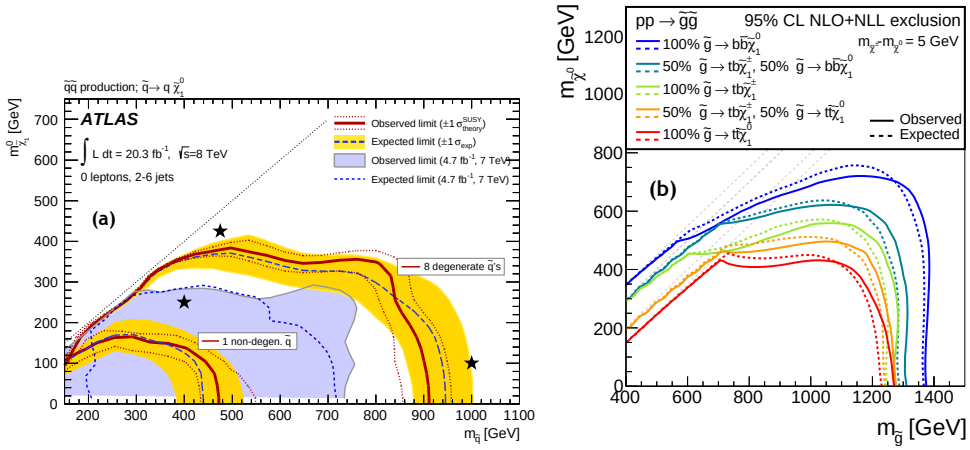

Figure 6: (a) Squark mass limits in the $m_{\tilde{q}}$-$m_{\tilde{\chi}_1^0}$ plane [25], and (b) gluino mass limits in the $m_{\tilde{g}}$-$m_{\tilde{\chi}_1^0}$ plane obtained for different gluino branching fraction models [27].

given its important role for addressing the gauge hierarchy problem. The dominant decay channel of the top squark varies over different SUSY scenarios and largely depends on available phase space for each decay mode. Results of complementary searches by ATLAS in different final states targeting different top squark decay modes are summarized in Fig. 7(a). The $\tilde{t}_1 \to t\tilde{\chi}_1^0$ decay mode is searched for in the 0-, 1-, and 2-lepton final states [32, 33, 34], and the mass exclusion extends up to about 700 GeV in the top squark mass. If $m_b + m_W + m_{\tilde{\chi}_1^0} < m_{\tilde{t}_1} < m_t + m_{\tilde{\chi}_1^0}$, the top squark often decays through $\tilde{t}_1 \to Wb\tilde{\chi}_1^0$, and searches in the 1- and 2-lepton channels provide sensitivities. If $m_{\tilde{t}_1} < m_b + m_W + m_{\tilde{\chi}_1^0}$, the top squark often decays through

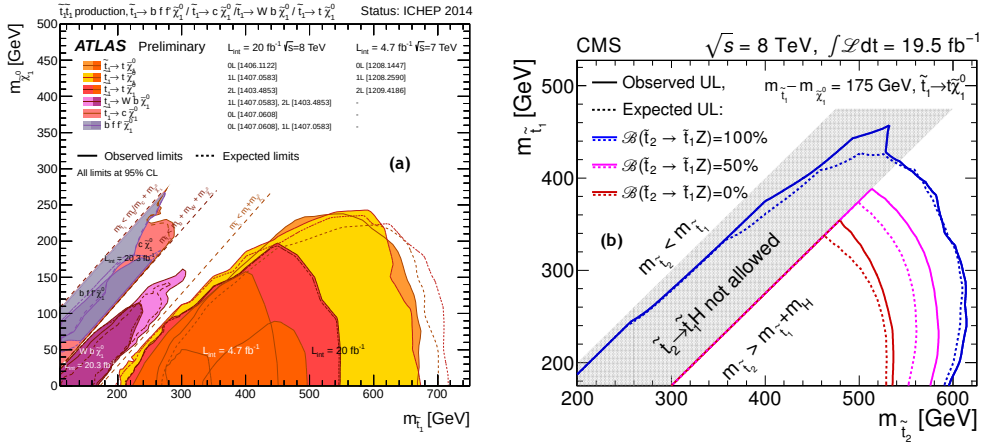

Figure 7: (a) Exclusion limits for top squark pair production from ATLAS [32, 33, 34, 35] shown in the $m_{\tilde{t}_1}$-$m_{\tilde{\chi}_1^0}$ plane. (b) Exclusion limits for $\tilde{t}_2$-pair production for different branching fractions of $\tilde{t}_2 \to Z(H)\tilde{t}_1$ [37].

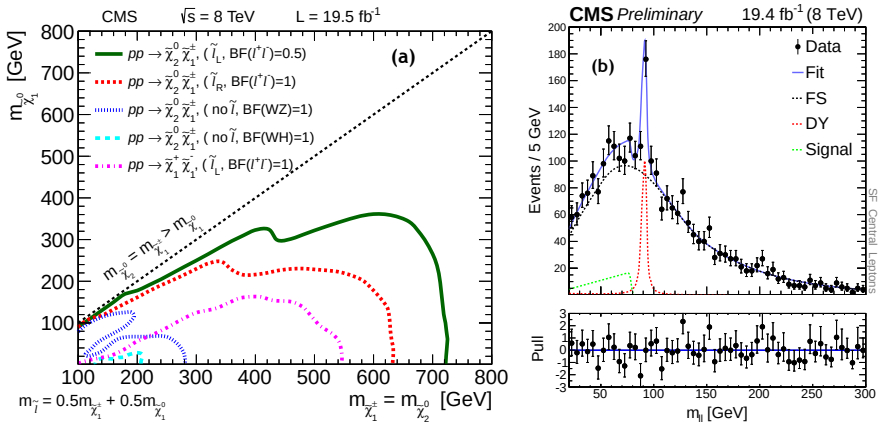

Figure 8: (a) Mass exclusions for $\tilde{\chi}_1^{\pm}\tilde{\chi}_2^0$ production with different decays, and for $\tilde{\chi}_1^{\pm}\tilde{\chi}_1^{\mp}$ production [38]. (b) Measured dilepton mass distributions with fits with the signal + background hypothesis in a dilepton mass spectrum endpoint search [44].

$\tilde{t}_1 \to c\tilde{\chi}_1^0$ or $\tilde{t}_1 \to bff'\tilde{\chi}_1^0$. In the case of $\tilde{t}_1 \to c\tilde{\chi}_1^0$ with the small mass splitting $m_{\tilde{t}_1} - m_{\tilde{\chi}_1^0}$, searches in the mono-jet + missing E_T final state provide sensitivities [31, 35]; however, as the mass splitting increases, mono-jet searches lose sensitivities and ATLAS performed a dedicated search with a charm-tagging [35] to fill this gap.

Gaining sensitivities to the top squark production remains difficult especially if $m_{\tilde{t}_1} - m_{\tilde{\chi}_1^0} \sim m_t$. If $m_{\tilde{\chi}_1^0}$ is small, the expected signal looks very similar to the SM $t\bar{t}$ production. ATLAS used the $t\bar{t}$ cross section measurement to place limits on the pair-production of top squarks with each top squark decaying to the top quark and LSP [36]. For higher $m_{\tilde{\chi}_1^0}$ values, CMS considered accessing such scenarios via the cascade decay of the heavier top squark ($\tilde{t}_2$), i.e., $\tilde{t}_2 \to \tilde{t}_1(H/Z) \to t(H/Z)\tilde{\chi}_1^0$ [37]. The results are shown in Fig. 7(b).

The production of charginos and neutralinos are also vigorously searched for by CMS and ATLAS. Searches for chargino-neutralino ($\tilde{\chi}_1^{\pm}\tilde{\chi}_2^0$) pair production were performed in a variety of final states with leptons and W, Z, and Higgs bosons [38, 39, 40, 41, 42]. These complementary searches provide sensitivities to $\tilde{\chi}_1^{\pm}\tilde{\chi}_2^0$ production with decays to left-handed sleptons ($\tilde{\ell}_L$), right-handed sleptons ($\tilde{\ell}_R$), or direct decays to Higgs and vector bosons as shown in Fig 8(a). The sensitivities and mass exclusions strongly depend on the branching fraction of $\tilde{\chi}_1^{\pm}$ and $\tilde{\chi}_2^0$. If $m_{\tilde{\ell}}$ is inbetween $m_{\tilde{\chi}_1^{\pm}}/m_{\tilde{\chi}_2^0}$ and $m_{\tilde{\chi}_1^0}$, the leptonic decay fractions of $\tilde{\chi}_1^{\pm}$ and $\tilde{\chi}_2^0$ increase, which enhances the sensitivities. For the scenarios in which $\tilde{\chi}_1^{\pm}/\tilde{\chi}_2^0$ decays to W/Z/H, sensitivities from the Run 1 searches are still modest, and the future LHC running will be essential to explore up to the TeV scale as shown in Fig. 9(c).

Searches are also performed in the HH and HZ final states [43]. A signal in these final states is expected from, e.g., the gauge-mediated SUSY model with the higgsino-like $\tilde{\chi}_{1,2}^0$ and $\tilde{\chi}_1^{\pm}$. A pair of $\tilde{\chi}_1^0$ with each $\tilde{\chi}_1^0$ decaying to H/Z and LSP (gravitino $\tilde{G}$), lead to these final states. The covered channels include $HH \to b\bar{b}b\bar{b}, \gamma\gamma(b\bar{b}, ZZ, WW, \tau\tau)$, and $HZ \to \gamma\gamma jj, \gamma\gamma\ell\ell, b\bar{b}\ell\ell$, and searches in these channels provide complementary sensitivities. Exclusions are set on the higgsino mass up to about 380 GeV in case the $\tilde{\chi}_1^0$ dominantly decays to Z and $\tilde{G}$; however, no exclusion is set on scenarios with high $\tilde{\chi}_1^0 \to H\tilde{G}$ branching fractions.

CMS has also performed a generic search for a kinematic endpoint in dilepton (e^+e^- and $\mu^+\mu^-$) mass spectra. If there is a decay process, e.g., $\tilde{\chi}_2^0 \to \ell\tilde{\ell} \to \tilde{\chi}_1^0\ell^+\ell^-$, opposite-sign same-flavor dilepton mass spectra are expected to show an endpoint (edge) at $m_{\rm edge} = \sqrt{(m^2_{\tilde{\chi}_2^0} - m^2_{\tilde{\ell}})(m^2_{\tilde{\ell}} - m^2_{\tilde{\chi}_1^0})}/m_{\tilde{\ell}}$. For this search, the signal and background contributions are determined from a kinematic fit where the dominant flavor-symmetric background is constrained with opposite-sign opposite-flavor ($e^+\mu^-$ and $e^-\mu^+$) leptons. A likelihood fit shown in Fig. 8(b) yields the observed significance of 2.4σ, which is not statistically significant, but it will be interesting to study it further with future runs.

5 Future prospects

The LHC will resume its operation in 2015 with the 13 TeV proton-proton collision energy, and the energy will go up to 14 TeV in the coming years. The energy increase from 8 to 13/14 TeV improves discovery sensitivities for high mass resonances, gluinos, and squarks drastically. The LHC is expected to deliver about 300 fb^{-1} of data by 2022, and the high-luminosity LHC (HL-LHC) will accumulate 10 times more data (i.e., about 3000 fb^{-1}) for the following 10 years after major upgrades of the LHC and CMS/ATLAS detectors. Such high luminosities help improving sensitivities particularly for weakly interacting massive particles produced with low cross sections. As examples, the estimated discovery sensitivities for gluino, top squark, and $\tilde{\chi}_1^\pm\tilde{\chi}_2^0$ production with 300 and 3000 fb^{-1} of data are shown in Fig. 9.

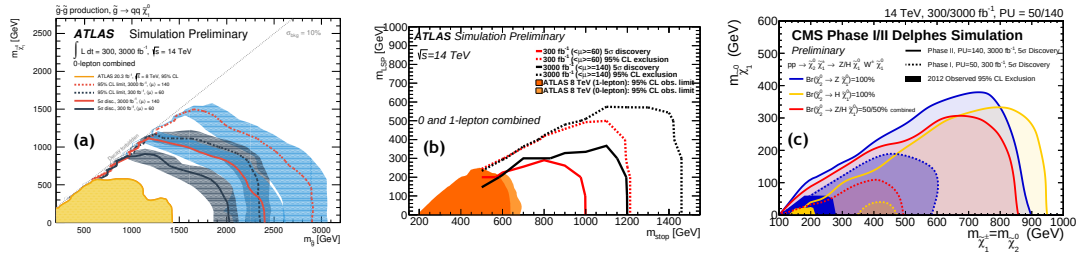

Figure 9: Discovery reaches for supersymmetry with 300 fb^{-1} (LHC Run 2+3) and 3000 fb^{-1} (HL-LHC) for (a) $\tilde{g}$-pair [45], (b) $\tilde{t}_1$-pair [45], and (c) $\tilde{\chi}_1^\pm\tilde{\chi}_2^0$ production [46].

6 Summary

The CMS and ATLAS collaborations have performed a wide variety of searches for physics beyond the standard model in the LHC Run 1 data. No new physics signature has not been observed yet, and only exclusion limits have been presented. However, our journey of new physics searches at the ∼TeV scale have just begun, and the LHC operation in the coming years will provide exciting opportunities to find new physics beyond the standard model.

References

[1] https://twiki.cern.ch/twiki/bin/view/CMSPublic/PhysicsResultsEXO
https://twiki.cern.ch/twiki/bin/view/CMSPublic/PhysicsResultsB2G

https://twiki.cern.ch/twiki/bin/view/CMSPublic/PhysicsResultsSUS
https://twiki.cern.ch/twiki/bin/view/CMSPublic/PhysicsResultsHIG
[2] https://twiki.cern.ch/twiki/bin/view/AtlasPublic/ExoticsPublicResults
https://twiki.cern.ch/twiki/bin/view/AtlasPublic/SupersymmetryPublicResults
https://twiki.cern.ch/twiki/bin/view/AtlasPublic/HiggsPublicResults
[3] CMS Collaboration, arXiv:1412.6302.
[4] ATLAS Collaboration, Phys. Rev. D **90**, no. 5, 052005 (2014) [arXiv:1405.4123].
[5] ATLAS Collaboration, Eur. Phys. J. C **74**, no. 12, 3134 (2014) [arXiv:1407.2410].
[6] CMS Collaboration, JHEP **05**, 108 (2014) [arXiv:1402.2176].
[7] CMS Collaboration, CMS-PAS-B2G-12-009.
[8] ATLAS Collaboration, arXiv:1410.4103.
[9] ATLAS Collaboration, arXiv:1408.0886.
[10] CMS Collaboration, Phys. Lett. B **729**, 149 (2014) [arXiv:1311.7667].
[11] CMS Collaboration, CMS-B2G-14-002.
[12] ATLAS Collaboration, JHEP **11**, 104 (2014) [arXiv:1409.5500].
[13] ATLAS Collaboration, ATLAS-CONF-2013-060.
[14] ATLAS Collaboration, ATLAS-CONF-2013-051.
[15] CMS Collaboration, arXiv:1408.3583.
[16] CMS Collaboration, arXiv:1410.8812.
[17] ATLAS Collaboration, Phys. Rev. Lett. **112**, no. 4, 041802 (2014) [arXiv:1309.4017].
[18] ATLAS Collaboration, Phys. Rev. D **90**, no. 1, 012004 (2014) [arXiv:1404.0051].
[19] ATLAS Collaboration, JHEP **09**, 037 (2014) [arXiv:1407.7494].
[20] CMS Collaboration, arXiv:1408.2745.
[21] CMS Collaboration, arXiv:1410.1149.
[22] ATLAS Collaboration, arXiv:1410.4031.
[23] CMS Collaboration, CMS-PAS-B2G-13-004.
[24] CMS Collaboration, Eur. Phys. J. C **74**, no. 8, 2980 (2014) [arXiv:1404.1344].
[25] ATLAS Collaboration, JHEP **09**, 176 (2014) [arXiv:1405.7875].
[26] CMS Collaboration, JHEP **06**, 055 (2014) [arXiv:1402.4770].
[27] CMS Collaboration, arXiv:1502.00300.
[28] ATLAS Collaboration, JHEP **10**, 24 (2014) [arXiv:1407.0600].
[29] CMS Collaboration, Eur. Phys. J. C **73**, no. 12, 2677 (2013) [arXiv:1308.1586].
[30] CMS Collaboration, CMS-PAS-SUS-13-015.
[31] CMS Collaboration, CMS-PAS-SUS-13-009.
[32] ATLAS Collaboration, JHEP **09**, 015 (2014) [arXiv:1406.1122].
[33] ATLAS Collaboration, JHEP **11**, 118 (2014) [arXiv:1407.0583].
[34] ATLAS Collaboration, JHEP **11**, 094 (2012) [arXiv:1209.4186].
[35] ATLAS Collaboration, Phys. Rev. D **90**, no. 5, 052008 (2014) [arXiv:1407.0608].
[36] ATLAS Collaboration, Eur. Phys. J. C **74**, no. 10, 3109 (2014) [arXiv:1406.5375].
[37] CMS Collaboration, Phys. Lett. B **736**, 371 (2014) [arXiv:1405.3886].
[38] CMS Collaboration, Eur. Phys. J. C **74**, no. 9, 3036 (2014) [arXiv:1405.7570].
[39] ATLAS Collaboration, JHEP **04**, 169 (2014) [arXiv:1402.7029].
[40] ATLAS Collaboration, JHEP **05**, 071 (2014) [arXiv:1403.5294].
[41] ATLAS Collaboration, JHEP **10**, 96 (2014) [arXiv:1407.0350].
[42] ATLAS Collaboration, arXiv:1501.07110.
[43] CMS Collaboration, Phys. Rev. D **90**, no. 9, 092007 (2014) [arXiv:1409.3168].
[44] CMS Collaboration, CMS-PAS-SUS-12-019.
[45] ATLAS Collaboration, ATL-PHYS-PUB-2013-011; ATL-PHYS-PUB-2014-010.
[46] CMS Collaboration, CMS-PAS-FTR-13-014; CMS-PAS-SUS-14-012.

Chapter 2

Quarks and gluons in hadrons, the hadron spectrum

Heavy Flavour Production in ATLAS with a focus on inclusive onia

R. W. L. Jones for the ATLAS Collaboration

Department of Physics, Lancaster University, Lancaster LA1 4YB, UK

DOI: http://dx.doi.org/10.3204/DESY-PROC-2014-04/218

ATLAS has a wide programme to study the production cross section and decay properties of particles with beauty, as well as charmonium and bottomonium states. This paper covers only the ATLAS results in the domain of charmonium production, including J/ψ, $\psi(2S)$ and χ_c states, B^+ production, a brief discussion of the Υ states and updates on the $D^{(*)}$ meson cross-section analysis. The analyses discussed include double-differential production cross-section measurements of the J/ψ, $\psi(2S)$ and P-wave charmonium states χ_{cJ}, extending upon previous measurements in precision and kinematic reach. Prompt and non-prompt modes are distinguished, as well as J/ψ vs $\psi(2S)$ and the contribution to J/ψ production from χ_c feed-down. Alongside the latter analysis, a competitive measurement of the branching fraction $B^{\pm} \to \chi_{c1} K^{\pm}$ was also performed. Results of these measurements are compared with the latest theoretical predictions from a variety of theoretical approaches.

1 Heavy flavour production in ATLAS

The ATLAS experiment at the Large Hadron Collider has copious heavy flavour production in pp collisions. It has the advantage of very high integrated luminosities, but largely relies on multi-muon triggers to select heavy flavour events. This paper will concentrate on the production of b and c hadrons in jets and has a focus on onium production. The two key sub-detector systems for the measurements here presented are the inner tracker immersed in a 2T solenoidal field, which has a coverage out to $|\eta| < 2.5$, and the muon system with coverage $|\eta| < 2.7$. The resultant tracking has a p_T resolution $\sim 0.05\% p_T(\text{GeV}) \oplus 1.5\%$ and $\sim 10 \mu m$ impact parameter resolution, which are important for the mass and lifetime resolutions in the analyses.

2 Open charm production

ATLAS has published results on $D^{*\pm}$ and D^0 production in jets [1]. It was found that neither leading order nor p_T and angular-ordered models give a good description of the momentum fraction carried but the charmed hadrons in jets, especially at low values of the fraction. A subsequent study of the $D^{*\pm}$, $D^{\pm}$ and D^0 differential cross sections as a function of the η and p_T of the charmed hadron show that these are described within the large uncertainty bands by models based on perturbative QCD [2].

3 Beauty hadron production

D^* mesons can be combined with muons as a signature of beauty hadron production in jets. ATLAS has used this technique to extract the single differential cross-sections for beauty hadrons in terms of the p_T and η of the hadron [3]. The results show that Next to Leading Order (NLO) models tend to underestimate the observed rates, despite the shapes of the distributions being reasonably reproduced by the several Monte Carlo models.

The production of B^+ hadrons has been studied using the decay to $J/\psi(\mu\mu)K^+$, where the double differential cross-sections in terms of p_T and rapidity y have been obtained [4]. The predictions from Monte Carlo and Fixed Order Next-to-Leading-Logarithm (FONNL) models [5] agree reasonably with the data, but again have a tendency to underestimate the cross-section.

4 Onium production

4.1 Prompt and non-prompt J/ψ production

ATLAS has made extensive studies of the production of heavy onia, using the production of dimuons in their decays to trigger the events. The J/ψ provides the template for the analyses [6]; the prompt and non-prompt components are separated using the pseudo-proper time of the decay candidates. The studies are in principle complicated by the different spin alignments possible, although recent CMS studies have indicated that there is little polarisation in the J/ψ production.

The production of prompt J/ψ agrees between the four main LHC experiments, though with some differences in the rapidity dependence. A multitude of models: Colour Singlet (CS); Colour Evaporation (CE); Colour Octet (CO), in various forms give a reasonable description of the observed ATLAS data, but none are perfect. It is clear that p_T spectra alone cannot distinguish between the models. (Please see the references in the ATLAS paper for the detailed models compared to the data.)

The fraction of non-prompt J/ψs is below 10% at low p_T and central rapidity, but rises with p_T to $\sim 70\%$; however, this increase is slower for forward rapidities. There is little evidence of an energy dependence in the behaviour, and comparing with CDF data, even the underlying process can have little effect. The non-prompt production with respect to p_T and rapidity is well described by perturbative QCD FONLL models with no free parameters.

4.2 Prompt and non-prompt $\psi(2S)$ production

A recent ATLAS study of the production of $\psi(2S)$ mesons has been published [7]. This study has many similarities with that of the J/ψ, except that instead of using the lower purity $\psi(2S) \to \mu\mu$ decays, the more copious $\psi(2S) \to J\psi(\mu\mu)\pi\pi$ mode is used instead. Again the prompt and non-prompt components are studied, the non-prompt fraction still rising to $\sim 70\%$ but less at high rapidity, see Figure 1. There is negligible feed-down to the $\psi(2S)$ from heavier states. ATLAS has extended the kinematic range of the studies of the prompt and non-prompt production as a function of p_T and rapidity; in the regions of overlap with studies by other LHC experiments, the agreement is good. For the prompt production, NLO combined with Non Relativistic QCD (NRQCD) predictions describe the data well across the range. However, Next-to-Next-to-Leading Order (NNLO) colour singlet models undershoot the data at higher p_T values, and k_T factorisation models undershoot the data for all values of p_T and rapidity.

The non-prompt production reveals a softer p_T spectrum and less variation with p_T than the NLO and FONLL approximation predictions. For the details of the all the predictions used for comparison, please see the references in [7].

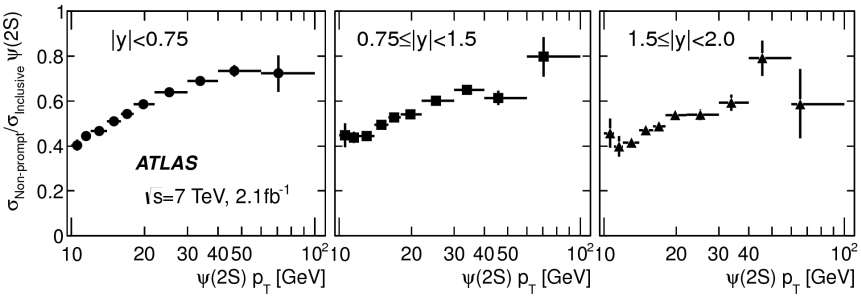

Figure 1: The non-prompt fraction with respect to the p_T of the $\psi(2S)$ for three regions of rapidity.

4.3 Prompt and non-prompt $\chi_{c1,2}$ production

ATLAS has recently studied the production of the $\chi_{c1,2}$ by reconstructing their de-excitation decays to $J/\psi\gamma$ [8]. The production differential cross-sections have been measured for both states in terms of the p_T of the χ_c and of the J/ψ. The prompt production for both states and p_T definitions is well predicted by NLO NRQCD models [9] . However, the non-prompt production shows a tendency to fall below the FONNL prediction at higher p_T. The relative production of χ_{c1} to χ_{c2} has been studied, and, under the assumption of isotropic decay, the measurements agree with NLO NRQCD predictions, though less so at higher p_T, see Figure 2. The figure also shows the fraction of prompt J/ψ produced from χ_c radiative decays, which again agrees with the NLO NRQCD predictions within the uncertainties. The relative fraction of non-prompt production shows that the production of the $\chi_{c1,2}$ is mostly prompt, even at high p_t, in contrast to the J/ψ and $\psi(2S)$ cases. Finally, ATLAS has also extracted a branching

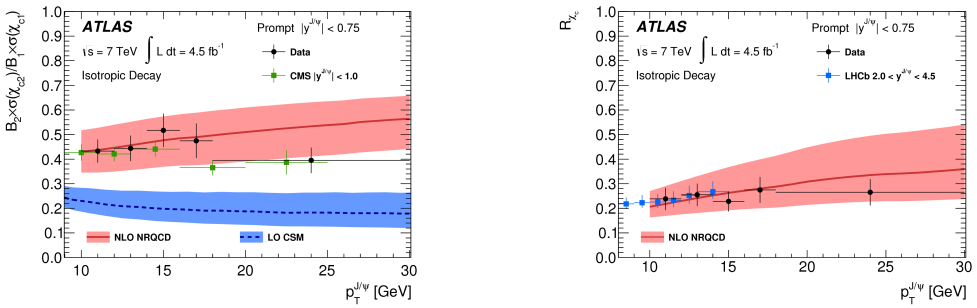

Figure 2: The relative production of prompt χ_{c1} and χ_{c2} with respect to the p_T of the J/ψ (left) and fraction of J/ψ produced from χ_c radiative decays (right).

fraction $B(B^+ \to \chi_{c1}K^+) = 4.9 \pm 0.9\,stat. \pm 0.6\,sys. \times 10^{-4}$; this is both in agreement with and

a significant improvement on measurements at previous hadron collider experiments, and is in agreement with existing B-factory measurements, thus showing good prospects for improved precision in Run 2.

4.4 The $\Upsilon(1S), \Upsilon(2S)$ and $\Upsilon(3S)$ production

Finally, ATLAS has produced double-differential cross-sections for $\Upsilon(1,2,3S)$ states[10], extending the available p_T range and providing finer detail than previous measurements from CMS and LHC. The measurements agree well with the previous measurements in the regions of overlap. Colour Singlet, Octet and Evaporation models all agree reasonably with the measured p_T spectra. The ratios of $\Upsilon(2S)/\Upsilon(1S)$ and $\Upsilon(3S)/\Upsilon(1S)$ production are dependent on the p_T of the upsilon, see Figure 3, confirming the existence of multiple mechanisms.

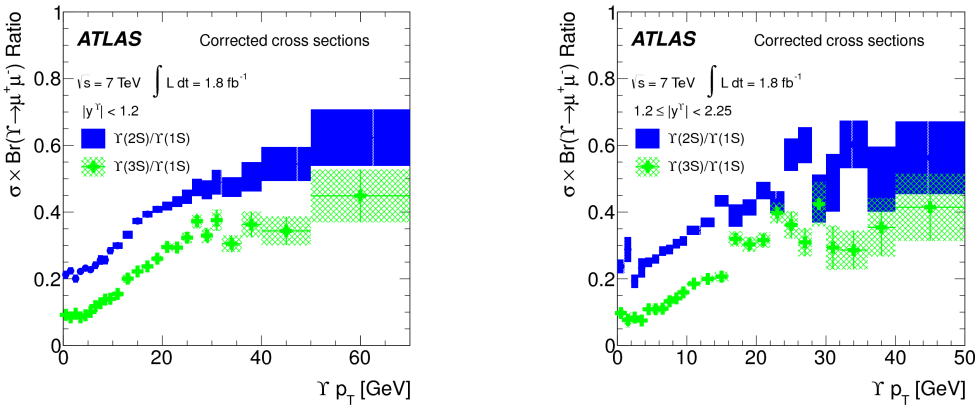

Figure 3: The relative production of prompt $\Upsilon 2S$ to $\Upsilon 1S$ and $\Upsilon 3S$ to $\Upsilon 1S$ with respect to the p_T of the Υ in the central (left) and forward (right) regions.

References

[1] ATLAS Collaboration, Phys. Rev. **D85** 052005 (2011).

[2] ATLAS Collaboration, ATLAS-CONF-2011-017 (2011); ATLAS-PUB-2011-012 (2011).

[3] ATLAS Collaboration, Nucl. Phys. **B864** 341 (2012).

[4] ATLAS Collaboration, JHEP **10** 042 (2013).

[5] M. Cacciari *et al.*, JHEP **10** 137 (2012);
M. Cacciari, M. Greco and P. Nason, JHEP **05** 007 (1998) .

[6] ATLAS Collaboration, Nucl. Phys. **B850** 387 (2011).

[7] ATLAS Collaboration, JHEP **1409** 79 (2014).

[8] ATLAS Collaboration, JHEP **1407** 154 (2014).

[9] Y.-Q. Ma, K. Wang and K.-T. Chao, Phys. Rev. **D 83** 111503 (2011);
H.-S. Shao, Comput. Phys. Commun. **184** 2562 (2013);
Y.-Q. Ma, K. Wang and K.-T. Chao, Phys. Rev. Lett. **106** 042002 (2011).

[10] ATLAS Collaboration, Phys. Rev **D87** 052004 (2013).

Medium-heavy Nuclei from Lattice Quantum Chromodynamics

Takashi Inoue[1] for the HAL QCD Collaboration

[1] Nihon University, College of Bioresource Sciences, Kanagawa 252-0880, Japan

DOI: http://dx.doi.org/10.3204/DESY-PROC-2014-04/26

Mass and structure of ^{16}O and ^{40}Ca are deduced from the quantum chromodynamics (QCD), the fundamental theory of the strong interaction. We derive two-nucleon potentials in lattice QCD simulations by the HAL QCD method. Then we apply the potentials to the nuclei using the Brueckner-Hartree-Fock theory. We find that these two nuclei are bound and possess shell structures, for a heavy quark mass corresponding to a pseudo-scalar meson mass of 469 MeV (a nucleon mass of 1161 MeV). Obtained total binding energies, 35 MeV for ^{16}O and 113 MeV for ^{40}Ca, are rather smaller than the experimental data indeed, but it is due to the unrealistic quark mass in our lattice QCD simulations.

1 Introduction

It is established that QCD is the fundamental theory of the strong interaction. However, explaining properties of nuclei starting from QCD still remains one of the most challenging problem in physics. There are several attempts to obtain mass of nuclei from lattice QCD simulations at heavy quark masses [1, 2], but direct calculations are limited only to very light nuclei, *i.e.* mass number $A \leq 4$, due to computation costs and, more severely, due to several fundamental difficulties. In this paper, we employ an alternative approach to study mass and structure of medium heavy nuclei starting from QCD.

The HAL QCD method was proposed to extract the nucleon-nucleon interaction from lattice QCD [3]. In this method, a non-local but energy independent potential of the interaction is defined and determined through the Nambu-Bethe-Salpeter wave function of the system which can be measured in lattice QCD numerical simulations. This method has been developed further and applied to many other systems [4]. The HAL QCD approach has several advantages over the direct calculations for multi-hadron system. First of all, this method does not require the ground-state saturation, which is unavoidable in the direct calculation but is usually very difficult or even impossible to achieve for multi-baryon systems, in particular on a large spacial-volume. Secondly, this method does not require the infinite-volume extrapolation, since the potential is insensitive to the lattice volume, as long as the spatial extension is larger than the interaction range between hadrons. On top of these advantages, there is one significant advantage, namely, one can extract many physical observables in this approach. For example, solving the two-body Schrödinger equation with the potential, one can obtain scattering phase-shifts as a function of energy as well as the scattering length. Moreover, combining the lattice QCD potentials with sophisticated many-body theories, one can study nuclei or even nucleon

matters based on QCD [5]. In this paper, we investigate ^{16}O and ^{40}Ca nuclei starting from QCD for the first time in history.

2 Method

There are several methods to investigate nuclei based on a free-space nucleon-nucleon interaction. The Green's function Monte Carlo method and the no-core shell model are successfully applied to nuclei around ^{12}C, but exact application to nuclei with $A > 14$ seems difficult at this moment. To study larger A nuclei, the Hartree-Fock mean field approximation has been applied traditionally. Since the Brueckner theory explains the independent particle nature of nuclei, which is a foundation of the mean field theory and shell models, the Brueckner-Hartree-Fock (BHF) theory became a standard framework for heavy nuclei [6]. In this paper, we adopt the lowest order BHF theory for our first study of medium heavy nuclei from QCD.

To study finite nuclei in the BHF theory, G matrix in a single-particle-orbit basis is needed and obtained by solving the integral Bethe-Goldstone equation

$$G(\omega)_{ij,kl} = V_{ij,kl} + \frac{1}{2}\sum_{m,n}^{>e_F} \frac{V_{ij,mn}\, G(\omega)_{mn,kl}}{\omega - e_m - e_n + i\epsilon} \tag{1}$$

where indices i to n stands for a single-particle energy-eigenstate and V is the two-nucleon interaction potential and the sum runs over excluding occupied states of the nucleus. With G matrix, single-particle potential U is given by $U_{ab} = \sum_{c,d} G(\tilde{\omega})_{ac,bd}\ \rho_{dc}$, where indices a, b, c, d corresponds to a basis-function for which we use a harmonic-oscillator wave function, and ρ is the density matrix in this basis, which is given with the wave function of energy-eigenstate Ψ^i by $\rho_{ab} = \sum_i^{occ} \Psi_a^i \Psi_b^{i*}$, where the sum runs over occupied states of the nucleus. While, the energy-eigenstates are given by solution of the Hartree-Fock equation $[K + U]\,\Psi^i = e_i \Psi^i$ with the potential U and the kinetic energy operator K. These equations are highly coupled, and self-consistent G, U, ρ, Ψ^i and e_i are determined in the iterative procedure. Finally, the Hartree-Fock ground state energy of the nucleus is given with the self-consistent U and ρ by,

$$E_0 = \sum_{a,b} \left[K_{ab} + \frac{1}{2} U_{ab} \right] \rho_{ba} - K_{\rm cm} \tag{2}$$

where $K_{\rm cm}$ is the kinetic energy of the spurious center-of-mass motion in the potential rest flame which is included in the first term.

The two-nucleon potential which we adopt at eq.(1) is the one which we derived from lattice QCD in ref. [5]. There, dynamical lattice QCD simulations ware carried out at five degenerated u, d, s-quark masses. Measured hadron masses $\{M_{\rm PS}\ ,\ M_{\rm B}\}$ ranges from $\{1171, 2274\}$ MeV to $\{469, 1161\}$ MeV, where PS and B abbreviate the pseudo-scalar meson and the octet baryon, respectively. Extracted two-nucleon potentials in $^1S_0$, $^3S_1$ and $^3D_1$ channels, share common features with phenomenological ones, *i.e.* the strong repulsive core at short distance, the attractive pocket at intermediate distance, and the strong $^3S_1$-$^3D_1$ coupling, and accordingly, reproduce experimental phase-shifts qualitatively [5]. In this paper, we include two-nucleon interaction in these three channels and omit that in higher partial waves due to a lack of lattice QCD data. We ignore the Coulomb force between protons for simplicity. For details of numerical procedure of BHF calculation, we follow ref. [7].

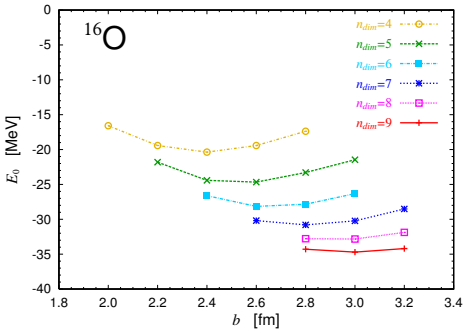

Figure 1: Ground state energy of ^{16}O at a quark mass of $M_{\rm PS} \simeq 469$ MeV

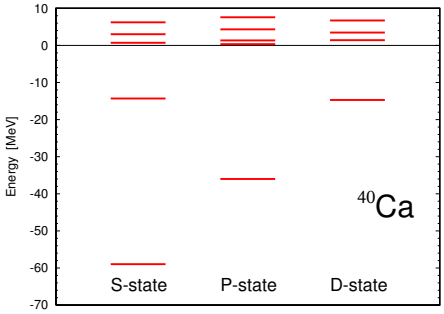

Figure 2: Single particle levels in the ^{40}Ca at a quark mass of $M_{\rm PS} \simeq 469$ MeV.

3 Results and discussion

Figure 1 shows obtained ground state energy of ^{16}O at the lightest quark mass corresponding to $M_{\rm PS} \simeq 469$ MeV, as a function of parameter b and number n_{dim} of the harmonic-oscillator wave function used as basis. We obtain a similar figure for ^{40}Ca at this quark mass. Consequently, we confirm that there are bound nuclei at this quark mass. While, we do not obtain any negative E_0 for both ^{16}O and ^{40}Ca at the other four quark masses, which at least exclude existence of tightly bound nucleus at these quark masses. In the following, we therefore consider only the lightest quark mass case, where pion mass is 469 MeV and nucleon mass is 1161 MeV. Since a computation of ^{40}Ca with $n_{dim} = 10$ is already tough on PC, we adopt $b = 3.0$ fm and $n_{dim} = 9$ for both ^{16}O and ^{40}Ca, according to the figure. Figure 2 shows obtained single particle levels of ^{40}Ca, where we can see a regular shell structure. These levels are already in good agreement with experimental data, but it could be accidental since quark masses are different.

Table 1 shows mass and structure of ^{16}O and ^{40}Ca nuclei obtained at the lightest quark, where single particle levels, total energy, and mean radius are given. Experimental data of the total energies are -127.62 MeV for ^{16}O and -342.05 MeV for ^{40}Ca. We see that the obtained binding energies are rather smaller than the experimental ones, but this is principally due to the large u, d-quark mass in our calculation. The root-mean-square radii are calculated without taking nucleon form factor and correction for the center-of-mass motion. Contrary to large discrepancies of E_0 from experimental data, these radii are more of less similar to experimental charge radius, 2.73 fm for ^{16}O and 3.48 fm for ^{40}Ca, probably due to an accidental cancellation between contributions from weaker attraction of the nuclear force and heavier nucleon mass than experimental values in this study.

In our previous papers [5], we studied the ^{4}He nucleus and the symmetric nuclear matter (SNM) from lattice QCD. We obtained energy per particle E_0/A as -1.3 MeV for ^{4}He and -5.4 MeV for SNM at the same lightest quark mass. We can see in Table 1 that the present E_0/A of ^{16}O and ^{40}Ca lie between these two values, which means that obtained E_0 are consistent with the previous results and reasonable for the nuclei at the quark mass. Moreover, in the real world, it is known that binding energy of nuclei are well described by the semi-empirical Bethe-Weizsäcker formula $E_0(A) = a_V A + a_S A^{2/3} + \cdots$. We find that E_0/A obtained from QCD at the quark mass are well described by the formula with $a_V = -5.46$ MeV and $a_S = 6.56$ MeV, when $E_0(n_{dim})$ of ^{16}O and ^{40}Ca are extrapolated for $n_{dim} \to \infty$ with $E_0(n_{dim}) = E_0(\infty) + c/n_{dim}$.

	Single particle level [MeV]				Total energy [MeV]		Radius [fm]
	$1S$	$1P$	$2S$	$1D$	E_0	E_0/A	$\sqrt{\langle r^2 \rangle}$
^{16}O	-35.8	-13.8			-34.7	-2.17	2.35
^{40}Ca	-59.0	-36.0	-14.7	-14.3	-112.7	-2.82	2.78

Table 1: Mass and structure of ^{16}O and ^{40}Ca nuclei obtained from QCD at a quark mass corresponding to pseudo-scalar meson mass of 469 MeV and octet baryon mass of 1161 MeV. Single particle levels, total energy, and root-mean-square radius are listed.

In this paper, we've obtained mass and structure of ^{16}O and ^{40}Ca nuclei from QCD at a heavy quark mass for the first time in history. This success is certainly a significant progress in theoretical nuclear physics, and demonstrates that the HAL QCD approach is quite promising.

In this study, we neglected P, F and higher partial-wave nuclear forces, in particular the LS force. It is known that the LS force is important for structures of nuclei, such as the magic number, especially at the region of heavy nuclei $A > 40$. We will include in our next study the LS force recently extracted in lattice QCD [8]. It is also known that three-nucleon force is necessary for quantitative explanation of mass and structure of nuclei. Study toward three-nucleon force from QCD is in progress [9]. Masses of u, d-quark in this study are much heavies than physical values, but this limitation will be removed in a few years, as lattice QCD simulations at the physical quark mass are currently underway on the K-computer at RIKEN AICS in Japan. Nuclear force obtained in such simulations by the HAL QCD approach will open a new connection between QCD and nuclear physics.

Acknowledgments

This research is supported in part by Grant-in-Aid of MEXT-Japan for Scientific Research (C) 23540321. Author thank ILDG/JLDG for providing storage to save our lattice QCD data.

References

[1] T. Yamazaki *et al.* [PACS-CS Coll.], Phys. Rev. D **81**, 111504 (2010); T. Yamazaki, K. Ishikawa, Y. Kuramashi and A. Ukawa, Phys. Rev. D **86**, 074514 (2012).

[2] S. R. Beane *et al.* [NPLQCD Coll.], Phys. Rev. D **85**, 054511 (2012); S. R. Beane, *et al.* [NPLQCD Coll.], Phys. Rev. D **87**, no. 3, 034506 (2013); W. Detmold and K. Orginos, Phys. Rev. D **87**, no. 11, 114512 (2013)

[3] N. Ishii, S. Aoki and T. Hatsuda, Phys. Rev. Lett. **99**, 022001 (2007); S. Aoki, T. Hatsuda and N. Ishii, Prog. Theor. Phys. **123**, 89 (2010); N. Ishii *et al.* [HAL QCD Coll.], Phys. Lett. B **712** (2012) 437.

[4] H. Nemura, N. Ishii, S. Aoki and T. Hatsuda, Phys. Lett. B **673**, 136 (2009); Y. Ikeda *et al.* [HAL QCD Coll.], EPJ Web Conf. **3**, 03007 (2010); K. Sasaki *at al.* [HAL QCD Coll.], Nucl. Phys. A **914**, 231 (2013).

[5] T. Inoue *et al.* [HAL QCD Coll.], Phys. Rev. Lett. **106**, 162002 (2011); T. Inoue *et al.* [HAL QCD Coll.], Nucl. Phys. A **881**, 28 (2012); T. Inoue *et al.* [HAL QCD Coll.], Phys. Rev. Lett. **111**, 112503 (2013).

[6] P. Ring and P. Schuck, *The Nuclear Many-Body Problem*, (Springer, 1980). G.E. Brown, T.T.S. Kuo, *et al.*, *The Nucleon-Nucleon Interaction And The Nuclear Many-Body Problem*, (World Scientific, 2010).

[7] K. T. R. Davies, M. Baranger, R. M. Tarbutton and T. T. S. Kuo Phys. Rev. **177**, 1519 (1969); P. U. Sauer, Nucl. Phys. A **150**, 467 (1970).

[8] K. Murano *et al.* [HAL QCD Coll.], Phys. Lett. B **735**, 19 (2014).

[9] T. Doi *et al.* [HAL QCD Coll.], Prog. Theor. Phys. **127**, 723 (2012).

Diquark and Baryon Masses in Composite Fermion Approach

A. Bhattacharya[1], *R.Ghosh*[1], *B.Chakrabarti*[2]

[1]Department of Physics, Jadavpur University,Calcutta 700032, India.
[2] Jogamaya Devi College, Kolkata, India.

DOI: http://dx.doi.org/10.3204/DESY-PROC-2014-04/128

A model for diquark has been suggested describing it as a Composite Fermion. The masses of the light [Λ^0, Σ^-, Ξ^-, Ω^-], heavy [Λ_c^+, Σ_c^+, Ξ_c^0, Ω_c^- and Λ_b^0, Σ_b^0, Ξ_b^0, Ω_b^-], doubly heavy [Ξ_{cc}^{++}, Ξ_{cc}^+, Ξ_{cb}^+, Ξ_{cb}^0, Ξ_{bb}^0, Ξ_{bb}^-, Ω_{cc}^+, Ω_{cb}^0, Ω_{bb}^-] and triply heavy [Ω_{ccc}, Ω_{ccb}, Ω_{bbc}, Ω_{bbb}] baryons have been studied for $J^P = \frac{1}{2}^+$ and $\frac{3}{2}^+$ states. The results are found to be in good agreement with available experimental data and other theoretical works.

1 Diquark and Baryon Masses in Composite Fermion Approach

At low energies the quark dynamics can be revisited in the light of new results of baryon and exotics spectroscopy. The regularities in hadons spectroscopy, parton distribution function, spin dependent structure function of hadrons etc hint at the existence of diquark correlation. In QCD both the gluon exchange interaction and Instanton Induced Interaction favour the spin singlet and colour anti-symmetric diquark combination. A deeply bound diquark system is one of the most important candidate for describing the baryonic and exotic system. The exact nature of the diquark correlation is under extensive study. In the present work diquarks have been described in the frame work of Composite Fermion (CF) model of quasi particle in an analogy with the electrons in strong magnetic field. The masses of the light, single heavy, doubly heavy and triply heavy baryons have been studied for $J^P = \frac{1}{2}^+$ and $\frac{3}{2}^+$ states considering the diquark-quark configuration with the suggested CF model of diquark. It has been suggested that the CFs can be described in gauge invariant way in the system of gauge interaction like the two dimensional electron gas in high magnetic field where electrons can be described as Composite Fermions [1]. This in turn may form Fermi liquid like state near the Fermi surface. CFs can have fractional charges and their spin is frozen. Such CFs are described as the stable quasi particles in the system. In the context of degenerate electron gas Raghavchari et al [2] have studied the quasi particle mass which is fully gauge invariant and can be expressed as a response function of the system. It has been observed that the strongly interacting particles sometimes behave like weekly coupled system and form a system of particles of new kind. The quasi particle behaviour of electron in a crystal is an example of such system. The electron in the lattice changes in behaviour and exists as an independent object. In the present work we have applied the idea of CF model describing a diquark as a composite fermion and have computed the masses of diquarks considering Fermi momentum (p_f) as cut off parameter.

Starting from the Hamiltonian of a CF with a momentum cut off λ the expression for the quasi particle mass in gauge invariant system can be obtained as [2] (with potential V=0):

$$\frac{1}{m^*} = \frac{1}{m}(1 + \frac{\Lambda^4}{2p_F^4}) \tag{1}$$

where m^* is the effective mass of the CF, m be the mass of each component, (p_f) is the Fermi momentum of CF and Λ is the cut off parameter. We have applied this CF picture for diquarks and computed the effective mass of diquarks. The Fermi momentum of corresponding diquarks have been estimated using the work of Bhattacharya et al [3, 4]. Considering baryon as a system of a quark and a diquark, under the influence of suitable binding energy and spin interaction the mass of heavy or light baryons can be expressed as :

$$M_B = m_q + m_D^* + E_{BE} + E_S \tag{2}$$

where m_q is quark mass, m_D^* is the diquark mass and E_{BE} is the binding energy of the quark-diquark corresponding to the potential expressed as V(r)= ar^2, where 'a' is the interaction parameter and 'r' is the baryon radius. We have used the wave function from the Statistical Model [3, 4] and the spin interaction term is expressed as :

$$E_S = \frac{8}{9}\frac{\alpha_S}{m_q m_D}\vec{S}_q \cdot \vec{S}_D|\psi(0)|^2 \tag{3}$$

where the symbols have their usual meanings. The masses of the respective baryons have been estimated by using the relation (2) and displayed in Tables 1 to 5. We have obtained very good results for Λ^0,but higher results for Σ^- and lower values for Ξ^- and Ω^-. For Σ_c^+, Λ_b^0 and Ω_c^- there is a very good agreement between our results and experimentalfindings [5, 6]. For Ξ_{cc}^{++} our proposed mass [3.5308 GeV for $J^P = \frac{1}{2}^+$] agrees reasonably with experimental value 3.5189 ± 0.0009 GeV. For doubly heavy and triply heavy Ω sectors the results have been compared with other theoretical works and there is a reasonable agreement. However it may be pointed out that the most uncertainty comes from the radii parameters which is not exactly known.

CF model is found to be quiet successful in reproducing the masses of the baryons over a wide range. Diquark in presence of chromo magnetic QCD vacuum may behave like a CF as an electron in strong magnetic field. The diquark as CF may throw some light on the understanding of structure and dynamics of the baryons.

Baryon	*Baryon* $Our-work$ $J^p=\frac{1}{2}^+$	$mass(GeV)$ $Expt.$[5, 6] $J^p=\frac{1}{2}^+$	*Baryon* $Our-work$ $J^p=\frac{3}{2}^+$	$mass(GeV)$ $Expt.$[5, 6] $J^p=\frac{3}{2}^+$
$\bigwedge^0$	1.1188	1.1156	1.3086	–
Σ^-	1.3295	1.1974	1.449	1.387
Ξ^-	1.2137	1.3217	1.3948	1.535
Ω^-	1.551	–	1.5200	1.672

Table 1: Mass Spectrum ($J^p=\frac{1}{2}^+$ and $\frac{3}{2}^+$) of Light baryons

$Baryon$	$Baryon$	$mass(GeV)$	$Baryon$	$mass(GeV)$
	$Our-work$	$Expt.$[5, 6]	$Our-work$	$Expt.$[5, 6]
	$J^p=\frac{1}{2}^+$	$J^p=\frac{1}{2}^+$	$J^p=\frac{3}{2}^+$	$J^p=\frac{3}{2}^+$
$\bigwedge_c^+$	2.9377	2.2864 ± 0.00014	3.04477	–
$\bigwedge_b^0$	5.5891	5.6202 ± 0.0016	5.7168	–
Σ_c^+	2.4577	2.4529 ± 0.0004	2.5690	2.518
Σ_b^0	5.5751	5.808	5.7169	5.829
Ξ_c^0	2.2687	$2.4708^{+0.00034}_{-0.0008}$	2.4464	2.646
Ξ_b^0	5.5069	5.7924 ± 0.003	5.7201	–
Ω_c^0	2.6724	2.6952 ± 0.0017	2.63122	2.768
Ω_b^-	5.9631	6.165 ± 0.023	5.9176	–

Table 2: Mass Spectrum ($J^p=\frac{1}{2}^+$ and $\frac{3}{2}^+$) of Heavy baryons

$Baryon$	$Baryon$	$mass$	(GeV)	$Baryon$	$mass$	(GeV)
	for	$J^p=$	$\frac{1}{2}^+$	for	$J^p=$	$\frac{3}{2}^+$
	$Ours$	$Expt.$[5, 6]	$Others$	$Ours$	$Expt.$	$Others$
Ξ_{cc}^{++}	3.9496	–	3.579	3.9807	–	3.708
			3.730			3.800
			3.480			3.610
Ξ_{cc}^+	3.5308	3.5189	3.584	3.6222	–	3.713
		± 0.0009	3.755			3.828
			3.480			3.610
Ξ_{cb}^0	6.9065	–	6.95	6.9205	–	7.02
			7.01			7.10
Ξ_{cb}^+	7.2534	–	6.965	7.2569	–	7.06
			± 0.09			± 0.09
Ξ_{bb}^0	10.6764	–	10.339	10.6873	–	10.468
			10.114			10.165
			10.093			10.330
Ξ_{bb}^-	10.5389	–	10.23	10.551	–	10.28
			10.344			10.473
			10.30			10.34

Table 3: Mass Spectrum ($J^p=\frac{1}{2}^+$ and $\frac{3}{2}^+$) of the Doubly Heavy Ξ baryon

$Baryon$	$Baryon$	$mass(GeV)$	$Baryon$	$mass(GeV)$
	$Our-work$	$Other-works$	$Our-work$	$Other-works$
	$J^p=\frac{1}{2}^+$	$J^p=\frac{1}{2}^+$	$J^p=\frac{3}{2}^+$	$J^p=\frac{3}{2}^+$
Ω_{cc}^+	3.6843	3.74 ± 0.07	3.8590	3.82 ± 0.08
		3.76		3.89
		3.718		3.847
Ω_{cb}^0	7.0225	7.045 ± 0.09	7.0769	7.12 ± 0.09
		7.05		7.11
		7.05		7.13
Ω_{bb}^-	10.6455	10.37 ± 0.1	10.6581	10.40 ± 0.1
		10.32		10.36
		10.34		10.38

Table 4: Mass Spectrum ($J^p=\frac{1}{2}^+$ and $\frac{3}{2}^+$) of the Doubly Heavy Ω baryon

$Baryon$	$Baryon$	$mass(GeV)$	$Baryon$	$mass(GeV)$
	$Our-work$	$Other-works$	$Our-work$	$Other-work$
	$J^p=\frac{1}{2}^+$	$J^p=\frac{1}{2}^+$	$J^p=\frac{3}{2}^+$	$J^p=\frac{3}{2}^+$
Ω_{ccc}	4.8508	–	$4,8916$	4.803
		–		4.925
		–		4.9(0.25)
Ω_{ccb}	8.355	8.229	8.3575	8.358
		8.018		8.025
		–		8.200
Ω_{bbc}	11.695	11.280	11.6974	11.287
		–		11.48
		11.609		11.738
Ω_{bbb}	15.0329	–	15.0449	15.118
		–		14.760
		–		14.7(0.3)

Table 5: Mass Spectrum ($J^p=\frac{1}{2}^+$ and $\frac{3}{2}^+$) of the Triply Heavy baryons

Acknowledgements

Authors are thankful to University Grant Commission, Govt. of INDIA for financial support.

References

[1] B.I.Helperin et al., Phys.Rev. **B47** 7312 (1993).

[2] A. Raghavchari et al., arXiv:cond.matt./9707055.

[3] A.Bhattacharya et al., Int. J. Mod. Phys. **A 15** 2053 (2003).

[4] A. Bhattacharya et al.,Eur. Phys. J. **C 2** 671 (1998).

[5] J. Beringer et al (PDG) Phys. Rev. **D 86** 010001 (2012).

[6] K. Nakamura et al (PDG)"Review of Particle Physics" Journal of Physics **G 37**(7A): 075021 (2010).

Polarised Drell-Yan measurement in the COMPASS experiment at CERN

Márcia Quaresma[1] for the COMPASS Collaboration

[1]LIP - Laboratório de Instrumentação e Física Experimental de Partículas, Av. Elias Garcia 14-1, 1000-149 Lisboa, Portugal, marcia@lip.pt

DOI: http://dx.doi.org/10.3204/DESY-PROC-2014-04/117

The COMPASS experiment at CERN has been contributing to the description of the nucleon spin structure, namely the transverse momentum dependent parton distribution functions (TMDs), through the Semi-Inclusive Deep Inelastic Scattering (SIDIS) using a muon beam impinging on polarised targets. These TMD functions are also accessible via the transversely polarised Drell-Yan (DY) process, which will be studied in the next COMPASS data taking, starting this Autumn. This process, in which the proton valence region will be explored, will be studied in collisions of a 190 GeV/c negative pion beam with a transversely polarised ammonia target. The QCD prediction that Sivers TMD change sign when accessed through SIDIS or via DY will be checked by the new COMPASS measurement. Considering one year of data taking, the Sivers azimuthal asymmetry statistical error is expected to be less than 2%. In addition to the polarised target, other nuclear targets will give the possibility to study unpolarised DY subjects. The experimental setup will be presented, and predictions and expectations will be discussed.

1 Introduction

The nucleon structure in leading order QCD, taking into account the quarks intrinsic transverse momentum, is described by 8 PDFs for each quark flavour. These so called TMD PDFs are accessible via either the single transversely polarised Drell-Yan measurement or the transversely polarised Semi-Inclusive DIS. The latter has been already measured in COMPASS and published [1]. The DY cross-section is written in terms of angular modulations, each containing a convolution of two PDFs, whereas in the SIDIS cross-section the amplitude of each modulation contains the convolution of one PDF and one fragmentation function. Because of that, DY is considered an excellent tool to access TMD PFDs. In addition, the TMD PDFs are expected to be sizeable in the valence quark region, being this region dominant in the foreseen COMPASS DY measurement regarding the use of a negative pion beam impinging on an ammonia target. Furthermore, the QCD TMD approach is valid in the region Q ($M_{\mu\mu} > 4$ GeV/c^2) $\gg \langle p_T \rangle \sim$ 1 GeV/c, which is also dominate in the COMPASS DY measurement.

The amplitudes present in the DY cross-section are accessed via the measurement of the azimuthal asymmetries between the two oppositely transversely polarised target cells. Each asymmetry contains the convolution of two TMD PDFs, giving access to Sivers, Boer-Mulders, transversity and pretzelosity functions.

The Sivers measurement is the main goal of the first polarised DY data. Theory predicts its sign should change when accessed through DY or SIDIS processes [2]. This is considered a crucial test of the QCD TMD approach. Figure 1 shows the phase space coverage of the two processes in COMPASS. The SIDIS result was extracted from the 2010 data and the DY from a MC simulation. The statistical error selecting just the overlap between the two measurements, i.e. with $Q^2 > 16$ GeV/c, is $\sim 1\%$ for both.

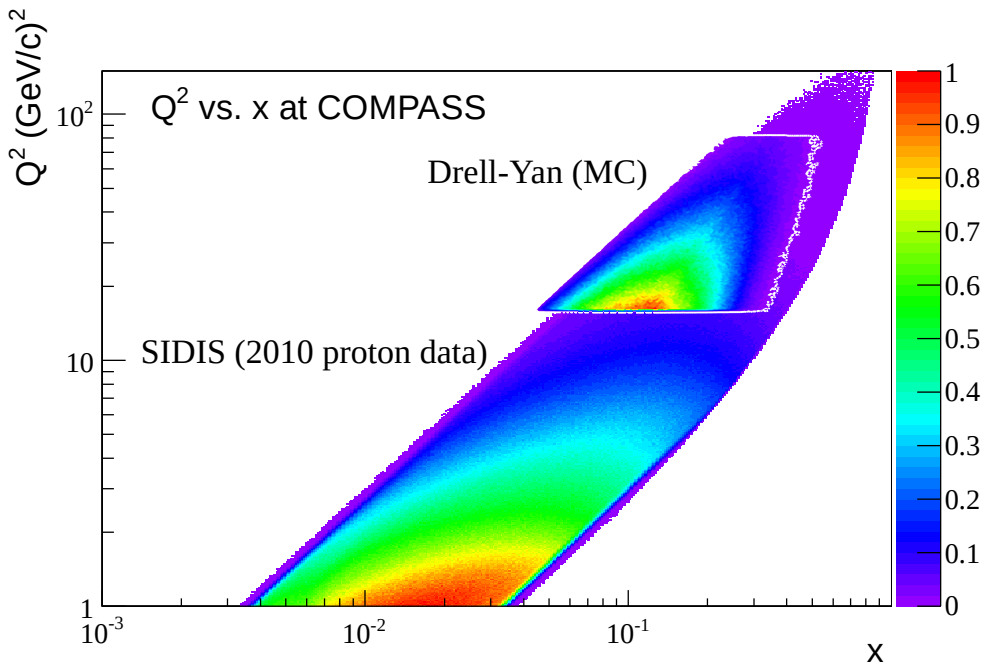

Figure 1: Q^2 versus x phase space coverage at COMPASS. Superposition of the SIDIS 2010 proton data with the DY MC simulation.

In addition to the azimuthal asymmetries measurements, several studies beyond the polarised DY measurement are possible, including the study of the flavour dependent EMC effect [3]. This will be possible by the use of nuclear targets in addition to the polarised ammonia target.

2 Experimental setup and feasibility of the experiment

COMPASS is a CERN experiment located at the end of the SPS M2 beam line. It is a fixed target experiment that consists in a two stage spectrometer giving the possibility to measure a wide angular and momentum range. The spectrometer is equiped with several tracking detectors, one hadron and one electromagnetic calorimeter in each spectrometer stage, two dedicated stations to identify muons and hodoscopes to perform the trigger. A complete description can be found in [4]. For the DY measurement, there is a hadron absorber with a beam plug in its central part, just downstream of the target, to stop the hadrons and the non-interacting beam.

The DY muons will suffer multiple scattering when crossing the absorber and this is responsible for a resolution degradation. Thus a scintillating fibre vertex detector is placed at the beginning of the absorber to improve the spatial resolution of the interaction vertex. Figure 2 shows a sketch of the hadron absorber and the vertex detector. The location of the aluminium nuclear target, necessary for the unpolarised DY studies is also shown. The polarised target is made of two target cells of ammonia which will be oppositely transversely polarised with respect to the beam direction. This polarisation will be reversed several times during the data taking, in order to cancel some systematic errors. A negative pion beam with an intensity of $10^9\pi$/s will be used.

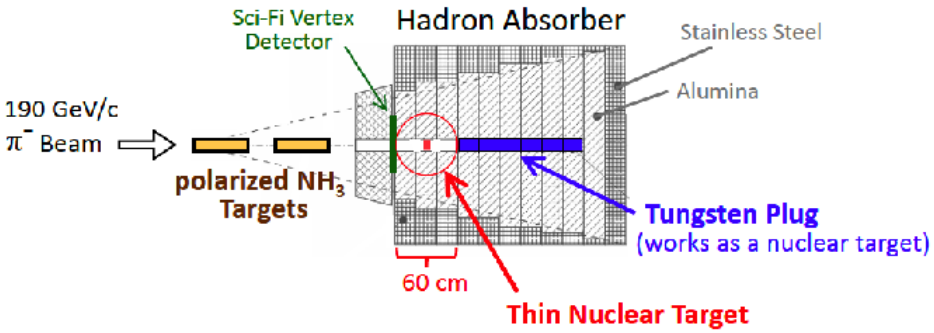

Figure 2: Sketch of the hadron absorber. In blue is visible the beam plug, in red the Al nuclear target and in green the vertex detector.

The DY pilot run has started in October. This is the opportunity to tune the experiment and analysis software before the next year's physics run. Prior to this pilot run, a beam test with a duration of three days was preformed in 2009 with success. At that time, a hadron absorber prototype was used, the trigger was based on calorimeter signals and the negative pion beam had a lower intensity, $1.5 \times 10^7\pi$/s. Now, for the pilot run everything is as it will be next year, which means the optimised absorber is installed, the trigger will be based on hodoscopes with a high efficiency, purity and target pointing capability, and we will have a high intensity pion beam available.

Figure 3 shows the dimuon mass distribution and the Z vertex distribution for the 2009 DY beam test. The J/ψ is visible and both its mass pole as well as the mass resolution are in agreement with the MC simulations. The expected J/ψ yields were confirmed regarding the involved efficiencies. The Z vertex distribution shows the separation between the two target cells and the beam plug, even in the absence of a vertex detector and the optimised absorber.

3 Event rates and statistical accuracy

The expected event rate in the mass region $4 < M_{\mu\mu} < 9$ GeV/c^2 of the polarised DY measurement is expected to be 2000 events/day. Being one year of data taking approximately 140 days, 285000 events are expected. For such a rate, the statistical errors of the asymmetries are expected to be less than 2%.

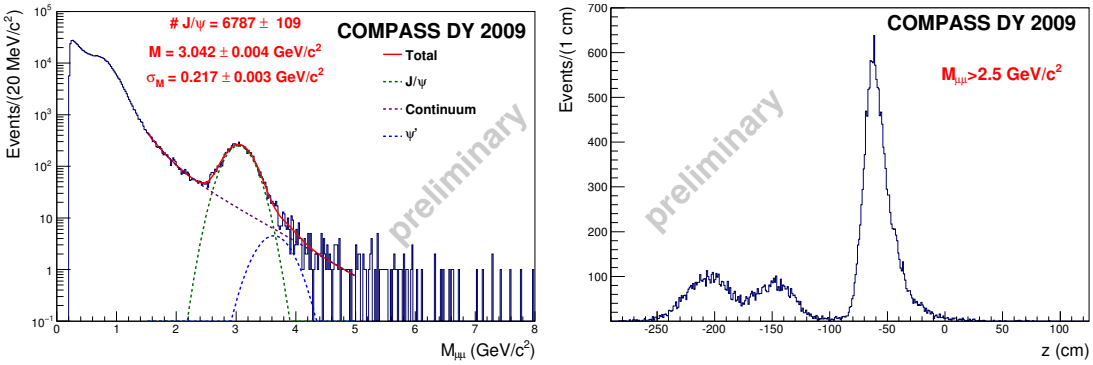

Figure 3: On the left hand side, the dimuon mass distribution is plotted. On the right hand side, the Z vertex distribution is plotted.

4 Conclusions

The DY pilot run has started in the beginning of October 2014 and will last for about two months. This is the opportunity to test the whole concept of the measurement and work out the data taking strategy for the next year's data taking. The main goals for next year are to extract the azimuthal asymmetries, in particular to check the Sivers function sign change when comparing the COMPASS SIDIS results and DY ones. By the use of nuclear targets, COMPASS also aims to contribute to the unpolarised DY studies, namely the EMC effect. Concerning the future, a second year of DY data taking before the Long Shut Down 2 at CERN, taking place in 2019, will be discussed soon. COMPASS will collect the first ever DY polarised data.

Acknowledgments

This work was partially supported by the Portuguese Fundação para a Ciência e a Tecnologia.

References

[1] C. Adolph *et al.* [COMPASS Coll.], Phys. Lett. **B717** 10 (2012).

[2] J.C. Collins, Phys. Lett. **B536** 43 (2002).

[3] D. Dutta *et al.*, Phys. Rev. **C83** 042201 (R) (2011).

[4] P. Abbon *et al.* [COMPASS Coll.], Nucl. Inst. Meth. **A577** 455 (2007).

Nucleon Transverse Structure at COMPASS

Nour Makke[1]

[1]Trieste University and INFN section of Trieste, Via A. Valerio 2, 34127 Trieste, Italy

DOI: http://dx.doi.org/10.3204/DESY-PROC-2014-04/140

COMPASS is a fixed target experiment at CERN. Part of its physics programme is dedicated to study the transverse spin and the transverse momentum structure of the nucleon using SIDIS. For these measurements, data have been collected using transversely polarised proton and deuteron targets. A selection of recent measurements of azimuthal asymmetries using data collected with transversely polarised protons is presented.

1 Introduction

The description of the partonic structure of the nucleon remains one of the main challenges in hadron physics. In the last few decades, a considerable theoretical and experimental progress has been accomplished and the relevance of the quark transverse spin and transverse momentum to study its structure has been assessed. The nucleon constituents are not only collinear moving objects but they may also have a momentum component transverse to the nucleon direction of motion. In the present theoretical framework, eight transverse momentum dependent parton distribution functions (TMD PDFs) are required for each quark flavour at leading twist, describing all possible correlations between the transverse momentum and spin of the quarks, and the spin of the nucleon. The most famous and studied one is the Sivers PDF. Integrating over the quark intrinsic transverse momentum, five among these functions vanish and three survive giving the well known number ($q(x, Q^2)$), helicity ($\Delta q(x, Q^2)$) and transversity ($\Delta_\perp q(x, Q^2)$) distribution functions. Experimentally, the latter is the least known one. Beside these, many other twist-2 distributions can be introduced, correlating the spin and the transverse momentum.

Many processes are being, and will be, studied to access the TMD PDFs, namely transversely polarised hard proton-proton collisions, Drell-Yan processes and semi-inclusive deep inelastic scattering (SIDIS). Although they are complementary, the last channel is nowadays the major source of information. Its main advantage is that TMD effects generate different azimuthal modulations in its cross section, which can be separately explored and extracted from the same experimental data set. The modulations depend on two angles, ϕ_S and ϕ_h which define the azimuthal angle of the initial nucleon spin and the produced hadron momentum respectively. These angles are defined in the so called gamma nucleon system in which the direction of the virtual photon is the z axis and the xz plane is defined by the lepton scattering plane. The modulation amplitudes are different structure functions, proportional to the convolution of the TMD PDFs and fragmentation functions (FFs).

The transversity distributions $\Delta_\perp q(x)$ can not be measured in inclusive DIS due to their chirally odd nature. They can instead be extracted from measurements of single-spin azimuthal

asymmetries in cross-sections for SIDIS of leptons on transversely polarised nucleons, in which a hadron is also detected. The measurable asymmetry, the Collins asymmetry, is due to a combined effect of $\Delta_\perp q$ and the chiral-odd Collins TMD-FF $\Delta_T^0 D_q^h$, which describes the spin-dependent part of the hadronization of a transversely polarised quark into a hadron with transverse momentum p_T. At leading order, the Collins mechanism leads to a modulation in the azimuthal distribution of the produced hadrons given by:

$$N(\phi_C) = \alpha(\phi_C) \cdot N_0(1 + A_{Coll} \cdot P_T \cdot f \cdot D_{NN} \sin\phi_C) \quad (1)$$

where α contains the apparatus efficiency and acceptance, P_T is the target polarisation, D_{NN} is the spin transfer coefficient and f is the fraction of polarisable nuclei in the target, $\phi_C = \phi_h - \phi_{S'} = \phi_h + \phi_S - \pi$ is the Collins angle, with ϕ_h the hadron azimuthal angle, $\phi_{S'}$ the final azimuthal angle of the quark spin and ϕ_S the azimuthal angle of the nucleon spin in the gamma-nucleon system.

2 The COMPASS experiment

COMPASS [1] (COmmon Muon and Proton Apparatus for Structure and Spectroscopy) is a fixed target experiment located at the CERN SPS taking data since 2002. Semi-inclusive DIS data have been collected using a 160 GeV longitudinally polarised muon beam and longitudinally or transversely polarised proton (NH_3) and deuteron (^{6}LiD) targets. The spectrometer comprises a variety of different tracking detectors, and allows to detect charged tracks in a broad momentum and angular range. Calorimeters, muon filters and a gas radiator RICH detector are available for particle identification.

3 Data Analysis and Results

Collins and Sivers asymmetries have been extracted as a function of x, z and p_T for positive and negative hadrons, pions and kaons, using lepton scattering off transversely polarised deuterons (2002-04) and protons (2007,2010). Using a deuteron target, the resulting Collins and Sivers asymmetries turned out to be compatible with zero [2],[3], an observation which has been interpreted as a cancellation between the u and d quark contributions in the isoscalar target. Using a proton target, a first measurement was performed separately versus x, z and p_T for unidentified hadrons, pions and kaons [4],[5],[6]. The Collins asymmetry is small, compatible with zero, except for $x \geq 0.05$ where a significant signal (up to 10 %) appears with opposite sign for positive and negative hadrons, pions and kaons. The results for the Sivers asymmetry are compatible with zero for negative hadrons and exhibit small positive values (up to 3%) for positive hadrons both at small and at large x. Compared with HERMES results measured at smaller Q^2, the results were found to be slightly smaller. A further investigation showed that the signal is concentrated at small W while at larger W, it tends to zero. Thus COMPASS data highlights a possible W dependence of the Sivers asymmetry for positive hadrons. The other six asymmetries were extracted from deuteron and proton data and were found to be compatible with zero.

Recently, further investigation of the previous observations has been performed by studying the x, z, p_T and W dependencies in different Q^2 regions: $Q^2 \in$ [1,4], [4,6.25], [6.25,16] and $Q^2 \geq 16$ (GeV/c)^2, using the data set collected in 2010 on a transversely polarised proton.

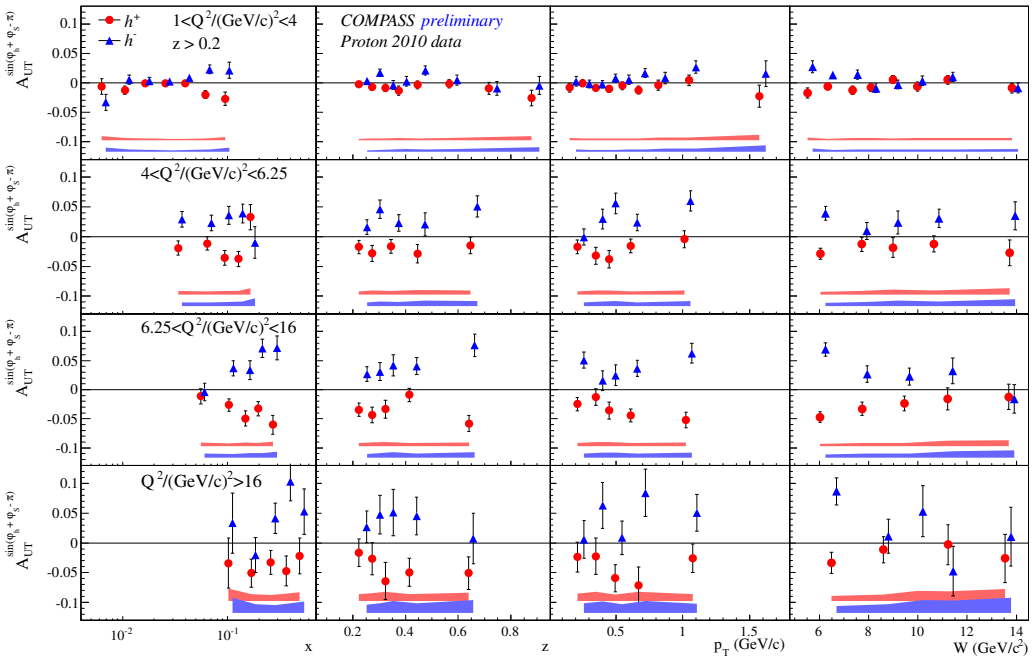

Figure 1: Collins asymmetry vs. x, z, p_T, W in four Q^2 ranges.

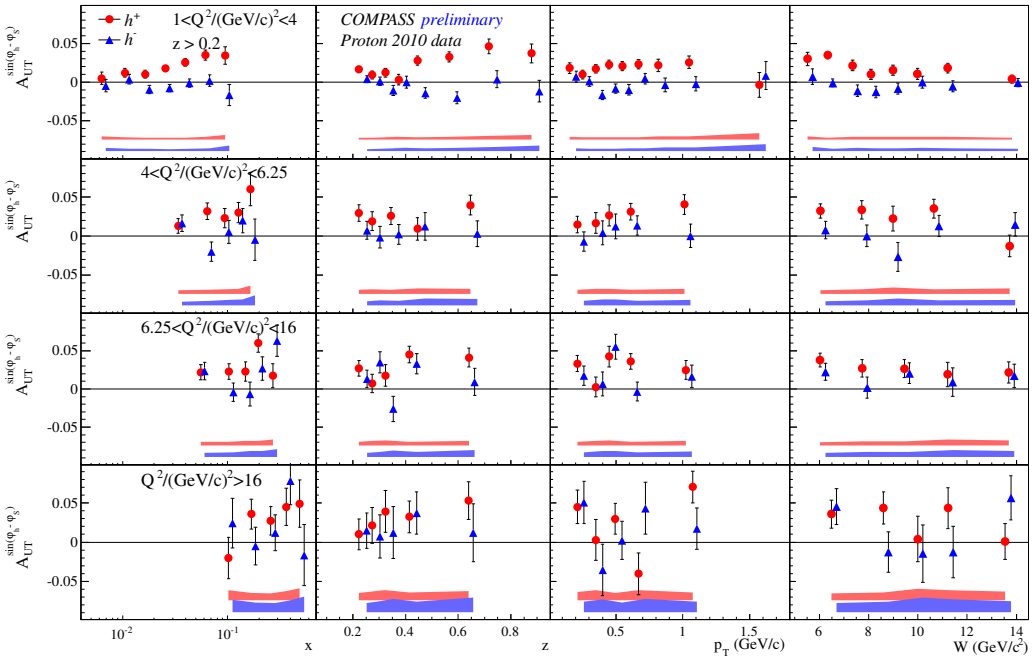

Figure 2: Sivers asymmetry vs. x, z, p_T, W in four Q^2 ranges.

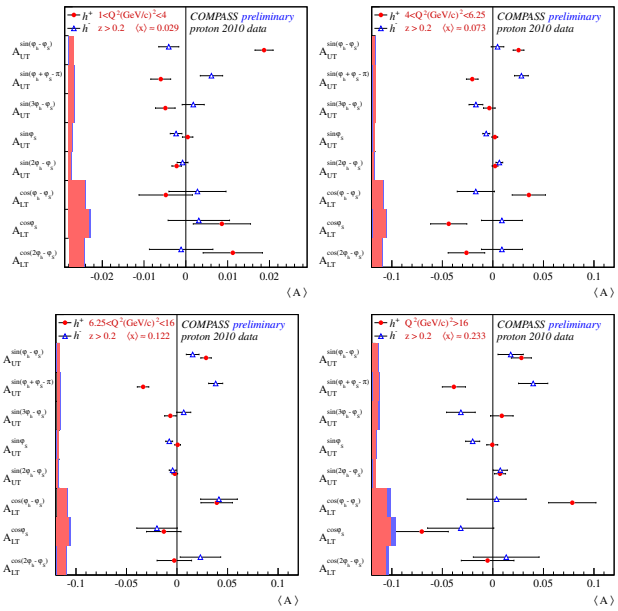

Figure 3: Mean of the eight asymmetries in four Q^2 regions.

These new results for Collins and Sivers asymmetries are shown in Fig. 1-2 versus x, z, p_T and W and the mean of the eight asymmetries are shown in Fig. 3. Error bars show only statistical uncertainties. The systematic uncertainties, estimated separately for each asymmetry and hadron charge, are shown by the bands. The increase of Collins asymmetry at large x and small W increases with Q^2. For Sivers asymmetry, the non-negligible signal for positive hadrons at large x is clearly visible, also at large Q^2, which is important for the Drell-Yan measurement foreseen by COMPASS in 2015. The other six asymmetries are compatible with zero.

4 Conclusions

A first study of the dependence of Collins, Sivers and the other six asymmetries upon kinematic variables x, z, p_T and W in different Q^2 regimes is performed, showing a non negligible Q^2 dependence of the Collins asymmetry. A more detailed multidimensional analysis of the eight asymmetries in simultaneous bins of (x,Q^2) and (x,z,p_T) is close to be finalised.

References

[1] P. Abbon *et al.* [COMPASS Collaboration], Nucl. Instrum. Meth. A **577** 455 (2007).
[2] Ageev E *et al.* [COMPASS Collaboration], Nucl. Phys. B **766** 31 (2007).
[3] Alekseev *et al.* [COMPASS Collaboration], Phys. Lett. B **673** 127 (2009).
[4] C. Adolph *et al.* [COMPASS Collaboration], Phys. Lett. B **717** 376 (2012).
[5] C. Adolph *et al.* [COMPASS Collaboration], Phys. Lett. B **717** 383 (2012).
[6] C. Adolph *et al.* [COMPASS Collaboration], hep-ex/1408.4405.

Timelike Compton Scattering off the Proton: beam and/or target spin asymmetries.

Marie Boër[1], *Michel Guidal*[1]

[1]Institut de Physique Nucléaire, CNRS-IN2P3, Université Paris-Sud F-91406 Orsay, France

DOI: http://dx.doi.org/10.3204/DESY-PROC-2014-04/256

We present a sample of results of our work to be published soon on Timelike Compton scattering off the proton, in the framework of the Generalized Parton Distributions formalism.

1 Introduction

More than 40 years after the discovery of point-like components within the proton, its quarks and gluons structure is still not well understood and is still intensively studied. Hard exclusive processes on the proton provide access to the Generalized Parton Distributions (GPDs) [1, 2, 3, 4] which contain informations about the longitudinal momentum and the spatial transverse distributions of partons inside the proton (in a frame where the nucleon has an "infinite" momentum along its longitudinal direction). Such a hard exclusive process is the Deeply Virtual Compton scattering process which corresponds to the reaction $\gamma^{(*)}P \to \gamma^{(*)}P$ and to the scattering of a high-energy virtual photon off a quark inside the proton. There are two particular cases of deep Compton processes. "Spacelike" Deeply Virtual Compton Scattering (DVCS) corresponds to the case where the incoming photon is emitted by a lepton beam and has a high spacelike virtuality and and where the final photon is real. The DVCS process has been studied for the past ∼15 years and is still intensively studied both theoretically and experimentally. The second particular case of deep Compton scattering is the Timelike Compton Scattering (TCS) process. It corresponds to the case where the incoming photon is real and the final photon has a high timelike virtuality and decays into a lepton pair (see Fig. 1). Contrary to DVCS, there is no published experimental data yet for TCS. Both DVCS and TCS give access to the same proton GPDs in the QCD leading twist formalism. The study of TCS in parallel to DVCS is a very powerful way to check the universality of GPDs and/or to study higher twist effects. The reaction $\gamma P \to e^+e^-P$ also involves the Bethe-Heitler process, where the incoming real photon creates a lepton pair, which then interacts with the proton. It is not sensitive to the GPDs but to the form factors. It can be calculated with a few percent accuracy.

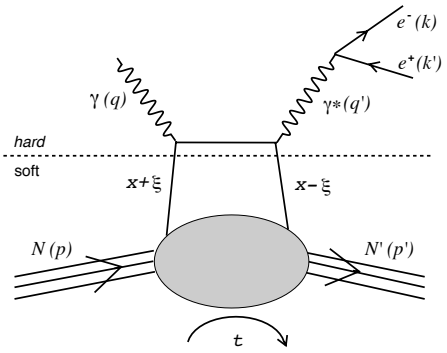

Figure 1: Leading twist TCS diagram.

2 Amplitudes and observables

The four vectors involved are indicated in Fig. 1. According to QCD factorization theorems, at sufficiently large $Q'^2 = (k + k')^2$ (photon's virtuality), we can decompose the TCS amplitude into a soft part, parameterized by the GPDs, and a hard part, exactly calculable by Feynman diagrams techniques. We work in a frame where the average protons and the average photons momenta, respectively P and $\bar{q}$, are collinear along the z-axis and in opposite directions. We define the lightlike vectors along the positive and negative z directions as $\tilde{p}^\mu = P^+/\sqrt{2}(1, 0, 0, 1)$ and $n^\mu = 1/P^+ \cdot 1/\sqrt{2}(1, 0, 0, -1)$, with $P^+ \equiv (P^0 + P^3)/\sqrt{2}$. We have the properties $\tilde{p}^2 = n^2 = 0$ and $\tilde{p} \cdot n = 1$. In this frame, the TCS amplitude can be written in the asymptotic limit (mass terms are neglected with respect to Q'^2) with the Ji convention for GPDs [5]:

$$
\begin{aligned}
T^{TCS} = & -\frac{e^3}{q'^2}\, \bar{u}(k)\, \gamma^\nu\, v(k')\, \epsilon^\mu(q) \\
& \left[\frac{1}{2}\, (-g_{\mu\nu})_\perp \int_{-1}^{1} dx\, \left(\frac{1}{x - \xi - i\epsilon} + \frac{1}{x + \xi + i\epsilon} \right) . \left(H(x,\xi,t) \bar{u}(p') \not{n} u(p) + E(x,\xi,t) \bar{u}(p') i\sigma^{\alpha\beta} n_\alpha \frac{\Delta_\beta}{2M}\, u(p) \right) \right. \\
& \left. - \frac{i}{2} (\epsilon_{\nu\mu})_\perp \int_{-1}^{1} dx\, \left(\frac{1}{x - \xi - i\epsilon} - \frac{1}{x + \xi + i\epsilon} \right) . \left(\tilde{H}(x,\xi,t) \bar{u}(p') \not{n} \gamma_5\, u(p) + \tilde{E}(x,\xi,t) \bar{u}(p') \gamma_5 \frac{\Delta . n}{2M}\, u(p) \right) \right] \quad (1)
\end{aligned}
$$

where x is the quark longitudinal momentum fraction, $\Delta = (p' - p)$ is the momentum transfer, $t = \Delta^2$ and ξ is defined as

$$\xi = -\frac{(p - p').(q' + q)}{(p + p').(q' + q)}. \quad (2)$$

In Eq. 1, we used the metric

$$(-g_{\mu\nu})_\perp = -g_{\mu\nu} + \tilde{p}_\mu n_\nu + \tilde{p}_\nu n_\mu \ , \quad (\epsilon_{\nu\mu})_\perp = \epsilon_{\nu\mu\alpha\beta}\, n^\alpha\, \tilde{p}^\beta. \quad (3)$$

The Bethe-Heitler amplitude reads:

$$T^{BH} = -\frac{e^3}{\Delta^2} \bar{u}(p') \left(\gamma^\nu F_1(t) + \frac{i\sigma^{\nu\rho}\Delta_\rho}{2\,M} F_2(t) \right) u(p)\, \epsilon^\mu(q) \bar{u}(k) \left(\gamma_\mu \frac{\not{k} - \not{q}}{(k-q)^2} \gamma_\nu + \gamma_\nu \frac{\not{q} - \not{k}'}{(q-k')^2} \gamma_\mu \right) v(k'), \quad (4)$$

where $F_1(t)$ and $F_2(t)$ are the proton Dirac and Pauli form factors. At fixed beam energy, the cross section of the photoproduction process depends on four independant kinematic variables, which we choose as: Q'^2, t and the two angles θ and ϕ of the decay electron in the γ^* center of mass. The 4-differential unpolarized cross section reads:

$$\frac{d^4\sigma}{dQ'^2 dt d\Omega}(\gamma p \to p' e^+ e^-) = \frac{1}{(2\pi)^4} \frac{1}{64} \frac{1}{(2ME_\gamma)^2}\, |\, T^{BH} + T^{TCS}\, |^2, \quad (5)$$

where $|\, T^{BH} + T^{TCS}\, |^2$ is averaged over the target proton and beam polarizations and summed over the final proton spins.

We define the single and double spin asymmetries as:

$$A_{\odot U}\ (A_{Ui}) = \frac{\sigma^+ - \sigma^-}{\sigma^+ + \sigma^-}, \quad A_{\odot i} = \frac{(\sigma^{++} + \sigma^{--}) - (\sigma^{+-} + \sigma^{-+})}{\sigma^{++} + \sigma^{--} + \sigma^{+-} + \sigma^{-+}}, \quad (6)$$

where the first index of A corresponds to the polarization state of the beam and the second one corresponds to the polarization state of the target. $A_{\odot U}$ is the circularly polarized beam spin

asymmetry. The + and − superscripts in σ correspond to the two photon spin states, right and left polarized. A_{Ui} are the single target spin asymmetries where the + and − superscripts refer to the target spin orientations along the axis $i = x, y, z$. The axis x and y are perpendicular to the incoming proton direction (along the z-axis) in the γP center of mass frame and are respectivelly in the scattering plane and perpendicular to this plane. $A_{\odot i}$ are the double spin asymmetries with a circularly polarized beam and with a polarized target. We finally define the single linearly polarized beam spin asymmetry as

$$A_{\ell U}(\Psi) = \frac{\sigma_x(\Psi) - \sigma_y(\Psi)}{\sigma_x(\Psi) + \sigma_y(\Psi)}, \tag{7}$$

where Ψ is the angle between the photon polarization vector and the $\gamma P \to \gamma^* P'$ plane and where σ_x (σ_y) indicate a photon polarized in the x-(y-)direction.

3 Numerical results and sensitivity to GPDs

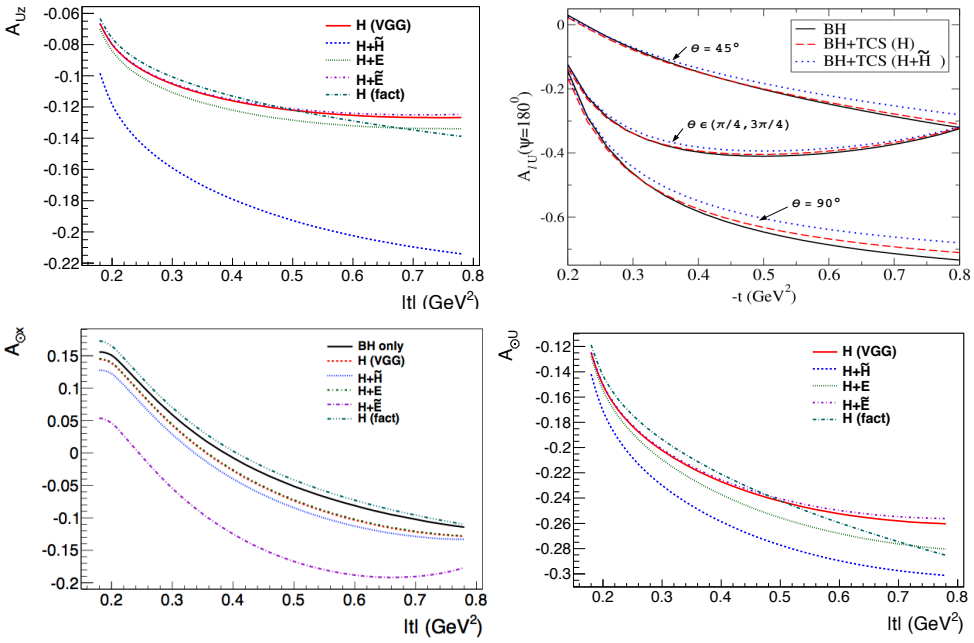

Figure 2: Spin asymmetries as a function of $-t$. Top left: $A_{\odot U}$ for BH+TCS. Top right: $A_{\ell U}$ for BH and BH+TCS. Bottom left: A_{Uz} for BH+TCS. Bottom right: $A_{\odot x}$ for BH and BH+TCS. All calculations are done at $\xi = 0.2$, $Q'^2 = 7$ GeV^2, $\phi = 90°$ and θ integrated over $[45°, 135°]$. $A_{\ell U}$ is also shown for $\theta = 45°$ and $\theta = 90°$.

We performed our calculations using the GPD parameterization of the VGG model [6, 7, 8]. We focus here on the spin asymmetries. Figure 2 shows the circularly (top row left) and linearly (top row right) polarized beam spin asymmetries as a function of t. One should note that $A_{\odot U}$

is particularly sensitive to the GPDs as it is exactly 0 for BH alone. It comes from the fact that this asymmetry is sensitive to the imaginary part of the amplitudes and the BH amplitude is purely real. We also show $A_{\odot U}$ with a factorized-t ansatz instead of a Reggeized-t ansatz for the H GPD which illustrates the sensitivity to the GPD modeling. In contrast, the $A_{\ell U}$ asymmetry, which is strong, is dominated by the BH and the TCS makes up only small deviations. Indeed, this asymmetry is sensitive to the real part of the amplitudes.

We display in Fig. 2 (bottom row) two examples of asymmetries with a polarized target: A_{Uz} and $A_{\odot x}$ (double spin asymmetry). We present the results for TCS+BH with different GPDs contributions and parameterizations. All single target spin asymmetries are zero for the BH alone as they are proportional to the imaginary part of the amplitudes. This makes the A_{Ui} asymmetries privileged observables to study GPDs. On the contrary, it is more difficult to access GPDs with double spin asymmetries as the BH alone produces a strong double spin asymmetry.

4 Discussion

We have presented a sample of our results to be published soon, namely the t-dependence of single and double spin asymmetries for the $\gamma P \to e^+e^-P$ reaction which we analyzed in the framework of the GPD formalism. We didn't discuss this here due to lack of space but we also compared our unpolarized cross sections and our single beam spin asymmetries with those of the earlier work of Refs [9, 10] and they are in agreement at the few percent level. We have introduced in our work the target polarization in order to define the single and double spin asymmetries with polarized targets. We have also introduced some higher twist corrections and gauge invariance restoration terms.

As the BH contribution alone doesn't contribute to single target spin asymmetries and to circularly polarized beam spin asymmetries, these observables are good candidates to study GPDs. Such measurements can be envisaged at the JLab 12 GeV facility. In particular, a proposal has been accepted for the CLAS12 experiment (JLab Hall B) to measure the unpolarized BH+TCS cross section [11]. The work that we presented here can open the way to new complementary experimental programs with polarized beams and/or targets.

References

[1] K. Goeke, M. V. Polyakov and M. Vanderhaeghen, Prog. Part. Nucl. Phys. **47**, 401 (2001).

[2] M. Diehl, Phys. Rept. **388**, 41 (2003).

[3] A.V. Belitsky, A.V. Radyushkin, Phys. Rept. **418**, 1 (2005).

[4] M. Guidal, H. Moutarde and M. Vanderhaeghen, Rept. Prog. Phys. **76**, 066202 (2013).

[5] X. Ji, Phys.Rev.Lett. **78**, 610 (1997); Phys.Rev.D **55**, 7114 (1997).

[6] M. Vanderhaeghen, P.A.M. Guichon and M. Guidal, Phys. Rev. Lett. **80** 5064 (1998)

[7] M. Vanderhaeghen, P. A. M. Guichon and M. Guidal, Phys. Rev. D **60** 094017 (1999).

[8] M. Guidal, M. V. Polyakov, A. V. Radyushkin and M. Vanderhaeghen, Phys. Rev. D **72** 054013 (2005).

[9] E. R. Berger, M. Diehl and B. Pire, Eur. Phys. J. C **23**, 675 (2002).

[10] A. T. Goritschnig, B. Pire and J. Wagner, Phys. Rev. D **89** (2014) 094031

[11] I. Albayrak et al. and the CLAS Collaboration, JLab PAC 39 Proposal, (2012).

Measurements of the Form Factor in VPγ^* Transitions and Study of the $\eta \to \pi^+\pi^-\pi^0$ Dalitz Plot at KLOE

Li Caldeira Balkeståhl[1] on behalf of KLOE-2 collaboration

[1]Department of Physics and Astronomy, Uppsala University, Box 516, SE-751 20 Uppsala, SWEDEN

DOI: http://dx.doi.org/10.3204/DESY-PROC-2014-04/141

The Vector→Pseudoscalar γ^* decays $\phi \to \eta e^+e^-$ and $\phi \to \pi^0 e^+e^-$ have been measured based on 1.7 pb^{-1} of data collected with the KLOE experiment, for extracting the branching ratios and transistion form factors.

With 1.6 pb^{-1} of data from the same experiment, we measure the Dalitz plot distribution of the $\eta \to \pi^+\pi^-\pi^0$ decay. Preliminary values are given for the Dalitz plot parameters a, b, d, f.

1 Transition form factors of VPγ^*

The differential decay rate of Vector→Pseudoscalar γ^*, with the virtual photon decaying in a lepton pair, is described by [1]:

$$\frac{d}{dq^2}\frac{\Gamma(\mathrm{V}\to \mathrm{P}l^+l^-)}{\Gamma(\mathrm{V}\to \mathrm{P}\gamma)} = \frac{\alpha}{3\pi}\frac{|F_{\mathrm{VP}}(q^2)|^2}{q^2}\sqrt{1-\frac{4m^2}{q^2}}\left(1+\frac{2m^2}{q^2}\right)\left[\left(1+\frac{q^2}{m_{\mathrm{V}}^2-m_{\mathrm{P}}^2}\right)^2-\frac{4m_{\mathrm{V}}^2q^2}{(m_{\mathrm{V}}^2-m_{\mathrm{P}}^2)^2}\right]^{\frac{3}{2}} \tag{1}$$

where q is the invariant mass of the lepton pair, F_{AB} is the transition form factor, m is the lepton mass and m_{A}, m_{B} are the masses of the mesons A and B. In the one pole approximation, the transition form factor is

$$F_{\mathrm{VP}}(q^2) = \frac{1}{1-q^2/\Lambda^2} \tag{2}$$

where Λ is the characteristic mass relevant to the process. The slope of the transition form factor is defined as

$$b_{\mathrm{VP}} = \frac{dF_{\mathrm{VP}}(q^2)}{dq^2}|_{q^2=0}$$

which for the one pole approximation gives $b_{\mathrm{VP}} = \Lambda^{-2}$.

The simple vector meson dominance model (VMD) can be used to calculate transistion form factors. This model is in general quite sucessful, but it puzzlingly fails for the decay $\omega \to \mu^+\mu^-\pi^0$, as shown by the Lepton-G [2] and NA60 [3, 4] experiments. Therefore it is important to verify other Vector→Pseudoscalar γ^* processes.

Recently, new theoretical approaches have been proposed to describe these deviations from VMD: one based on dispersion theory [5], one based on an effective field theory including light vector mesons as degrees of freedom [6] and one based on chiral effective field theory with resonances [7]. To descriminate between these models, more data on VPγ^* transition form factors, for different vector and pseudoscalar mesons, is needed.

1.1 $\phi \to \eta e^+ e^-$

The existing experimental data on the $\phi \to \eta e^+ e^-$ decay are very scarce. The branching ratio has been measured by two experiments, in units of 10^{-4} the world average is equal to 1.15 ± 0.10 (PDG [8], the result comes from SND [9] and CMD-2 [10] experiments). The slope of the transition form factor was determined only by the SND experiment with very large error, $b_{\phi\eta} = 3.8 \pm 1.8$ GeV^{-2} [9], while the value expected from VMD is $b_{\phi\eta} \simeq 1$ GeV^{-2}.

With the KLOE detector, using 1.7 pb^{-1} of data, we have measured $\phi \to \eta e^+ e^-$ with $\eta \to 3\pi^0$, with a total of 29 626 $\pm$178 events in the final sample. This results in a branching ratio of $\left(1.075 \pm 0.038_{\rm norm} \pm 0.007_{\rm stat}{}^{+0.006}_{-0.002\ \rm syst}\right) \cdot 10^{-4}$, where the normalization error comes from the uncertainty in the ϕ meson production cross-section and in the luminosity measurement. A fit of the lepton pair invariant mass spectrum to Equation 1 using Equation 2 is shown in Figure 1. This gives $b_{\phi\eta} = 1.17 \pm 0.10(\text{stat})^{+0.07}_{-0.11}(\text{syst})$.

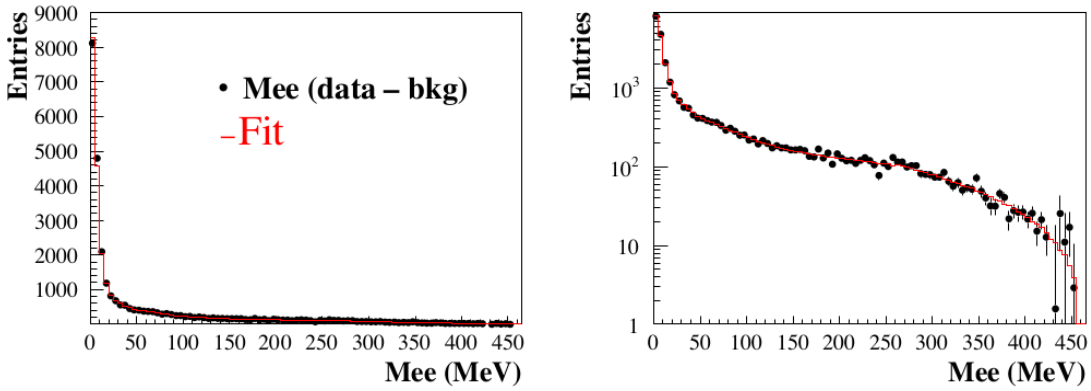

Figure 1: Observed (not corrected for acceptance) experimental distribution of invariant mass of the lepton pair for the $\phi \to \eta e^+ e^-$ signal after background subtraction. The red lines represent the best fit using Eq. 1 with single pole form factor paremetrization Eq. 2.

The modulus squared of the transition form factor as a function of the lepton pair invariant mass can be extracted by dividing, for each bin in q, the data by the number of reconstructed events simulated with $F_{\phi\eta} = 1$. This is shown in Figure 2, where the Monte Carlo data sample has been normalized to the experimental data in the first bin. A fit of this distribution to the one-pole approximation formula (Eq. 2) results in $b_{\phi\eta} = (1.25 \pm 0.10)$ GeV^{-2}, in agreement with the slope extracted directly from the acceptance uncorrected differential decay distribution.

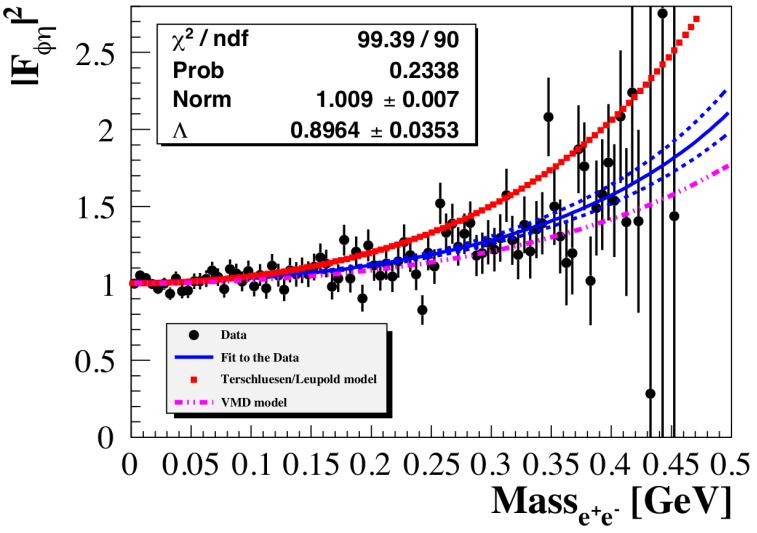

Figure 2: $|F_{\phi\eta}|^2$ as a function of the invariant mass of the lepton pair. In blue (full line with dashed error band) the result from the fit to Equation 2, in pink (dash dot line) the VMD prediction and in red (full line) the theoretical calcualtion of [6].

1.2 $\phi \to \pi^0 e^+ e^-$

For the decay $\phi \to \pi^0 e^+ e^-$ there is no data on the transition form factor slope, and the branching ratio measurements have large errors: the world average is $(1.12 \pm 0.28) \cdot 10^{-5}$ (PDG [8], the result comes from SND [11] and CMD-2 [12] experiments).

An analysis of this decay using 1.7 pb^{-1} of data collected at KLOE is underway. At the end of the analysis chain there are 14 680 events, of which Monte Carlo simulation shows about 22% are $e^+e^- \to e^+e^-\gamma\gamma$ background and 20% are $\phi \to \pi^0\gamma$ background (with conversion of the photon in the detector). The background could be subtracted bin by bin in order to extract the invariant mass distribution of the lepton pair. Results on both branching ratio and transition form factor are forthcoming.

2 Decay dynamics of $\eta \to \pi^+\pi^-\pi^0$

The isospin breaking decay $\eta \to \pi^+\pi^-\pi^0$ is sensitive to the difference of the up and down quarks, since electromagnetic effects in this decay are small [13, 14, 15, 16]. The decay width

$$\Gamma(\eta \to \pi^+\pi^-\pi^0) \propto Q^{-4} \quad \text{where } Q^2 \equiv \frac{m_s^2 - \hat{m}^2}{m_d^2 - m_u^2} \quad \text{and } \hat{m} = \frac{1}{2}(m_d + m_u),$$

allows to determine Q, thus setting an elliptical constraint in the light quark mass plane $\frac{m_u}{m_d}$ *vs* $\frac{m_s}{m_d}$ [17]. The chiral perturbation theory calculations for the decay width show a slow converge ($\Gamma_{LO} = 66$ eV, $\Gamma_{NLO} = 160 \pm 50$ eV [18] and $\Gamma_{NNLO} = 295 \pm 17$ [19], $\Gamma_{exp} = 295 \pm 16$ eV [8]). This indicates the importance of the final state interactions between pions, which can be taken

into account by the use of dispersive theory [20, 21]. Calculations have also been performed in a non-relativistic effective field theory approach [22].

A more complete comparison between theory and experiment is facilitated by the Dalitz plot, containing full information on the dynamics of the decay. For the $\eta \to \pi^+\pi^-\pi^0$ decay, the normalized variables X and Y are used

$$X = \sqrt{3}\frac{T_{\pi^+} - T_{\pi^-}}{Q_\eta} \qquad Y = \frac{3T_{\pi^0}}{Q_\eta} - 1 \qquad (Q_\eta = T_{\pi^+} + T_{\pi^-} + T_{\pi^0})$$

where T_{π^i} is the kinetic energy of the π^i in the η rest frame. The squared amplitude of the decay can be expanded around $X = Y = 0$ as

$$|A(X,Y)|^2 \simeq N(1 + aY + bY^2 + cX + dX^2 + eXY + fY^3 + gX^2Y)$$

and the coefficients a, b, c, d, e, f, g are called Dalitz plot parameters.

Using 1.6 pb^{-1} of data collected at KLOE we extract the Dalitz plot distribution for $\eta \to \pi^+\pi^-\pi^0$. The preliminary results for the Dalitz plot parameters are shown in Table 1, compared to earlier experimental results. Note that the present analysis includes only statistical errors as the systematic effects are under investigation.

Experiment	-a	b	d	f
Gormley[23]	1.17(2)	0.21(3)	0.06(4)	-
Layter[24]	1.080(14)	0.03(3)	0.05(3)	-
CBarrel[25]	1.22(7)	0.22(11)	0.06(fixed)	-
KLOE[26]	$1.090(5)(^{+19}_{-8})$	0.124(6)(10)	$0.057(6)(^{+7}_{-16})$	0.14(1)(2)
WASA[27]	1.144(18)	0.219(19)(47)	0.086(18)(15)	0.115(37)
This work	1.104(3)	0.144(3)	0.073(3)	0.155(6)

Table 1: Experimental results for the Dalitz plot parameters of $\eta \to \pi^+\pi^-\pi^0$.

References

[1] L. G. Landsberg, Phys. Rept. **128**, 301 (1985).

[2] R. I. Dzhelyadin *et al.*, Phys. Lett. **B102**, 296 (1981).

[3] R. Arnaldi *et al.* (NA60 Collaboration), Phys. Lett. **B677**, 260 (2009).

[4] G. Usai (NA60 Collaboration), Nucl. Phys. A **A855**, 189 (2011).

[5] S. P. Schneider, B. Kubis and F. Niecknig, Phys. Rev. **D86**, 054013 (2012).

[6] C. Terschlusen and S. Leupold, Phys. Lett. **B691**, 191 (2010).

[7] S. Ivashyn, Prob. Atomic Sci. Technol. **2012N1**, 179 (2012).

[8] J. Beringer *et al.* (Particle Data Group), Phys. Rev. **D86**, 010001 (2012).

[9] M. N. Achasov *et al.*, Phys. Lett. **B504**, 275 (2001).

[10] R. R. Akhmetshin *et al.* (CMD-2 Collaboration), Phys. Lett. **B501**, 191 (2001).

[11] M. N. Achasov *et al.*, JETP Lett. **75**, 449 (2002).

[12] R. R. Akhmetshin *et al.* (CMD-2 Collaboration), Phys. Lett. **B503**, 237 (2001).

[13] D. G. Sutherland, Phys. Lett. **23**, 384 (1966).

[14] J. S. Bell and D. G. Sutherland, Nucl. Phys. **B4**, 315 (1968).

[15] R. Baur, J. Kambor and D. Wyler, Nucl. Phys. **B460**, 127 (1996).
[16] C. Ditsche, B. Kubis and U.-G. Meißner", Eur. Phys. J. **C60**, 83 (2009).
[17] H. Leutwyler, Phys. Lett. **B378**, 313 (1996).
[18] J. Gasser and H. Leutwyler, Nucl. Phys. **B250**, 539 (1985).
[19] J. Bijnens and K. Ghorbani, JHEP **0711**, 030 (2007).
[20] G. Colangelo, S. Lanz, H. Leutwyler and E. Passemar, POS **EPS-HEP2011**, 304 (2011)
[21] K. Kampf, M. Knecht, J. Novotný and M. Zdráhal, Phys. Rev. **D84**, 114015 (2011).
[22] S. P. Schneider, B. Kubis and C. Ditsche, JHEP **1102**, 028 (2011)
[23] M. Gormley *et al.*, Phys. Rev. **D2**, 501 (1970).
[24] J.G. Layter *et al.*, Phys. Rev. **D7**, 2565 (1973).
[25] A. Abele *et al.* (Crystal Barrel Collaboration), Phys. Lett. **B471**, 197 (1998).
[26] F. Ambrosino *et al.* (KLOE collaboration), JHEP **0805**, 006 (2008).
[27] P. Adlarson *et al.* (WASA-at-COSY collaboration), Phys. Rev. **C90**, 045207 (2014).

Generalized Parton Distributions at COMPASS: Present Results and Future Perspectives

Eric Fuchey[1] on behalf of COMPASS collaboration

[1]CEA Saclay, IRFU/SPhN 91191 Gif-sur-Yvette, France

DOI: http://dx.doi.org/10.3204/DESY-PROC-2014-04/103

Understanding the nucleon structure remains one of the key challenges of nuclear physics. The Generalized Parton Distributions (GPDs) grant a new insight for the study of the nucleon structure, as they provide a three-dimensional picture of the nucleon. COMPASS at CERN has a great potential for GPD studies, with its forthcoming measurement of deeply virtual Compton scattering and exclusive meson production off the proton with both μ^+ and μ^-. The current COMPASS GPD program will be discussed, as well as an overview of the investigation on future possible developments. Existing results of exclusive meson production will also be presented.

1 Reminder on Generalized Parton Distributions

The Generalized Parton Distributions (GPDs) constitute a new, three dimensional parametrization of the nucleon structure. They correlate the momentum distribution of the partons inside the proton, parametrized by the parton distribution functions, to the transverse spatial distribution of those partons, parametrized by the form factors. As such, those objects grant access to the orbital angular momentum of the quarks [1, 2, 3].

GPDs can be accessed thanks to exclusive processes such as Deeply Virtual Compton Scattering (DVCS $\ell p \to \ell p \gamma$), or exclusive meson production off the nucleon. In such reactions, the virtual photon (with a high virtuality Q^2) emitted by the lepton selects a quark in the nucleon with a longitudinal momentum fraction $x + \xi$, which re-emits a photon (in the case of DVCS) or produces a hadron (in the case of meson production), and is reabsorbed in the proton with a momentum $x - \xi$. During the reaction, a quadrimomentum t is transferred to the nucleon (Figure 1).

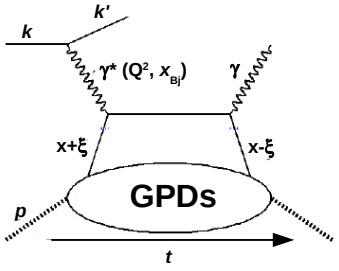

Figure 1: Feynman diagram of DVCS at lowest order.

We count four chiral-even GPDs (which do not involve quark-helicity flip), H, E, $\tilde{H}$, $\tilde{E}$, and as many chiral-odd GPDs (which involve quark-helicity flip). Those GPDs are functions of x, ξ, and t. The second moment in x of the sum of H and E for a given quark flavor gives the quark total angular momentum. This property is called the Ji sum rule [3]. As a consequence, the study of H and E are of first importance to understand the content of the proton in spin, and COMPASS at CERN has the ability to study them both.

2 The COMPASS experiment at CERN

2.1 COMPASS experimental setup

COMPASS (Common Muon Proton Apparatus for Structure and Spectroscopy) at CERN is a large acceptance magnetic spectrometer dedicated to the study of hadronic physics. It is installed on one of the Super-Proton-Synchrotron beam lines, and is able to receive beams of various types: protons, pions, and both positive and negative polarized muons (polarization $\simeq$ 80 %).

The experimental setup is composed of two dipoles and of a large number of tracking detectors for charged particle reconstruction and momentum measurement. A ring imaging Cherenkov detector provides particle identification, and two calorimeters provide energy measurement. A more complete description of the detectors is provided in [4]. Such an apparatus grants COMPASS with a wide kinematic range.

The experimental setup described above can be modified or completed to measure a specific process. Let us review the modifications that have been done for DVCS measurement.

2.2 Compass configuration for DVCS measurement

At COMPASS, the DVCS ($\mu p \to \mu p \gamma$) will be measured using the high intensity ($\sim 4 \times 10^7\,\mu\,\mathrm{s}^-1$) polarized muon beam. DVCS is a relatively low cross section process, so the luminosity will be maximized with a 2.5 meter long liquid hydrogen target. In the DVCS kinematics, the photon is produced at forward angle, and the proton recoils at very large angle. To measure and identify the recoil proton, a 4-meter long Time-Of-Flight detector called CAMERA is surrounding the target. To extend the kinematic coverage of DVCS detection to the higher x_{Bj}, a large angle electromagnetic calorimeter has also been added. With such an apparatus, COMPASS can measure the DVCS process on a wide x_{Bj} range (from 0.005 to $\simeq 0.3$) with a Q^2 up to $\simeq 20\,\mathrm{GeV}^2$ (limited by integrated luminosity).

3 The COMPASS GPD program

Thanks to several advantageous features, which we are going to discuss, COMPASS has the ability to study both GPD H [5] and GPD E. First, both μ^+ and μ^- beams are available at COMPASS (Sec. 2.1), each having one polarization direction. This feature is currently unique, and will provide useful additional information for the extraction of GPDs thanks to DVCS measurement (see Secs. 3.1 and 3.2). In addition to this, the x_{Bj} range covered by COMPASS ($0.005 < x_{Bj} < 0.3$) spans over the existing gap between the DVCS data from HERA in the gluon region ($x_{Bj} \leq 10^{-2}$) on the one hand, and the data from HERMES and Jefferson Lab in the valence region ($x_{Bj} \geq 0.1$). COMPASS is also a versatile detector, in this sense that it is able to measure simultaneously DVCS and several exclusive neutral meson channels, such as π^0, ρ^0, ϕ, ω.

3.1 Study of GPD H

The GPD H is studied with DVCS measurements on unpolarized hydrogen. A 10-day long test run, recorded in 2009 at COMPASS with a reduced DVCS setup (40 cm liquid hydrogen target, short recoil proton calorimeter, no additional calorimetry), proved the capability of such

a setup to measure exclusive photon production, but also the capability to isolate, at high x_{Bj} values, a DVCS signal among the total $\mu p \to \mu p \gamma$ signal (composed of the interference of DVCS and Bethe-Heitler, where the photon is radiated by the incident or the scattered lepton).

In 2012, a four-week long pilot run has been recorded, with a mostly complete DVCS setup (full scale recoil proton detector, full luminosity, partially equipped large angle calorimeter). This run, which is still under analysis, has proved that the recoil proton detector is able to detect and identify protons. The results from this run will be available soon.

The full DVCS run will occur in 2016 and 2017 [5]. Interesting information will come from the $\mu p \to \mu p \gamma$ cross sections measurements with both muon charge states ($d\sigma(\mu^{+,\to})$ and $d\sigma(\mu^{-,\leftarrow})$) both from their sum $\mathcal{S}_{CS,U}$ and their difference $\mathcal{D}_{CS,U}$.50.0 The DVCS cross section can be isolated from $\mathcal{S}_{CS,U}$. Its t-dependence, expected to be in $\exp(-Bt)$, provides the size of the proton $r_\perp$ at the measured x_{Bj}, knowing that $\langle r_\perp^2(x_{Bj})\rangle \simeq 2B(x_{Bj})$. The t-slope parameter B has been measured at HERA at $x_{Bj} < 0.01$ (square and triangles on Fig. 2). In this region, B is measured to be constant. In the x_{Bj} range covered by COMPASS, the proton size is expected to shrink (solid and dashed lines on Fig. 2), and the projected COMPASS uncertainties with two years of data (circles on Fig. 2) should be able to determine the x_{Bj}-slope, α' of this shrink.

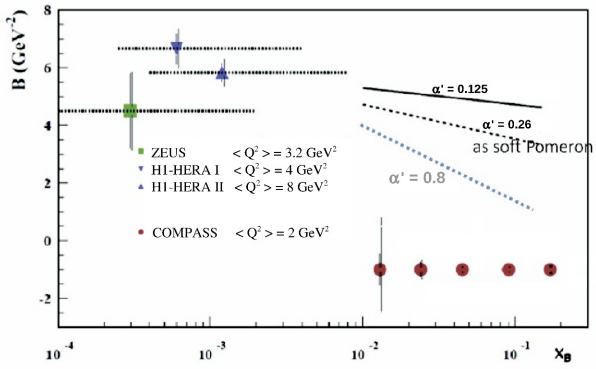

Figure 2: t-slope parameter as a function of x_{Bj} measured by HERA (square and triangles), and projected statistical uncertainty with two years of data at COMPASS (circles).

The study of the ϕ modulation of the Bethe-Heitler-DVCS interference term in $\mathcal{S}_{CS,U}$ and $\mathcal{D}_{CS,U}$ allow to isolate their first ϕ moment (respectively $s_1^{Int}\sin(\phi_{\gamma\gamma})$ and $c_1^{Int}\cos(\phi_{\gamma\gamma})$), which depend respectively on the imaginary part and real part of $F_1 \times \mathcal{H}$. ($\mathcal{H}$ being the observable of the GPD H, called Compton form factor).

3.2 Study of GPD E

The measurements of DVCS and exclusive channels on polarized hydrogen allow to study the GPD E, which allows for nucleon spin flip.

The exclusive production of ρ^0 meson on a transversely polarized hydrogen target (without recoil detection) has been performed with muon data recorded at COMPASS between 2007 and 2010. Eight target spin asymmetries, depending on ϕ and ϕ_S (ϕ_S being the angle between muon scattering plane and proton polarization) have been extracted [6, 7] and successfully interpreted in terms of GPDs [8].

Among these quantities (available on Fig. 3), the $\sin(\phi - \phi_S)$ term sets a good constraint on GPDs E, confirming that the *total* contribution of E for *all* quark flavors and gluons are small [7]. The combined information of the $\sin(2\phi - \phi_S)$ and $\sin\phi_S$ terms also indicate that the chiral-odd GPD H_T should not be small.

In the future, COMPASS might also be able to measure DVCS on a transversely polarized target, with recoil proton detection. The measurement of first moment in $\phi - \phi_s$ of the charge spin cross section difference on a transversely polarized target, $\mathcal{D}_{CS,T}$, provides access to both Compton form factors $\mathcal{H}$ and $\mathcal{E}$ on the same footing. With two years of data, COMPASS could improve by a factor 2 the statistical accuracy on this quantity compared to its previous measurement by HERMES [9], [5]. This challenging prospect is still under investigation, as it is currently technically limited by the combination of a transversely polarized target (which, by order, is surrounded by a magnet) with recoil proton detection.

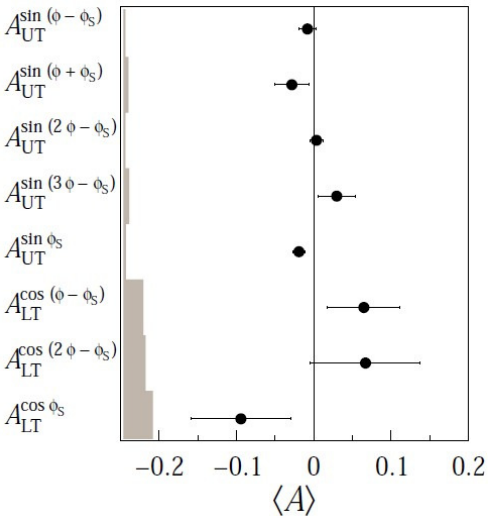

Figure 3: Target spin asymmetries on $\mu p^{\uparrow\downarrow} \to \mu p \rho^0$ measured at COMPASS [6, 7].

4 Summary

The study of the GPDs is one of the hot topics in the structure of the nucleon. The COMPASS experiment, with its unique features (Sec. 3), offers a very promising GPD program. The few existing results (Secs. 3.1 and 3.2) are very encouraging to go forward the forthcoming full DVCS run (2016-2017), which will provide a good accuracy for the measurement of several observables of interest (proton size, Compton form factor $\mathcal{H}$). The possibility to measure DVCS on transversely polarized target at COMPASS, though being a technical challenge, is also being investigated.

Acknowledgments

We would like to acknowledge the P2IO Excellence Laboratory for its financial support.

References

[1] D. Mller, D. Robaschik, B. Geyer, F.-M. Dittes and J. Hoeji, Fortsch. Phys. **42** (1994) 101 [hep-ph/9812448].

[2] A. V. Radyushkin, Phys. Rev. D **56** (1997) 5524 [hep-ph/9704207].

[3] X. D. Ji, Phys. Rev. Lett. **78** (1997) 610 [hep-ph/9603249].

[4] P. Abbon *et al.* [COMPASS Collaboration], Nucl. Instrum. Meth. A **577** (2007) 455 [hep-ex/0703049].

[5] F. Gautheron *et al.* [COMPASS Collaboration], CERN-SPSC-2010-014.

[6] C. Adolph *et al.* [COMPASS Collaboration], Phys. Lett. B **731** (2014) 19 [arXiv:1310.1454 [hep-ex]].

[7] C. Adolph *et al.* [COMPASS Collaboration], Nucl. Phys. B **865** (2012) 1 [arXiv:1207.4301 [hep-ex]].

[8] S. V. Goloskokov and P. Kroll, Eur. Phys. J. C **74** (2014) 2725 [arXiv:1310.1472 [hep-ph]].

[9] A. Airapetian *et al.* [HERMES Collaboration], JHEP **0806** (2008) 066 [arXiv:0802.2499 [hep-ex]].

Deeply pseudoscalar meson electroproduction with CLAS and Generalized Parton Distributions

Michel Guidal[1], *Valery Kubarovsky*[2]

[1]Institut de Physique Nucléaire Orsay, CNRS-IN2P3, Université Paris-Sud, France
[2]Thomas Jefferson National Accelerator Facility, Newport News, Virginia 23606

DOI: http://dx.doi.org/10.3204/DESY-PROC-2014-04/33

We discuss the recent data of exclusive π^0 (and π^+) electroproduction on the proton obtained by the CLAS collaboration at Jefferson Lab. It is observed that the cross sections, which have been decomposed in $\sigma_T + \epsilon\sigma_L$, σ_{TT} and σ_{LT} structure functions, are dominated by transverse amplitude contributions. The data can be interpreted in the Generalized Parton Distribution formalism provided that one includes helicity-flip transversity GPDs.

The formalism of Generalized Parton Distributions (GPDs) which has appeared in the last two decades (Refs. [1, 2, 3] for the original articles and Ref. [4] for a recent review) allows to interpret the exclusive electroproduction of photons or mesons on the nucleon in terms of quarks and gluons (i.e. partons), the fundamental degrees of freedom of Quantum Chromodynamics (QCD). It has been shown [5] that for these processes, at sufficiently large virtuality of the photon $Q^2 = (e-e')^2$, there is a factorization between a "hard" elementary scattering part at the quark or gluon level, exactly calculable in perturbative QCD, and a non-perturbative nucleon structure part, which encodes all the complex partonic structure of the nucleon and which is parametrized by GPDs. This factorization is illustrated in Fig. 1 for the case of π^0 electroproduction on the proton, on which we will focus in this article. For pseudoscalar meson production, it is shown that, at leading-twist QCD, this factorization is valid only for longitudinal incoming photons, that the longitudinal part of the cross section σ_L should dominate at asymptotically large Q^2 valuse and that two quark helicity-conserving GPDs contribute to the process: $\tilde{H}$ and $\tilde{E}$. These two GPDs correspond to the amplitudes where the nucleon spin remains unchanged or has been flipped respectively. At QCD leading-order, the GPDs depend on three independent variables: x, ξ and t. In simple terms, GPDs represent, in a frame where the nucleon goes to the speed of light in a certain direction, the probability amplitude of finding a quark in the nucleon with a longitudinal momentum fraction $x+\xi$ and of putting it back

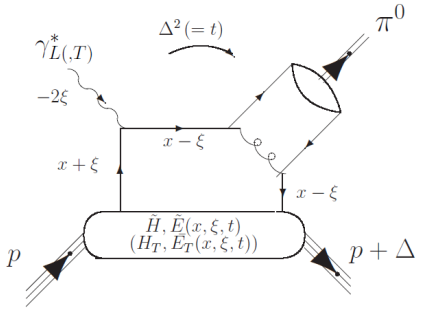

Figure 1: The "handbag" diagram for exclusive π^0 electroproduction on the proton in terms of GPDs. When longitudinal photons are involved, only the helicity-conserving GPDs $\tilde{H}$ and $\tilde{E}$ enter, while for transverse photons, the helicity-flip GPDs H_T and $\tilde{E}_T$ also enter the process. The various kinematical variables are explained in the text.

into the nucleon with a different longitudinal momentum fraction $x - \xi$, plus some transverse momentum "kick", which is represented by t. For the particular case of $\xi = 0$, the momentum transfer Δ (with $\Delta^2 = t$) is the conjugate variable of the impact parameter $b_\perp$ so that the GPDs encode both the longitudinal momentum distributions of partons inside the nucleon through their dependence on x and their transverse position distributions through their dependence on t. This allows for a sort of tomography of the nucleon where one can probe the transverse size of the nucleon for different quark momentum slices.

Recently, the CLAS collaboration has measured at Jefferson Lab with a 5.75-GeV electron beam the 4-fold differential cross sections $d^4\sigma/dtdQ^2dx_Bd\phi_\pi$ [1] of the $ep \to ep\pi^0$ reaction, thus extracting the structure functions $\sigma_T + \epsilon\sigma_L, \sigma_{TT}$ and σ_{LT} as functions of t over a wide range of Q^2 and x_B [6]. Fig. 2 shows a sample of these results (1800 kinematic points in bins of Q^2, x_B, t and ϕ_π were measured in all). These results are in agreement with the results of Ref. [7], which published high accuracy cross sections in a limited kinematical range in the lower Q^2, W and $|t|$ regions of the present experiment. One observes that the $d\sigma_{TT}/dt$ structure function (which is negative) is comparable in magnitude with the unpolarized structure function $d\sigma_U/dt = d\sigma_T/dt + \epsilon d\sigma_L/dt$). Furthermore, $d\sigma_{LT}/dt$ is small in comparison with $d\sigma_U/dt$ and $d\sigma_{TT}/dt$. In the same vein, in an earlier CLAS measurement [8], sizeable beam-spin asymmetries (proportional to the fifth structure function $\sigma_{LT'}$), were found for this same channel. Such non-zero asymmetries imply that both transverse and longitudinal amplitudes participate in the process. Similarly, at higher energies, the HERMES collaboration measured the transverse target spin asymmetry in the "cousin" channel of π^+ electroproduction [9]. The sizeable results can also only be explained by significant transverse amplitude contributions.

All these experimental observations point to the model-independent conclusion that the asymptotic leading-order handbag approach for which the longitudinal part of the cross section is dominant is not applicable at the present values of Q^2. Although model-dependent, this is confirmed by theoretical calculations of the handbag diagram for longitudinal virtual photons based solely on the $\tilde{H}$ and $\tilde{E}$ GPDs which are found to underestimate the measured cross sections by more than an order of magnitude, even after including finite–size corrections through Sudakov form factors[10].

This failure to describe these experimental results for exclusive pseudo-scalar meson electroproduction with quark helicity-conserving GPDs recently stimulated the consideration of the role of the chiral-odd quark helicity-flip contributions (i.e. where the active quark in Fig. 1 undergoes a helicity-flip), in particular through the introduction of so-called transversity GPDs; namely: H_T, which characterizes the quark distributions involved in nucleon helicity-flip, and $\bar{E}_T (= 2\widetilde{H}_T + E_T)$ which characterizes the quark distributions involved in nucleon helicity-non-flip processes [11, 12].

Pseudoscalar meson electroproduction, and in particular π^0 production, was identified [10, 13, 14] as especially sensitive to the quark helicity-flip subprocesses. The produced meson has no intrinsic helicity so that the angular momentum of the incident photon is either transferred to the nucleon via a quark helicity-flip or involves orbital angular momentum processes. In addition, for π^0 production the structure of the amplitudes further suppresses the quark helicity-conserving amplitudes relative to the helicity-flip amplitudes [10].

The results of two GPD-based models which include transversity GPDs [14, 15] are superimposed in Fig. 2. The GL and GK approaches, though employing different models of GPDs,

[1] The standard x_B Bjorken variable is related to ξ: $\xi \simeq x_B/(2 - x_B)$ and ϕ_π is the azimuthal angle between the leptonic and hadronic planes.

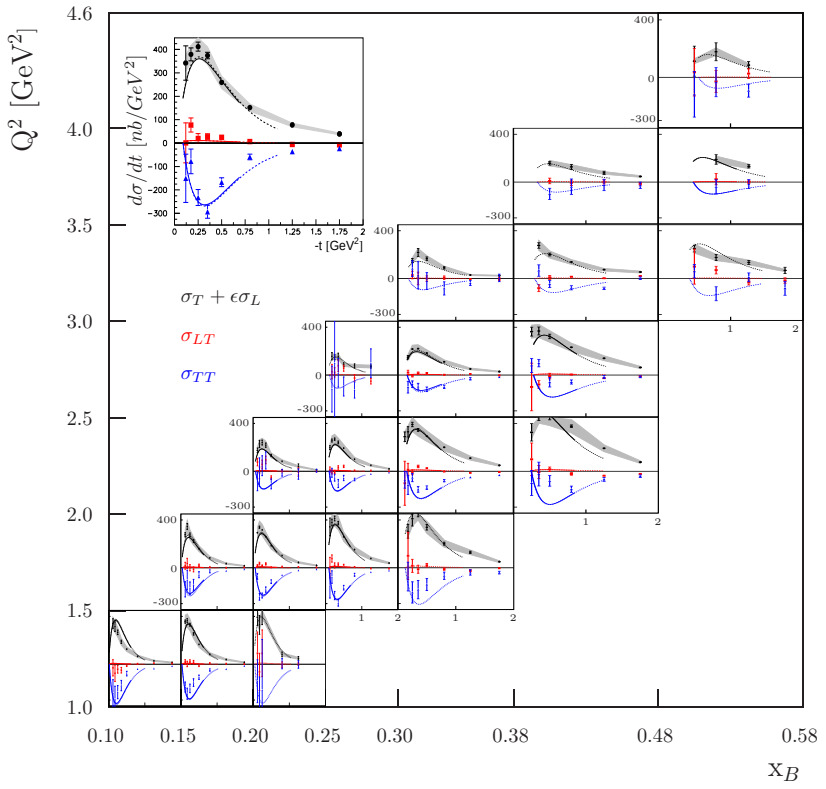

Figure 2: The extracted structure functions vs. t as measured by CLAS. The data and curves are as follows: black (filled circles) - $d\sigma_U/dt = d\sigma_T/dt + \epsilon d\sigma_L/dt$, blue (triangles) - $d\sigma_{TT}/dt$, and red (squares) - $d\sigma_{LT}/dt$. The curves are theoretical predictions produced with the models of Refs. [14] (solid) and [15] (dashed).

lead to transverse photon amplitudes that are much larger than the longitudinal amplitudes. These latter account for only a small fraction (typically less than 10%) of the unseparated structure functions $d\sigma_T/dt + \epsilon d\sigma_L/dt$ in the kinematic regime under investigation. With such inclusion of the quark-helicity non-conserving chiral-odd GPDs, which contribute primarily to $d\sigma_T/dt$ and $d\sigma_{TT}/dt$ and, to a lesser extent, to $d\sigma_{LT}/dt$, the model of Ref. [14] agrees rather well with the data. Deviations in shape become greater at smaller $-t$ for the unseparated cross section $d\sigma_U/dt$. The behavior of the cross section as $|t| \to |t|_{min}$ is determined by the interplay between H_T and $\bar{E}_T$. For the GPDs of Ref. [14] the parameterization was guided by the lattice calculation results of Ref. [12], while Ref. [15] used a GPD Reggeized diquark-quark model to obtain the GPDs. The results in Fig. 2 for the model of Ref. [14] (solid curves), in which $\bar{E}_T$ is dominant, agree rather well with the data. In particular, the structure function σ_U begins to decrease as $|t| \to |t|_{min}$, showing the effect of $\bar{E}_T$. In the model of Ref. [15] (dashed curves) H_T is dominant, which leads to a large rise in cross section as $-t$ becomes small so that the contribution of $\bar{E}_T$ relative to H_T appears to be underestimated. One can make a similar conclusion

from the comparison between data and model predictions for σ_{TT}. This shows the sensitivity of the measured π^0 structure functions for constraining the transversity GPDs.

We also mention that π^+ electroproduction has also been measured by the CLAS collaboration [16] in the same phase space. It is found that the GK model describes also qualitatively the low-t unseparated cross sections over the whole (x_B, Q^2) domain, when the same transversity GPDs are included. In π^+ production, the role of transversity GPDs is less apparent because of the presence and dominance of the longitudinal π^+-pole term (which is absent in π^0 production). However, this latter contribution has an important contribution only in the low $|t|$ domain and only for the lowest x_B and the largest Q^2 values, leaving sensitivity to other contributions, namely transversity GPDs.

In conclusion, differential cross sections of exclusive π^0 (and π^+) electroproduction on the proton have been obtained in the few-GeV region in a wide Q^2, x_B, t, ϕ_π phase space with the CLAS detector at JLab, from which the structure functions $d\sigma_U/dt$, $d\sigma_{TT}/dt$ and $d\sigma_{LT}/dt$ could be extracted. It is found that $d\sigma_U/dt$ and $d\sigma_{TT}/dt$ are comparable in magnitude with each other, while $d\sigma_{LT}/dt$ is very much smaller than either pointing to the dominance of transverse amplitude contributions to the process.

Within the handbag interpretation, there are two independent theoretical calculations [14, 15] which confirm that the measured unseparated cross sections are much larger than expected from leading-twist handbag calculations which are dominated by longitudinal photons. When including transversity GPDs, the general shapes and magnitudes of the various structure functions are reproduced. Extensive new CLAS measurements of beam spin, target spin and double-spin asymmetries for exclusive pseudo-scalar electroproduction on the proton are currently under analysis. Comparison of these results with theoretical models will allow to confirm (or not) the GPDs interpretations that we have outlined here.

This material is based upon work supported by the U.S. Department of Energy, Office of Science, Office of Nuclear Physics under contract DE-AC05-06OR23177.

References

[1] D. Mueller, D. Robaschik, B. Geyer, F. M. Dittes and J. Horejsi, Fortsch. Phys. **42** (1994) 101.

[2] X. D. Ji, Phys. Rev. Lett. **78** (1997) 610, Phys. Rev. D **55** (1997) 7114.

[3] A. V. Radyushkin, Phys. Lett. B **380** (1996) 417, Phys. Rev. D **56** (1997) 5524.

[4] M. Guidal, H. Moutarde and M. Vanderhaeghen, Rept. Prog. Phys. **76** (2013) 066202.

[5] J. C. Collins, L. Frankfurt and M. Strikman, Phys. Rev. D **56** (1997) 2982.

[6] I. Bedlinskiy *et al.* [CLAS Collaboration], arXiv:1405.0988 [nucl-ex].

[7] E. Fuchey, A. Camsonne, C. Munoz Camacho, M. Mazouz, G. Gavalian, E. Kuchina, M. Amarian and K. A. Aniol *et al.*, Phys. Rev. C **83** (2011) 025201.

[8] R. De Masi *et al.* [CLAS Collaboration], Phys. Rev. C **77** (2008) 042201.

[9] A. Airapetian *et al.* [HERMES Collaboration], Phys. Lett. B **682** (2010) 351.

[10] S. V. Goloskokov and P. Kroll, Eur. Phys. J. C **65** (2010) 137.

[11] M. Diehl and P. Hagler, Eur. Phys. J. C **44** (2005) 87.

[12] M. Gockeler *et al.* [QCDSF and UKQCD Collaborations], Phys. Rev. Lett. **98** (2007) 222001.

[13] S. Ahmad, G. R. Goldstein and S. Liuti, Phys. Rev. D **79** (2009) 054014.

[14] S. V. Goloskokov and P. Kroll, Eur. Phys. J. A **47** (2011) 112.

[15] G. R. Goldstein, J. O. Hernandez and S. Liuti, Phys. Rev. D **84** (2011) 034007, Int. J. Mod. Phys. Conf. Ser. **20** (2012) 222, J. Phys. G **39** (2012) 115001.

[16] K. Park *et al.* [CLAS Collaboration], Phys. Rev. C **85** (2012) 035208.

New JLab/Hall A Deeply Virtual Compton Scattering results

Maxime Defurne[1] for the Hall A DVCS collaboration

[1]CEA, Centre de Saclay, IRFU/SPhN/LSN, F-91191 Gif-sur-Yvette, France

DOI: http://dx.doi.org/10.3204/DESY-PROC-2014-04/32

New data points for unpolarized Deeply Virtual Compton Scattering cross sections have been extracted from the E00-110 experiment at Q^2=1.9 GeV^2 effectively doubling the statistics available in the valence region. A careful study of systematic uncertainties has been performed.

Generalized Parton Distributions (GPDs) correlate the spatial and momentum distributions of partons inside the nucleon. They are nowadays the main way to study the orbital angular momentum of quarks via the Ji's sum rule. As GPDs are accessible through deep exclusive processes, a worldwide experimental program has been developped to study them [1]. Experiment E00-110 has been designed to investigate the electroproduction of photons ($ep \rightarrow ep\gamma$). Beam helicity dependent cross sections at x_B=0.36 and Q^2 = {1.5,1.9,2.3} GeV^2 have been published by Munoz *et al.* in 2006 [2]. An additional unpolarized cross section at the highest value of Q^2 was extracted at 2.3 GeV^2. Here we present the extraction of the unpolarized cross section at the intermediate Q^2= 1.9 GeV^2.

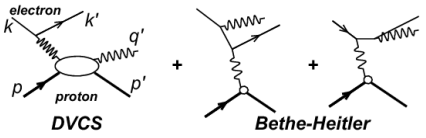

Figure 1: Lowest order QED diagrams for DVCS and Bethe Heilter processes. Defining $q = k - k'$, Q^2=$-|q|^2$ and t=$|p - p'|^2$. x_B is given by $\frac{Q^2}{2p \cdot q}$.

1 Phenomenological framework

Photon electroproduction in the deep inelastic kinematics includes the coherent contribution of Bethe-Heitler, where the photon is emitted by the incoming or scattered electron, and Deeply Virtual Compton Scattering (DVCS) where the photon is emitted by the proton (see figure 1). The amplitude for DVCS is parametrized by Compton form factors (CFF) which are complex integral of GPDs. The interference between these two processes makes the photon electroproduction a golden channel because it gives access to the real and imaginary parts of CFFs. Kumericki and Muller [3] performed a Fourier expansion of the different contributions according to ϕ, the angle between the leptonic and the hadronic plane. The information about the GPD is embedded in the Fourier coefficients of the DVCS amplitude and the interference term. The

amplitude of photon electroproduction $A_{ep\to ep\gamma}$ is given by:

$$\begin{aligned} |A_{ep\to ep\gamma}|^2 &= |A_{DVCS}|^2 + |A_{BH}|^2 + I_{BH/DVCS}, \text{ with} \\ |A_{DVCS}|^2 &\propto c_0^{DVCS} + \sum_{n=1}^{2} \Big(c_n^{DVCS} cos(n\phi) + s_n^{DVCS} sin(n\phi) \Big) \\ I_{BH/DVCS} &\propto c_0^{I} + \sum_{n=1}^{2} \Big(c_n^{I} cos(n\phi) + s_n^{I} sin(n\phi) \Big) \end{aligned} \tag{1}$$

Indeed c_n^{DVCS} and s_n^{DVCS} (respectively c_n^I and s_n^I) are bilinear (respectively linear) combinations of CFFs. The amplitude of the Bethe Heitler is exactly known assuming a reliable parameterization of the form factors of the nucleon. The beam helicity independent cross section is mostly sensitive to $\mathcal{H}\mathcal{H}^*$ and Re$\mathcal{H}$, and the difference of beam helicity dependent cross sections to Im$\mathcal{H}$.

2 Experimental setup

The experiment ran in the Hall A of Jefferson Laboratory [4] in the spring of 2004, using the 80%-polarized 5.75 GeV continuous electron beam provided by CEBAF impinging on a 15-cm long liquid hydrogen target. The left high resolution spectrometer was dedicated to the scattered electron detection.

A dedicated electromagnetic calorimeter made of $11 \times 12 = 132$ lead fluoride blocks read by photomultiplier tubes (PMTs) was used to detect the outgoing photon.

A recoil detector was built for the proton detection but it was demonstrated that a cut on the squared missing mass associated to the reaction $ep \to e\gamma X$ was enough to ensure the exclusivity. As the proton detector was limiting the acceptance, it was not used in this analysis.

3 Subtraction of π^0 contamination

In their center-of-mass frame, π^0 isotropically decay into two photons, emited back-to-back. While, in the laboratory frame, due to the directionality of the Lorentz boost, the decay photons share the energy asymetrically in most cases. As a result, one of them may get most of the energy and the other one almost nothing, impossible to detect because of the 1 GeV threshold imposed on the calorimeter. In that case, as exclusive π^0 have an energy close to the one of an exclusive photon, we will interpret it as an exclusive photon.

To subtract this contamination, The sample of π^0's whose two photons have been detected is used. Knowing their 4-momenta, we simulate their decay N_{gen}=5000 times thanks to a Monte Carlo simulation. Among the N_{gen} decays, there are:

- n_0 events where none of the photons have been detected, or only one photon detected but with an associated missing mass not compatible with an exclusive photon event.
- n_2 events where the two photons are detected.
- n_1 events where one photon is detected with a missing mass compatible with an exclusive photon event.

For each of the n_1 decays, the kinematic variables t, ϕ are computed as if it was an exclusive photon event. Then this event is considered with the weight $\frac{1}{n_2}$ in the corresponding experimental bin. At the end of the day, the contamination is estimated in all the experimental bins.

This method naturally includes the π^0 electroproduction cross section in the subtraction. Since it relies strongly on our ability to detect the two photons of the decay, we apply a geometrical cut on the calorimeter surface to remove its edges and corners.

4 Monte Carlo simulation

The Monte Carlo simulation has been upgraded to Geant4. Radiative corrections are applied following the method described in [5]. Emission of soft photons from internal bremmstrahlung is handled using the equivalent radiator method.

Because of radiation damage, blocks close to the beam have a poorer energy resolution than the ones far from the beam. As a consequence, the exclusivity peak in the $M^2_{ep\to e\gamma X}$ will be larger close to the beam than far from it. Since binning in t and ϕ translates into geometrical cuts in the calorimeter, it is vital to have a good match between the Monte Carlo and the experimental missing mass spectrum.

To estimate the error due to the exclusivity cut, we studied the cross section variations when changing the missing mass cut.

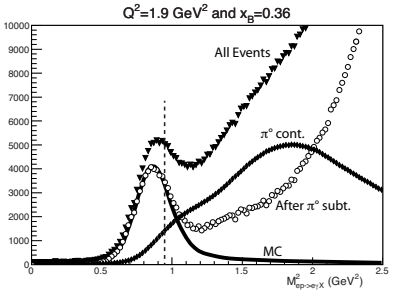

Figure 2: Missing mass spectrum associated to $ep \to e\gamma X$. To ensure exclusivity, we require a value below 0.95 GeV^2.

5 Cross section and CFF extraction

Using the formalism developped in [3], we parameterize the cross section in terms of CFFs. However there are too many unknowns with respect to our data. By assuming twist-2 dominance and a sizeable $|DVCS|^2$ contribution (as hinted in [2]), we end up using three parameters in order to fit each data bin in ϕ and t (equation 4). We studied 5 bins in t, each of them with 24 bins in ϕ, giving a total number of bins N_{bin}=120.

To fit each of the 5 t-bins, we minimize the following χ^2:

$$\chi^2 = \sum_{k=0}^{N_{bin}} \left(\frac{N_k^{exp} - N_k^{sim}}{\sigma_k^{exp}} \right)^2 \tag{2}$$

where N_k^{exp} is the number of counts in bin k from data after subtraction of contamination, and σ_k^{exp} represents the statistical uncertainty on the number of counts in the bin k. N_k^{sim} the

number of counts in the bin k expected with the Monte Carlo simulation and is given by:

$$N_k^{sim} = L \int_{\Phi_k} \frac{d^4\sigma}{d\Phi} d\Phi_k, \quad (3)$$

$$\frac{d^4\sigma}{d\Phi} = \frac{d^4\sigma_{BH}}{d\Phi} + \Gamma^{\mathcal{C}^{DVCS}_{unp}} \times \mathcal{C}^{DVCS}_{unp} + \Gamma^{\mathcal{C}^I(\mathcal{F})} \times Re\mathcal{C}^I(\mathcal{F}) + \Gamma^{\mathcal{C}^I(\mathcal{F}_{eff})} \times Re\mathcal{C}^I(\mathcal{F}_{eff}), \quad (4)$$

with L the integrated luminosity of the experiment and Φ_k the phase space of the experimental bin.

The coefficients Γ in equation 4 are given by [3] and depend on ϕ, t, x_B and Q^2. Their integral is performed using the Monte Carlo simulation and help us to take into account most of the kinematic dependences. Finally, by evaluating the coefficients Γ at the vertex and applying selection cuts on the variables reconstructed by the detectors, we correct for bin migration.

At the end of the day, we obtain unpolarized photon electroproduction cross sections at x_B=0.36 and Q^2=1.9 GeV^2. The photon electroproduction cross sections will be published at the end of the year 2014.

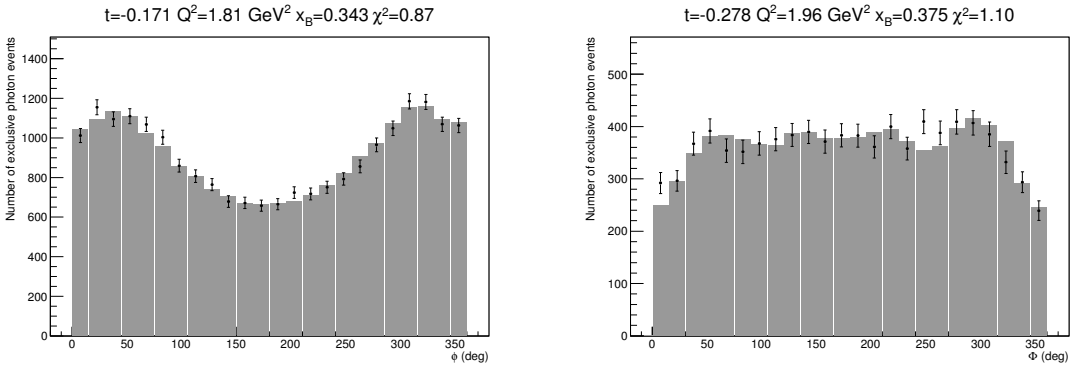

Figure 3: The markers are the number of counts from experiment. The histograms represent the number of counts expected by the Monte Carlo simulation once the cross section has been extracted by the fitting procedure.

References

[1] M. Guidal, H. Moutarde, and M. Vanderhaeghen, "Generalized Parton Distributions in the valence region from Deeply Virtual Compton Scattering," *accepted in Rep. Prog. Phys.*, vol. 76, 2013.

[2] C. Muñoz Camacho *et al.*, "Scaling tests of the cross-section for deeply virtual compton scattering," *Phys.Rev.Lett.*, vol. 97, p. 262002, 2006.

[3] A. Belitsky and D. Mueller, "Exclusive electroproduction revisited: treating kinematical effects," *Phys.Rev.*, vol. D82, p. 074010, 2010.

[4] J. Alcorn *et al.*, "Basic instrumentation for hall a at jefferson lab," *Nucl. Instrum. Meth.*, vol. A522, pp. 294–346, 2004.

[5] M. Vanderhaeghen, J. M. Friedrich, D. Lhuillier, D. Marchand, L. Van Hoorebeke, and J. Van de Wiele, "Qed radiative corrections to virtual compton scattering," *Phys. Rev.*, vol. C62, p. 025501, 2000.

COMPASS Polarized Target for Pion-Induced Drell–Yan Experiment

Jan Matoušek[1] on behalf of the COMPASS collaboration

[1]Charles University, Faculty of Mathematics and Physics, Prague, Czech Republic

DOI: http://dx.doi.org/10.3204/DESY-PROC-2014-04/35

The first ever polarized Drell–Yan (DY) measurement is under preparation at COMPASS experiment at CERN. One of the key parts is the low-temperature polarized target. Modifications are required to cope with the intense pion beam that will be used. Solid NH_3 will serve as a transversely-polarized target. Polarization is expected to be up to 90%. Two 55 cm long target cells give the target volume of about 690 cm^3. The data taking is expected to start on fall 2014 and to continue in 2015 (approximately 180 days). Current status of the target, the modifications and future plans are presented.

1 Introduction

COMPASS [1] is a fixed-target experiment situated at CERN Super Proton Synchrotron (SPS) North Area. For physics data taking it uses either hadron or muon beams[1]. The beam interacts with a target, which can be polarized. COMPASS detector is a universal spectrometer with good particle tracking and identification capability.

COMPASS experiment focuses on spin structure studies and hadron spectroscopy [2]. The first ever measurement of a single-polarized Drell–Yan (DY) process using a pion beam and a transversely-polarized proton target was proposed [3]. Its goal is to test some crucial predictions of QCD, namely a change of sign of the Sivers and Boer–Mulders TMDs when measured in Semi-Inclusive Deep-Inelastic Scattering (SIDIS) and in DY processes.

As the DY cross section is small, the luminosity should be as high as possible. In the case of COMPASS this corresponds to the beam intensity of about 10^8 pions/s. That is the highest hadron beam intensity COMPASS has used so far, which leads to several challenges for the detection, data acquisition and the polarized target.

2 Polarized target

The low-temperature polarized target [1, 4] is a key instrument for COMPASS spin structure studies. It is one of the biggest systems of its kind in the world[2] and can provide degree of polarization higher than 80% in the case of H in NH_3 and 50% in the case of D in ^{6}LiD [5].

[1]Produced by proton beam from the SPS hitting a Be target. The beam can be either positive or negative with momentum up to 280 GeV/c. Muons are naturally longitudinally polarized.

[2]The target volume has cylindrical shape with about 4 cm in diameter and is about 120 cm long.

The target material is polarized by Dynamic Nuclear Polarization (DNP) method [6] at about 0.5 K. When the optimal polarization is reached, the target is switched to a *frozen spin* mode at about 50 mK. A long spin-lattice relaxation time at such temperature (in order of 10^3 hours) allows to perform reasonably efficient experiment. Two microwave systems for DNP allow to have target cells with opposite polarization to reduce systematic errors in measured asymmetries.

The polarization is measured by a continuous-wave NMR. The cooling is provided by a dilution refrigerator, which has a power of about 5 mW at 75 mK [7]. A large-aperture superconducting magnet provides a field up to 2.5 T parallel and 0.64 T perpendicular to the beam axis. Homogeneity of the longitudinal field is about 10^{-5} T. Combination of the two fields allows measurement with transverse polarization and polarization rotation.

3 Drell–Yan program at COMPASS

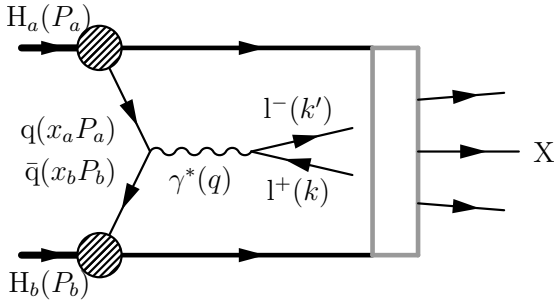

Figure 1: The Drell–Yan process. A quark-antiquark pair from the two hadrons annihilate, producing a lepton-antilepon pair in final state. The grey box denotes hadronization.

The Feynman graph on Fig. 1 shows the Drell–Yan (DY) process, which has lately attracted much attention as a tool for polarized hadron structure studies. Its main advantage is that only leptons are measured in the final state, which means that the cross section does not involve any fragmentation function but only convolution of structure functions of both hadrons. The process is well calculable, dedicated calculations of the pion-induced DY process for the COMPASS kinematics were recently published [8].

The disadvantage of the DY process is a small cross section. To collect a good statistics a beam with intensity up to 10^8 pions/s will be used resulting in a large secondary-hadron flux. A special hadron absorber was designed to stop the non-interacting beam and all secondary particles except muons right after the target to avoid a spectrometer flooding-up [3]. It is made of stainless steel and alumina, with a tungsten beam plug in the centre to stop the beam.

The high intensity pion beam together with the hadron absorber will cause slightly higher radiation dose in the experimental building than in previous runs. Because of that the control room will be moved to another building.

4 Modifications of the target for the DY program

The DY program, namely the intense hadron beam and the presence of the absorber brought need for modification of the target. New target cells were made. There are two cells (4 cm in diameter, 55 cm long) with 20 cm long microwave stopper in between[3]. The gap between the cells prevents event migration between oppositely-polarized cells. It is wider than in the SIDIS runs since the hadron absorber introduces significant multiple scattering, which worsens the vertex resolution. A special adapter was designed for the microwave cavity to accommodate two cells with one stopper instead of two.

The NMR system for polarization measurement has 10 coils. Three coils are placed outside of each cell and are oriented for measurement in the longitudinal field. Two coils are placed inside each cell near the ends for polarization homogeneity monitoring.

The target superconducting magnet was refurbished by CERN magnet group. In addition to the fixed trim coils it got various upgrades, e. g. better thermal insulation and new control and safety system.

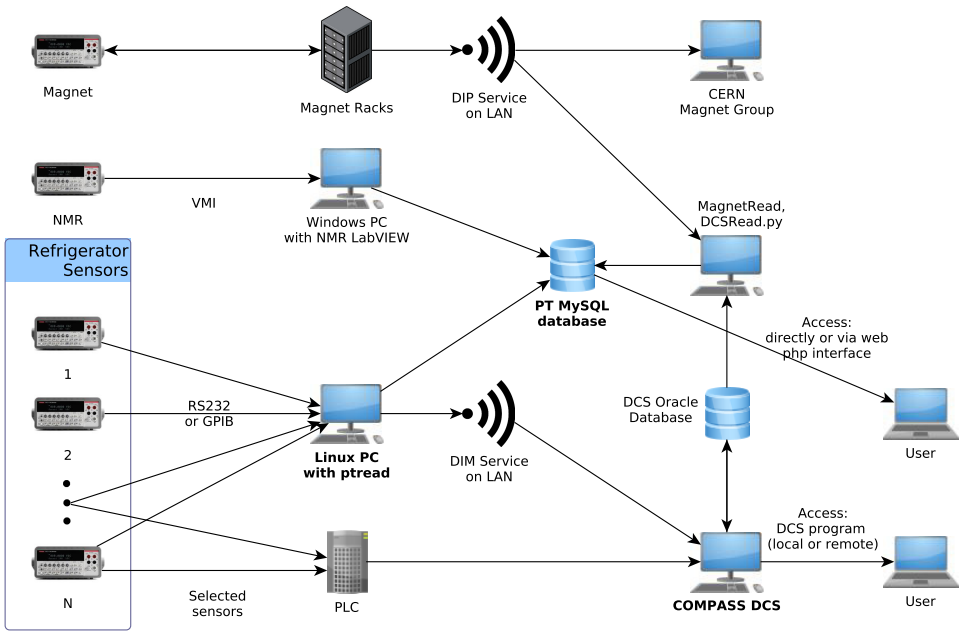

Figure 2: Diagram of target monitoring. The Linux computer with ptread package reads refrigerator sensors. Data can be stored locally in SQLite database, sent to MySQL database and published by DIM server for COMPASS DCS. The magnet is monitored by CERN experts and NMR by a LabVIEW^{TM} program.

Since the control room was moved from the experimental building, a remote control is necessary. For most systems the current COMPASS centralised Detector Control System (DCS) was working well, but the dilution refrigerator was only partly monitored by it. It was decided

[3]The SIDIS design was three cells (30-60-30 cm long, 4 cm in diameter) with 5 cm long stoppers.

to abandon the old LabVIEW^{TM} system [9] for refrigerator monitoring and to develop a new, more robust, Linux-based software called *ptread* instead. It can communicate with the DCS using DIM library [10] and insert data into MySQL and SQLite databases. These features are important for the remote monitoring. The main advantage is that the software package is modular and easily adjustable. Figure 2 shows how various subsystems of the target (including the refrigerator) are monitored.

In addition to the *ptread* PC there is a Programmable Logic Controller (PLC) unit that monitors the most important parameters of the refrigerator [9]. It is powered from a source insensitive to power failures.

5 Conclusion

The magnet was refurbished and is being cooled down and commissioned. Dilution refrigerator was tested and mounted in place. Its sensors are connected to the new Linux-based monitoring system. The new target cells are ready. The target will be prepared for the physics data taking, that is scheduled from the beginning of November 2014. Second run is planned for 2015. In total there should be about 180 days of data taking.

Acknowledgements

This work was supported in part by the European Community-Research Infrastructure Activity under the FP7 programme (Hadron Physics 3), Czech Republic MEYS grants.

References

[1] P. Abbon *et al.*, NIM **A 577** 455 (2007).

[2] The COMPASS Collaboration, *List of COMPASS publications*, `http://wwwcompass.cern.ch/compass/publications/`

[3] The COMPASS Collaboration, *COMPASS-II Proposal*, CERN SPSC **014** 340 (2010).

[4] J. H. Koivuniemi *et al.*, JPCS **150** 012023 (2009).

[5] K. Kondo *et al.*, NIM **A 526** 70 (2004).

[6] A. Abragam, M. Goldman, Rep. Prog. Phys. **41** 395 (1978).

[7] N. Doshita *et al.*, NIM **A 526** 138 (2004).

[8] M. Aicher, A. Schäfer and W. Vogelsang, Phys. Rev. **D 83** 114023 (2011).

[9] F. Gautheron *et al.*, NIM **A 526** 147 (2004).

[10] C. Gaspar *et al.*, *Distributed information management system*, `http://dim.web.cern.ch/dim/`.

Soft QCD Measurements at LHCb

A. T. Grecu on behalf of the LHCb Collaboration

Horia Hulubei National Institute for Physics and Nuclear Engineering (IFIN-HH),
30 Reactorului, RO-077125, Bucharest-Măgurele, Romania

DOI: http://dx.doi.org/10.3204/DESY-PROC-2014-04/249

Its forward acceptance puts the LHCb in a unique position at the LHC to measure soft QCD phenomena at large rapidities and low transverse momenta. Recent results on charged particle multiplicities, energy flow, and inclusive cross-sections are presented.

1 The LHCb experiment at LHC

The LHCb experiment at LHC was designed to test the flavour aspect of the Standard Model through precision measurements of rare b and c hadron decays [1]. The LHCb detector [2] is built as a single arm forward spectrometer fully instrumented for measurements in the forward pseudorapidity (η) region $2 < \eta < 5$. The primary pp interaction region is located within a silicon-strip vertex detector (VELO) which allows reconstruction of tracks without momentum information also in the backward pseudorapidity interval $-3.5 < \eta < -1.5$. The high-precision tracking system [3] continues with a large area silicon tracker located upstream of a magnetic dipole with a bending power of 4 Tm and three stations of silicon-strip detectors and straw drift tubes situated downstream of the magnet. A calorimetry system is used to measure the neutral component and muons are detected by a dedicated system of alternating layers of iron and multi-wire proportional chambers [4]. The LHCb experiment is operated at a low and consistent number of visible proton-proton (pp) interactions.

Monte Carlo (MC) simulated events were used to compute detection efficiencies, estimate systematic uncertainties and compare model predictions with respect to the measurements. Full simulation samples are produced using PYTHIA6.4 [6] configured according to established tunes [7] or the LHCb specific tune [8].

2 Vector meson central exclusive production

Exclusive vector meson photoproduction provides a rich testing ground for QCD. At high meson masses the process can be predicted using perturbative calculations [9]. The light meson production is best described in the frame of the Regge theory [10]. The elastic pp interaction is mediated by the exchange of a colourless object such as a gamma photon or a pomeron, which is replaced by two gluons at hard scales. The colliding protons propagate undetected in the beam pipe. Here, we review the central elastic exclusive production of the J/ψ and $\psi(2S)$ vector mesons decaying to two muons [11] as an update of a previous measurement [12] where a smaller data sample was analysed. The main difference is in the method for determining the background due to production of J/ψ and $\psi(2S)$ mesons in inelastic pp collisions where

the additional particles leave the LHCb acceptance and remain undetected. This is the main source of background. It is determined from a fit of the squared momentum of the muon pair (p_T^2) distribution that follows closely HERA measurement [13] extrapolations according to Regge theory. Additional non-resonant background (muon pairs created in the QED process) is estimated from side-bands in the invariant mass spectrum and feed down background from exclusive production of heavier meson decays is evaluated from simulation. The cross-section times the branching fraction of the decay mode to two muons, each inside the LHCb fiducial range ($2.0 < \eta_{\mu^\pm} < 4.5$), is in good agreement with various theoretical predictions. Figure 1 shows the comparison to the LO and NLO predictions from a fit on a combined HERA and LHCb data sample. The NLO prediction tends to better reproduce the differential cross-section shape in data.

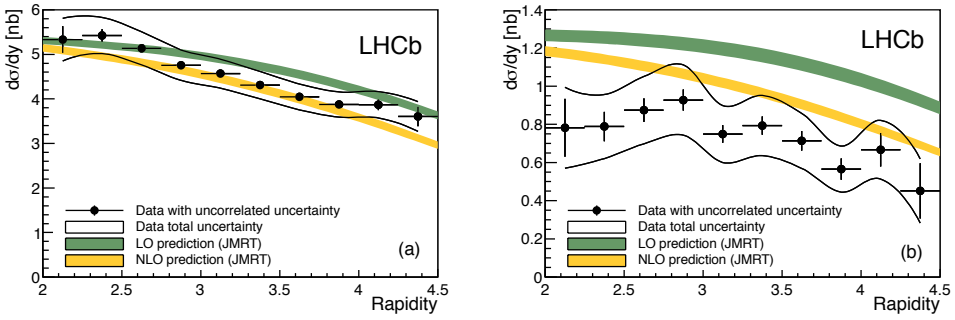

Figure 1: Differential cross-section for (a) J/ψ and (b) $\psi(2S)$ central exclusive production compared to LO and NLO predictions of [14]. The bands indicate the total uncertainties which are mostly correlated between bins. Errors bars contain only the statistical uncertainty.

The measured photoproduction cross-section shows a deviation from the power law established at HERA [15] which can be accounted to higher order or saturation effects. In the low parton fractional momentum (x) domain accessible to the LHCb detector saturation effects manifest due to gluon recombination. Thus, theoretical saturation models can be constrained by measurement through their dependence on the gluon parton density function. The considered models [16] are found in good agreement with the LHCb data.

3 Energy flow and charged particle multiplicities

The final state of an inelastic hadron-hadron collision can be described in QCD as the combined effect of hard and soft scattering processes of the hadron constituents, initial- and final-state radiation and the fragmentation of coloured final state into colour-neutral hadrons. While the hard scattering is well predicted by perturbative QCD, the theoretical modelling of the soft component, also called the underlying event (UE), remains a challenge. The phenomenological approach to this issue is done differently in various generators leading to model parameters to be constrained by experiment for specific beam particles and energies. Recently, LHCb studied two basic observables describing the UE in the forward region, the energy flow [17] which is sensitive to the multi-parton interactions arising especially at low x where the parton densities are high, and the prompt charged particle multiplicities and densities [18, 19] as physical quantities characterizing the overall UE activity.

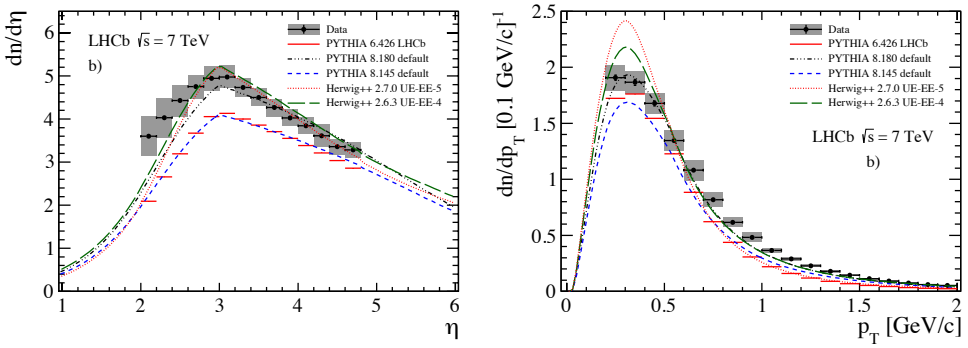

Figure 2: Charged particle density as function of (left) η and (right) p_T compared to PYTHIA8 and HERWIG++ predictions. Error bars represent the statistical negligible uncertainty. Grey bands give the extent of the combined uncertainties.

The energy flow is defined as the average energy created in a particular η range normalised by the range size. The charged forward energy flow measurement was performed using only tracking information, approximating the energy with the value of the momentum. The total energy flow is computed using data-constrained estimates from simulation corrected with informations from the calorimeter system to get the neutral component. The events are split in four classes: inclusive minimum bias, hard scattering with at least one high p_T track, diffractive enriched events requiring that there be no track in the backward region ($-3.5 < \eta < -1.5$) and the alternative non-diffractive enriched ones. Corrections are done in each η bin using MC. The dominant uncertainties come from the simulation model uncertainty on the bin-by-bin correction factors. The energy flow distributions are compared to the predictions of a series of PYTHIA tunes [7, 20] and cosmic-ray interaction models [21]. PYTHIA 8.135 emulates best the data in all event classes except for the hard scattering interactions. Among the cosmic-ray interaction models SYBILL closely follows the PYTHIA8 behaviour. The hard scattering events are better described by QGSJET. Experimental uncertainties are lowest in the forward region where the largest divergences between models are seen. This aspect confirms the energy flow as an important observable for generator tuning.

The measurement of charged particle multiplicities and densities follows closely a previously published measurement [18] adding the measurement of momentum. Prompt charged particles are defined as particles originating from PV or a decay chain in which the sum of the mean lifetimes is below 10 ps, thus the decay products of b and c hadrons are prompt. Only events with at least one track in $2.0 < \eta < 4.8$ having $p_T > 0.2$ GeV/c and $p > 2$ GeV/c are considered. Furthermore only tracks traversing the full tracking system are included in the analysis. The analysis kinematic range is $0.2 < p_T < 2.0$ GeV/c; $2.0 < \eta < 4.5$. Distributions are corrected in each bin for reconstruction artefacts and non-prompt particle contamination, the effect of unobserved events especially at low multiplicities, pile-up events and various other detection inefficiencies. The systematic uncertainties are dominated by the uncertainty on the amount of detector material contributing to the production of non-prompt particles.

Charged particle densities and multiplicities are compared to estimates obtained for various PYTHIA6 tunes and PHOJET [22] which fail to match the magnitude of the distributions. Overall data shape is well described qualitatively by all the generators including PYTHIA8 and HERWIG++ [23] tuned to central region measurements (see Fig. 2). Never-

theless, HERWIG++ largely overestimates at low p_T and PYTHIA8 underestimate the data at large p_T, so none of the considered event generators can describe the entire range of the measurements which make these results valuable reference points toward a successful tuning of generators in the forward region.

Acknowledgements

The author kindly acknowledges financial support through grant PN-II-ID-PCE-2011-3-0749 (56/07.10.2011), IDEI program and contract LHCb 3/03.01.2012, program PN-II:Capacităţi-3.

References

[1] B. Adeva *et al.* arXiv:hep-ex/0912.4179 (2009).

[2] A. A. Alves Jr. *et al.*, JINST **3** S08005 (2008).

[3] R. Aaij *et al.*, JINST **9** 09007 (2014);
R. Aaij *et al.* arXiv:hep-ex/1408.1251 (2014).

[4] A.A. Alves Jr. *et al.*, JINST **8** P02022 (2013);
F. Archilli *et al.*, JINST **8** P10020 (2013).

[5] R. Aaij *et al.*, JINST **8** P04022 (2013).

[6] T. Sjostrand, S. Mrenna, and P. Z. Skands, JHEP **0605** 026 (2006).

[7] P. Z. Skands, Phys. Rev. **D82** 074018 (2010).

[8] I. Belyaev *et al.*, J. Phys.: Conf. Ser. **331** 032047 (2011).

[9] A.D. Martin, C. Nockles, M. G. Ryskin, and T. Teubner, Phys. Lett. **B662** 252–258 (2008).

[10] P.D.B. Collins, *An Introduction to Regge Theory and High-Energy Physics* (Cambridge Univ. Press, Cambridge, 1977).

[11] R. Aaij *et al.*, J. Phys. G: Nucl. Part. Phys. **40** 045001 (2013).

[12] R. Aaij *et al.*, J. Phys. G: Nucl. Part. Phys. **41** 055002 (2014).

[13] C. Adloff *et al.*, Phys. Lett. **B541** 251-264 (2002); arXiv:hep-ex/0205107.

[14] S.P. Jones, A.D. Martin, M.G. Ryskin, and T. Teubner, JHEP **1311** 085 (2013).

[15] C. Alexa *et al.*, Eur. Phys. J. **C73** 2466 (2013).

[16] L. Motyka and G. Watt, Phys. Rev. **D78** 014023 (2008);
M. B. Gay Ducati, M.T. Griep, and M.V.T. Machado, Phys. Rev. **D88** 017504 (2013).

[17] R. Aaij *et al.*, Eur. Phys. J. **C73** 2421 (2013).

[18] R. Aaij *et al.*, Eur. Phys. J. **C72** 1947 (2012).

[19] R. Aaij *et al.*, Eur. Phys. J. **C74** 2888 (2014).

[20] T. Sjostrand, S. Mrenna, and P. Z. Skands. Comput. Phys. Commun. **178** 852–867 (2008).

[21] T. Pierog and K. Werner, Nucl. Phys. Proc. Suppl. **196** 102–105 (2009);
S. Ostapchenko, AIP Conf. Proc. **928** 118–125 (2007);
E.-J. Ahn, R. Engel, T. K. Gaisser, P. Lipari, and T. Stanev, Phys. Rev. **D80** 094003 (2009).

[22] R. Engel, Z. Phys. **C66** 203–214 (1995).

[23] M. Bahr *et al.*, Eur. Phys. J. **C58** 639–707 (2008);
J. Bellm *et al.*, arXiv:hep-ph/1310.6877 (2013).

Polarization Observables T and F in single π^0- and η-Photoproduction off quasi-free Nucleons

Thomas Strub

Department of Physics, University of Basel, Klingelbergstrasse 82, 4056 Basel, Switzerland

DOI: http://dx.doi.org/10.3204/DESY-PROC-2014-04/175

Meson photoproduction has developed into a powerful tool to study the nucleon excitation spectrum and test effective quark models which operate in the non-perturbative regime of QCD. An insight into the J^P configurations and isospin decompositions of the contributing resonances is gained by measuring a minimal set of polarization observables on both the proton and the neutron.

Single π^0- and η-photoproduction off a transversally polarized d-butanol target has been measured with circularly polarized bremsstrahlung photons generated by the MAMI-C electron microtron. With the nearly 4π acceptance of the combined Crystal Ball/TAPS setup the double polarization observable F and the target asymmetry T can be extracted for the first time for polarized, quasi-free neutrons over a wide energy and angular range.

1 Introduction

The nucleon and its excitation spectrum has been of great interest since many decades in order to study quantum chromodynamics in the non-perturbative regime. Due to the fact that many broad, overlapping resonances contribute to the excitation spectrum within a small energy range it cannot be understood from differential cross sections alone. While, for a long time, the method of choice to explore nucleon resonances was pion scattering with its large cross sections the attention came to photo- and electroproduction experiments when reaching higher intensity polarized electron beams, highly polarized targets with long relaxation times, and modern detector systems.

In the most general relativistic approach single pseudoscalar meson photoproduction gives access to four complex production amplitudes from which 16 real-valued polarization observables can be constructed [1]. These observables depend on beam, target and recoil polarization, and are, as well as the production amplitudes, functions of the invariant mass W and the production angle of the meson θ. The θ-dependence can be expanded in a partial-waves series by means of the electric and magnetic multipols $E_{l\pm}$ and $M_{l\pm}$, respectively, where l denotes the angular momentum. Thus, high statistic measurements of these observables in the (W, θ)-space allow to construct a uniquely determined solution of the production amplitudes up to a global phase through the partial wave analysis (PWA). It can be shown that eight carefully chosen observables have to be measured in order to find such a unique solution, which is called *complete experiment* [2].

Since the electromagnetic interaction does not conserve isospin the production vertex for single pseudoscalar meson photoproduction decomposes, in general, into three isospin ampli-

tudes, namely one isoscalar ($\Delta I = 0$), A^{IS}, and two isovector ($\Delta I = 0, \pm 1$), A^{IV} and A^{V3} (cf., e.g., [3]). Due to the fact that pions form an isospin triplet ($I = 1, I_3 = 0, \pm 1$) all three amplitudes contribute to π-photoproduction. In contrast, since η is an isospin singlet state, the isospin changing amplitude A^{V3} will not contribute to η-photoproduction. This makes photoproduction of isoscalar mesons especially interesting because it is selective to $N^*(I = 1/2)$ resonances only, whereas $\Delta(I = 3/2)$ resonances will not contribute. Nevertheless, in both cases, it is necessary to measure not only photoproduction off the proton but also off the neutron in order to fix all isospin amplitudes. A second reason for the interest in η-photoproduction off the neutron is the recent observation of a narrow structure around $W = 1670$ MeV which is not seen for the proton channel [4].

Due to the lack of free neutron targets photoproduction measurements off the neutron have always to be made with neutrons (weakly) bound in light nuclei within the quasi-free approximation. This gives rise to additional nuclear effects such as final state interactions (FSI). Indeed, a suppression of the free total cross section of about 25% is observed in π^0-photoproduction off quasi-free protons from the deuterium target [5]. However, η-photoproduction off quasi-free protons from the deuterium target does not show a significant difference [6]. In any case, it is reasonable to assume that this effect cancels out when measuring polarization observables.

In the following we present a preliminary analysis of the polarization observables T and F for single π_0- and η-photoproduction. Following the notation of [7] the differential cross section for a circularly polarized photon beam and a transversally polarized target reads

$$\frac{d\sigma}{d\Omega} = \frac{1}{2}\frac{d\sigma_0}{d\Omega}\left(1 + T P_T \sin\phi + F P_\odot P_T \cos\phi\right),$$

where P_T and $P_\odot$ denote the target and beam degree of polarization, respectively and ϕ is the angle between the target spin an the reaction plane.

2 Experiment and analysis

The experiment was performed at the MAMI-C accelerator in Mainz, Germany, which delivered a longitudinally polarized electron beam with energy of 1.557 GeV and a polarization degree of about 80%. Circularly polarized bremsstrahlung photons were produced in a radiator foil and were energy tagged with the Glasgow-Mainz photon tagger with energies between 0.47 GeV and 1.45 GeV. The resulting degree of polarization of bremsstrahlung photons from relativistic electrons depends on the photon energy E_γ and is described by Olsen and Maximon [8]. Transversally polarized target nucleons were provide by polarized deuterons of a frozen spin d-butanol (C_4D_9OD) target with a mean degree of polarization of about 80%.

The target was surrounded by the cylindrical particle identification detector (PID) made of 24 plastic scintillator strips, each covering an azimuthal angle of 15°. The PID was surrounded by a multi-wire proportional chamber (MWPC), which was not used in the current analysis. The spherical Crystal Ball calorimeter (CB) surrounding the MWPC consists of 672 NaI(Tl) crystals and covers polar angles from 20° to 160°. The forward direction was covered by the hexagonal two arm photon spectrometer (TAPS) built from 72 $PbWO_4$ (inner two rings) and 366 BaF_2 crystals (ring 3 to 11). A VETO wall in front of TAPS was used for particle identification. The combined CB/TAPS setup gives an almost 4π acceptance in the center of mass frame with a high angular and energy resolution.

The fist step of the data analysis was to select only events with the correct number of charged and neutral hit information from the detector. For the neutron channel the photons were

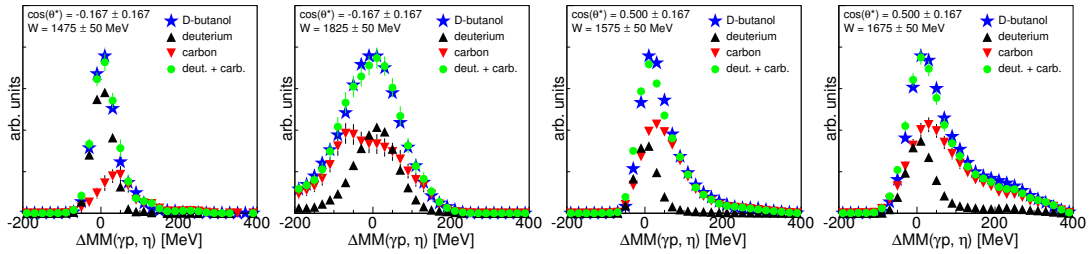

Figure 1: (Color online) Missing mass spectra for $\gamma p \to \eta p \to 2\gamma p$ for the carbon background subtraction. The spectra for deuterium and carbon are fitted to the d-butanol spectra. The ratio of carbon and deuterium, withing the missing mass cuts, is equal to the dilution factor.

identified by a χ^2-test finding the best combination for the meson invariant mass. Coincidence time cuts were applied to all photons and to eliminate accidentally coincident tagger photons, a random background subtraction was performed.

In order to separate the background channels kinematic cuts were applied separately for each W-θ-bin. Since all relevant events come from the polarized deuterons from the d-butanol target all cuts were determined from deuterium data. First, a coplanarity cut on the meson-nucleon system was applied. Then, an invariant mass cut on the reconstructed meson was performed. Finally, a γp-η missing mass cut was used to eliminate most of the background. The last step was to reconstruct the full event using four-momentum conservation, i.e., the Fermi momentum of the initial nucleon was determined from the knowledge of the incident photon energy and the complete final state. With this, the kinematics was transferred into the center of mass frame.

The observables were extracted using two opposite spin states for both, the photon helicity and nucleon spin. The above definition of the polarization observables can then be rewritten and reads, for F (and analogous for T),

$$F\cos\phi = \frac{1}{P_\odot}\frac{1}{P_T}\frac{d\sigma^+ - d\sigma^-}{d\sigma_0} = \frac{1}{P_\odot}\frac{1}{P_T}\frac{d\sigma^+ - d\sigma^-}{d\sigma^+ + d\sigma^-} = \frac{1}{P_\odot}\frac{1}{P_T}\frac{N^+_{\rm db} - N^-_{\rm db}}{N^+_{\rm db} + N^-_{\rm db}}\frac{1}{1-d}.$$

Here, the superscripts $(+,-)$ refer to the two photon helicity states, $N^\pm_{\rm db}$ denotes the count rate from d-butanol data and $d = d\sigma_0^{\rm carbon}/d\sigma_0^{\rm deuterium}$ is the dilution factor.

The last equality in the above equation holds for the following two reasons. First, flux normalization and efficiency corrections cancel out. Second, the cross sections refer to the reaction on the deuteron. However, unpolarized carbon and oxygen contributions only cancel in the numerator. Therefore, the additional contribution in the denominator has to be factorized out by the determination of the dilution factor. Figure 1 shows, for some selected bins, missing mass spectra of deuterium and carbon data fitted to the spectrum of d-butanol data. From this we can determine the unwanted contribution of events from carbon and oxygen from the d-butanol data.

3 Preliminary results and conclusion

Figure 2 shows some selected preliminary results for the polarization observables T and F for single π^0- and η-photoproduction off quasi-free protons and neutrons, respectively. Moreover, preliminary results for the reaction off the free proton and some model results are included.

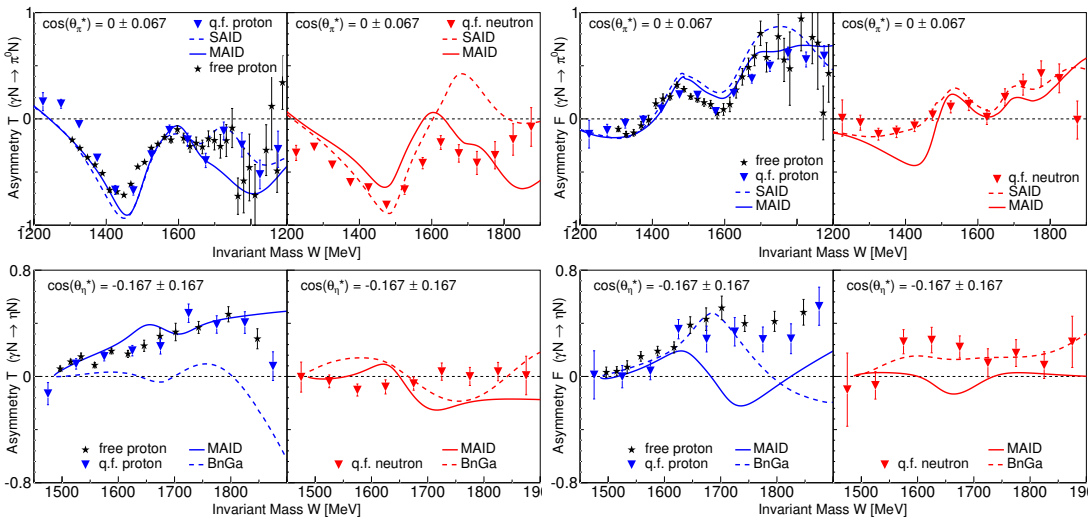

Figure 2: (Color online) Preliminary results for the polarization observables T and F. Top (bottom) row: π^0- (η-)photoproduction. Left (right) side: observable T (F) off free/quasi-free proton and quasi-free neutron. *Free proton data:* V. Kashevarov (preliminary); for final free proton $\gamma p \to \eta p$ results c.f. [9].

The free and quasi-free proton data are in nice agreement. The main contribution to the systematic uncertainties comes from the determination of the dilution factors caused by poorly matching missing mass spectra (only statistical errors are shown).

The best agreement with model predictions is found for π^0-photoproduction off the proton at lower energies, which is the best-known channel. There, the different models also make the same predictions. However, for higher energies the models deviate from each other and cannot reproduce the data consistently for both observables. For π^0-photoproduction off the quasi-free neutron the models already disagree at lower energies and for η-photoproduction off quasi-free protons and neutrons, respectively, the models even disagree down to the production threshold.

The final results will contribute to the complete experiment and will hopefully help to improve the model predictions and give a better understanding of the underlying physics.

References

[1] G.F. Chew, M.L. Goldberger, F.E. Low and Y. Nambu, Phys. Rev. **106** 1345 (1957).

[2] W.-T. Chiang and F. Tabakin, Phys. Rev. **C55** 2054 (1997).

[3] B. Krusche and S. Schadmand, Prog. Part. Nucl. Phys. **51** 399 (2003).

[4] D. Werthmüller *et al.*, Phys. Rev. Lett. **111** 232001 (2013).

[5] M. Dieterle *et al.*, Phys. Rev. Lett. **112** 142001 (2014).

[6] D. Werthmüller *et al.*, Phys. Rev. **C90** 015205 (2014).

[7] A.M. Sandorfi *et al.*, J. Phys. **G38** 053001 (2011).

[8] H. Olsen and L.C. Maximon, Phys. Rev. **114** 887 (1959).

[9] C.S. Akondi *et al.*, Phys. Rev. Lett. **113** 102001 (2014).

Measurement of $\sigma_{1/2}$ and $\sigma_{3/2}$ in Photoproduction of $\pi^0\pi^0$ Pairs off Neutrons in the Nucleon Resonance Region

Manuel Dieterle[1]

[1] Department of Physics, University of Basel, Klingelbergstrasse 82, 4056 Basel, Switzerland

DOI: http://dx.doi.org/10.3204/DESY-PROC-2014-04/168

Helicity dependent cross sections $\sigma_{1/2}$ and $\sigma_{3/2}$ of photoproduction of $\pi^0\pi^0$ meson pairs off quasi-free protons and off quasi-free neutrons in the second and third nucleon resonance region have been measured for the first time at the Mainzer Mikrotron (MAMI) electron accelerator facility. The knowledge of $\sigma_{1/2}$ and $\sigma_{3/2}$ will put stringent constraints on the different resonances that contribute to the nucleon excitation spectrum and will clearly help to improve its theoretical understanding.

1 Introduction

Meson photoproduction offers unique possibilities to investigate the nucleon and its excited states. Double meson photoproduction has the great advantage of enabling access to higher lying nucleon resonances that have no significant decay mode to the nucleon ground state via photoproduction of single mesons. Among the different meson pairs $2\pi^0$ is in particular interesting as non-resonant background terms (i.e. pion-pole, Kroll-Rudermann) are strongly suppressed because photons couple only weakly to neutral pions. Whereas for the reactions on the proton a lot of experimental data is available, data for the reactions on the neutron are sparse. In addition, even though in recent years much progress in the theoretical description of the results was achieved, the available models are still controversial even at low energies where only few resonances contribute. From the total cross sections of e.g. π^0 or η meson photoproduction off quasi-free protons and neutrons it is well known that rather different resonances contribute to the reactions on the proton compared to those on the neutron [1, 2, 3, 4]. The measurement of single and double polarization observables will help to reveal the different resonance contributions and thereby serve as an important input for the theoretical description of the structure and the excitation spectrum of the nucleon.
The double polarization observable E is defined as the asymmetry of the two helicity dependent cross sections $\sigma_{1/2}$ and $\sigma_{3/2}$ (1/2 (3/2): photon and target spins anti- (parallel)) normalized by the sum of both:

$$E = \frac{\sigma_{1/2} - \sigma_{3/2}}{\sigma_{1/2} + \sigma_{3/2}} = \frac{\sigma_{1/2} - \sigma_{3/2}}{2 \cdot \sigma_{\text{unpol}}} \tag{1}$$

2 Experiment

The experiment was performed at the MAMI electron accelerator at Mainz, Germany. The primary longitudinally polarized electron beam of 1.557 GeV was directed onto a 10 μm thick cobalt-iron radiator foil where a cirularly polarized photon beam of energies in the range of 0.45 GeV and 1.5 GeV was produced by the bremsstrahlung process. In order to determine the energy of the photons, the scattered electrons were detected in the focal plane of the Glasgow-Mainz Tagged Photon Spectrometer to analyze their momentum. The produced photon beam impinged on a longitudinally polarized deuterated Butanol (C_4D_9OD) target of 2 cm length and 2.2 cm diameter which was mounted in the center of the Crystal Ball (CB) detector. An additional electromagnetic calorimeter, the TAPS detector, was placed as forward wall downstream of the target. A charged particle identification detector (PID) mounted around the target inside CB and plastic scintillators (Vetos) in front of each of the crystals of TAPS allowed for the identification of charged particles. The experiment provided almost 4π angular coverage. The degree of target polarization was up to 60% and of the photon beam, depending on the energy, up to 80%.

3 Analysis

Double π^0 photoproduction was analyzed in coincidence with recoil protons and neutrons in the reactions $\gamma p(n) \rightarrow \pi^0\pi^0 p(n)$ and $\gamma n(p) \rightarrow \pi^0\pi^0 n(p)$. The nucleon in brackets is treated as undetected spectator nucleon. The photons, protons and neutrons have been identified in an analysis that combined the energy deposited in CB and the PID, the Vetos, the time-of-flight versus energy and a pulse-shape analysis in TAPS. The π^0 pairs were identified from the measured invariant mass of the photon pairs. In order to achieve a clean identification of the reaction, conditions on the coplanarity of the two-meson system and the recoil nucleon as well as a missing mass analysis have been determined on data from a comparable experiment with a liquid deuterium (LD_2) target. In the latter case, no background contribution from unpolarized nuclei inside carbon or oxygen contribute to the spectra, allowing for a much more precise determination of the kinematical limits. The data from deuterated butanol were then analyzed and only the events within these limits have been accepted and resulted in nearly background free invariant mass distributions (see figure 1).

To subtract the contribution from reactions on the unpolarized carbon and oxygen nuclei inside the deuterated butanol target, an additional experiment using the same setup and target but filled with carbon foam (^{12}C) of identical geometry and of about the same density was performed and analyzed in the same way as the deuterated butanol data.

In order to determine the double polarization observable E according to equation (1) either the sum of the two helicity dependent cross sections or the unpolarized cross section can be used for the normalization of the asymmetry. Both calculations have been carried out to ensure that the contributions from unpolarized nuclei are well under control. The contribution of reactions on such unpolarized nuclei was determined by a comparison of the missing mass spectra of the three datasets: deuterated butanol, liquid deuterium and carbon. The result is presented in figure 2. It is clearly visible that in each spectrum the yield from the LD_2 and ^{12}C data perfectly add up to the C_4D_9OD data, as expected.

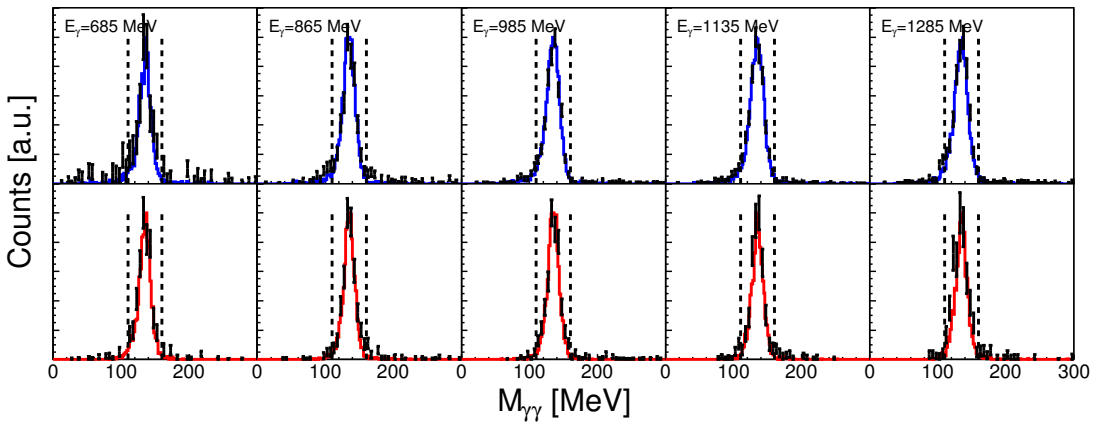

Figure 1: Final invariant mass spectra for five selected energy bins of one selected angular bin. Upper row: Reaction $\gamma p(n) \rightarrow \pi^0\pi^0 p(n)$, Lower row: Reaction $\gamma n(p) \rightarrow \pi^0\pi^0 n(p)$. Points: data, solid line: MC yield. Vertical dashed lines: region of the invariant mass cut.

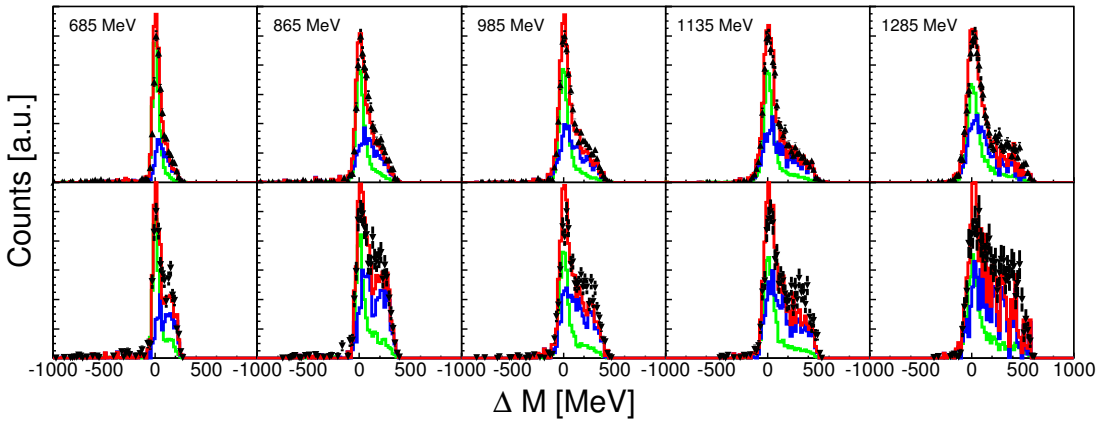

Figure 2: Carbon subtraction method using missing mass for five selected energy bins of one selected angular bin. Upper row: Reaction $\gamma p(n) \rightarrow \pi^0\pi^0 p(n)$, Lower row: Reaction $\gamma n(p) \rightarrow \pi^0\pi^0 n(p)$. Solid triangles: dButanol data. Solid lines: LD_2 (green), Carbon (blue) and sum of both (red).

4 Preliminary Results

Preliminary results for the helicity dependent cross sections $\sigma_{1/2}$ and $\sigma_{3/2}$ (middle and right) as well as the double polarization observable E (left) are presented in figure 3 and are compared to the model predictions from Bonn-Gatchina [5] (currently only available for the reaction $\gamma p(n) \rightarrow \pi^0\pi^0 p(n)$) and MAID [6]. It is clearly visible that both normalization methods are in perfect agreement with each other indicating that the subtraction of the contributions from reactions on the unpolarized nuclei from carbon and oxygen is well understood. The comparison of the data with the theoretical descriptions again reveal the impact of the helicity dependent

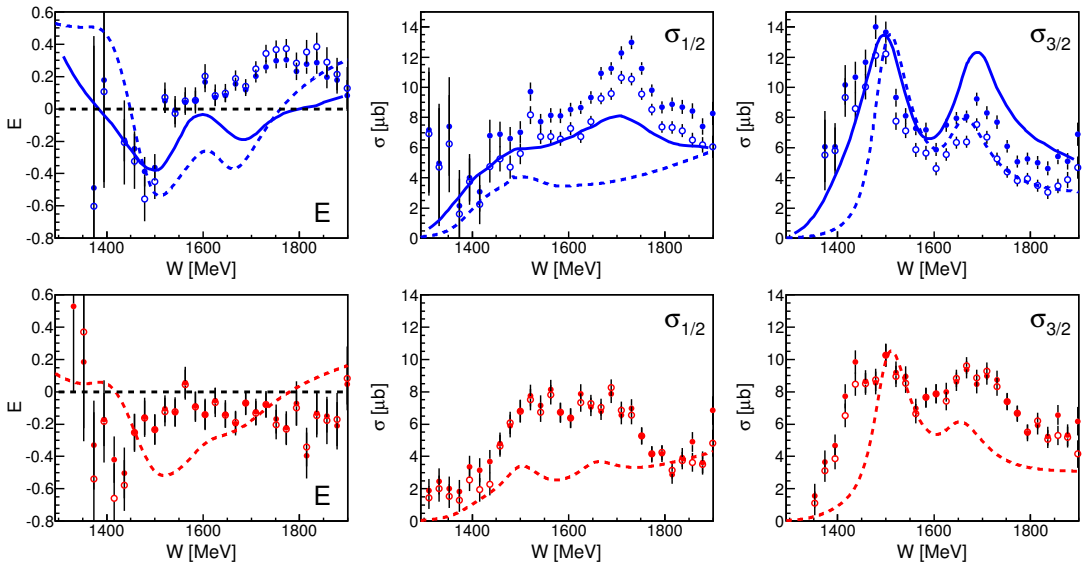

Figure 3: Preliminary results of the helicity dependent cross sections $\sigma_{1/2}$, $\sigma_{3/2}$ and double polarization observable E. Upper row: Reaction $\gamma p(n) \rightarrow \pi^0\pi^0 p(n)$, Lower row: Reaction $\gamma n(p) \rightarrow \pi^0\pi^0 n(p)$. Solid circles: normalized with carbon subtracted dButanol data, open circles: normalized with unpolarized total cross section. Solid line: BnGa model[5], dashed line: MAID model[6].

cross sections. Whereas the $\sigma_{1/2}$ cross section on the proton is better described by the BnGa model than by the MAID model, the opposite is true for the $\sigma_{3/2}$ cross section. Consequently neither one manages to describe the double polarization observable E, although the BnGa is closer to the result. Also for the neutron, the MAID model predicts a much better result for $\sigma_{3/2}$ than for $\sigma_{1/2}$. Obviously these results will clearly help to improve the models and to constrain the different resonance contributions.

References

[1] M. Dieterle *et al.*, Phys. Rev. Lett. **112**, 142001 (2014) [10.1103/PhysRevLett.112.142001].

[2] D. Werthmüller *et al.*, Phys. Rev. C **90**, 015205 (2014) [10.1103/PhysRevC.90.015205].

[3] D. Werthmüller *et al.*, Phys. Rev. Lett. **111**, 232001 (2013) [10.1103/PhysRevLett.111.232001].

[4] L. Witthauer *et al.*, Eur. Phys. J. A **49**, 154 (2013)

[5] *private communication*, A. Sarantsev, Bonn-Gatchina partial wave analysis $BG2014-02$.

[6] A. Fix and H. Arenhovel, Eur. Phys. J. A **25**, 115 (2005) [nucl-th/0503042].

Update on the OLYMPUS two-photon exchange experiment

Noaryr Akopov[1] for the OLYMPUS Collaboration

[1]Yerevan Physics Institute, Alikhanyan Br. 2, 0036 Yerevan, Armenia

DOI: http://dx.doi.org/10.3204/DESY-PROC-2014-04/143

The OLYMPUS experiment performed on the DORIS accelerator at DESY was designed to measure the e^-p to e^+p elastic cross sections ratio with high accuracy (<1%) in order to determine the effect of the two-photon exchange. Presence of such effect can explain the existing difference in electric to magnetic elastic form factors ratio measured in unpolarized and polarized ep elastic scattering.

1 Introduction

The nucleon electric and magnetic elastic form factors $G_E^{(p,n)}$ and $G_M^{(p,n)}$ are fundamental observables reflecting the composite structure of the nucleon consisting of quarks and gluons. More than fifty years, since the famous measurements, performed by Hofstadter [1] the only experimental information on these form factors and their ratios was available with the unpolarized cross section measurements using the Rosenbluth separation method [2]. During the last fifteen years thanks to polarization techniques developed at JLab [3], independent experimental measures of the form factor ratio were obtained, and the ratio of $G_{E(p)}/G_{M(p)}$ as a function of squared four-momentum transfer Q^2 was found to be distinctly different from that measured before with the Rosenbluth method: $G_E^p/G_M^p \approx 1/\mu_p$, with μ_p being the proton anomalous magnetic moment. Such a difference (see Fig. 1) is puzzling and it suggests the two photon exchange contribution to the elastic ep cross section could explain this puzzle. The only direct way to estimate experimentally the two photon exchange contribution is the measurements of the ratio of e^+p/e^-p elastic cross sections. The OLYMPUS experiment performed on the DORIS accelerator at DESY has collected huge sample of data (more than 4.4 fb^-1 of integrated luminosity) with e^+p and e^-p elastic scattering, and will provide very precise results on the cross section ratio (less than 1% of total uncertainties).

2 The OLYMPUS experiment

The OLYMPUS experiment was designed to measure the ratio of the elastic cross sections e^+p/e^-p over a wide kinematic range with the high precision. The experiment used the intense e^-, e^+ beams stored in the DORIS ring at 2 GeV interacting with an internal windowless hydrogen gas target [4] with the scattered/recoiling e/p measured in the range of $(20^o < \theta < 80^o, -15^o < \phi < 15^o)$. The spectrometer [5] (see Fig. 2) consists of the following main components: the time-of-flight (ToF) scintillation detectors to provide the elastic trigger

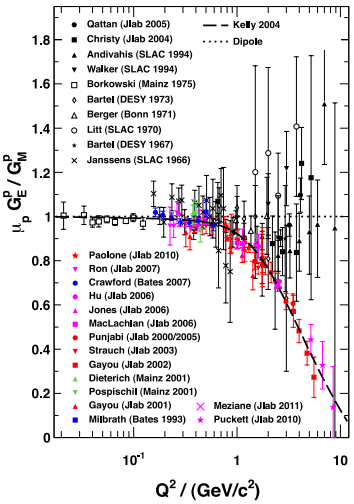

Figure 1: Proton electric to magnetic form factor ratio from unpolarized measurements (data points slightly deviated around unity) using the Rosenbluth method and from double polarization experiments (data points rapidly decreasing with Q^2). Also shown are two recent parametrization.

as well the particle identification, the drift chambers to provide the tracking and second level

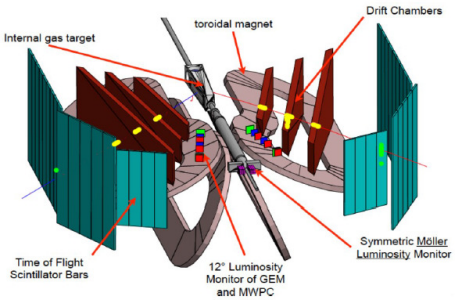

Figure 2: Schematic overview of the OLYMPUS spectrometer

trigger, and toroidal magnet to define the track momentum. To determine the relative e^+p/e^-p luminosity three sets of monitors were used, the first based on slow control information on target density and beam current, the second based on MWPC+GEMs tracking telescopes at 12^o, and the third based on symmetric Mőller-Bhabha calorimeters installed at 1.3^o. The high efficiency of the spectrometer operating together with the excellent performance of the accelerator, both provided the successful data taking. The DORIS accelerator was operated in top-up injection mode, which allowed the target density to be increased beyond the design value. An integrated luminosity of 4.4 fb^{-1} was achieved, the collected data consists of about equal amount of e^+

(44.1%) and e^- (43.3%) beam luminosities for positive toroid polarity. Due to the high background smaller data sets: 5.4% with the e^- beam and 7.2% with the e^+ beam were taken with the negative polarity, which are mainly used for systematic studies.

3 Data Analysis

The analysis framework is based on ROOT C^{++}/Geant4 providing the opportunities to analyze the real data as well the Monte Carlo samples equivalently. The radiative corrections which are very important to define the final ratio of $\frac{\sigma(e^+p)}{\sigma(e^-p)}$ are implemented in Monte Carlo generator, also a pion generator to estimate the inelastic background has been developed and tested. The digitization for all detector components to perform a realistic Monte Carlo studies to estimate possible systematic uncertainties is done. The calibration constants for the ToF are well advanced which allows the lepton/proton separation (see Fig. 3) based on particle squared mass distribution defined with:

$$M^2 = p^2[(cT/L)^2 - 1],$$

where p is the track momentum, c is the speed of light, T is the time of ToF hit and L is the track path length from the interaction point to the ToF hit. The algorithm for the reconstruction

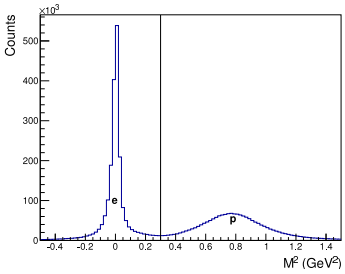

Figure 3: Particle squared mass distribution

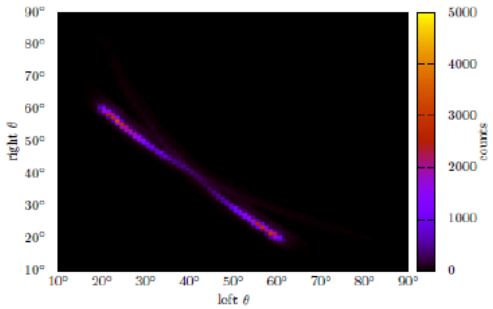

Figure 4: Polar left-right angles correlation with all elastic cuts applied

code is essentially improved, the massive production of the reconstructed runs is started. The set of kinematic and geometric constraints to select the elastic events such as the left and right

tracks vertex difference, momentum balance, coplanarity is developed and optimized for certain bins over Q^2 and virtual photon polarization ϵ. The typical "elastic" picture with the left-right polar angles correlation after all cuts applied is shown on Fig. 4. The present level of the Monte Carlo data agreement can be seen in Fig. 5. One should note that still the data are

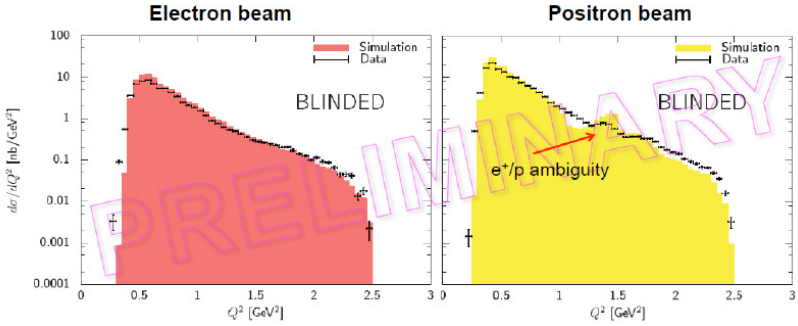

Figure 5: Q^2 distributions for selected elastic events for e^- sample (left panel) and e^+ sample (right panel). The dashed area on both panels is the Monte Carlo simulation.

blinded in order to prevent a bias in several independent analyzes. The data analysis is close to be completed. Two other experiments [6, 7] are close to publish the final results with the measured $\frac{\sigma(e^+p)}{\sigma(e^-p)}$ ratio. The preliminary results from the OLYMPUS collaboration are expected to be released at the end of 2014.

References

[1] R. Hofstadter, Rev. Mod. Phys. **28**, 214 (1956).

[2] M.N. Rosenbluth, Phys. Rev. **79**, 615 (1950).

[3] V. Punjabi et al., Phys. Rev. **C71**, 055202 (2005); Erratum-ibid. Phys. Rev. **C71**, 069902(E) (2005);
M. Jones et al., Phys. Rev. Lett. **84**, 1398 (2000);
O. Gayou et al., Phys. Rev. Lett. **88**, 092301 (2002);
G. MacLachlan et al.,Nucl. Phys. **A764**, 261 (2006).

[4] J.C. Bernauer et al., NIM **A755**, 20 (2014).

[5] R. Milner et al., NIM **A741**, 1 (2014).

[6] B.A. Raue for the CLAS Collaboration, AIP Conf.Proc. **1257**, 617 (2010);P. Bennett dor the CLAS Collaboration, AIP Conf.Proc. **1441**, 156 (2912).

[7] A.V. Gramolin et al., Nucl.Phys.Proc.Suppl. **225-227**, 316 (2012).

Helicity Dependent Cross Sections in η Photoproduction off Quasi-Free Protons and Neutrons

Lilian Witthauer[1]

[1] Department of Physics, University of Basel, Klingelbergstrasse 82, 4056 Basel, Switzerland

DOI: http://dx.doi.org/10.3204/DESY-PROC-2014-04/169

Preliminary results for the double polarisation observable E and the corresponding helicity dependent cross sections $\sigma_{1/2}$ and $\sigma_{3/2}$ of η photoproduction off quasi-free protons and neutrons have been obtained by a recent experiment at the MAMI electron accelerator at Mainz, Germany. The results will help to constrain the origin and quantum numbers of the bump-like structure in the η cross section off the neutron.

1 Introduction

The identification of the relevant effective degrees of freedom of QCD is the most important step in order to understand the structure of the nucleon. Since the resonances which contribute to the excitation spectrum are often broad and overlapping, the comparison of experimental data and theoretical models is rather difficult. Single and double polarization observables allow for the determination of the quantum numbers of the contributing resonances and are therefore an ideal tool to investigate the excitation spectrum of the nucleon.
A very selective channel in this context is the photoproduction of η mesons. Due to the isoscalar property of the η, Δ ($I = 3/2$) resonances cannot decay to the ground state by emitting an η. Furthermore $P_{11}(1440)$ and $D_{13}(1520)$ resonances have a very small branching ratio into the Nη final state (close to threshold high orbital angular momenta are strongly suppressed). Especially, the investigation of this photoproduction channel is very interesting as the resulting cross section on the neutron shows a large resonance-like structure, beyond the dominating $S_{11}(1535)$, which is not seen on the proton. The structure has been reported by different collaborations [1, 2, 3, 4] and is visible on different nucleon systems (deuterium and helium), excluding origin from nuclear effects [5, 6]. Theoretical model descriptions have not yet lead to consistent results.
Using a circularly polarised photon beam and a longitudinally polarised target, the double polarisation observable E can be determined:

$$E = \frac{\sigma_{1/2} - \sigma_{3/2}}{\sigma_{1/2} + \sigma_{3/2}} = \frac{\sigma_{1/2} - \sigma_{3/2}}{2\sigma_{tot}^{unpol}} \tag{1}$$

The corresponding helicity dependent cross-sections $\sigma_{1/2}$ (photon and target spin anti-parallel) and $\sigma_{3/2}$ (photon and target spin parallel) give direct hints to the spin of the underlying resonances and are therefore ideally suited to reveal the origin of the narrow structure on the neutron.

2 Experiment and Analysis

The experiment was carried out by the A2 collaboration at the electron accelerator facility MAMI in Mainz, Germany. A circularly polarised, tagged photon beam with energies up to 1.557 GeV impinged onto the longitudinally polarised deuterated Butanol target. The target had a diameter of 2.2 cm, a length of 2 cm and an effective density of 0.66 g/cm^3. A deuteron polarisation of around 60% was reached, the photons had a polarisation degree of up to 80%. The almost 4π covering detector system consisted of the two electromagnetic calorimeters Crystal Ball and TAPS. The particle identification detector surrounding the target and the plastic vetos in front of the TAPS detector were used to distinguish charged from neutral particles. To determine the contribution of the unpolarised carbon and oxygen nuclei inside the deuterated butanol target, additional background measurements using a dedicated carbon foam target have been performed.
Both decay channels, $\eta \to 2\gamma$ and $\eta \to 3\pi^0 \to 6\gamma$, have been analysed using standard invariant mass and χ^2-techniques. Additional cuts have been applied to the missing mass of the nucleon and to the coplanarity of the meson-nucleon system. Using the two different scintillation components of the TAPS BaF_2 crystals, a Pulse-Shape-Analysis has been performed to distinguish neutrons from photons. The Fermi motion of the deuteron has been removed, the procedure is explained in detail in [5].

Two different methods have been used to determine the double polarisation observable E.

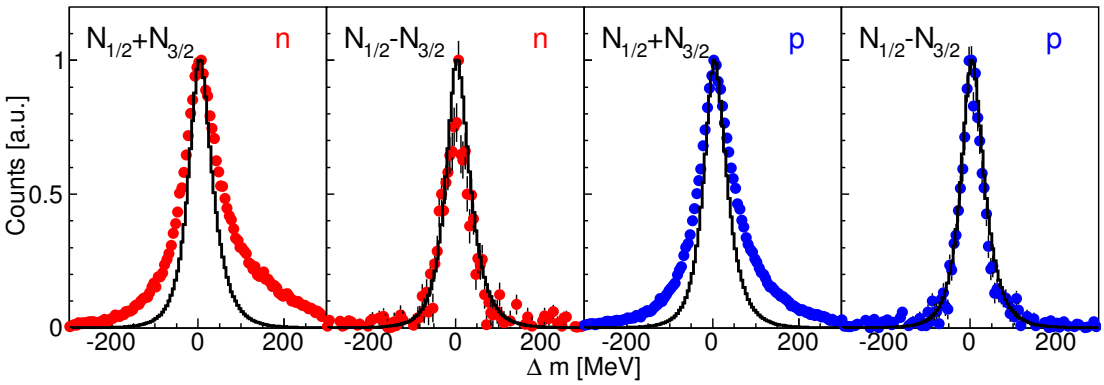

Figure 1: The missing mass of the sum (first and third figure) and the difference (second and fourth figure) of the two helicity states. Data (dots) are compared to simulation (line). The two left-hand figures show the situation for the neutron, the two right-hand for the proton. In both cases the carbon contribution in the sum of the two helicity states is clearly visible and leads to a broadening of the peak compared to the simulation. In the countrate difference, the carbon contribution automatically drops out and the data are consistent with the simulation.

First, a direct approach was chosen, the difference of the two helicity states has been divided by the known unpolarised total cross section (second part of equation 1). In this case the unpolarised carbon automatically drops out (see figure 1), but a accurate total normalisation is needed. In the second approach the carbon background measurement was used and the difference was divided by the carbon subtracted sum of the two helicity states (first part in equation 1). Whereas in this case the overall normalisation cancels out, the carbon contribution has to

be known exactly. The contribution of the carbon is determined by fitting the missing mass spectra of the deuteron and carbon data to the one of butanol, see Figure 2. The fitting procedure was performed for every bin of photon energy and polar angle. In the range of the missing mass cut (vertical black lines) the contribution of unpolarised carbon and oxygen nuclei is well under control.

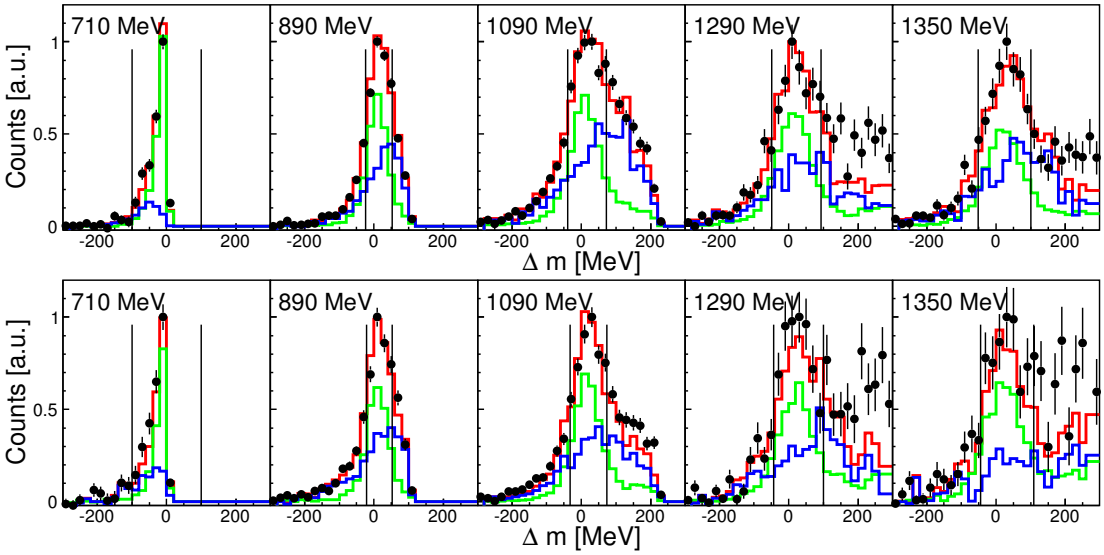

Figure 2: Upper (lower) row: the missing mass distribution of the proton (neutron) for the $\eta \to 2\gamma$ channel for five different photon energy bins intergrated over all angular bins. Solid lines: The contributions of the reactions on the deuteron (green) and the carbon (blue) and the sum of both (red). Within the range of the missing mass cut (vertical black lines), the sum is consistent with the measured distribution on the deuterated butanol (black dots).

3 Preliminary Results

The preliminary results of the double polarisation observable E as well as the helicity dependent cross sections $\sigma_{1/2}$ and $\sigma_{3/2}$ as a function of the center-of-mass energy W are shown in figure 3. The direct method (open circles) and the carbon subtraction method (solid circles) are in good agreement. As predicted by the models, the contribution from the helicity 1/2 state is significantly larger than the contribution from 3/2. This is mainly caused by the dominating $S_{11}(1535)$ resonance. Even at higher energies, the contribution of the helicity 3/2 state is very small. The resonance like structure on the neutron only appears in $\sigma_{1/2}$, as predicted by the BnGa model [7]. The MAID model [8] with the strong contributing $D_{15}(1675)$ in $\sigma_{3/2}$ does not reproduce the helicity dependent cross-sections for the neutron. For the proton the overall situation seems to be well understood by the models.

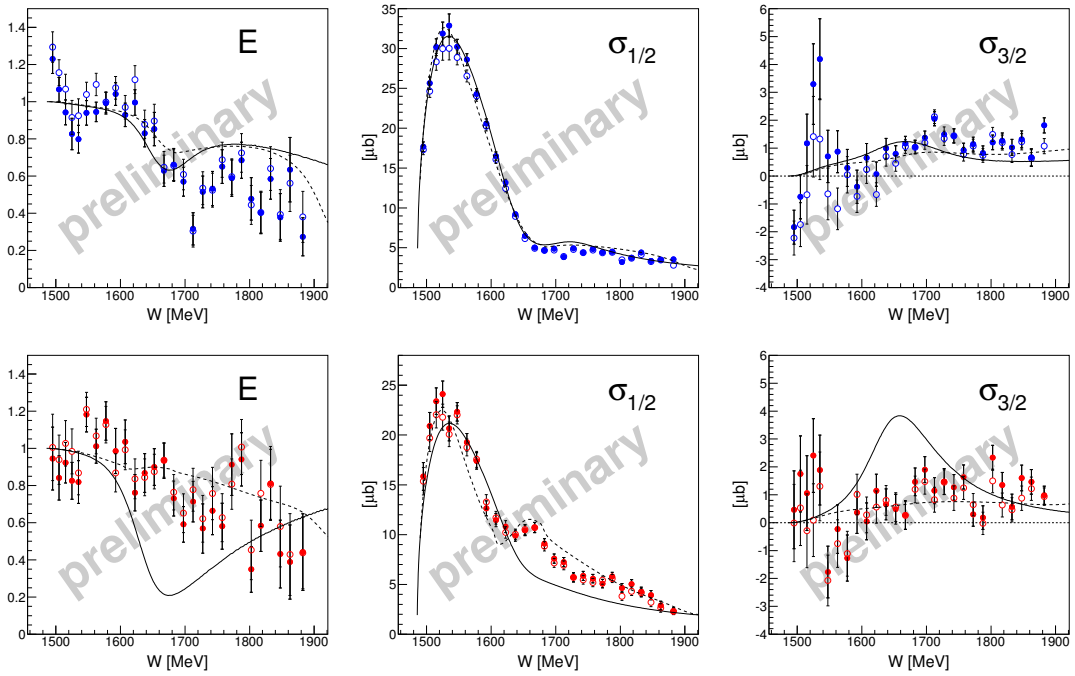

Figure 3: Preliminary Results. Double polarisation observable E and helicity dependent cross sections $\sigma_{1/2}$, $\sigma_{3/2}$ for η photoproduction on the proton (upper row) and on the neutron (lower row). Solid circles: normalised with carbon subtracted deuterated butanol, open circles: normalised with unpolarised total cross section. The results are compared to the BnGa model [7] (dashed line) and the MAID model [8] (solid line).

References

[1] V. Kuznetsov *et al.*, Phys. Lett. B **647**, 23 (2007) [10.1016/j.physletb.2007.01.041].

[2] I. Jaegle *et al.*, Eur. Phys. J. A **47**, 11 (2011) [10.1140/epja/i2011-11011-x].

[3] F. Miyahara et al., Prog. Theor. Phys. Suppl. 168, 90 (2007) [10.1143/PTPS.168.90].

[4] D. Werthmüller *et al.*, Phys. Rev. Lett. **111**, 232001 (2013) [10.1103/PhysRevLett.111.232001].

[5] D. Werthmüller *et al.*, Phys. Rev. C **90**, 015205 (2014) [10.1103/PhysRevC.90.015205].

[6] L. Witthauer *et al.*, Eur. Phys. J. A **49**, 154 (2013) [10.1140/epja/i2013-13154-0].

[7] A.V. Anisovich *et al.*, Eur. Phys. J. A, **48**, 15 (2012) [10.1140/epja/i2012-12015-8].

[8] W.-T. Chiang *et al.*, Nucl. Phys. A **700**, 429-453 (2002) [nucl-th/0110034].

Physics opportunities in electron-hadron collisions at the future eRHIC

Salvatore Fazio

Brookhaven National Laboratory, PO BOX 5000, 11973 Upton NY, USA

DOI: http://dx.doi.org/10.3204/DESY-PROC-2014-04/113

Our understanding of the structure of nucleons is described by the properties and dynamics of quarks and gluons in the theory of quantum chromodynamics. With advancements in theory and the development of phenomenological tools we are preparing for the next step in subnuclear tomographic imaging at a future electron-ion collider. A large range of center-of-mass energies ($\sqrt{s} \approx 45 - 150$ GeV) in combination with extremely high luminosities ($> 10^{33}$ cm^{-2}s^{-2}) will open a unique opportunity for very high precision measurements, allowing for a detailed investigation of the proton and nuclear hadronic substructure in multi-dimensions. In addition, highly polarized nucleon ($P \approx 70\%$) and electron ($P \approx 80\%$) beams can probe the parton polarizations in previously unexplored kinematic regions and with unprecedented accuracy, as well as address the role of orbital angular momentum with respect to the nucleon spin. This talk will summarize the eRHIC physics case for electron-proton collisions, the expected impact over the current knowledge and some of the technical challenges of such a versatile experimental endeavor.

1 Introduction

The BNL proposal for a future Electron-Ion Collider, eRHIC [1], is a major new research facility that builds on the existing RHIC accelerator complex to advance the long-term vision for Nuclear Physics to discover and understand the emergent phenomena of QCD, i.e. the creation of mass and spin of the visible matter. Its design concept incorporates new and innovative accelerator techniques to provide a cost-effective design to add a polarized electron beam colliding with the full array of RHIC hadron beams at a luminosity beyond 10^{33}cm^{-2}s^{-1}.

Such a facility will address directly and with high precision questions that relate to our fundamental understanding of QCD:

- How are the sea quarks and gluons, and their spins, distributed in space and momentum inside the nucleon?
- Where does the saturation of gluon densities set in?
- How does the nuclear environment affect the distribution of quarks and gluons and their interactions in nuclei?

eRHIC will address the above questions with the highest, unprecedented precision and at one facility.

2 electron-proton scattering at eRHIC

eRHIC will open up the unique opportunity to go far beyond our current largely one-dimensional picture of the nucleon. It will enable partonic "tomographic images", providing essential insight into QCD dynamics inside hadrons. Moreover it can unravel how the proton spin derives from its constituents: the quarks and the gluons, a formidable challenge that goes directly to the heart of exploring and understanding the QCD dynamics of matter.

2.1 Proton's helicity structure

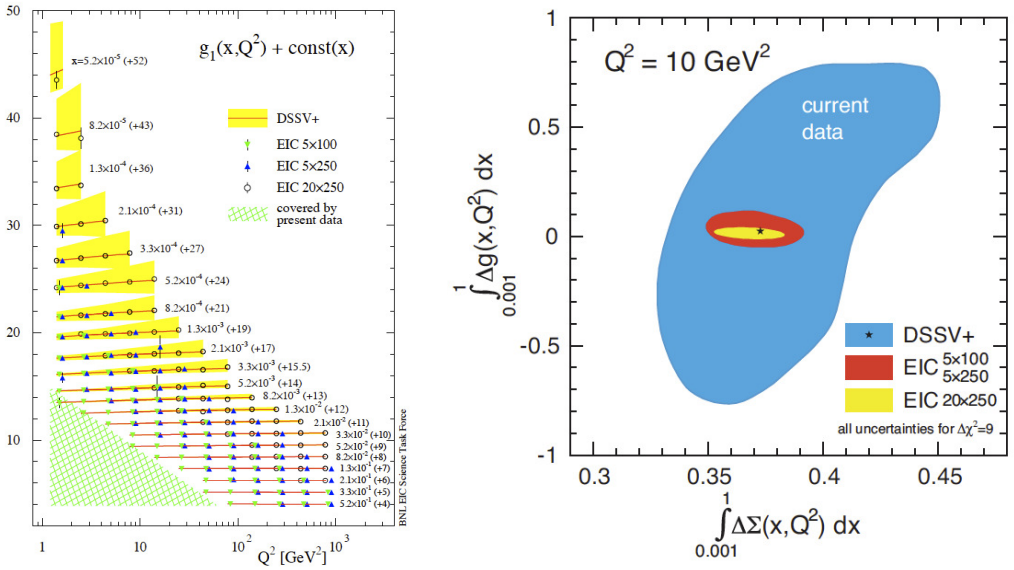

Figure 1: (*left*)Projected eRHIC data for the structure function g_1 for different combinations of electron and proton beam energies; (*right*) Correlated uncertainties for the flavor singlet combination $\Delta\Sigma$ and the gluon helicity density Δg.

Helicity-dependent parton densities encode the information to what extent quarks and gluons with a given momentum fraction x tend to have their spins aligned with the spin direction of a nucleon and are related to how the spin of a nucleon is composed of the spins and orbital angular momenta of quarks and gluons. The integrals of helicity PDFs over all momentum fractions x at a resolution scale Q^2, $\Delta f(Q^2) = \int_0^1 \Delta f(x, Q^2) dx$, provide information about the contribution of a given parton flavor f to the spin of the nucleon. A precise determination of the polarized gluon $\Delta g(x, Q^2)$ and quark $\Delta q(x, Q^2)$ distribution functions in a broad kinematic regime is a primary goal of eRHIC.

Current determinations of Δg suffer from both a limited $x - Q^2$ coverage and fairly large theoretical scale ambiguities in polarized p+p collisions for inclusive (di)jet and pion production [2]. Several channels are sensitive to Δg in e+p scattering at collider energies such as DIS jet or charm production, but QCD scaling violations in inclusive polarized DIS have been identified as the golden measurement.

Figure 1(*left*) illustrates the simulated data sets for inclusive polarized DIS at eRHIC for the three different choices of c.m. energies. The error bars reflect the expected statistical accuracy for a integrated luminosity of 10fb^{-1} and assuming 70% beam polarizations.

The simulated data are used in a fit to study what can be achieved for the first moments of the flavor singlet combination $\Delta\Sigma$ and the gluon helicity density Δg, which both enter the proton spin sum rule $\frac{1}{2} = \frac{1}{2}\Delta\Sigma + \Delta g + \Sigma_q L_q^z + L_g^z$, with $L_{q,g}^z$ denoting the contribution from orbital angular momentum (not accessible in inclusive DIS). Figure 1(*right*) shows how eRHIC will greatly reduce the uncertainties, in particular for Δg which is largely unconstrained so far.

2.2 Multidimensional imaging of quarks and gluons

With its wide range in energy, nuclear beams and high luminosity, eRHIC will offer an unprecedented opportunity for precision measurements, allowing us to study the momentum and space-time distribution of gluons and sea quarks in nucleons and nuclei.

One of the main goals will be a precise determination of the Generalized Parton Distribution functions (GPDs), which describe the distribution of quarks and gluons in the nucleon with respect to both position and momentum. Moreover, GPDs allow us to study how the orbital motion of quarks and gluons in the nucleon contributes to the nucleon spin, completing the spin sum role (see Sec. 2.1).

A golden measurement toward the determination of the whole set of GPDs is Deeply Virtual Compton Scattering (DVCS), which is the exclusive production of a real photon. This theoretical and experimentally clean process is sensitive to both quarks and gluons (via evolution).

Presently available DVCS measurements provide some limited information on GPDs and more precise data, in a wider phase space and including transversely polarized target spin asymmetry, are required to pin them down [3].

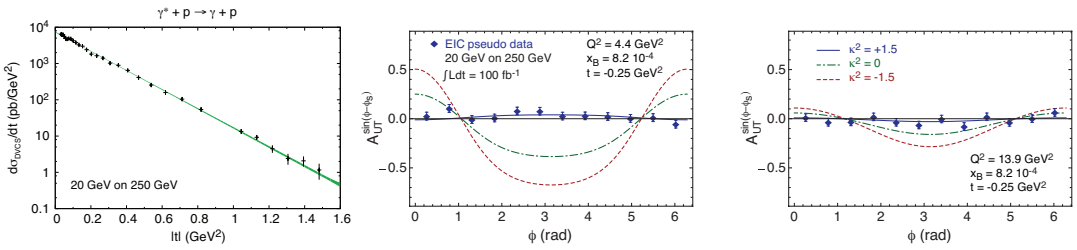

Figure 2: Expected uncertainties for a DVCS $|t|$-differential cross section (*left*) measurement in a particular x, Q^2 bin, and for A_{UT} (*center-right*) compared to theory model with large positive (*solid*), vanishing (*dot − dashed*), and large negative (*dashed*) E^{sea} contributions.

An access to GPDs requires a large data set with small errors. As an example of the precision achievable at eRHIC, Fig. 2 (*left*) shows the expected uncertainty for a measurement of the DVCS $|t|$-differential cross section in a particular x, Q^2 bin. Figure 2(*center-right*) shows the expected uncertainty for the transverse target-spin asymmetry (A_{UT}) as a function of the azimuthal angle ϕ between the production and the scattering planes for a particular $x_{Bj}, Q^2, |t|$ bin, compared to theoretical expectations. The simulation proves that eRHIC can perform accurate measurements of cross sections and asymmetries in a very fine binning and with a very low statistical uncertainty.

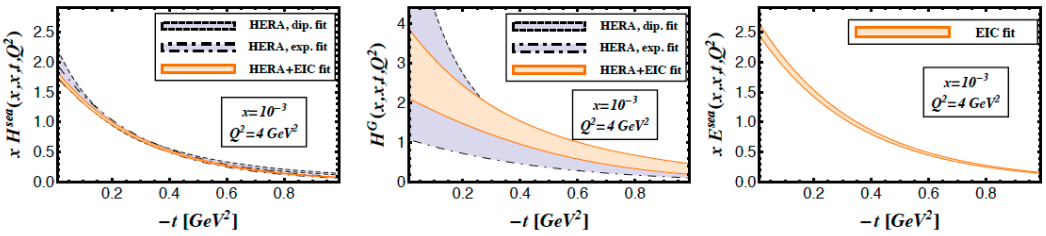

Figure 3: Extraction of GPD H for sea quarks ($left$) and gluons ($center$) and GPD E for sea quarks ($right$) in a particular x, Q^2 bin. The violet band is the uncertainty obtained excluding the eRHIC pseudo-data to the global fit procedure.

A global fit, including the eRHIC simulated data together with all the data presently available has been done. Figure 3 shows how eRHIC can largely improve the knowledge on GPD H for gluons. Moreover, a precise measurement of the transversely polarized target spin asymmetry A_{UT}, which allows for a decomposition of GPD H and E contributions, leads to the accurate extraction of GPD E, which at the moment remains almost unconstrained [3], providing an estimate of the angular momentum carried by sea quarks.

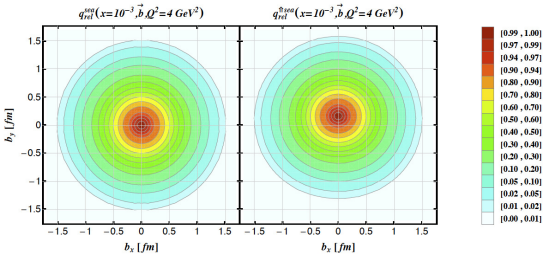

Figure 4: Tomographical picture of the sea-quuarks distribution in the impact parameter space for an unpolarized ($left$) and a polarized ($right$) proton beam.

Fourier-transforming the GPDs, it is possible to obtain the quarks and gluons distributions in the impact parameter space. Fig. 4 shows an example of a tomographic (2+1 D) picture of the see-quarks distribution as resulting from eRHIC pseudo-data analysis, in a particular bin, for the case of an unpolarized and a polarized proton-beam. The shift observed in the polarized case comes from the GPD E contribution.

References

[1] E.C. Aschenauer *et al.*, "eRHIC Design Study: An Electron-Ion Collider at BNL", arXiv:1409.1633

[2] E.C. Aschenauer, "The RHIC Spin Program: Achievements and Future Opportunities, arXiv:1304.0079

[3] E.C. Aschenauer, S. Fazio, K. Kumericki, and D. Mueller, JHEP 09 (2013) 093

Transverse single-spin asymmetries in $W^{\pm}$ and Z^0 bosons production in p+p collisions at RHIC

Salvatore Fazio

Brookhaven National Laboratory, PO BOX 5000, 11973 Upton NY, USA

DOI: http://dx.doi.org/10.3204/DESY-PROC-2014-04/112

The non universality of the quark Sivers function is a fundamental prediction from the gauge invariance of QCD. The experimental test of the Sivers function sign change between semi-inclusicve DIS and Drell-Yan processes is one of the open questions in hadronic physics, and can provide a direct verification of TMD factorization. While a precise measurement of asymmetries in Drell-Yan production is challenging, $W^{\pm}/Z^0$ production is equally sensitive to the predicted sign change. We present the preliminary measurement of the transverse single spin asymmetry of weak bosons by the STAR experiment at RHIC using transversely polarized proton-proton collisions at $\sqrt{s} = 500$ GeV.

1 Introduction

Transversely polarized spin effects are connected to transverse momentum dependent (TMD) distributions, leading to a multi-dimensional picture of the proton and a possible test of the framework and the underlying theory of perturbative QCD. For a quantitative application of the TMD framework to transverse single-spin asymmetries measured in proton-proton collisions, the required two scales (typically Q^2 and P_T) are not well defined, with Drell-Yan di-lepton (DY) and $W^{\pm}/Z^0$ boson production two of the exceptions. Thus, DY and weak boson production can be used to test the so-called Sivers TMD function [1], $f_{1T}^{\perp}$, which describes the correlation of parton transverse momentum with the transverse spin of the nucleon. There is evidence of a quark Sivers effect in semi-inclusive DIS (SIDIS) measurements [2] where the quark Sivers function is associated with a final state effect from the gluon exchange between the struck quark and the target nucleon remnants. On the other hand, for the virtual photon production in the DY process, the Sivers asymmetry originates from the initial state of the interaction. As a consequence, the quark Sivers functions are of opposite sign in SIDIS and in DY [3]

$$f_{q/h^{\uparrow}}^{\mathrm{SIDIS}}(x, k_{\perp}) = -f_{q/h^{\uparrow}}^{\mathrm{DY}}(x, k_{\perp}), \tag{1}$$

and this non-universality is a fundamental prediction from the gauge invariance of QCD.

The experimental test of this sign change is one of the open questions in hadronic physics, and can provide insights on the TMD factorization. While luminosity and experimental requirements for a meaningful measurement of asymmetries in Drell-Yan production are challenging, weak boson production is equally sensitive to the predicted sign change and can be well measured at STAR. The results can also provide essential input to study the TMD evolution effects, because of the high Q^2 in the $W \to e\nu$ production due to the large boson mass. The STAR experiment at RHIC is currently the best place where these effects can be tested.

The transverse single spin asymmetry, A_N, solely calculated from the lepton decay is predicted to be diluted [4] due to smearing, thus a full reconstruction of the produced boson kinematics is crucial for a meaningful measurement. Based on the transversely polarized data sample collected in the year 2011 at $\sqrt{s} = 500$ GeV ($L_{int} = 25$ pb^{-1}), an analysis has been performed at STAR to fully reconstruct the $W^{\pm}$ bosons from the lepton decay and all other particles in the recoil from the initial hard scattering. This analysis also includes a first look at A_N in Z^0 production. A proposed measurement with increased statistics will be directly competitive with a Drell-Yan measurement in pion-proton scattering at CERN.

2 Weak boson selection and asymmetry measurement

A data sample characterized by the $W \to e\nu$ signature as in Ref. [5], requires an isolated high $P_T > 25$ GeV electron and a total recoil $P_T > 18$ GeV. In order to fully reconstruct the W kinematics, the momenta of all decay products must be measured. The momentum of the neutrino produced in the leptonically decayed W can only be indirectly deduced from conservation of the transverse momentum.

We define the missing transverse energy as a vector restoring the balance in the event

$$\vec{\not{E}}_T = - \sum_{\substack{i \in \text{tracks,} \\ \text{clusters}}} \vec{P}_{i,T}. \tag{2}$$

At the STAR detector, due to a limited tracker acceptance of $|\eta| \sim 1$, the problem with measuring the missing momentum from the hadronic recoil is that particles with high rapidities escape the detector. At the same time, the beam remnants with high longitudinal momentum carry away only a little portion of the total transverse momentum. We accounted for the unmeasured tracks and clusters by using an event-by-event Monte Carlo correction to the data, using PYTHIA 6.4 with "Perugia 0" tune. Knowing its transverse momentum, the longitudinal component of the neutrino's momentum can be reconstructed solving the quadratic equation for the invariant mass of the produced boson

$$M_W^2 = (E_e + E_\nu)^2 - (\vec{P}_e + \vec{P}_\nu)^2, \tag{3}$$

where we assumed the nominal value of the W-mass. Eq. 3 leads to two possible solutions for P_L^ν, and we chose the smaller one in magnitude which, as shown by a Monte Carlo study, leads to a more truthful reconstruction of the original kinematics.

Background sources coming from $W^{\pm} \to \tau^{\pm}\nu_\tau$, $Z^0 \to e^+e^-$ and QCD events have been estimated to be at most a few percent of the selected sample, as shown in table 1.

Proc.	$W^{\pm} \to \tau^{\pm}\nu_\tau$	$Z^0 \to e^+e^-$	QCD
B/S	1.88% (W^+); 1.39% (W^-)	0.88% (W^+); 2.94% (W^-)	1.59% (W^+); 3.40% (W^-)

Table 1: Background over signal in the W^+ and W^- samples respectively.

The transverse single spin asymmetry is expressed as: $A_N = \frac{\sigma_\uparrow - \sigma_\downarrow}{\sigma_\uparrow + \sigma_\downarrow}$. We bin our data sample in three observables: the rapidity y, the azimuthal angle ϕ, and the P_T of the produced boson. Thus, we calculate A_N using the formula in Eq. 4, which helps to cancel out unwanted effects due to geometry and luminosity [6].

$$A_N \sin(\phi) = \frac{1}{< P >} \frac{\sqrt{N_\uparrow(\phi_i) N_\downarrow(\phi_i + \pi)} - \sqrt{N_\uparrow(\phi_i + \pi) N_\downarrow(\phi_i)}}{\sqrt{N_\uparrow(\phi_i) N_\downarrow(\phi_i + \pi)} + \sqrt{N_\uparrow(\phi_i + \pi) N_\downarrow(\phi_i)}}, \tag{4}$$

where N is the number of recorded events in the $i-th$ bin with a certain spin ($\uparrow\downarrow$) configuration in the "left" (ϕ_i) or in the "right" ($\phi_i + \pi$) side of the detector and $< P > \simeq 53\%$ is the average RHIC beam polarization for 2011 transverse p+p run.

The STAR preliminary results for the A_N measurement of the W^+ and W^- boson production are shown separately in Fig. 1 as a function of y^W and P_T^W. The systematic uncertainties, added in quadrature, have been evaluated via a Monte Carlo challenge using a theoretical prediction for the asymmetry from [7]. The 3.4% overall systematic uncertainty on beam polarization measurement is not shown in the plots.

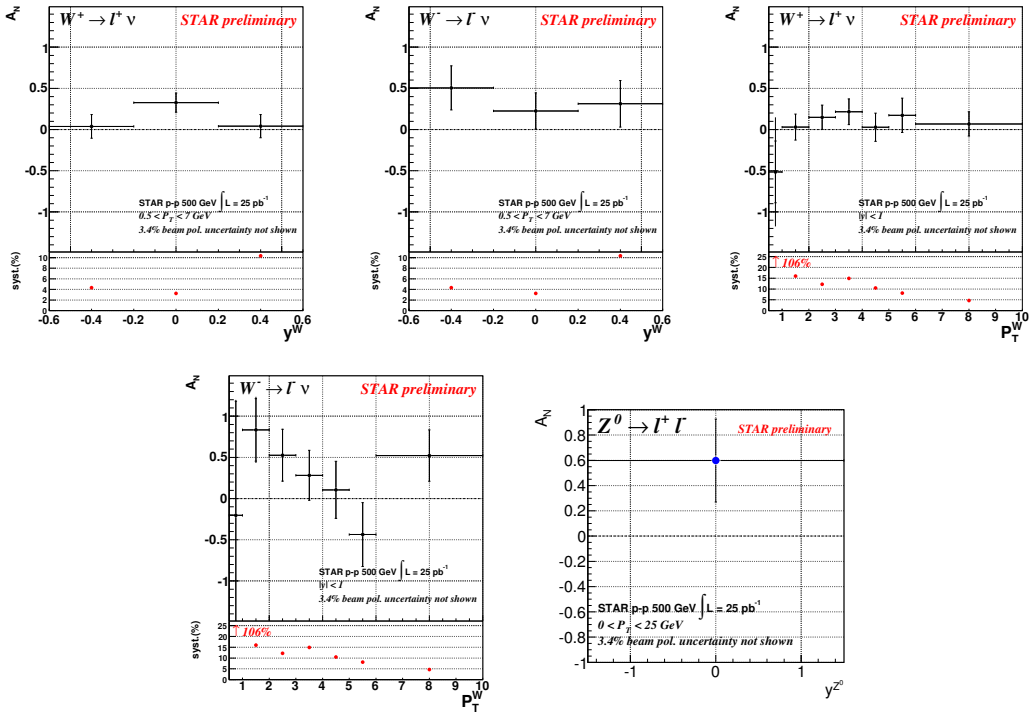

Figure 1: Transverse single spin asymmetry amplitude for $W^{\pm}$ and Z^0 boson production measured at STAR in a pilot run at $\sqrt{s} = 500$ GeV with a recorded luminosity of 25 pb^{-1}.

The $Z^0 \to e^+e^-$ process has many advantages: it is experimentally very clean and the boson kinematics are easy to reconstruct since there is no neutrino in the final decay (thus it carries only the overall systematics coming from the polarization measurement), it is background free and the asymmetry is expected to be the same size as the $W^{\pm}$ one. The only big disadvantage is the much lower cross section which makes the measurement very statistics hungry.

A data sample characterized by the Z^0 signature has been selected, requiring two isolated high $P_T > 25$ GeV electrons, of opposite charge and with an invariant mass within $\pm 20\%$ of

the nominal value. The STAR preliminary result for the A_N measurement of the Z^0 boson production in a single y^Z, P_T^Z bin is shown in Fig. 1.

3 Conclusions and outlook

This preliminary study, based on a pilot run of transverse polarized p+p collisions at $\sqrt{s}$ = 500 GeV with a recorded integrated luminosity of 25 pb^{-1}, is a proof-of-principle which shows that STAR is capable of measuring the transverse single spin asymmetry for fully reconstructed $W^{\pm}$, Z^0 bosons. The preliminary results from Fig. 1 can be compared with the most up-to-date theoretical A_N predictions for $W^{\pm}$, Z^0 boson production including TMD-evolution from reference [7], shown in Fig. 2, where the error bands have been updated accounting for the current almost complete uncertainty on sea-quark functions in the fits [8]. RHIC is capable of delivering 900 pb^{-1} in 14 weeks running using a dynamic β* squeeze [9] through the fill. Future STAR measurements of weak boson production , with a much higher collected luminosity (for projections see [10]), can lead to the first experimental test of the sign change of the Sivers function. Furthermore, it will provide an ideal tool to study the spin-flavor structure of sea quarks inside the proton, in an x-range where the measured asymmetry in the $\bar{u}$ and $\bar{d}$ unpolarized sea quark distribution [11] can only be explained by strong non-pQCD contributions.

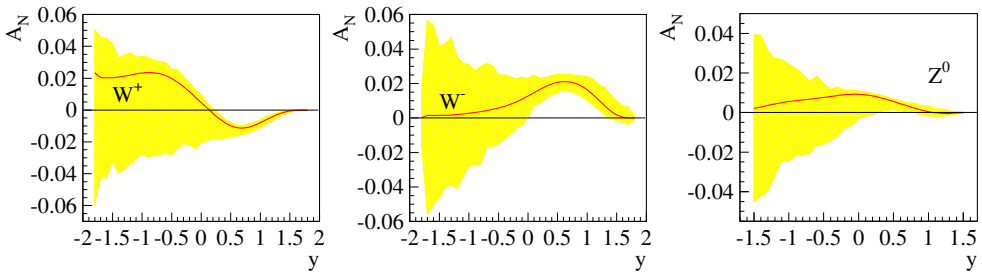

Figure 2: Theoretical prediction of A_N for $W^{\pm}$ and Z^0 boson production in p+p collisions at $\sqrt{s}$ = 500 GeV including TMD-evolution [7].

References

[1] D. W. Sivers, Phys. Rev. **D41**, 83 (1990), 43, 261 (1991)
[2] M. Anselmino *et al.*, Eur. Phys. J. **A39**, 89 (2009)
[3] J. C. Collins, Phys. Lett. **B536**, 43 (2002)
[4] Z.-B. Kang and J. -W. Qiu, *Phys. Rev. Lett.* **103**, 172001 (2009)
[5] L. Adamczyk *et al.*,The STAR Collaboration, arXiv:1404.6880 [nucl-ex]
[6] Bültmann S *et al.*, Phys. Lett. **B632** 167 (2006)
Bültmann S *et al.*, Phys. Lett. **B647** 98 (2007)
Ohlsen G G and Keaton Jr P W, Nucl. Instr. Meth. **109** 41 (1973)
[7] M. G. Echevarria, A. Idilbi, Z.-B. Kang, I. Vitev, Phys. Rev. D**D89**, 074013 (2014)
[8] Z.-B. Kang, private communication
[9] D. Trbojevic, J. Yichao, Y. Luo, BNL-102458-2013-CP
[10] S. Fazio and D. Smirnov (for the STAR Collaboration), PoS (DIS2014) 237
[11] E. A. Hawker *et al.*, Phys. Rev. Lett. **80**, 3715 (1998)

The OZI Rule and Spin Alignment of Vector Mesons at COMPASS

Karin Schönning[1] for the COMPASS collaboration

[1]Dept. of Physics and Astronomy, Uppsala University, Box 516, 751 20 Uppsala, Sweden and CERN, 1211 Geneve 23, Switzerland

DOI: http://dx.doi.org/10.3204/DESY-PROC-2014-04/36

The reaction $pp \to pVp$ ($V = \omega$, ϕ) has been studied with the COMPASS spectrometer in 2008 and 2009, using a 190 GeV/c proton beam impinging on a liquid hydrogen target. The measured cross section ratio ratio violates the OZI prediction by a factor of ≈4. Its kinematic dependence of the Feynman x_F and the M_{pV} mass is discussed in terms of diffractive production of baryon resonances in competition with central production. The $M_{p\omega}$ spectrum has a rich structure, indicating the importance of baryon resonances decaying into $p\omega$, in sharp contrast to the structureless $M_{p\phi}$ spectrum. Outside the resonant region, the OZI violation factor is about 8, independently of x_F. The spin density matrix element ρ_{00} of the vector mesons is studied in selected reference frames. Dependences of the vector meson spin alignment on x_F and M_{pV} are found.

The Okubo-Zweig-Iizuka (OZI) rule [1] states that all hadronic processes with disconnected quark lines are suppressed. As a consequence, the production of ϕ mesons from non-strange hadrons would only be allowed due to its deviation from ideal mixing with the ω meson. Using the known deviation of the mixing angle, $\delta_{\mathrm{V}} = 3.7^{\circ}$, the cross section ratio for ϕ and ω production is predicted to be $\sigma(AB \to X\phi)/\sigma(AB \to X\omega) = \tan^2 \delta_{\mathrm{V}} = 0.0042$, where A, B and X are non-strange hadrons [2]. At low energies, the ratio can be expressed in terms of meson-meson or meson-nucleon couplings: $g^2_{\phi\rho\pi}/g^2_{\omega\rho\pi} = g^2_{\phi NN}/g^2_{\omega NN} = \tan^2 \delta_{\mathrm{V}} = 0.0042$, assuming the coupling ratios $g_{\phi\rho\pi}/g_{\omega\rho\pi}$ and $g_{\phi NN}/g_{\omega NN}$ are equal [3].

The OZI rule has been tested in several experiments and has been found to be remarkably well fulfilled [4, 5]. Apparent violations of the OZI rule – observed in $p\bar{p}$ annihilations at rest and in nucleon-nucleon collisions – can be interpreted either as a true violation due to gluonic intermediate states [6] or as an evasion from the OZI rule because of a hidden strangeness component in the nucleon [7].

The COMPASS collaboration here presents a study of the OZI violation in $p_{\mathrm{beam}}\, p_{\mathrm{target}} \to p_{\mathrm{fast}}\, V\, p_{\mathrm{recoil}}$ at a beam momentum of 190 GeV/c. For simplicity, this will from now on be denoted $p\,p \to p\,V\,p$. Unless otherwise stated explicitly, p without subscript and the Feynman variable $x_{\mathrm{F}} = p_L/p_{L\mathrm{max}}$, p_L denoting the longitudinal momentum, will refer to the fast proton. The reduced 4-momentum transfer squared is $t' = |t| - |t|_{\mathrm{min}}$, where $t = (p_{p\mathrm{beam}} - (p_{p\mathrm{fast}} + p_V))^2$. In the region where the COMPASS data are collected, *i.e.* $t' > 0.1$ (GeV/c)^2, production of vector mesons occur either by resonant production, where the beam proton dissociates diffractively to an intermediate baryon resonance, or non-resonant production, which can be either central Pomeron-Reggeon fusion or a shake-out of a $q\bar{q}$ pair [7] from the sea of the beam nucleon when interacting with a Pomeron or a Reggeon emitted from the

target. In resonant production, the dynamics of the vector meson depends on the intermediate baryon resonance whereas in non-resonant production it depends on the exchange object(s).

The production mechanism is reflected in the decay angular distributions which can be expressed in terms of the spin density matrix [8]. When the inital state is unpolarised, symmetries leave one independent element of the spin density matrix, ρ_{00}, which is a measure for spin alignment (tensor polarisation). It can be extracted from distributions of the angle between the decay plane (3-body decay) or decay axis (2-body decay) of the vector meson and a well-chosen reference axis [9].

The COMPASS spectrometer set-up [10] is suitable for this kind of measurements due to the large angular acceptance and high momentum resolution. COMPASS is a two-stage fixed-target magnetic spectrometer at the CERN SPS. The analysis is based on the 2008 and 2009 data taking with a positively charged hadron beam impinging on a liquid hydrogen target. The hadron beam contains 75% protons which are tagged by CEDARs (differential Cherenkov detectors). Pions, protons and kaons in the final state are identified with a RICH detector in the first stage and electromagnetic (ECAL) and hadronic calorimeters in both stages of the set-up. The trigger system selects events with a recoiling proton in a cylindrical time-of-flight detector surrounding the target (RPD) which results in a minimum bias on the forward kinematics. Since the ω and ϕ mesons are measured simultaneously with the same set-up and triggers, many systematic uncertainties cancel.

For the analysis, events from the reactions $pp \rightarrow p\,\omega\,p$, $\omega \rightarrow \pi^+\pi^-\pi^0$ and $pp \rightarrow p\,\phi\,p$, $\phi \rightarrow K^+K^-$ are selected. The recoil proton is detected in the RPD, whereas charged pions, kaons and fast protons are detected in the spectrometer. RICH identification is required for the π^+ from the ω decay and the K^+ from the ϕ decay. The π^0 mesons from the ω decays are identified from the invariant mass distribution of two photons detected in the ECAL's. The ω mesons are identified from the $\pi^+\pi^-\pi^0$ invariant mass distribution and the ϕ mesons from the K^+K^- mass distribution. Additional cuts on exclusivity and coplanarity are applied. The x_F is required to lie within the interval 0.6-0.9 and t' within 0.1-1.0 $(\mathrm{GeV/c})^2$ to assure that the ϕ and the ω samples belong to the same phase space region. To separate signal from background, a Breit-Wigner function folded by a gaussian on top of a polynomial background has been fitted to the data. The acceptance is corrected for event-by-event using a 3-dimensional acceptance matrix in t', $M_{p\mathrm{V}}$ and x_F. The systematic uncertainties are estimated to 12%, where the largest contributions come from the RICH and ECAL efficiencies. More details on the analysis is given in Refs. [11, 12].

The invariant mass of the pV system, M_{pV}, has been studied for ω and ϕ. In the case of the ω, the data are divided into four different ranges in x_F (0.2-0.6, 0.6-0.7, 0.7-0.8 and 0.8-0.9). Several structures are then discernible in the $M_{p\omega}$ spectrum, located at about 1800 $\mathrm{MeV/c^2}$, 2200 $\mathrm{MeV/c^2}$ and 2600 $\mathrm{MeV/c^2}$. These can be interpreted as N^* resonances that have been observed in other experiments, mainly in $N\pi$ final states [13]. The $M_{p\phi}$ spectrum appears structureless.

The cross section ratio $R_{\phi/\omega} = \frac{d\sigma(p\,p \rightarrow p\,\phi\,p)/dx_\mathrm{F}}{d\sigma(p\,p \rightarrow p\,\omega\,p)/dx_\mathrm{F}}$ has been measured in three x_F intervals: 0.6-0.7, 0.7-0.8 and 0.8-0.9. The OZI violation factor is defined as the cross section ratio divided by the value predicted by the OZI rule: $F_\mathrm{OZI} = R_{\phi/\omega}/\tan^2\delta_\mathrm{V}$, with $\tan^2\delta_\mathrm{V} = 0.0042$. The results are shown in Figure 1. The ratio is between 2.9 and 4.5 and depends on x_F. The abundance of intermediate baryon resonances in ω production, observed in the $p\omega$ mass spectrum, suggests that resonant production is dominant in the case of ω but not for ϕ. In order to compare ω and ϕ samples produced with the similar mechanisms, the resonant region was removed by imposing a cut in the momentum of the vector meson in the rest frame of the

proton - vector meson system, p_V. This is shown in the left panel of Fig. 1. Since no structures are observed in the $M_{p\omega}$ spectrum above $M_{p\omega} = 3.3$ GeV/c^2, which corresponds to $p_V = 1.4$ GeV/c, the F_{OZI} factor was measured for $p_V > 1.4$ GeV/c. In this region, the value of F_{OZI} converges to about 8, independent of x_F. The SPHINX collaboration used $p_V > 1.0$ GeV/c [14] and we therefore carried out the same measurement for comparison. The COMPASS result is consistent with SPHINX [11].

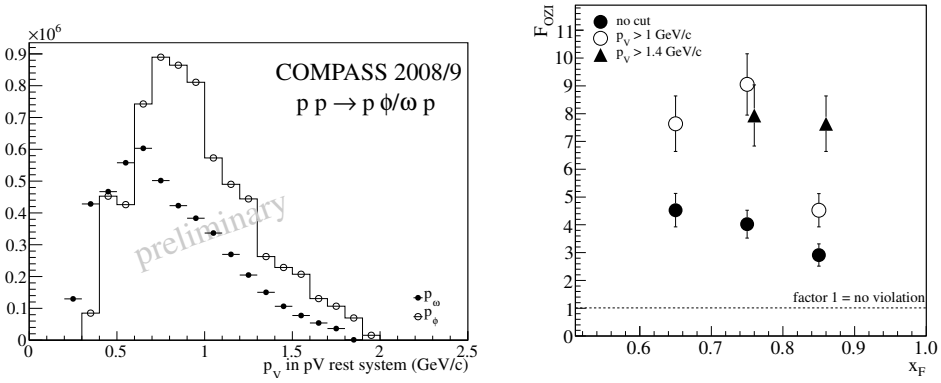

Figure 1: Left: The vector meson momentum p_V in the rest frame of the pV system, where V refers to ϕ (white dots) or ω (black dots. The ϕ histogram has been scaled by a factor of 100. Right: OZI violation factor F_{OZI} as a function of x_{F} for different p_V cuts.

The spin alignment, quantified by the first element of the spin denisty matrix, ρ_{00}, has also been measured. The differential cross section can be parameterised in terms of ρ_{00} and the angle between the analyser (the normal of the decay plane in the case of the $\omega \to \pi^+\pi^-\pi^0$ decay and the direction of one of the decay kaons in the case of the $\phi \to K^+K^-$ decay) and some reference axis. Two different reference axes have been tested: the direction of the pV system in the rest system of V (the helicity frame) and the direction of the transferred momentum from the beam proton to the fast proton, $\Delta\vec{P}$ (the transferred momentum frame). The ω meson is significantly aligned in the helicity frame and the value of ρ_{00} depends strongly on $M_{p\omega}$, as shown in the left panel of Figure 2. This is in line with the abundance of structures in the $M_{p\omega}$ spectrum and emphasises the importance of intermediate baryon resonances in the production of ω mesons. Above the resonant region, ρ_{00} approaches 1/3 which corresponds to an unaligned ω spin. The ϕ meson spin is unaligned in the helicity frame in the two measured $M_{p\phi}$ intervals, consistent with the absence of resonances in the $M_{p\phi}$ spectrum [11]. In non-resonant production, the helicty frame becomes irrelevant since the pV system does not correspond to a resonant state. In such cases, the transferred momentum frame should be a more natural choice. The results, presented in the right panel of Figure 2, show that this is indeed the case for both ω and ϕ. The ϕ meson spin is strongly aligned in this frame and the alignment becomes stronger with increasing x_F, *i.e.* when the contribution from central production increases. The results for the ω meson spin show the same behavious though the alignment is weaker than for ϕ. After removing the resonant region in the ω data, the results are consistent with those of the ϕ meson.

To summarise, this study shows that intermediate baryon resonances play a very important role in the production of ω mesons. This is supported by structures in the $M_{p\omega}$ spectrum, the p_V dependence of the OZI violation factor and the strong $M_{p\omega}$ dependence of the ω meson spin alignment in the helicity frame. The corresponding measurement for ϕ indicates an absence

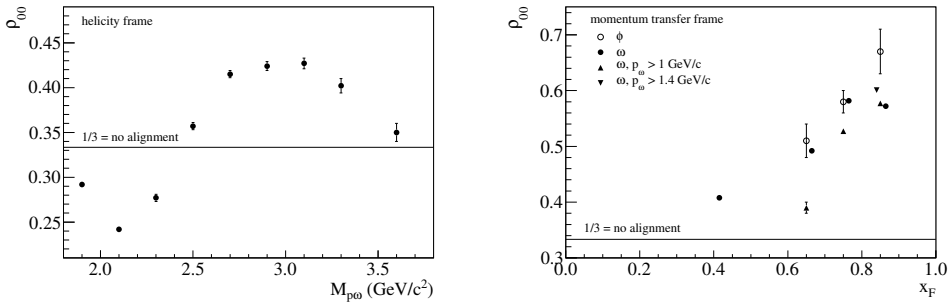

Figure 2: Left: Spin alignment ρ_{00} as a function of $M_{p\omega}$. Right: Spin alignment ρ_{00} extracted using $\Delta\vec{P}$ as reference axis as a function of x_F for different p_V cuts.

of baryon resonances in ϕ production. Other processes, *e.g.* central Reggeon-Pomeron fusion or the shake-out of a $q\overline{q}$ state in the nucleon sea may instead contribute here. The strong x_F dependence of the spin alignment with respect to the transferred momentum from the beam proton to the fast proton speaks in favour of the former. The latter could be investigated by comparing the results presented here, obtained with a proton beam, to results obtained with a pion beam. With a pion beam, no contribution from a $q\overline{q}$ shake-out can occur.

Another interesting finding is that outside the $p\omega$ resonant region, the OZI violation factor converges to a value of about 8, independently of x_F. This is in remarkable agreement not only with the SPHINX analysis [14] after removal of the low-$M_{p\omega}$ region, but surprisingly also with data close to threshold from ANKE [15], DISTO [16] and COSY-TOF [17, 18].

References

[1] S. Okubo, Phys. Lett. **5** (1963) 165; G. Zweig, Developments in the Quark Theory of Hadrons, Volume 1. Edited by D. Lichtenberg and S. Rosen. pp. 22-101; J. Iizuka, Prog. Theor. Phys. Suppl. **37** (1966) 21.

[2] H. J. Lipkin, Int. J. Mod. Phys. E **1** (1992) 603.

[3] H. J. Lipkin, Phys. Lett. B **60** (1976) 371.

[4] V. P. Nomokonov and M. G. Sapozhnikov, Phys. Part. Nucl. **34** (2003) 94 [Fiz. Elem. Chast. Atom. Yadra **34** (2003) 189].

[5] A. Sibirtsev and W. Cassing, Eur. Phys. J. A **7** (2000) 407.

[6] S. J. Lindenbaum, Nuovo Cim. A **65** (1981) 222.

[7] J. R. Ellis, M. Karliner, D. E. Kharzeev and M. G. Sapozhnikov, Phys. Lett. B **353** (1995) 319; J. R. Ellis, M. Karliner, D. E. Kharzeev and M. G. Sapozhnikov, Nucl. Phys. A **673** (2000) 256.

[8] K. Gottfried and J. D. Jackson, Nuovo Cim. **33** (1964) 309.

[9] K. Schilling, P. Seyboth and G. E. Wolf, Nucl. Phys. B **15** (1970) 397 [Erratum:ibid. B **18** (1970) 332].

[10] P. Abbon *et al.* [COMPASS Collaboration], Nucl. Instrum. Meth. A **577** (2007) 455.

[11] C. Adolph *et al.* [COMPASS Collaboration], Nucl. Phys. B **886** (2014) 1078.

[12] J. Bernhard, Ph.D. thesis, Mainz University (2014).

[13] J. Beringer *et al.* [Particle Data Group Collaboration], Phys. Rev. D **86** (2012) 010001.

[14] S. V. Golovkin *et al.*, Z. Phys. A **359** (1997) 435.

[15] M. Hartmann *et al.* [ANKE Collaboration] Phys. Rev. Lett. **96** (2006) 242301

[16] F. Balestra *et al.* [DISTO Collaboration], Phys. Rev. C **63** (2001) 024004

[17] S. Abd El-Samad *et al.* [COSY-TOF Collaboration], Phys. Lett. B **522** (2001) 16

[18] M. Abdel-Bary *et al.* [COSY-TOF Collaboration], Phys. Lett. B **647** (2007) 351

Studies of light Mesons at COMPASS

Sebastian Uhl on behalf of the COMPASS Collaboration

Technische Universität München, James-Franck-Straße, 85748 Garching, Germany

DOI: http://dx.doi.org/10.3204/DESY-PROC-2014-04/118

The COMPASS experiment has taken a large data set with a negative pion beam impinging on a liquid-hydrogen target to study the spectrum of light mesons in diffractive dissociation reactions. The properties of known resonances are studied, and new, possibly spin-exotic states are searched in three-pion final states. A new state at about $1.4\,\mathrm{GeV}/c^2$ with a_1 quantum numbers is observed in the decay to $f_0\,(980)\,\pi$. The spin-exotic 1^{-+} wave is investigated in order to search for the controversial $\pi_1\,(1600)$.

1 Introduction

The **Co**mmon **M**uon and **P**roton **A**pparatus for **S**tructure and **S**pectroscopy (COMPASS) is a fixed-target experiment located at CERN's Super Proton Synchrotron (SPS). It is aimed to study the structure and dynamics of hadrons. The spectrum of light mesons is investigated using reactions of a negative hadron beam, consisting mostly of pions, with a liquid-hydrogen target. Isovector states are diffractively produced and dissociate into multi-particle final states. The decay products are detected in a two-stage magnetic spectrometer equipped with an electromagnetic and hadronic calorimeter in each spectrometer stage [1]. The apparatus provides full coverage for charged and neutral particles, resulting in a homogenous acceptance over a rather wide kinematic range.

The diffractive dissociation of a beam pion into a three-pion final state is the dominant reaction in the data COMPASS collected by impinging a $190\,\mathrm{GeV}/c$ pion beam on a liquid-hydrogen target. A recoil-proton detector in the trigger selected events with a reduced four-momentum transfer squared t' from the beam to the target between 0.1 and $1.0\,\mathrm{GeV}^2/c^2$. In COMPASS the three-pion final state can be detected simultaneously in two different channels, $\pi^-\pi^-\pi^+$ and $\pi^-\pi^0\pi^0$. About 50 million exclusive $\pi^- p \to \pi^-\pi^-\pi^+ p$ and 3.5 million exclusive $\pi^- p \to \pi^-\pi^0\pi^0 p$ have been recorded.

The process is sketched in Fig. 1. The beam pion is excited to an intermediate state X^-, which subsequently decays into three pions. In order to study the intermediate state a partial-wave analysis using the isobar model is employed, decomposing the three-pion spectrum into its spin-parity components. In the isobar model the decay of the state X^- happens via successive two-body decays. In the case of the three-pion final state, X^- first decays to a bachelor pion and an isobar $R_{\pi\pi}$, which then decays to two pions. The $\rho\,(770)$, $f_0\,(980)$, $f_2\,(1270)$, $f_0\,(1500)$, $\rho_3\,(1690)$, and a broad $(\pi\pi)_S$ component are used as isobars in the present analysis. The fit model considers partial waves with the spin J of X^- up to 6. Also the relative orbital angular momentum L between the isobar $R_{\pi\pi}$ and the bachelor pion can go up to 6. Of the possible combinations, 87 waves with non-negligible intensity are kept for the final analysis:

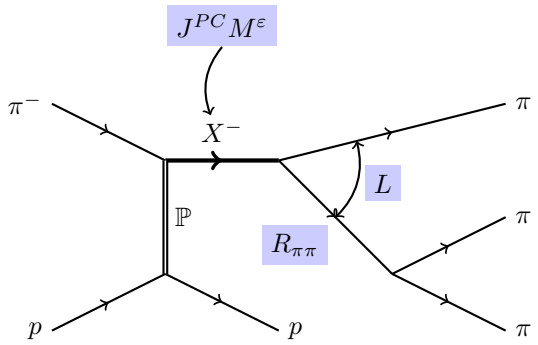

Figure 1: Sketch of the diffractive dissociation process under study.

80 with a positive reflectivity $\varepsilon = +1$ and 7 with $\varepsilon = -1$. In addition one incoherent wave with an isotropic angular distribution is included. The wave names $J^{PC}M^{\varepsilon}R_{\pi\pi}\pi L$ encode the quantum numbers of the intermediate state X^- and the information on the decay channel. The three-pion mass range between 500 and 2500 MeV/c^2 is divided into bins of 20 MeV/c^2 for the $\pi^-\pi^-\pi^+$ channel, and 40 MeV/c^2 for the $\pi^-\pi^0\pi^0$ channel. In addition the data are also divided into eleven bins of t' for $\pi^-\pi^-\pi^+$ and eight bins for $\pi^-\pi^0\pi^0$, such that all bins contain approximately the same number of events. The general features of this partial-wave analysis fit have been described before [2, 3].

2 The spin-exotic $J^{PC} = 1^{-+}$ wave

The existence of the $\pi_1(1600)$ is disputed. Previous experiments have claimed its observation [4], but could not reproduce this result on a larger sample with an extended set of waves in a limited range of t' [5]. COMPASS has also observed this state scattering a pion beam off a lead disk [6].

The partial-wave intensity of the spin-exotic $1^{-+}1^+\rho(770)\pi P$ wave found in the liquid-hydrogen data used for the present analysis is depicted in Fig. 2 (blue points) for the $\pi^-\pi^-\pi^+$ channel. A strong dependence of the intensity on the squared four-momentum transfer t' is observed. At lower values of t' only a broad structure is found, whereas when going towards higher t' a bump above 1600 MeV/c^2 is becoming more evident. This behavior is also observed in the $\pi^-\pi^0\pi^0$ channel.

Such a behavior could be caused by the interference of a genuine resonance with a large non-resonant contribution, for which the Deck effect [7] is a possible explanation. In order to study this Monte Carlo events were generated using the model from [8]. The same partial-wave decomposition was performed as for real data. The contribution to the exotic wave is displayed in Fig. 2 (green points). The intensity of the Deck model has been rescaled such that the total intensities in this wave over all mass and t' bins match. At lower values of t' a large part of the intensity can be described as coming from the Deck effect by this ansatz, at higher t' it is almost negligible.

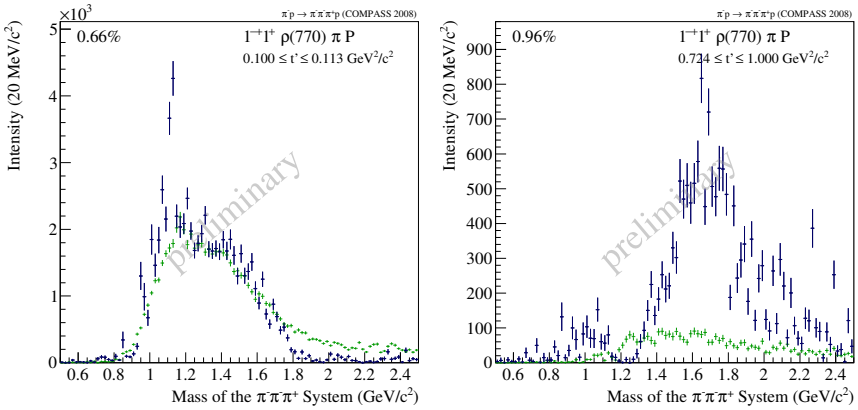

Figure 2: Partial-wave intensity of the spin-exotic $1^{-+}1^{+}\rho\,(770)\,\pi P$ wave (blue points) overlaid with a projection of a simulated Deck-effect into this wave (green points) for the lowest (left) and the highest (right) t' bin.

3 A new axial-vector state $a_1\,(1420)$

Compared to the previous COMPASS analysis [6] the number of partial-waves has almost been doubled. This is owed to the huge number of events allowing us to search also for smaller signals. One particularly interesting signal was found in the $1^{++}0^{+}f_0\,(980)\,\pi P$ wave. Fig. 3 shows the intensity of this wave for the two channels $\pi^-\pi^-\pi^+$ and $\pi^-\pi^0\pi^0$. A narrow structure around $1400\,\mathrm{MeV}/c^2$ is observed in both channels. In addition to the peak in the intensity spectrum, also rapid phase-motions with respect to the other waves are observed. This previously unobserved signal would correspond to a new state $a_1\,(1420)$. Different parameterizations for the isobar, in particular for the $f_0\,(980)$ and the broad $(\pi\pi)_S$ component have been tested in order to exclude a possible artifact from the used model.

Resonance parameters for this state and some well-known resonances are extracted from a fit of Breit-Wigner amplitudes to a subset of the spin-density matrix for the $\pi^-\pi^-\pi^+$ channel. This fit does not only describe the intensities of the individual waves, but also takes into account the interference between them. In the current analysis six waves are used, at least one resonant contribution is put into each wave: the $a_1\,(1260)$ and an a_1' in the $1^{++}0^{+}\rho\,(770)\,\pi S$ wave, the $a_2\,(1320)$ and an a_2' in the $2^{++}1^{+}\rho\,(770)\,\pi D$, the $\pi_2\,(1670)$ and $\pi_2\,(1880)$ in the $2^{-+}0^{+}f_2\,(1270)\,\pi S$, the $\pi\,(1800)$ in the $0^{-+}0^{+}f_0\,(980)\,\pi S$, the $a_4\,(2040)$ in the $4^{++}1^{+}\rho\,(770)\,\pi G$, and finally the new $a_1\,(1420)$ in the $1^{++}0^{+}f_0\,(980)\,\pi P$ wave. In addition there is one non-resonant contribution in each wave. The Breit-Wigner parameters are obtained from a simultaneous χ^2 fit to the spin-density submatrix of the six waves in all t' bins.

The extracted parameters of the major resonances are in agreement with previous measurements by COMPASS and other experiments [6]. Fig. 3 shows the result from this fit for the new $a_1\,(1420)$. A well determined mass of $M = 1412 - 1422\,\mathrm{MeV}/c^2$ and a narrow width of $\Gamma = 130 - 150\,\mathrm{MeV}/c^2$ is obtained. This is in contrast to other signals of similar magnitude like the a_1', the a_2' or the $\pi_2\,(1880)$ for which a larger uncertainty in mass and width is retrieved from the same fit.

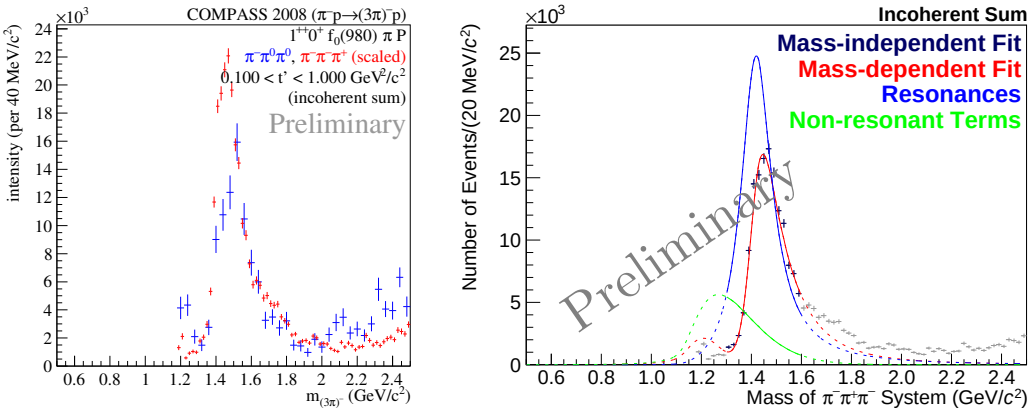

Figure 3: Left: Partial-wave intensity of the $1^{++}0^+ f_0\,(980)\,\pi P$ wave for the $\pi^-\pi^0\pi^0$ (blue) and the $\pi^-\pi^-\pi^+$ (red) channel. Right: Mass-dependent fit for the $\pi^-\pi^-\pi^+$ channel.

4 Conclusions

COMPASS has collected a huge data set of three-pion events to study the spectrum of light mesons. A possible new resonance with a_1 quantum numbers with a mass around $1420\,\mathrm{MeV}/c^2$ and a width below $150\,\mathrm{MeV}/c^2$ is found in the $f_0\,(980)\,\pi P$ decay mode. Compared to other small resonances the parameters are well constrained. The corresponding wave shows a rapid phase-motion with respect to the reference waves. The t'-resolved analysis provides valuable insight into the spin-exotic candidate $\pi_1\,(1600)$. Large parts of the intensity found in the corresponding wave at lower t' can be described with the Deck effect, which vanishes at higher t'. Work is ongoing to make a statement on the resonant nature of this state.

Acknowledgments

The author acknowledges financial support by the German Bundesministerium für Bildung und Forschung (BMBF), by the Maier-Leibnitz-Laboratorium der Universität und der Technischen Universität München, and by the DFG Cluster of Excellence "Origin and Structure of the Universe" (Exc153).

References

[1] COMPASS collaboration, P. Abbon *et al.*, Nucl. Instrum. Meth. A **577**, 455 (2007), arXiv:hep-ex/0703049; COMPASS collaboration, P. Abbon *et al.*, submitted to Nucl. Instrum. Meth. A, arXiv:1410.1797.

[2] S. Paul on behalf of the COMPASS Collaboration, proceedings of the MENU 2013, arXiv:1312.3678.

[3] S. Uhl on behalf of the COMPASS Collaboration, PoS(Hadron 2013)087, arXiv:1401.4943.

[4] S.U. Chung *et al.*, Phys. Rev. D **65**, 072001 (2002).

[5] A.R. Dzierba *et al.*, Phys. Rev. D **73**, 072001 (2006).

[6] COMPASS collaboration, M.G. Alekseev *et al.*, Phys. Rev. Lett. **104**, 241803 (2010).

[7] R.T. Deck, Phys. Rev. Lett. **13**, 169 (1964).

[8] C. Daum *et al.*, Nucl. Phys. B **182**, 269 (1981).

Measuring Luminosity at OLYMPUS

Dmitry Khaneft[1] for the OLYMPUS Collaboration[1]

[1]Johannes Gutenberg-Universität Mainz, Mainz, Germany

DOI: http://dx.doi.org/10.3204/DESY-PROC-2014-04/144

The OLYMPUS experiment [1] seeks to provide a high-precision measurement (<1% error) of the positron-proton versus electron-proton elastic scattering cross-section ratio. This requires fine control of all systematic uncertainties, including the calculation of the luminosity. For this purpose, multiple independent subsystems were operated alongside the main spectrometer during data taking to allow for empirical determination of the luminosity as a function of time. An approximate value is computed based on the parameters of the lepton beam and gaseous target, while small-angle elastic scatters of known cross-section are counted by two sets of ionization-based detector systems. The most precise value comes from counting coincidences of high-rate (pure QED) lepton-lepton scatters using a pair of calorimetric lead fluoride Cherenkov detectors.

1 Introduction

The OLYMPUS experiment was equipped with an eight-coil toroidal magnet and detectors located in two horizontal sectors on both sides of the beamline (see Fig. 1). Each side consisted of drift chambers for particle tracking and a set of time-of-flight scintillator bars for triggering and measurements of energy deposition, particle position, and timing. Two luminosity monitors were used: symmetric Møller/Bhabha (SYMB) calorimeters at $\theta = 1.291^\circ$ and detector telescopes at 12° in both sectors, each consisting of three gas electron multiplier (GEM) detectors interleaved with three multi-wire proportional chambers (MWPCs). In additional the luminosity could be measured using the slow control system.

2 Slow control system

The slow control system (see Fig. 2a) was used to control the gas feed to the target [2]. Together with the beam current measurements and the detector live time the slow control system allowed for a luminosity measurement using the following equation:

$$\mathcal{L} = I \cdot \rho \cdot \Delta t,$$

where I is the beam current, ρ is the target density, and Δt is the measurement time. Although the slow control was not precise enough ($\pm 15\%$ absolute and $\pm 3\%$ relative uncertainty) for the cross-section ratio determination, it made possible an on-line luminosity measurement that proved useful during the data taking period.

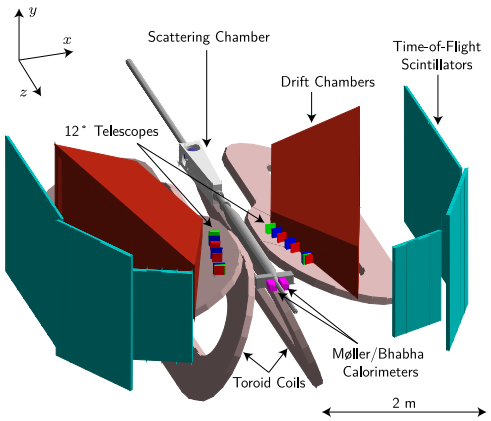

Figure 1: A solid-model representation of the OLYMPUS detector with the top four magnet coils removed to show the instrumented horizontal sectors

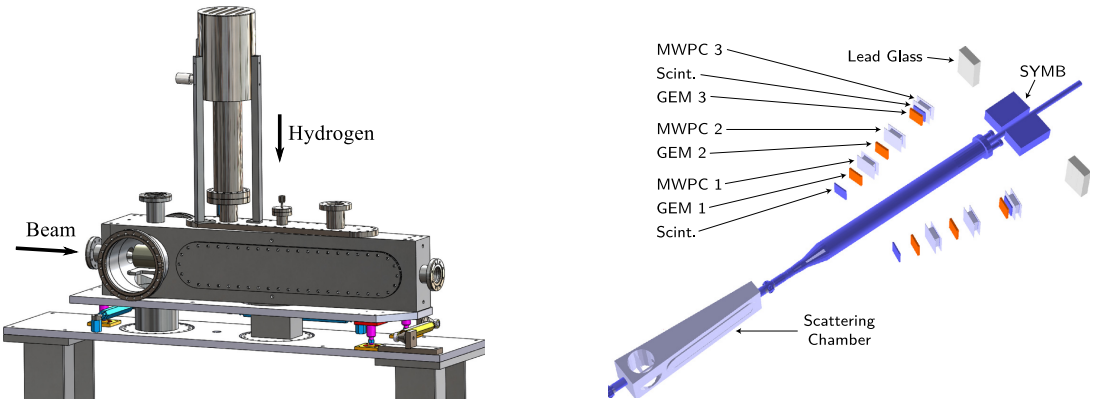

(a) (b)

Figure 2: CAD model of the OLYMPUS scattering chamber (a) and the layout of the $\theta = 12°$ luminosity monitors and the symmetric Møller/Bhabha calorimeters (b).

3 12° monitors

The 12° luminosity monitors (see Fig. 2b) measured elastic lepton-proton scattering in coincidence with the recoil proton detected in drift chambers. With a designed statistical precision of less than 1% per hour of data taking it is capable to measure the electron-proton to positron-proton elastic scattering cross-section ratio, as well as serve as a cross check for other luminosity monitors.

Fig. 3a and Fig. 3b show lepton reconstructed vertex and scattering angle. One can see that acceptance is similar for opposite beam charge and toroid polarity combinations but because the most of data were taken using positive magnet polarity a correction using a Monte Carlo simulation has to be performed.

Fig. 3c and Fig. 3d show lepton reconstructed vertex and scattering angle together with

corresponding Monte Carlo simulations, for a positive magnet polarity. The Monte Carlo results reproduce the data very well with only a small difference in scaling.

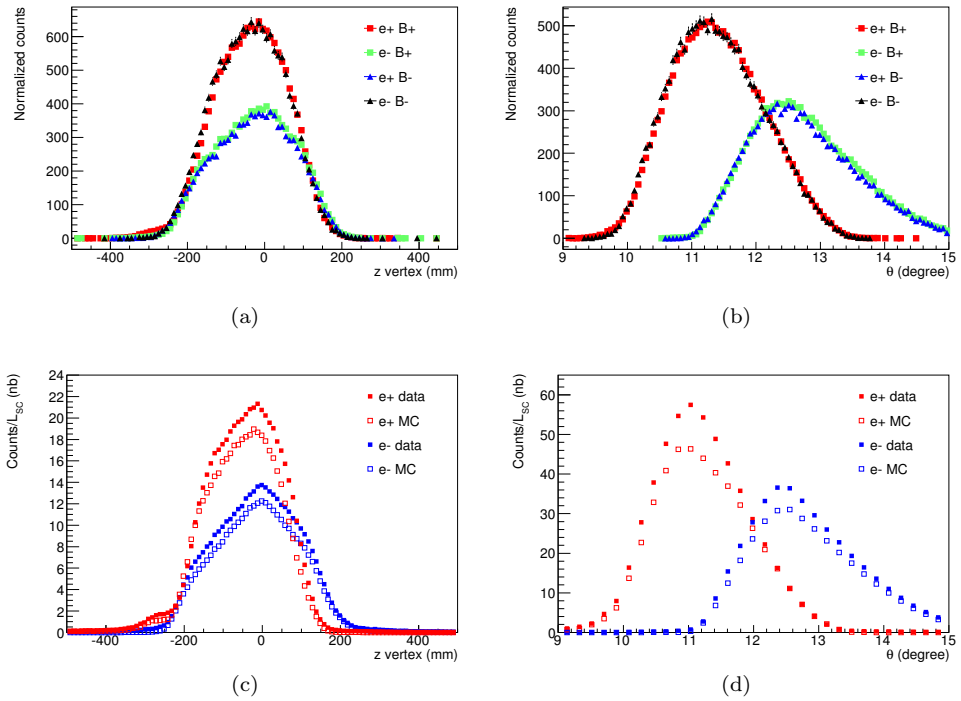

Figure 3: Lepton reconstructed vertex (a,c) and scattering angle (b,d).

4 Symmetric Møller/Bhabha monitor

Symmetric Møller/Bhabha monitor was designed for a high precision luminosity measurements. It detected lepton pairs from symmetric ($\theta = 1.29°$ for a beam energy of 2 GeV) Møller/Bhabha scattering. High event rates made possible to measure a luminosity on the timescale of minutes.

Fig. 4a shows SYMB signal in the coincidence (central crystal in both detectors should had the highest signal amplitude, i.e., contained the center of the electromagnetic shower) mode. Møller/Bhabha events can be seen as a red ellipse in the top right corner. Lines going out of the ellipse correspond to events when one of the leptons lost part of it's energy due to a collision with a collimator. Fig. 4b shows the data taken in the Master/Slave (central crystal in one of the detectors should have the highest signal amplitude) mode. In this mode electronics allowed to detect leptons from lepton-proton elastic scattering that can be seen as a yellow area at the right bottom edge of the figure.

As Møller/Bhabha cross-sections strongly depend on a scattering angle, it is crucial to know the exact position of detectors in respect to the target, as well as the offset and slope of the beam. Monte Carlo simulation (see Fig. 5a and Fig. 5b) shows counts dependency from

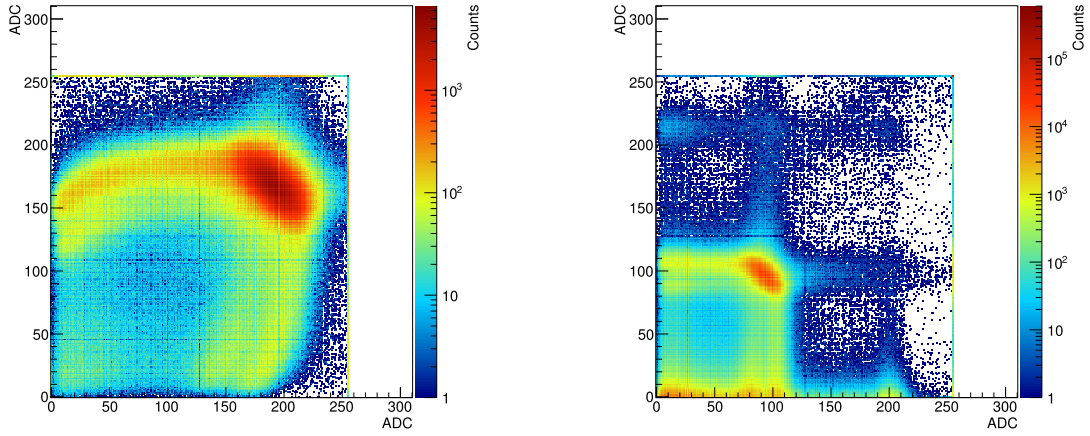

(a) (b)

Figure 4: Typical signal of the SYMB in the coincidence mode (a) and Master/Slave mode (b).

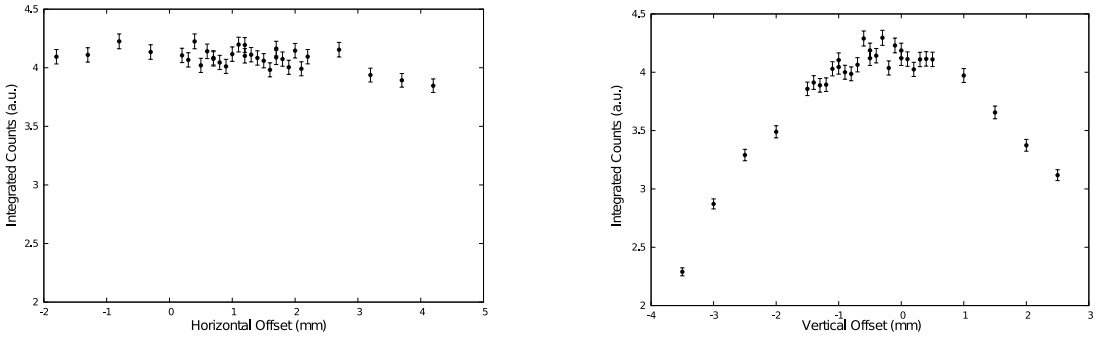

(a) (b)

Figure 5: Counts dependency from horizontal (a) and vertical (b) beam offsets.

horizontal and vertical beam offsets. It can be seen that the SYMB detector is very sensitive to the vertical beam offset, while changing horizontal position has much smaller effect.

References

[1] R. Milner, D. Hasell, M. Kohl, U. Schneekloth, N. Akopov, et al. The OLYMPUS experiment. *Nuclear Instruments and Methods in Physics Research Section A*, 741:1–17, 2014.

[2] J. C. Bernauer, V. Carassiti, G. Ciullo, et al. The OLYMPUS internal hydrogen target. *Nuclear Instruments and Methods in Physics Research Section A*, 755:20–27, 2014.